Westfälische
Wilhelms-Universität
Münster

Development, Simulation and Test of Transition Radiation Detector Prototypes for the Compressed Baryonic Matter Experiment at the Facility for Antiproton and Ion Research

Cyrano S.H. Bergmann, Dissertation 2014

Institut für Kernphysik
Westfälische Wilhelms-
Universität

Experimentelle Physik

Development, Simulation and Test of Transition Radiation Detector Prototypes for the Compressed Baryonic Matter Experiment at the Facility for Antiproton and Ion Research

Inaugural-Dissertation
zur Erlangung des Doktorgrades
der Naturwissenschaften im Fachbereich Physik
der Mathematisch-Naturwissenschaftlichen Fakultät
der Westfälischen Wilhelms-Universität Münster

vorgelegt von
Cyrano S. H. Bergmann
aus Frankfurt am Main

- 2014 -

Dekan:	Prof. Dr. M. Donath
Erster Gutachter:	Prof. Dr. J. P. Wessels
Zweiter Gutachter:	Apl. Prof. Dr. A. Khoukaz

Tag der Disputation:
Tag der Promotion:

Make things as simple as possible, but not simpler. (A. Einstein)

Inhaltsverzeichnis

1. Motivation

The motivation for all science is to fill the blank spots on the map of knowledge. Physicists all over the world are using nucleus-nucleus collision experiments and Quantum Field Theory (QFT) (namely Quantum ChromoDynamic QCD) to investigate on the blank spots in the field of strongly interacting matter under extreme conditions: high temperatures and/or high baryonic density.
At low temperatures strongly interacting matter can be described treating separated hadrons like molecules or atoms in a gas. In the regime of $T \leq 125\,\mathrm{MeV}$ this gas consists basically of pions. For higher temperatures above the critical temperature T_c ($T_c \simeq 160\,\mathrm{MeV}$ [A+09b]) the hadrons 'melt' and the gas becomes a plasma of the subcomponents, quarks and gluons. Here, the Quark-Gluon Plasma (QGP) is reached, a phase of deconfined matter, in which quarks and gluons can propagate without being bound inside color neutral objects.
There are different phase diagram predictions from the theoretical side depending on the underlying models and the region of the phase diagram (One example is presented in figure 1.1). They are compilations of results from model calculations, empirical

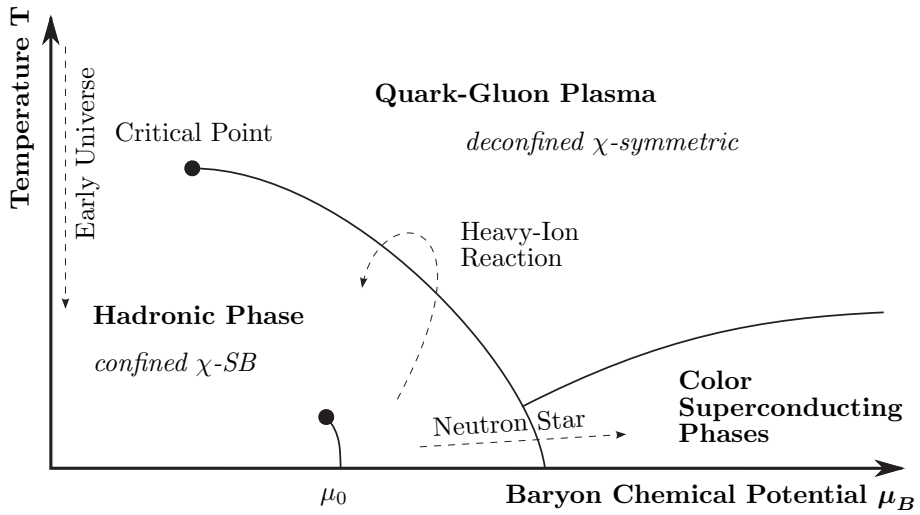

Fig. 1.1: Sketch of the QCD phase diagram. The baryon density of normal nuclear matter is located at μ_0. The phase transition between the hadron gas and QGP may end in a critical point. At high temperature and low baryon density a cross-over region is located. It is assumed that this region was passed in the early universe after the Big Bang. An other phase is expected at high baryon density and low temperatures called color superconducting phase which is expected to exist in the interior of neutron stars. Different regions of the phase diagram can be probed over short time-scales in heavy-ion collisions.

nuclear physics, as well as first principle lattice QCD calculations and perturbative calculations in asymptotic regimes as discussed in [Ste06]. Recent lattice QCD calculations at finite baryon chemical potential predict a QCD critical endpoint at $\mu_B \approx 400\,\mathrm{MeV}$ and $T \approx 160\,\mathrm{MeV}$, while other models do not exhibit a critical point. A compilation of different lattice QCD calculations as well as experimental data for kinetic freeze-out temperatures and chemical potentials are presented in figure 1.2.
One of the goals of future nuclear physics experiments is to map out the phase structure and properties of hadronic matter, as function of temperature and baryon density. A precise measurement of the dilepton invariant mass spectrum provides information on the in-medium properties of the vector-meson spectral function which could be a signal of the chiral symmetry restoration in the hot and dense matter (see chapter 1.1). The

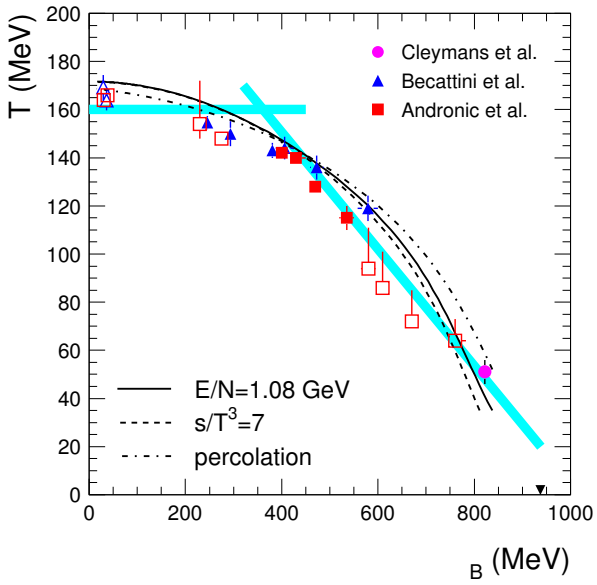

Fig. 1.2: The kinetic freeze-out temperatures and chemical potentials extracted by Statistical Model fits to experimental data. The open points are obtained from fits to mid-rapidity whereas the full-points to 4π data. The inverse triangle at T = 0 indicates the position of normal nuclear matter. The lines are different model calculations to quantify these points. The shaded lines are drawn to indicate different regimes in this diagram [A$^+$09b].

deconfinement phase transformation is expected to modify charm particle ratios such as the $\psi'/(J/\psi)$ ratio and the $(J/\psi)/D$ ratio and flow of strangeness $(K, \Lambda, \Sigma, \Xi, \Omega)$ and charm $(J/\psi, \psi', D^0, D^{\pm}, \Lambda_c)$ as well as leading to charmonium suppression, observable for J/ψ and ψ'. Lattice calculations indicate large variations of the baryon, charge and strangeness susceptibilities in the vicinity of the QCD critical endpoint. These phenomena can be related to event-by-event fluctuations of conserved quantities such as net baryon number, net charge, and net strangeness. Fluctuations of the kaon, pion and proton multiplicities measured as a function of beam energy, are expected to be sensitive indicators for the location of the critical point. In order to obtain a complete picture, a comprehensive set of observables has to be measured in proton-proton, proton-nucleus, and nucleus-nucleus collisions [FHK$^+$11].

1.1. Onset of Chiral Symmetry Restoration

A chiral (from the greek word $\chi\epsilon i\rho$ for hand) object or reaction is one that is not identical to its mirror image after reflection across a line. Chiral symmetry in particle physics characterizes the orientation of a particle's spin relative to its direction of motion. This quantity is also known as helicity $\mathcal{H}$, the projection of the spin onto the direction of the particle motion. In massless QCD helicity cannot be changed by emission or absorption of gluons. As a consequence the baryon number should be conserved for right- and left-handed quarks separately. In nature only the total baryon number is conserved, thus chiral symmetry is broken. Chiral symmetry is expected to be restored in the QGP phase where the constituent quark masses of the light u, d and s quarks vanish above T_c and only the much smaller masses generated by the Higgs field (BEH mechanism) remain as shown in figure 1.3. An *additional* spontaneous symmetry breaking is due to the strength of the strong interaction between quarks. It can be shown that the vacuum expectation value for a quark-antiquark pair is nonzero [TW01] even for vanishing quark masses. This

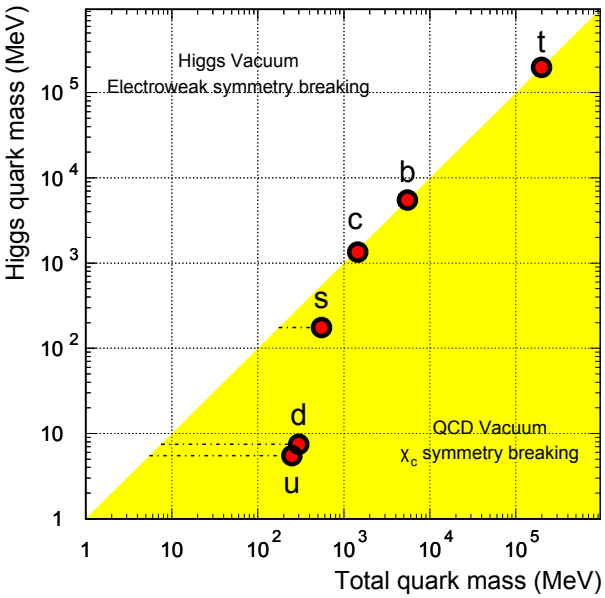

Fig. 1.3: Quark masses in the QCD vacuum and the Higgs vacuum. A large fraction of the light quark masses is due to the chiral symmetry breaking in the QCD vacuum [ZBH+07].

indicates that the ground state is restructured in a way that the chiral symmetry of the underlying QCD Lagrangian is lost. It means, that the QCD vacuum contains at any given time a finite number of $q\bar{q}$ pairs, the so-called chiral condensate with an non zero expectation value $\langle\bar{q}q\rangle$. These $q\bar{q}$ pairs can interact with a (massless) quark traversing the vacuum and change its helicity, the quark 'slows' down, as if it gained mass the so-called constituent quark masses of u and d. It has to be mentioned that the quark condensate is not an experimental observable. These constituent quark masses are two orders of magnitude larger compared to the current quark masses derived for asymptotically free quarks. As consequence of each spontaneously broken global symmetry is the existence of massless Goldstone bosons. They can be identified with the eight pseudo-scalar mesons $(\pi^{\pm}, \pi^0, K^{\pm}, K^0, \bar{K}^0, \eta)$, the eight lightest hadrons. The fact that these bosons are not massless and have instead large mass differences in nature, reflects the finite masses of the three lightest quarks, the explicit breaking of the symmetry. If the backwards transition occurs very rapidly random fluctuations between the production amplitudes of the pion isospin-triplet (π^+, π^0, π^-), different from the usual value of $N_{\pi^x}/(N_{\pi^+} + N_{\pi^0} + N_{\pi^-}) \approx 1/3$ are expected to be one possible signature for the creation of a disoriented chiral condensate (DCC). An additional observable, the chiral symmetry restoration, is an in-medium modification of the mass and decay width of the light vector mesons ρ, ω, and ϕ. The properties of these short lived mesons are accessible via the decay daughter particles [FHK+11].

1.1.1. In-Medium Modification of Light Vector Mesons

The lepton pairs from the decay of short-lived vector mesons are a good observable to study in-medium effects. The statistics of these lepton pairs is limited by the branching ratio (see table 1.1), but they provide undisturbed information on the evolution of the fireball because of their negligible final-state interactions. The in-medium modification of the meson properties have been proposed as a signature for the restoration of chiral symmetry in quark matter by R. D. Pisarski in 1982 [Pis82].
Due to their short lifetime, ρ^0 mesons have higher probability of decaying in medium,

Tab. 1.1: Properties of vector mesons [A+08b]. Branching ratios are given at the pole mass.

	Mass (MeV/c^2)	Width Γ (MeV/c^2)	$c\tau$ (fm)	Main decay	$\frac{\Gamma e^+e^-}{\Gamma_{tot}}$	$\frac{\Gamma \mu^+\mu^-}{\Gamma_{tot}}$	$\frac{\Gamma \pi^0\gamma}{\Gamma_{tot}}$
ρ^0	775.49	149.4	1.3	$\pi^+\pi^-$	$4.7 \cdot 10^{-5}$	$4.6 \cdot 10^{-5}$	$6.0 \cdot 10^{-4}$
	± 0.34	± 1.0		(99.9%)	$\pm 0.4 \cdot 10^{-5}$	$\pm 0.3 \cdot 10^{-5}$	$\pm 0.8 \cdot 10^{-4}$
ω	782.65	8.49	23.2	$\pi^+\pi^-\pi^0$	$7.2 \cdot 10^{-5}$	$9.0 \cdot 10^{-5}$	$8.9 \cdot 10^{-2}$
	± 0.12	± 0.08		(89%)	$\pm 0.2 \cdot 10^{-5}$	$\pm 3.1 \cdot 10^{-5}$	$\pm 0.2 \cdot 10^{-2}$
ϕ	1019.45	4.26	46.2	K^+K^-	$29.7 \cdot 10^{-5}$	$28.6 \cdot 10^{-5}$	$12.7 \cdot 10^{-4}$
	± 0.02	± 0.04		(49%)	$\pm 0.4 \cdot 10^{-5}$	$\pm 1.9 \cdot 10^{-5}$	$\pm 0.6 \cdot 10^{-4}$

while ω and ϕ are more likely to penetrate the fireball at moderate momenta and tend to decay outside. The extraction of pure dilepton invariant-mass spectra originating from these mesons is quite challenging since there are many hadronic sources like Dalitz decays e.g. from π^0 or other sources like γ-conversion contributing leptons to the combinatorial background. These pairs can be suppressed by their small opening angles and low masses [FHK+11].

1.1.2. Experimental Programs

The existing and ongoing experimental programs are manifold and the results are not distinct. A schematic overview on ranges covered by different experiments of the predicted amplitude of chiral condensate as function of temperature and density is presented in figure 1.4. The most important measurements carried out and foreseen in different energy

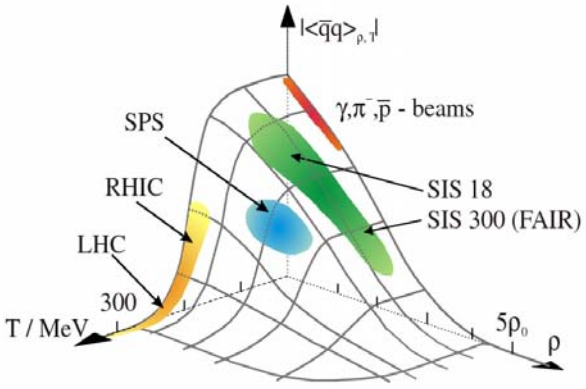

Fig. 1.4: Predicted evolution of chiral condensate $\langle \bar{q}q \rangle$ as function of temperature T given in MeV and density ρ as multiples of the nuclear density ρ_0 [Dja12]. Different regions covered by existing and planned experiments are sketched. The fully chiral symmetry restoration is predicted to be reached for $\langle \bar{q}q \rangle = 0$

ranges and collision systems will be summarized in the following. A detailed comprehensive review of different models and experimental results on in-medium modification of hadron properties has been done by Hayano and Hatsuda in *'Hadron properties in the nuclear medium'* [HH08].

The first anomalous dilepton excess of about a factor 6-7 (or factor 3 including the ρ-meson modifications in the medium) in the mass range between 0.15 and 0.4 GeV/c^2 compared with transport theory calculations was reported by the DLS (DiLepton Spectrometer) experiment at Bevalac running at 1 AGeV Ca+Ca, C+C, He+Ca, and d+Ca

in 1998 [P+97], [BCRW98]. This result has been confirmed by the HADES (High Acceptance DiElectron Spectrometer) experiment in the mass range of 0.15 to 0.5 GeV/c^2 using 1 AGeV C+C collision system [A+07]. More recent measurements of p+p and p+n and improved Hadron-String Dynamics (HSD) transport models favor an enhanced NN Bremsstrahlung cross section as the reason for the dilepton excess for beam energies between 1 and 2 AGeV [BC08]. The range between 40 and 200 AGeV was addressed at the Conseil Européen pour la Recherche Nucléaire (CERN) Super Proton Synchrotron (SPS) by the ChErenkov Ring Electron Spectrometer CERES (e^+e^- channel), HELIOS/3 and NA60 (both $\mu^+\mu^-$ channel) experiments. HELIOS/3 found in the low mass region below 0.7 GeV/c^2 a dimuon increase by $76 \pm 4\%$ in S+W relative to Minimum Bias (MB) p+W and even higher in the region above 0.7 GeV [A+00c]. The NA60 experiment resolved ω and ϕ peaks in the In+In collisions at 158 AGeV and observed a considerable broadening, but essentially no shift of the ρ-peak position [A+06], [Dam07]. CERES covered the low-mass dielectron range up to 1.5 GeV/c^2 and did not observe a dielectron enhanced in p+Be or p+Au [A+98], while a substantial excess of a factor 5 was found in S+Au collisions in the range of 0.2-1.5 GeV/c^2 [A+95], [A+08a] as shown in figure 1.5.

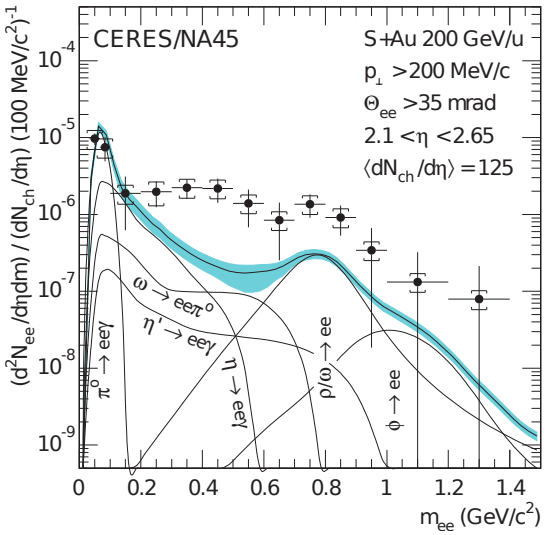

Fig. 1.5: Inclusive invariant mass spectrum of e^+e^- pairs in 200 AGeV S+Au collisions measured by the CERES experiment [A+95]. The data is represented by the full circles and the lines denote to the various contributions from hadron decays. The shaded region indicates the systematic error on the summed contributions.

This observation has been attributed to pion annihilation in the fireball with a strong in-medium modification of the intermediate ρ [BR02], such as mass dropping or broadening [RW00]. An enhancement by a factor +2.45 over the cocktail is also observed in Pb+Au at $\sqrt{s_{NN}}$=158 AGeV in the mass range of 0.2 to 1.1 GeV/c^2 [A+08a]. It was concluded that a substantial in-medium broadening of the ρ is favored over a density dependent shift of the ρ pole mass [HH08]. The Pioneering High Energy Nuclear Interaction eXperiment (PHENIX) at the Relativistic Heavy Ion Collider (RHIC) has observed a dielectron yield enhancement over the cocktail by a factor of +3.4 in Au+Au MB collisions at $\sqrt{s_{NN}}$=200 GeV in the mass range between 150 and 750 MeV/c^2 [Toi08]. In the invariant mass spectra measured by the experiment E325 at the National Laboratory for High Energy Physics in Tokyo (KEK), a 12 GeV Proton Synchrotron for C and Cu targets in proton-induced nuclear reactions, a significant excess can be seen on the low-mass side of the ω peak, which could not be fitted with the cocktail. The disappea-

rance of ρ and the appearance of the excess may be due to the in-medium dropping of the ρ mass, smearing the strength towards the excess region. For the ρ/ω region, E325 concluded that both ρ and ω masses are shifted by 9% at the normal nuclear density [N$^+$06]. Fit results favored the zero-broadening case which is in conflict with the J-Lab Continuous electron beam accelerator facility Large Acceptance Spectrometer (CLAS) g7 result [HH08]. The CLAS experiment g7 used a tagged photon beam with an energy range of 0.61-3.82 GeV on liquid deuterium, carbon, iron, titanium and lead targets. The results for the ρ spectrum are consistent with collisional broadening without mass modification [W$^+$08]. An enhancement of +1.77 is observed by the Solenoidal Tracker At RHIC (STAR) in $\sqrt{s}$=200 GeV Au+Au in the mass region of 0.30-0.76 GeV/c^2 [A$^+$13]. Significant experimental work has been done to detect the possible in-medium 'mass shift' of vector mesons, both using heavy-ion collisions and using elementary particle beams. There are still some inconsistencies clearly showing that experimental results have not yet converged to a consistent understanding of the in-medium behavior of vector mesons. Analysis of dilepton spectra of the ongoing A Large Ion Collider Experiment (ALICE) at the Large Hadron Collider (LHC) will help to complete the picture of in-medium modification of light vector mesons at high temperature but moderate density. The CBM experiment is designed to investigate on in-medium light meson modifications at high densities and low temperatures as indicated in figure 1.4.

1.2. Direct Photons

There are different sources of photons known in proton-proton and nucleus-nucleus collisions. Hadronic decays make up the overwhelming part of all photons. The most dominant decays are $\pi^0 \to \gamma\gamma$ ($\sim$ 80%) and $\eta \to \gamma\gamma$ ($\sim$ 18%). Direct photons are those photons not originating from hadronic decays. This can be subdivided by source classes called thermal photons from QGP, thermal photons from hadron gas, *mixed* non thermal photons. They are usually further classified into prompt photons produced in early hard scatterings, and thermal photons emitted from a thermally equilibrated phase. Prompt and thermal photons cannot be separated experimentally.

1.2.1. Thermal Photons

Thermal photons are emitted by the QGP as well as by the Hot Hadronic Gas (HHG) phase following the QGP phase. The mean free path of these photons inside the hot dense medium is expected to be larger compared to the size of the fireball, resulting in low interaction probability of the photons with the medium. The most probable production mechanisms of photons in the QGP are quark-gluon Compton scattering ($q + g \to \gamma + q$) and annihilation ($q + \bar{q} \to \gamma + g$). Higher order Bremsstrahlung process $q + g \to g + q^* \to g + p + \gamma$, in which a quark radiates a photon also contribute.

1.2.2. Prompt Photons

Prompt photons are produced in early hard scatterings happening before thermalisation. The basic underlying processes are the same as in the QGP. However, photons can also be produced during the fragmentation process of scattered partons. An additional source of non-thermal direct photons arises from the pre-equilibrium phase, where the theoretical description is rather difficult due to the uncertainties in the formation time of the thermalized phase. The passage of high energy quark jets through the QGP leads to Compton scattering with thermal gluons $q_{hard} + g_{QGP} \to \gamma + q$ and annihilation with

thermal antiquarks $q_{hard} + \bar{q}_{QGP} \rightarrow \gamma + g$. This has also been considered as a source for direct photons.
Direct photons provide a penetrating probe to access information on the early state and the evolution of the dense medium. In particular the transverse momentum spectra of photons are suggested to provide information on the maximum temperature of the system. There are two ways to measure photons: the classical method using an electromagnetic calorimeter, and the reconstruction of low momentum photons converted in the target or any other material via the resulting e^+e^- pair, in particular.
For CBM, the measurement of photons converted in the target material into an e^+e^- pair might be favorable as the momentum resolution from tracking is at a 1% level down to momenta of 0.5 GeV/c in simulations [KB09]. By combining two reconstructed photons π^0 and η mesons can be identified in the invariant mass spectrum. Their identification probability appends quadratically on the single-photon efficiency. Measuring photons from π^0 decay in addition to the inclusive ones is an important tool to extract direct photons as this allows the construction of double ratios as

$$\left(\frac{\gamma_{incl.}}{\gamma_{decay}}\right)_{meas.} / \left(\frac{\gamma_{incl.}}{\gamma_{decay}}\right)_{sim.} \tag{1.1}$$

in data analysis. The direct photon signal can be extracted via the subtraction method (see e.g. [Wil12]):

$$\gamma_{direct} = \gamma_{incl.} - \gamma_{decay} = \left(1 - \frac{\gamma_{decay}}{\gamma_{incl.}}\right) \cdot \gamma_{incl.} \tag{1.2}$$

This method can use the photon conversion products to measure the inclusive photon yield where the decay photon yield is estimated by a cocktail parametrization or measurements, if available. The systematic uncertainties can be minimized by using the ratio

$$\frac{\gamma_{incl.}}{\gamma_{decay}} = \left(\frac{\gamma_{incl.}}{\pi^0}\right) / \left(\frac{\gamma_{decay}}{\pi^0_{param.}}\right) \tag{1.3}$$

as it was done in ALICE. The low p_T photon signal is expected to have thermal contributions. The inverse slope parameter of an exponential fit is debated to be used to extract the average effective temperature of the collision system, in which a QGP might by created.

1.2.3. Experimental Programs

The first experimental program measuring upper limits for direct photon yields was the HELIOS experiment [Å$^+$89]. Photon yields in heavy-ion collisions have been measured by the WA80/WA93 and CERES experiments at CERN. The WA93 collaboration only measured inclusive photon spectra [VvE$^+$94]. Direct photon measurements have first been available from the WA98 collaboration which found first evidence for direct-photon production in central Pb+Pb collisions at $\sqrt{s_{NN}}$=17.3 GeV [A$^+$00a], [A$^+$00b], [A$^+$03a]. A significant direct-photon signal within statistical and systematic errors was seen at a p_T range between 1.5 GeV/c and 3.5 GeV/c. The direct-photon spectra have been determined via the statistical subtraction of the calculated yield of photons from hadron decays from the total photon yield. The NA45 Collaboration (CERES experiment) measured photon yields by the conversion method, which is described above.

Within the systematic errors of 11%, no excess of the measured inclusive p_T spectrum over the expected yield from hadronic sources has been found [Irm94]. Later, PHENIX at RHIC confirmed these results in Au+Au collisions at $\sqrt{s_{NN}}$=200 GeV using the same technique as WA98 [A$^+$05]. Moreover, in PHENIX direct photons at low p_t are observed in a measurement of internal photon conversions [A$^+$09a]. In central Au+Au collisions, an excess over p+p is observed, which is exponential in p_T, with an inverse slope parameter $T_{RHIC} = 221 \pm 23(stat) \pm 18(sys)$ MeV. A measurement of direct-photon invariant yield in Pb+Pb collisions at $\sqrt{s_{NN}}$ =2.76 TeV for 0-40% centrality for 0.8 GeV/c $< p_T <$ 2.2 GeV/c has been carried out by the ALICE experiment to determine the temperature by an inverse slope parameter $T_{LHC} = 304 \pm 51^{stat+sys}$ MeV [Wil12]. The result obtained for $\sqrt{s}$=7 TeV p+p collisions is consistent with insignificant direct-photon signal over the measured p_T range. The systematic uncertainties are too large to make a final statement about direct photon production. The double ratio in Pb+Pb at $\sqrt{s_{NN}}$=2.76 TeV shows a clear signal over the whole range of p_T. The direct-photon signal should contain a significant part of thermal photons below 4 GeV/c [Wil12]. A comparison of ALICE and PHENIX results is presented in figure 1.6.

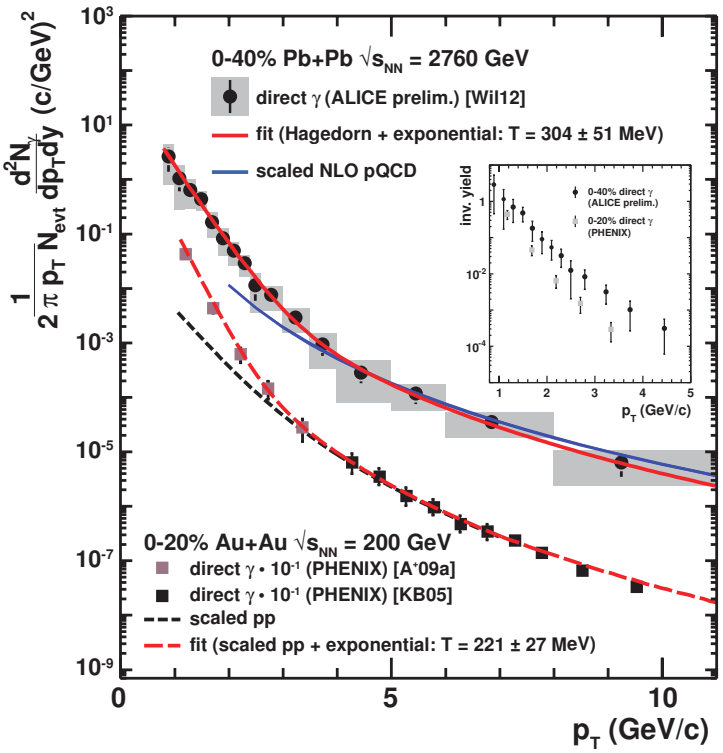

Fig. 1.6: Comparison of direct photon yield measured in central Pb+Pb [Wil12] and Au+Au collisions [KB05], [A$^+$09a]. The PHENIX data are scaled by a factor 10^{-1} in order to optimize visualization. A clear enhancement at low p_T is seen in both cases above the scaled p+p measurement and the high-p_T Next-to-Leading Order (NLO) perturbative QCD trend. It can be parameterized by an exponential with slope $T_{RHIC} = 221 \pm 27$ MeV and $T_{LHC} = 304 \pm 51$ MeV, respectively. The inset shows the direct comparison of the direct photon yield PHENIX and ALICE at low p_T without the offset factor of 10^{-1} [KB13].

The CBM experiment will offer the possibility to measure the direct photon yield with high statistical accuracy due to the very high luminosity provided by SIS100 and SIS300.

2. Facility for Antiproton and Ion Research Physics and Accelerator Program

A sketch of the Facility for Antiproton and Ion Research (FAIR) with the existing GSI facilities is presented in figure 2.1. The existing accelerators are colored in blue where

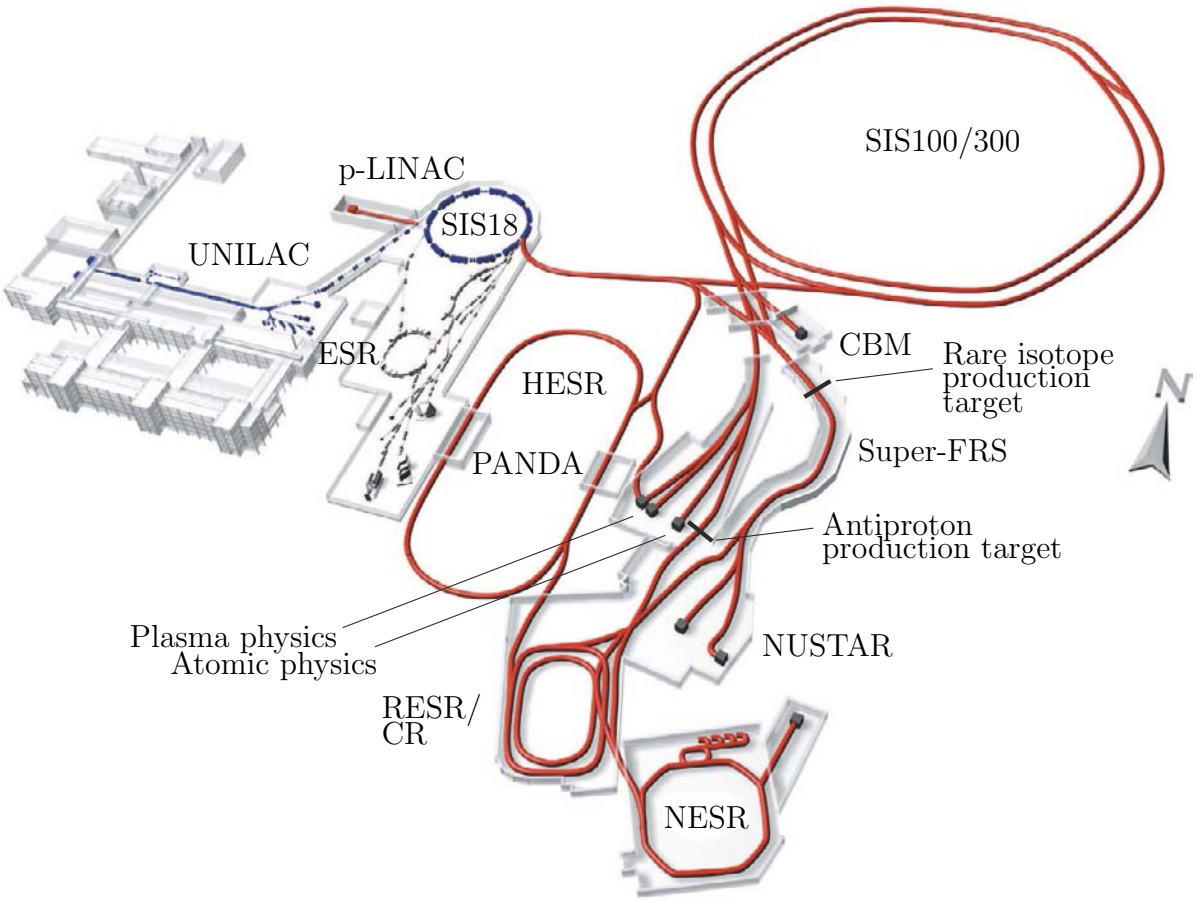

Fig. 2.1: Layout of FAIR (accelerators and beam lines in red) including the existing GSI facilities, accelerators and beam lines colored in blue [KB09].

the planed FAIR beam lines are red colored. UNILAC and SIS 18, the existing GSI accelerators, will serve as injectors for the new FAIR accelerator complex based on two synchrotrons (ø= 1083 m) with rigidities of 100 Tm and 300 Tm (SIS100/300). In addition FAIR comprises the Superconducting Fragment Separator (Super-FRS), the storage ring for antiprotons (High-Energy Storage Ring HESR), the Collector Ring (CR), and the New Experimental Storage Ring (NESR). The experimental program covered by FAIR include the anti-Proton ANhilation at DArmstadt (PANDA) detector for hadron physics experiments using cooled high-energy antiproton beams provided by the HESR, the NUclear STructure, Astrophysics and Reactions (NUSTAR) detectors used for experiments on the structure of unstable nuclei and on nuclear astrophysics, and several experimental setups for plasma physics and atomic physics and the Compressed Baryonic Matter (CBM) experiment. First beams from SIS100 are scheduled for the year 2018, from SIS300 about 2-5 years later. The available kinetic beam energy per nucleon depends on the bending power $B \cdot r$ provided by the dipole magnets:

$$E/A = \sqrt{(0.3 \cdot B \cdot r \cdot Z/A)^2 + m^2} - m \tag{2.1}$$

Z and A correspond to the charge and atomic number of the ion, and m to the mass of the nucleon. The beam energies obtained for the beam rigidity of SIS100 and SIS300 are listed in table 2.1 for different ions, which are included in the CBM physics program. The minimal available ion beam energy is about 2 AGeV. The planned average interaction rate for the SIS100 Au+Au scenario is 10^7 Hz to measure J/ψ [FHK+11].

Tab. 2.1: Ion species and their maximum kinetic energy per nucleon for a beam rigidity of 100 Tm at the SIS100 and 300 Tm at the SIS300 [FHK+11].

beam	Z	A	E at 100 Tm (AGeV)	E at 300 Tm (AGeV)
p	1	1	29	89
d	1	2	14	44
Ca	20	40	14	44
Ni	28	58	13.6	42
In	49	115	11.9	37
Au	79	197	11	35
U	92	238	10.7	34

3. The Compressed Baryonic Matter Experiment

At very high collision energies, as available at the RHIC and the LHC, the experimental focus is the study of the deconfined QCD matter at very high temperatures and almost zero net baryon densities (compare to figure 1.1). The goal of the Compressed Baryonic Matter (CBM) experiment at the Facility for Antiproton and Ion Research (FAIR) is to explore the QCD phase diagram in the region of very high baryon densities and moderate temperatures by usage of the SIS100/300 accelerator system. In particular, the experiment will focus on the search for the phase transition between hadronic matter and quark-gluon plasma and the QCD critical endpoint as mentioned in chapter 1. The maximum net-baryon density at freeze-out is expected to be reached at low CERN-SPS or FAIR energies according to an analysis of particle yields in heavy-ion collisions [RC06]. The critical freeze-out line as function of temperature and net-baryon density is shown in figure 3.1. The results indicate, the highest net-baryon density in heavy-ion experiments can be reached by using beam energies between 30 and 40 AGeV or energy between $\sqrt{s_{NN}} = 6$ and 10 AGeV. There are several experimental programs

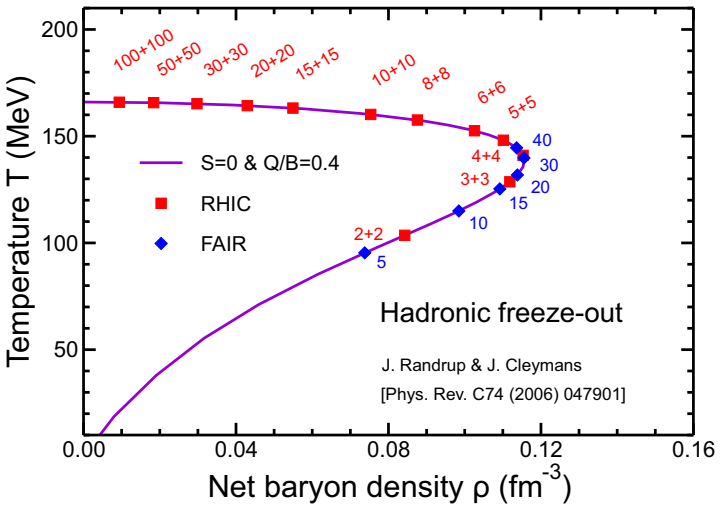

Fig. 3.1: The hadronic freeze-out line as function of temperature and net-baryon density. The values are obtained in the statistical model with experimental measurement data of μ_B and T. The purple line corresponds to Au+Au collisions at beam energies (AGeV) represented by the red (total energy of each beam for collider experiments) and blue (kinetic energy for fixed target experiments) symbols [RC06] and [RC09].

aiming to investigate the hadronic phase diagram like STAR and PHENIX at RHICH, NA61/SHINE at CERN-SPS and CBM at FAIR. The experimental programs of STAR, PHENIX and NA61/SHINE are or will be focused on bulk observables. These observables are (except for elliptic flow and photons) predominantly sensitive to the late and dilute phase of the collision. Diagnostic probes of the early dense phase of the collision are particles containing charm quarks, which are expected to be created in the very first stage of the reaction. As leptons are not affected by final-state interactions, the decay of vector mesons like ρ, ω and ϕ mesons into lepton pairs offers the possibility to investigate on the early evolution of the fireball as discussed in section 1.1. Also multi-strange hyperons are useful to study the dense phase of the collision, due to their small hadronic cross sections, in particular via their collective flow. These diagnostic probes of the early dense phase of the collision will be assessed mainly by the CBM experiment. The experimental program of CBM offers the best potential to study on signatures of partonic degrees of freedom, to study the deconfinemet phase transition and discover its critical

endpoint. Another part of the physics program of the CBM experiment is to study in-medium modifications of hadron properties. The observation of such phenomena are key observations for chiral symmetry restoration in dense hadronic and partonic matter. The measurement of these probes is quite challenging, since most of them are produced rarely, either because of the low cross section like the charmed probes or the small branching ratio into lepton pairs of ρ, ω and ϕ mesons. This demands very fast and extreme radiation hard detectors and electronics with high acceptance and online data acquisition of the CBM experiment and high beam luminosity to the FAIR accelerator. A detailed summary of the CBM experiment can be found at [Heu12]. The CBM research program consists of a comprehensive scan of observables, beam energies in different collision systems. The aim is to measure the physical observables, including charmonia and open charm, low mass dilepton pairs, but also collective flow of rare and bulk particles, correlations and fluctuations for the first time with unprecedented precision in spite of the very low multiplicities. The measurement of certain rare observables like open charm (which are the most challenging measurements) will be performed at highest reaction rates up to 10 MHz in order to compensate for the low production yields. These conditions require the development of data acquisition systems which are able to perform a high speed online tracking and selection of displaced vertices with highest precision, which are needed for open charm measurements. The experimental studies at FAIR and especially at CBM will depend on the availability of the accelerators. In the first FAIR construction stage the beams will be delivered by the SIS100 accelerator with energies up to 11 AGeV for Au, 14 AGeV for Ca, and 29 GeV for protons. A reduced version of the CBM detector will be installed foreseen to perform measurements of multi-strange hyperons in heavy-ion collisions, and of charmed particles in proton induced reactions at SIS100. The full CBM setup will be prepared in parallel to the construction of the SIS300 accelerator (beam energies of 35 AGeV for Au and 89 GeV for protons), which will be able to measure the full experimental program. A summary of different future and existing experimental programs on dense baryonic matter is listed in table 3.1.

Tab. 3.1: Energy ranges, reaction rates (limited by luminosity [ll] or limited by detector [ld]) and observables (hadrons, correlations and/or fluctuations, di-leptons, and charm) measured or to be measured at $\sqrt{s_{NN}} = 8$ GeV in Au/Pb beams by current (STAR, PHENIX, NA61/SHINE) and future experiments (MPD, HADES@FAIR, CBM) on dense baryonic matter [Höh12].

Experiment	$\sqrt{s_{NN}}$ (GeV)	Reac. rates (Hz)	Observables			
			hadrons	correl., fluct.	di-leptons	charm
PHENIX& STAR@RHIC	7-200	1-800 [ll]	✓	✓	-[1]	-
NA61/SHINE @SPS	6.4-17.4	80 [ld]	✓	✓	-	-
MPD@NICA	4-11	1000 [-[2]]	✓	✓	-	-
CBM& HADES@FAIR	2.7-8.3	10^5-10^7 [ld]	✓	✓	✓	✓

Measurements at SIS100 energies will focus on the investigation of the properties of resonance matter and the relevant degrees-of-freedom in the transition region of the

[1] ✓with the planned second beam energy scan at RHIC (BES II) after upgrading the accelerator, di-leptons might become accessible also at lower RHIC energies.

[2] design luminosity of $10^{27}\text{cm}^{-2}\text{s}^{-1}$ for HI

QCD phase diagram. The yields and momenta of hadrons will be analyzed event-wise in order to search for non-statistical fluctuations, which are predicted to occur when the system passes through second order phase transition. CBM is designed to observe the properties of hadrons as function of baryon density. First measurements of dilepton pairs using the CBM SIS100 version permit to investigate on in-medium modifications of low-mass vector mesons. Such dilepton measurements have not been performed in this energy range up to now. The equation-of-state of nuclear matter at neutron star core densities can be explored as well as charm production and propagation at threshold beam energies in nuclear collisions with proton beams of energies up to 29 GeV. These experiments will give a detailed look into production mechanism of charm-anticharm pairs at threshold energies, and the physical properties of charmed particles in nuclear matter at saturation density. The variation of the target nucleus size allow to study the propagation of charm in cold nuclear matter. Another component of the physics program at SIS100 energy is the production and observation of multi-strange hyperons [FHK+11]. The production of multi-strange hyperons like Ξ and Ω is favored at nuclear collision systems providing high densities and therefore short mean free path between consecutive collisions. This leads to a strong dependency of the multi-strange hyperon yield on the density and compressibility of baryonic matter as function of the densities. A detailed measurement of the multiplicities and the collective flow of multi-strange hyperons in heavy-ion collisions at beam energies between 2 and 11 AGeV will provide new information on the equation-of-state of nuclear matter at high densities comparable to neutron star core densities. Measurements of hadrons including multi-strange hyperons will be performed with a start version of CBM. This version will comprise the dipole magnet, the silicon tracking system, a RICH, and a time-of-flight wall [FHK+11] (see chapter 3.1).

3.1. CBM Detector Concept

The sketch of the detector setup status 2009 can be seen in figure 3.2. Main differences to

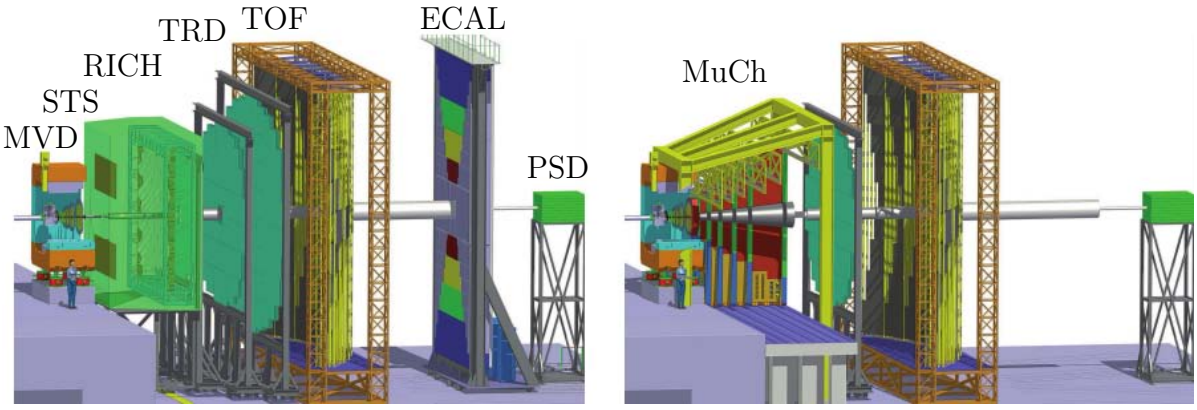

Fig. 3.2: Electron (left) and muon setup (right) for the CBM experiment planned for SIS100 at FAIR [Sen09]. The planned setups foresee a Micro-Vertex Detector (MVD), Silicon Tracking Station (STS) within the Magnet (details can be found in [Mag12]), Ring Imaging Cherenkov detector (RICH) for the electron setup, Muon Chambers (MuCh) for the muon setup, Transition Radiation Detector (TRD), RPC Time Of Flight (TOF) wall, Electromagnetic CAlorimeter (ECAL), and Projectile Spectator Detector (PSD).

the current detector development status are geometrical details e.g. final detector dimensions, services, mechanical support structures, and detector spacing as well as position in beam-direction. The detector system (two main setups) will consist of the micro-vertex

detector (MVD) for the high-precision measurement of the decay vertices of charmed hadrons. The next detector in beam direction will be a silicon tracking system (STS) with large aperture (polar angle acceptance 2.5°-25° for all azimuth angles). The STS will measure the trajectories of the produced particles in the vertical magnetic dipole field, determine their momenta and reconstruct hyperons by their decay topology. The first detector outside of the magnet will be the Ring Image CHerencov (RICH) detector identifying electrons and positrons with momenta below 8 GeV/c e.g. from the decay of low-mass vector mesons. The SIS100 start version includes an intermediate tracking and Particle IDentification (PID) detector with four (or up to 10 layers in case of SIS300) Transition Radiation Detector (TRD) layers allowing to match tracks reconstructed in the STS to the Time-Of-Flight detector (TOF). The TRD will also provide electron identification for momenta above 1.5 GeV/c. The RICH and the TRD are being designed to obtain a combined pion-rejection factor of about 10^4. This level is required in order to suppress the background from misidentified pions, such that the combinatoric is dominated by physical sources, mainly electrons created by γ-conversion and π^0 and η Dalitz decays. Hadron identification will be done based on a time-of-flight measurement which will be provided by multi-gap Resistive Plate Chambers (RPC) arranged in the TOF wall. A muon detection system (MuCh) will be used for the measurement of charmonium via its decay into muon pairs. The MuCh SIS100 version, consisting of three detector triplets and will be upgraded to the full system with six triplets for SIS300. Both the MuCh and the RICH detector will be movable in order to be used alternatively for muon or electron measurements. The direct and decay photons (e.g. from light vector mesons) will be measured by the Electromagnetic CALorimeter (ECAL). A calorimeter like the one foreseen for CBM identifies photons due to an energy loss measurement from electromagnetic showers in the sampling scintillator-lead structures. The average photon reconstruction efficiency estimated in simulations for energies $E > 0.5$ GeV is (35-40)% depending on the photon production angle [FHK+11]. A forward calorimeter, named Projectile Spectators Detector (PSD), will be used to determine the collision centrality and the reaction plane. The detector combination/layout of CBM can be modified according to the physics program. The observables and required detector sets are summarized in table 3.2.

Tab. 3.2: Observables and required detectors: Micro-Vertex Detector (MVD), Silicon Tracking Station (STS), Ring Imaging Cherenkov detector (RICH), Muon Chambers (MuCh), Transition Radiation Detector (TRD), RPC Time Of Flight (TOF) wall, Electromagnetic Calorimeter (ECAL), and Projectile Spectator Detector (PSD). Detectors marked as (x) can be used to suppress background [FHK+11].

Observables	MVD	STS	RICH	MuCh	TRD	TOF	ECAL	PSD
π, K, p		x	(x)		(x)	x		x
Hyperons	(x)	x			(x)	(x)		x
Open charm	x	x	(x)		(x)	(x)		x
$e^{\pm}$	x	x	x		x	x		x
$\mu^{\pm}$		x		x		(x)		x
γ							x	x
γ via $e^{\pm}$ conversion	(x)	x	x		x	x		x

3.1.1. Micro-Vertex Detector (MVD)

The measurement of short lived D mesons ($\tau_{D^0} = 123\,\mu$m/c and $\tau_{D^\pm} = 314\,\mu$m/c) is based on their weak hadronic decay into pions and kaons requiring a high precision secondary vertex determination. This demands excellent position resolution and very low material budget to reduce multiple scattering. These requirements are fulfilled by Monolithic Active Pixel Sensors (MAPS). The intended pixel size will be between $25 \times 25\,\mu$m^2 and $40 \times 40\,\mu$m^2 leading to a position resolution of $3\,\mu$m in case of $40\,\mu$m^2 pixels. The intended total radiation length for complete detector stations including mechanical support is a total thickness of 300-500 μm silicon equivalent. The MVD will consist of a first (optional) station at 50 mm followed by two layers at 100 and 200 mm downstream from the target. This detector concept will allow to determine the secondary decay vertex of a D meson with a resolution along the beam axis of about 50-100 μm. The actual resolution will depend on the thickness of the first MAPS station and the distance between the target and the first station. The detector has to cope with radiation dose of 10^{13} n_{eq} (equivalent of 10^{12} minimum bias Au+Au collisions at 25 AGeV). At SIS300 reaction rate the detector can be operated about 4 months. Afterwards the inner part of the first MVD layer has to be replaced. Therefore MVD will only be used and installed for dedicated parts of the CBM physics program like measurements of open charm, electron measurements and to improve hyperon identification [FHK+11].

3.1.2. Silicon Tracking System (STS)

The STS will provide track reconstruction and momentum measurement of all charged particles at multiplicities up to 600 charged particles per event within the detector acceptance. The STS is positioned in the dipole magnet with a bending power of 1 Tm. The up to date STS version consists of eight silicon detector layers located at distances relative to the target between 30 cm and 100 cm. The design goal for the momentum resolution is $\Delta p/p = 1\%$ which can only be achieved with a detector material budget limit of 400-800 μm silicon equivalent in order to reduce multiple-scattering. This results in challenging demands on the detector including front-end electronics, cooling concepts and mechanical support structures. The detector concept of STS foresees double-sided silicon micro-strip detectors with a thickness of 250-300 μm mounted on light-weight ladder-like support structures (details can be found in the STS technical design report [STS12]). Each sensor will be read-out through sandwiched polyimide-Aluminum multilayer micro-cables. The read-out electronics will be placed between the magnet and the outer parts of the STS station to guarantee sufficient cooling and power supply with a minimum material budget within the sensitive volume. The typical achieved hit resolution will be of the order of 25 μm. The material of a full detector station, including support structures, may be of about 800 μm silicon equivalent [FHK+11].

3.1.3. Ring Imaging CHerenkov detector (RICH)

The RICH detector is designed to provide electron identification with a pion suppression of the order of 500-1000 in the momentum range below 8 GeV/c. The design concept of the RICH consists of an enclosed 2.9 m long detector volume filled with CO_2 as radiator gas ($\gamma_{th} = 33$, $p_{th,\pi} = 4.65$ GeV/c), two spherical mirrors and a PhotoMultiplier Tube (PMT) array with fast self-triggered read-out electronics as photon detectors. The usable wavelength range of Cherenkov photons is limited by the self-absorption in the CO_2 radiator for $\lambda \leq 175$ nm. The Cherenkov light cones are projected to the PMT

array planes by a modular spherical glass mirror of appr. 11.8 m^2. The reflectivity at $\lambda \geq 180$ nm of the mirrors is enhanced by an Al+MgF_2 coating. The Hamamatsu H8500 MAPMT offers a good time resolution, a pixel size matching the requirements of CBM RICH, and convenient coverage of the photo detector plane of 2.4 m^2. In order to extend the sensitivity of the MAPMT down to the absorption edge of CO_2, a wavelength-shifting film coating is applied to the PMT window [H$^+$10]. A detailed description can be found in [RIC12].

3.1.4. Muon Chamber system (MuCh)

The MuCh detector system is designed to perform a momentum depending muon identification in conjunction with the STS even for lowest particle momenta. This will be done by tracking the particles trough a hadron absorber sandwich which will consist of iron plates of 60, 20, 20, 30, 35, and 100 cm thickness. The tracking will be done by triplets of gaseous tracking chambers sandwiched between the six absorber stations. The absorber/detector system has been designed as compact as possible in order to reduce the effect of meson decays into muons. The muon chambers are based on Gas Electron Multiplier (GEM) technology to cope with hit rates of up to 1 hit/cm^2 per event in the first detector layers after the first carbon absorber. This design was chosen to have fast and highly granular gaseous detectors. In total, the MuCh covers an active area of about 70 m^2 with about half a million read-out channels. The penetration depth of the muons varies with the mass of the vector meson and its total energy depending on the beam energy. The low particle multiplicities behind the last muon absorber enable the implementation of a trigger on muon pairs originating from vector meson decays. Short track segments measured in the last tracking station triplet are extrapolated in target direction and selected by vertex quality. This trigger concept is designed to lead to a reduction of the triggered event rate by a factor of about 600 for J/ψ measurements in minimum bias Au+Au collisions [FHK$^+$11].

3.1.5. Transition Radiation Detector (TRD)

The TRD will consist of 10 detector layers for particle tracking with a position resolution of σ = 300-500 μm across and 3-30 mm along the pad as well as for electron identification for momenta $p \geq 1$ GeV/c a pion suppression of 100 at 90% electron efficiency. The detector layers will be located between appr. 4.1 and 8.7 m downstream the target. The total active detector area will be about 600 m^2. The requirements for the TRD are high electron identification performance, and highly granular and fast gaseous detectors in particular for the inner part of the detector planes. For the inner detector part close to the beam-pipe particle rates of the order of 100 kHz/cm^2 for 10 MHz minimum bias Au+Au collisions at 25 AGeV are expected. In a central collision, particle densities of about 1/20 cm^{-2} are reached. In order to keep the occupancy below 10% the minimum size of a single cell should be about 1 cm^2. The pad area is increased by scaling the pad length, keeping a constant pad width. Every second TRD layer is rotated by 90°.

3.1.6. Timing Resistive Plate Chamber (RPC) Time Of Flight wall (TOF)

Hadron identification will be performed via a Time Of Flight (TOF) measurement. The TOF wall is located at variable position behind the target and will cover a total area of 120 m^2 with an array of Resistive Plate Chambers (RPC). The design goal is a time resolution of 80 ps at rates up to 20 kHz/cm^2 for 10 MHz minimum bias Au+Au collisions

in the innermost part of the detector. The pad area in this region is $5\,\mathrm{cm}^2$ leading to an occupancy of below 5% at SIS300 environments. A position resolution of 6 mm across the pads is expected whereas the resolution along the pads depends on the pad length. The pad length increases for larger distances with respect to the beam-pipe [FHK+11].

3.1.7. Electromagnetic CALorimeter (ECAL)

A 'shashlik' ECAL will be used to measure direct photons and decay photons from neutral mesons like π^0 and η. The ECAL will consist of modules of 140 layers of 1 mm lead followed by 1 mm scintillator. Three cell sizes of $3\times3\,\mathrm{cm}^2$, $6\times6\,\mathrm{cm}^2$, and $12\times12\,\mathrm{cm}^2$ are foreseen. The geometrical arrangement of the modules is not fixed yet. Considered are either a wall or in a geometry with variable distance from the target [FHK+11].

3.1.8. Projectile Spectator Detector (PSD)

The last detector component of the CBM setup is the PSD . It will be used to determine the collision centrality and the orientation of the reaction plane. A very precise measurement of this parameter is of importance for the analysis of event-by-event observables and to study collective flow. The reaction plane has to be determined by a method not involving particles participating in the collision to be independent of effects originating from the collision itself. The PSD is a full compensating, modular (12×9 modules) lead-scintillator calorimeter providing very good and uniform energy resolution. Each module consists of 60 lead/scintillator layers with a surface of $10 \times 10\,\mathrm{cm}^2$. The light signal is read-out from the scintillators via WaveLength Shifting (WLS) fibers by Multi-Avalanche Photo-Diodes (MAPD) with an active area of $3 \times 3\,\mathrm{mm}^2$ and a pixel density of $104\,\mathrm{mm}^{-2}$ each [FHK+11]. A detailed description can be found in [PSD12]

3.1.9. Online Event Selection and Data Acquisition

Since all detectors of the CBM experiment are self-triggered an efficient online event selection and Data AcQuisition (DAQ) system is crucial to perform efficient measurements of rare probes at high reaction rates with high statistics. The system has to cope with event rates of 10 MHz, corresponding to a beam intensity of 10^9 ions/s and a 1% interaction target. Assuming a storage rate of 1 GByte/s and an event data volume of about 40 kByte (minimum bias Au+Au collisions), a maximum event rate of 25 kHz can be processed by the DAQ. This demonstrates the requirement of online event selection algorithms to separate and select events of physical interest from background events. The event selection will be done based on a fast online event reconstruction running on a PC farm (called Green cube). Different many-core architectures developed by Intel, IBM, NVIDIA and AMD are under investigation to make best use of parallel programming on the heterogeneous CPU/GPU systems. The open charm trigger will be based on an online search for secondary vertices. This requires high speed tracking and event reconstruction based on STS and MVD data. The highest background suppression factor has to be achieved for J/ψ measurements. The trigger will require a high-energetic pair of electrons or muons in the TRD or in the MuCh. An online selection for low-mass electron pairs is not possible due to the large number of δ-electrons produced in the STS measured in the RICH. In the case of low-mass muon pairs some background rejection at the trigger level seems to be feasible (see chapter 3.1.4) [FHK+11].

4. Transition Radiation Detector

The TRD of the CBM experiment will be used to track all charged particles with a position resolution (PR) of 200-300 μm at highest rates up to 100 kHz/cm^2 and high multiplicities. It will also serve for particle identification of electrons with a pion contamination of 1% at an electron efficiency of 90%. A Multi Wire Proportional Chamber (MWPC) was chosen for this CBM TRD, since this detector technology is relatively cheap, easy to build and has shown good performance in other experiments with large area TRDs, like ALICE at LHC. The idea of TRD is to increase the particle identification performance of a detector, which uses only the signal of the ionization energy loss by electromagnetic interaction (see figure 4.9), by an additional signal: Transition Radiation (TR) photons. The TR-production process had been predicted by Ginzburg and Frank in 1946 [GF46]. The energy of the emitted TR-photons is within the X-ray domain. For highly-relativistic charged particles ($\gamma \geq 1000$, see figure 4.2), while the emission probability for such an X-ray photon per media boundary crossed is of the order of $1/\alpha$. The additional absorption of TR-photons within a gas proportional counter leads to a relatively large energy deposit compared to the average energy deposit via ionization.

4.1. Radiators

Radiators are devices used to produce TR-photons emitted at periodic material boundaries between materials with different dielectric constants ϵ. Such boundaries can be realized in different ways: there are regular foil, foam and fiber radiators. The essential property of the radiator material is the plasma frequency ω_P. To calculate this property the average electron density n_e is needed, which is correlated to the average atomic number Z of the material. Z, A, ρ, and ω_P values of different materials can be found in table 6.1. There are two main classes of radiators, the regular radiators mostly made from equally spaced foils and the irregular radiators made from foams or fiber mats. The regular radiators utilize coherent interference and produce a larger number of photons per electron and boundary, whereas the mean number of photons is lower in case of irregular radiators due to the missing coherent interference and/or the smaller structure size in foams or fiber mats. This lower number of photons and smaller mean photon energy can be partly compensated by a higher number of boundaries per unit length, due to smaller structure size.

4.1.1. Regular Radiators

The simplest scenario of TR-production by a relativistic particle with a relativistic Lorentz factor γ is a single interface, which is crossed by the charged particle. The double differential description for $\gamma \gg 1$, $(\omega_{P,i}/\omega)^2 \ll 1$, and $\vartheta \ll 1$ is

$$\left(\frac{d^2N}{d\omega d\vartheta}\right)_{interface} = \frac{\alpha}{\pi^2} \cdot \left(\frac{\vartheta}{\gamma^{-2} + \vartheta^2 + (\omega_{P,1}/\omega)^2} - \frac{\vartheta}{\gamma^{-2} + \vartheta^2 + (\omega_{P,2}/\omega)^2}\right)^2 \tag{4.1}$$

with ϑ being the emission angle relative to the direction of motion, the foil (i=1) and gap (i=2) plasma frequency $\omega_{P,i}$ and α the fine structure constant [AYM75]. The plasma frequency is then given by

$$\omega_{P,i} = \sqrt{\frac{n_e \cdot e^2}{\epsilon_0 \cdot m_e}} = \sqrt{\frac{4\pi\alpha n_e \hbar c}{m_e/c^2}} \tag{4.2}$$

where α is the fine-structure constant and m_e is the electron mass [AW11]. The average electron density n_e can be calculated as follows

$$n_e = \frac{\rho \cdot N_A \cdot Z}{A} \tag{4.3}$$

where ρ is the density, N_A the Avogadro constant and A the average mass number. The average atomic number Z can be approximated for i materials by using the relative weighting factor w_i

$$Z = \sum_i w_i \cdot Z_i \tag{4.4}$$

This scenario can be expanded to a full foil with two surfaces

$$\left(\frac{d^2N}{d\omega d\vartheta}\right)_{foil} = \left(\frac{d^2N}{d\omega d\vartheta}\right)_{interface} \cdot 4\sin^2\left(\frac{\varphi_1}{2}\right) \tag{4.5}$$

with $\varphi_i \simeq l_i/z_i$ and z_i being the *formation zone* (equation 4.6) for the two media [CMPT74]. Both foil thickness l_1 and gap dimension l_2 should be greater than the formation zone z_i which is typically of the order of 10 μm for plastic and 700 μm for gases like air. z_i is given by

$$z_i = \frac{2\beta c}{\omega} \cdot \left(\gamma^{-2} + \vartheta^2 + \left(\frac{\omega_{P,i}}{\omega}\right)^2\right)^{-1} \tag{4.6}$$

where ω is the photon frequency and ϑ the photon emission angle with respect to the particle trajectory. All formulas up to now do not include self-absorption due to the radiator material. Self-absorption is most dominant in the low energetic part of the spectrum, below a few keV. The production probability for a photon at a single foil is of the order of $1/\alpha$. To increase the particle separation performance, the number of interfaces has to be enhanced within a single radiator. A periodic radiator with N_f layers of thickness l_1 and spacing l_2 can be described by

$$\left(\frac{d^2N}{d\omega d\vartheta}\right)_{stack} = \left(\frac{d^2N}{d\omega d\vartheta}\right)_{foil} \cdot \exp\left(\frac{(1-N_f)\sigma}{2}\right) \frac{\sin^2\left(\frac{N_f\phi_{12}}{2}\right) + \sinh^2\left(\frac{N_f\sigma}{4}\right)}{\sin^2\left(\frac{\phi_{12}}{2}\right) + \sinh^2\left(\frac{\sigma}{4}\right)} \tag{4.7}$$

with $\phi_{12} = \phi_1 + \phi_2$ and

$$\phi_i \simeq \frac{1}{2}\left(\gamma^{-2} + \vartheta^2 + \left(\frac{\omega_{P,i}}{\omega}\right)^2\right)\omega l_i \tag{4.8}$$

and σ being the total photon absorption cross section σ ($\sigma = \mu_1 \cdot l_1 + \mu_2 \cdot l_2$) for one foil and gas layer [AW11]. The mass attenuation coefficient μ/ρ for different elements, compounds and mixtures can be found in the National Institute of Standards and Technology (NIST) XCOM database [BHS+98]. The photon mass attenuation length (or mean free path) $\lambda = 1/(\mu/\rho)$ of various elemental absorbers as a function of photon energy in the range between 10 eV and 100 GeV can be seen in figure 4.1. The most important region for the simulation of regular radiators is below 50 keV. The emission angle ϑ integral of this formula can be approximated to be:

$$\frac{dN}{d\omega} = \frac{4\alpha}{\omega(\kappa+1)} \frac{\left(1-e^{(-N\sigma)}\right)}{\left(1-e^{(-\sigma)}\right)} \cdot \sum_n \Theta_n \left(\frac{1}{\varrho_1+\Theta_n} - \frac{1}{\varrho_2+\Theta_n}\right)^2 \left[1-\cos(\varrho_1+\Theta_n)\right] \tag{4.9}$$

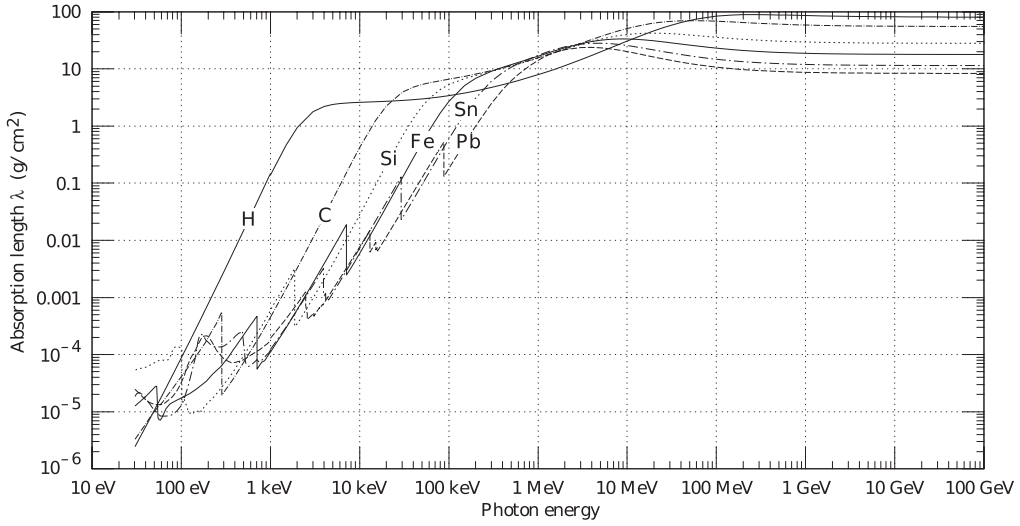

Fig. 4.1: The photon mass attenuation length (or mean free path) $\lambda = 1/(\mu/\rho)$ for various elemental absorbers as a function of photon energy. The mass attenuation coefficient is μ/ρ, where ρ is the density. The intensity I remaining after traversal of thickness t (in mass/unit area) is given by $I = I_0 \exp(-t/\lambda)$. The accuracy is a few percent. For a chemical compound or mixture, $1/\lambda_{eff} \approx \sum_{elements} w_Z/\lambda_Z$, where w_Z is the proportion by weight of the element with atomic number Z [N+11].

according to [Maz00]. This equation includes coherent and incoherent effects as well as the self-absorption of gap and foil material. Therefore it was used to calculate the total yield per keV in the following section. The precision of this equation is given with 15% [FS75] with

$$\varrho_i = \frac{\omega l_1}{2c}\left(\gamma^{-2} + \left(\frac{\omega_{P,i}}{\omega}\right)^2\right), \tag{4.10}$$

and

$$\kappa = \frac{l_2}{l_1} \tag{4.11}$$

$$\Theta_n = \frac{2\pi n - (\varrho_1 + \kappa\varrho_2)}{1+\kappa} > 0. \tag{4.12}$$

Systematic deviations between measurements and theoretical predictions arising from the material budget between radiator and MWPC and radiator material and regularity can be compensated by adding an scaling factor a [0, 1], with:

$$\left(\frac{dN}{d\omega}\right)_{measurement} = a \cdot \left(\frac{dN}{d\omega}\right)_{theoretical}. \tag{4.13}$$

From the given approximation material specific values can be calculated like the threshold for the relativistic Lorentz factor $\gamma_{th.}$ where the TR-yield begins to increase [AYM75], [Maz00]

$$\gamma_{th.} = 2.5 \cdot \omega_{P,1} \cdot l_1 \tag{4.14}$$

or the saturation of the TR-yield as function of γ above $\gamma_{sat.}$ [AYM75], [Maz00]

$$\gamma_{sat.} \sim \gamma_{th.}\sqrt{\frac{l_2}{l_1}} = 2.5 \cdot \omega_{P,1}\sqrt{l_1 \cdot l_2} \tag{4.15}$$

where l_1 is the thickness of the foil and l_2 the thickness of the gap material. The calculated γ dependence of the emitted TR-photon yield for different particles is shown in figure 4.2. The first relevant spectral maximum can be found for a frequency

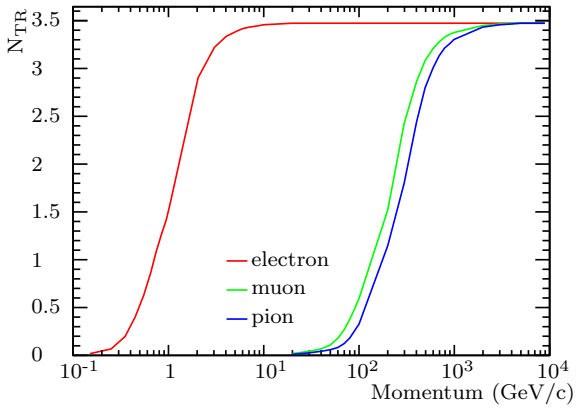

Fig. 4.2: γ-factor dependence of TR-yield simulated for a Polyethylene radiator with $N_f = 200$, $l_1 = 15\,\mu$m, $l_2 = 750\,\mu$m and different particles.

$$\omega_{max} = \frac{{l_1 \cdot \omega_{P,1}}^2}{2\pi c} \tag{4.16}$$

4.1.2. Irregular Radiators

A spectral distribution of TR-photon production in an irregular radiator, consisting of randomly parallel plates of arbitrary thickness, is given by Garibian et al. [GGY75]. This formulation has been modified to take into account the presence of a material in the gap. The average number of produced photons taking into account the self-absorption is given by:

$$\left\langle \frac{d^2N}{d\omega d\Theta} \right\rangle = \frac{2\alpha}{\pi\omega}\left(\frac{1}{1-\beta^2\epsilon_1+\theta^2} - \frac{1}{1-\beta^2\epsilon_2+\theta^2}\right)^2 \Theta^3 I. \tag{4.17}$$

Here

$$I = 2\frac{1-p^N}{1-p}\mathrm{Re}\frac{\left(\frac{1+p}{2}-h_1\right)-\left(p-h_1\frac{1+p}{2}\right)h_2}{1-h_1h_2} + 2\mathrm{Re}\frac{(1-h_1)(p-h_1)h_2(p^N-h_1^Nh_2^N)}{(1-h_1h_2)(p-h_1h_2)} \tag{4.18}$$

is the factor due to the superposition of the radiation fields in the plates and in the gaps. The other parameters are:

$$\epsilon_k = 1-(\omega_k/\omega)^2 + i/(5\lambda_k\omega), \tag{4.19}$$

$$h_k = \langle \exp(-i\phi_k l_k)\rangle, \tag{4.20}$$

$$\phi_k = 5\omega\left(\beta^{-1} - \sqrt{\epsilon_k - \sin^2\Theta}\right) = \phi_k^{'} + i\phi_k^{''}, \tag{4.21}$$

and

$$p = \langle \exp(-l_1/\lambda_1)\rangle\langle \exp(-l_2/\lambda_2)\rangle. \tag{4.22}$$

The angle brackets denote the averaging of random quantities with a distribution determined by the distributions of l_1 and l_2. For most irregular radiators the random foil and the gap thickness can be described by a gamma distribution [Fab77]. In this way one finds that [GGY75]:

$$h_k = |h_k|\exp(i\varphi_k), \tag{4.23}$$

$$|h_k| = \left(\left(1 + \frac{\langle l_k \rangle}{2\lambda_k \alpha_k} \right)^2 + \left(\frac{\phi_k' \langle l_k \rangle}{\alpha_k} \right)^2 \right)^{-\alpha_k/2}, \tag{4.24}$$

$$\varphi_k = -\alpha_k \arctan \frac{\phi_k' \langle l_k \rangle}{\alpha_k + \langle l_k \rangle / (2\lambda_k)}, \tag{4.25}$$

$$p = \left(1 + \frac{\langle l_1 \rangle}{\lambda_1 \alpha_1} \right)^{-\alpha_1} \left(1 + \frac{\langle l_2 \rangle}{\lambda_2 \alpha_2} \right)^{-\alpha_2}. \tag{4.26}$$

The parameters α_k represent the degree of irregularity: $\alpha_k = (\langle l_k \rangle / \sigma_k)^2$ where $\langle l_k \rangle$ and σ_k are the mean values and the mean squared deviations respectively of foil ($k = 1$) and gap ($k = 2$) thickness distributions [CFG+88]. Irregular radiators with a fixed solid structure size but random gap dimension like most fiber radiators can be modeled according to [Ege98b] by the following expression. Assuming the spacings follows a Γ distribution

$$f(x) = \frac{\beta_0^\alpha x^{\alpha-1} \exp(-\beta_0 x)}{\Gamma(\alpha)} \tag{4.27}$$

where α, β_0 are real parameters, $\alpha > 0$, $\beta > 0$. $\Gamma(\alpha)$ is Euler's gamma-function (compared with the corresponding formula of [GGY75], in this publication the substitution $\alpha + 1 \to \alpha$ has been done) [GGY75]. The average and the root mean square deviation of the distance between two foils are given by

$$\langle l \rangle = \frac{\alpha}{\beta} \qquad \text{and} \qquad \sigma(l) = \frac{\langle l \rangle}{\sqrt{\alpha}} \tag{4.28}$$

[Ege98b]. Based on these assumptions, the relative foil spacing distribution and the resulting photon spectrum is presented for different degrees of irregularity in figure 4.3. It can be seen, that the mean energy value of the spectrum as well as the total emitted

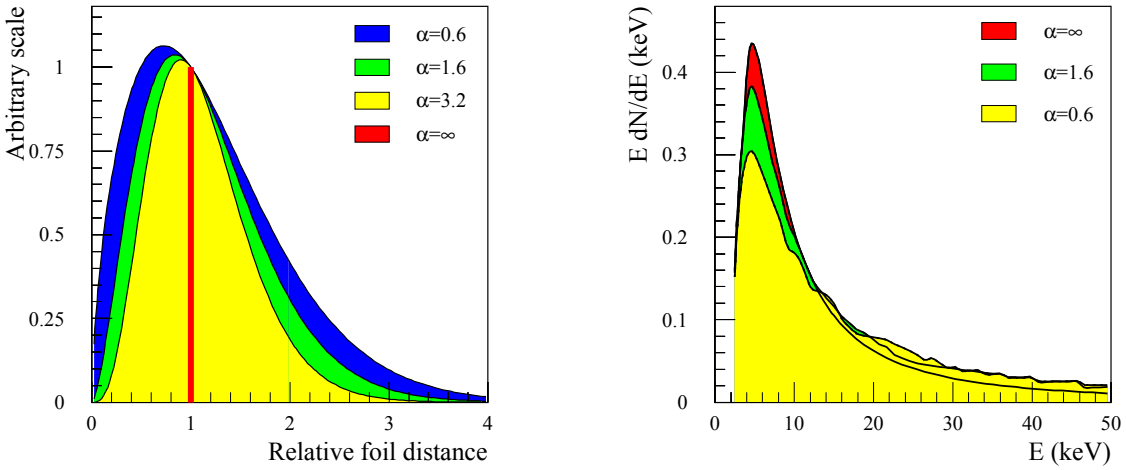

Fig. 4.3: Left: The distribution of foil distance around the mean for different values of α in a Γ distribution. Regular foil spacing corresponds to $\alpha = \infty$. Right: The energy spectrum of TR-photons from a stack of foils with irregular spacing [Ege98b].

energy per electron (integral of the spectrum) is shifted towards smaller energies for increasing width of the foil and gap thickness distribution. From this one can conclude, that both thickness distributions should be as narrow as possible ($\alpha \to \infty$). The usage of

this model is quite challenging since it implies perfect knowledge of the two distributions of the foil and gap thicknesses. In reality this causes problems especially in case of foam radiator materials. The bubble size depends on several parameters and vary within the same foam over a wide range as shown in figure 6.22. These distributions are not homogeneous in all three dimensions within the same foam sample. The bubble diameters can vary due to gravitation. Large bubbles accumulate at the top of the foam since they have lower average material density, and smaller bubbles at the bottom. Such density gradients are more distinct for foams with longer hardening time and/or low viscosity of the solid respectively liquid components. The most homogeneous distribution in commercial Polyethylene (PE) foams have been found for rather thin foam sheets (sheet thickness only up to 1-3 times larger as the average bubble size) which are not produced as parts of a larger piece. A characteristic schematic drawing of a liquid/gas or solid/gas foam bubble is presented in figure 4.4. The films are thin sheets of liquid (solid,

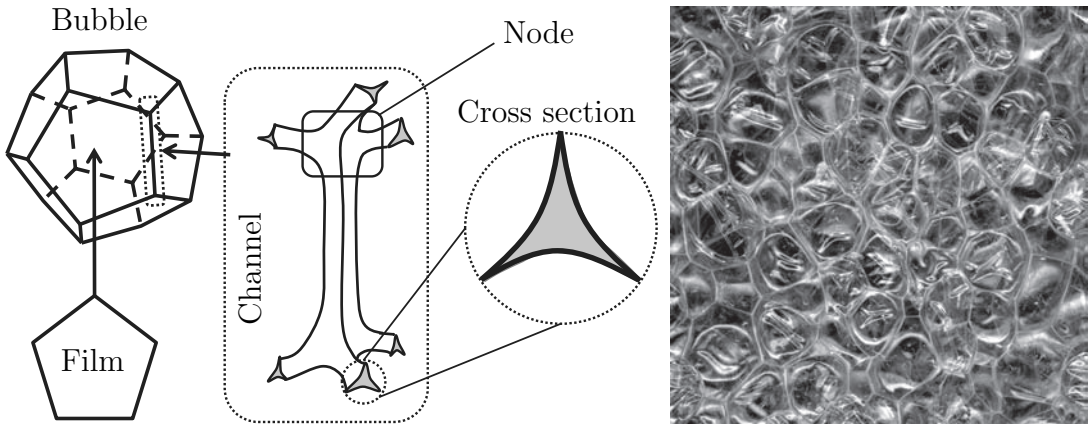

Fig. 4.4: Left: Schematic of a dodecahedral bubble and the wall channel based on [CTF$^+$13]. Right: Foam structure of a 19×19 mm^2 and 5 mm thick Cell-air polyethylene foam sample.

after hardening) separating two bubbles. The channels are thin liquid or solid columns formed at the intersection of three bubbles. The channels are also known as plateau borders. The cross section of a channel resembles a triangle with edges curved toward the interior. The channels form a network of pipes that allow liquid to flow through the foam. The junctions where the channels intersect are called nodes, and four channels meet at a single node [CTF$^+$13]. This description implies a very complex inner structure of the foam with thin film structures, relatively thick channels and more or less spheric bubbles.

The description of the solid fiber or fleece components is in most cases easier. The fiber diameter observed during my material pre-selection showed only a small variation within the same sample, but at the same time a broad spectrum of gap spacings as presented in figure 4.5. Nevertheless the description of gap distribution is very complex in case of fleece materials and depending on too many parameters like: fiber length, diameter, bendability and production process and would demand on a three dimensional measurement without any outer forces on the material disturbing the material properties.

Based on the previous argumentation and the fact that the pure photon spectrum defies any attempt of direct measurement with a MWPC, the presented description of irregular radiators are not used in test beam analysis nor in the CbmRoot framework. Instead, the emission and absorption spectra, presented in the following, are based on a realistic material budget but are calculated for a regular toy model radiator using equation 4.9 with the average parameters $\langle l_1 \rangle$, $\langle l_2 \rangle$ and $\langle N_f \rangle$. The resulting spectrum will be scaled

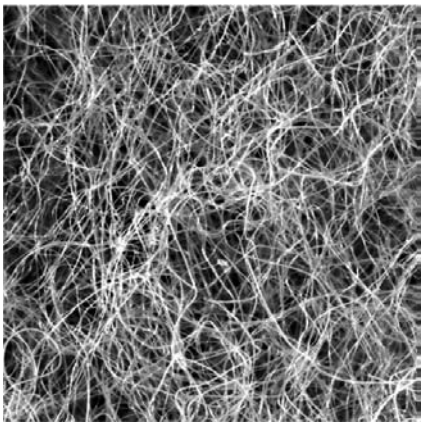

Fig. 4.5: Fiber structure of a $10\times10\,\mathrm{mm}^2$ Polypropylene fleece sheet.

by a weighting factor a to suit the measured total energy loss spectra (dE/dx+TR) as good as possible.

4.1.3. TR-photon Interaction with Matter

The TR-photons can interact via three different processes with the detector material. The photoelectric effect dominates at low energies, but also Compton scattering, Rayleigh scattering (elastic scattering), and photo-nuclear absorption contribute. A schematic of the two dominant processes together with pair production is presented in figure 4.6. For

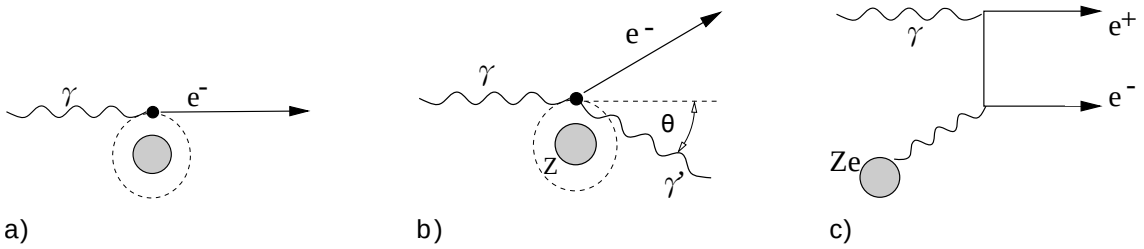

Fig. 4.6: Three photon interaction processes with matter: a) photoelectric effect b) Compton scattering c) pair production
`http://www-zeuthen.desy.de/~kolanosk/astro0607/skripte/cosmics03.pdf`

photon energies below the MeV range the cross section is characterized by absorption edges which correspond to thresholds for photo-ionization of various atomic levels. For increasing photon energies this dependence goes as Z to the 5^{th} power:

$$\sigma_{\mathrm{photoeffect}} \sim \frac{Z^5}{E_\gamma^{7/5}}. \tag{4.29}$$

The cross section for Compton scattering is proportional to the number of bound electrons of the material. For the maximum energy transfer the cross section is

$$\sigma_{\mathrm{Compton}} \sim \frac{\ln(E_\gamma)}{E_\gamma}. \tag{4.30}$$

The conversion of the photon into an $\mathrm{e}^+\mathrm{e}^-$ pair is possible in the electromagnetic field of a nucleus or an electron, if a total energy of twice the electron mass is reached. Above a photon energy of 100 MeV pair production is the dominant process and saturates at

some higher photon energy. The cross section for pair production is proportional to Z^2 starting at a threshold photon energy equivalent to the rest mass of an electron positron pair. Since the dominant part of the TR-spectrum is below 50 keV, pair production can be neglected. The absorption probability of different detectors varies over a wide range. Therefore it is advantageous to optimize the radiator photon emission spectrum to the detector absorption probability spectrum. The absorption probability can be varied by the choice of gas mixture (noble and quenching gas) in case of gaseous detectors. The absorption length for the most common noble gases are shown in figure 4.7. Some

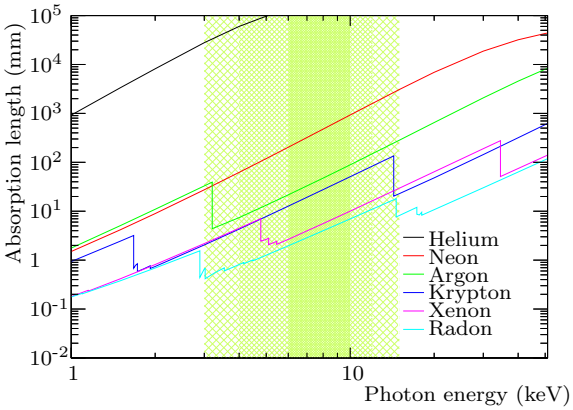

Fig. 4.7: Photon absorption length in different noble gases for photon energies between 1 and 50 keV [HS04]. Regime of typical TR-photon energy is green colored.

noble gases have to be excluded due to their isotopic mixture, which gives inherent radioactivity and/or short lifetime like Radon (^{222}Rn (90%), $t_{1/2}$ =3.824 d). The best detection efficiency is reached using the gas with the shortest absorption length in the most probable TR-photon energy region between 3-15 keV, depending on the radiator characteristics (see chapter 6). Xe is therefore a good choice, as it has an absorption length between 1 and 10 mm for typical TR-photon energies. The electron identification is further enhanced by the favorable ionization energy loss, dE/dx in Xe, which has the highest value of the Fermi plateau of all noble gases.

4.2. Multiwire-Proportional-Chamber

There are two different types of MultiWire-Proportional-Chamber (MWPC) as depicted in figure 4.8; the symmetric MWPC, which has one anode wire plane consisting of a set of thin, parallel, and equally spaced wires, symmetrically sandwiched between two cathode planes and the asymmetric (Drift-MWPC) or Time-Expansion Chamber (TEC) like with an additional cathode wire plane (sometimes also called drift wires). These cathode wires have usually a larger diameter compared to the anode wires and are placed between one cathode plane and the anode wire plane leading to a symmetric distance between cathode plane anode wires and cathode wires. The volume between cathode plane, and cathode wire plane, with the anode wire plane in the middle, is called amplification region, where the volume between cathode wire plane and the second cathode plane (or drift plane) is the drift region. The volume between the cathode planes is usually filled with a gas mixture of a heavy noble gas (main component) and so called quenching gas like CO_2 or CH_4. The applied potential of a symmetric MWPC is chosen in a way that the electrons are guided towards the anode wires and the positive ions drift in direction of the cathode planes. The cathode wire plane and cathode plane next to the anode wire plane

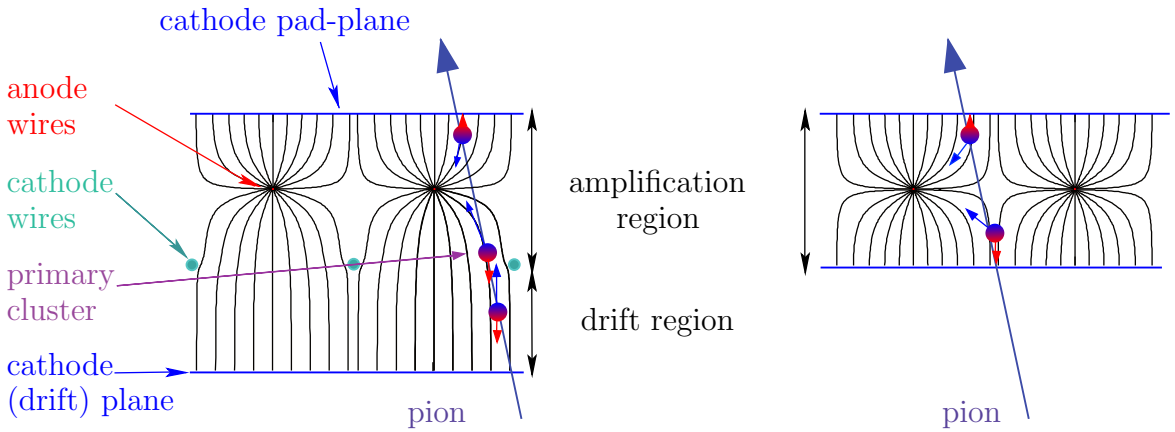

Fig. 4.8: Schematic of an asymmetric MWPC (left) and a symmetric MWPC (right).

of asymmetric MWPCs is usually set to ground potential, while a negative potential is applied to the second cathode plane. In general the field potentials are chosen to separate primary ionized electrons from ions and guide the electrons towards the anode wires, respectively the ions towards the cathode plane(s).

4.2.1. Charged Particle Interaction with Matter

The ionization energy loss of the charged particles is typically a few keV per centimeter of gas under normal conditions. The mean specific energy loss for charged particles heavier than electrons is described by the Bethe-Bloch formula [A+08b]:

$$-\frac{dE}{dx} = Kz^2\frac{Z}{A}\cdot\frac{1}{\beta^2}\left[\frac{1}{2}\ln\left(\frac{2m_ec^2\beta^2\gamma^2T_{max}}{I^2} - \beta^2 - \frac{\delta_{corr}(\beta\gamma)}{2}\right)\right] \tag{4.31}$$

where K is a constant representing $4\pi N_A r_e^2 m_e c^2$, Z and A denoting to the atomic number and charge of the traversed material and m_e, r_e giving the electron mass and classic radius. I corresponds to the mean excitation energy and T_{max} to the maximum kinetic energy loss. N_A is called the Avogadro constant. β gives the velocity in terms of the speed of light (v/c) and correlated to the Lorentz factor γ via $1/\sqrt{1-(\beta)^2}$. Density effect correction to ionization energy loss are taken into account by $\delta_{corr}(\beta\gamma)$. The stopping power is visualized for positive muons in copper as function of muon momentum in figure 4.9. For electrons (see [SCS11] and [N+11]), the energy loss is slightly different due to their small mass and their indistinguishability with respect to the shell electrons. These effects are included by the Berger-Seltzer-formula:

$$-\left.\frac{dE}{dx}\right|_{T<T_{cut}} = \frac{2\pi r_e^2 m_e c^2 n_e}{\beta^2}\left[\ln\frac{2(\gamma+1)}{(I/mc^2)^2} + F^{\pm}(\tau,\tau_{up}) - \delta(\log(\gamma\beta))\right] \tag{4.32}$$

with n_e representing the electron density of the material, $\tau = \gamma - 1$, τ_{up} being the minimum value for electrons between $\tau_c = T_{cut}/m_ec^2$ and $\tau/2$ and T_{cut} representing the minimum threshold for δ-electron production. $F^{\pm}(\tau,\tau_{up})$ and $\delta(\log(\gamma\beta))$ are complex correction functions . Can also be written as a modified Bethe-Bloch-formula for scattering of identical, indistinguishable particles with T being the kinetic energy of electron $T/2 = T_{max}$ [SCS11]:

$$-\left\langle\frac{dE}{dx}\right\rangle_{el.} = K\frac{Z}{A}\cdot\frac{1}{\beta^2}\left[\ln\left(\frac{m_ec^2\beta^2\gamma^2(T_{max}/2)}{2I^2}\right) + F(\gamma)\right]. \tag{4.33}$$

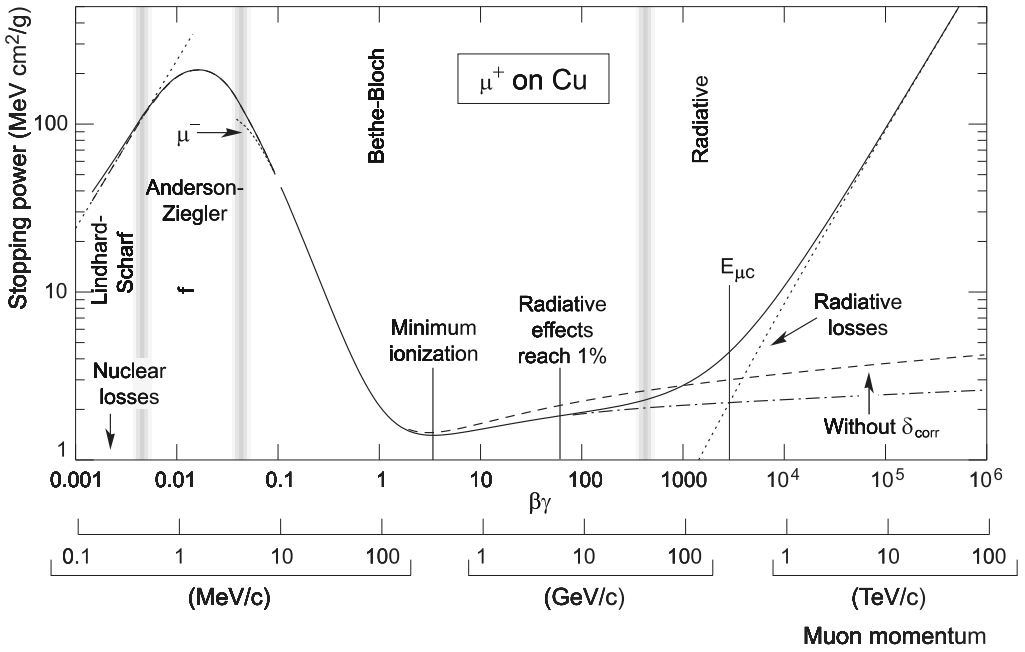

Fig. 4.9: Stopping power for positive muons in copper as function of $\beta\gamma = p/Mc$ over nine orders of magnitude in momentum (12 orders of magnitude in kinetic energy) [A$^+$08b]. The curves with and without density-effect correction for the energy loss due to ionization and excitation are shown. The solid curve indicates the total energy loss which is the sum of the energy loss due to ionization and the energy loss due to Bremsstrahlung.

At low energies electrons and positrons primarily lose energy by ionization, as well as Møller scattering and Bhabba scattering but the contribution of this effects decrease for higher energies. Positrons lose in addition energy by annihilation at lower energies (see figure 4.10). The dominant part of the energy loss of electrons at higher energy are due

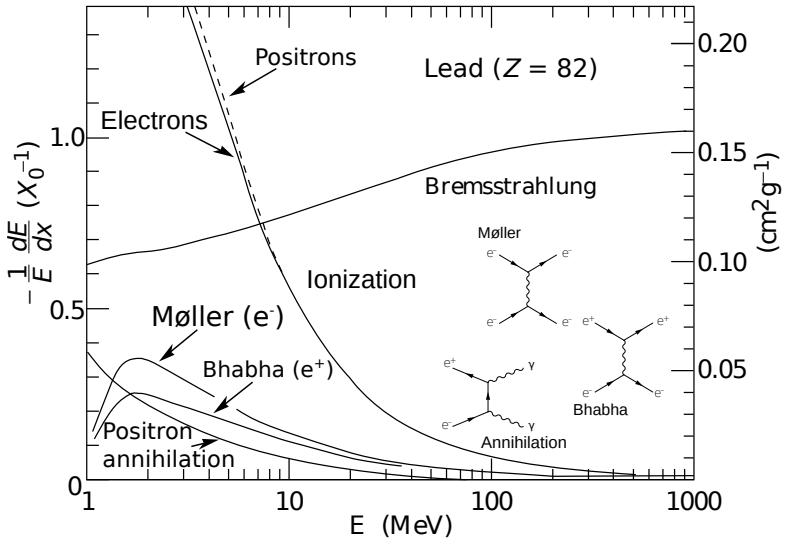

Fig. 4.10: Fractional energy loss per radiation length in lead as a function of electron or positron energy. Electron (positron) scattering is considered as ionization when the energy loss per collision is below 0.255 MeV and as Møller (Bhabha) scattering when it is above[N$^+$11]. The Feynman graphs for Møller and Bhabha scattering are added as well as the one for positron annihilation.

to Bremsstrahlung which can be approximated to be:

$$-\frac{dE}{dx} = \frac{4\alpha N_A Z^2 z^2}{A}\left(\frac{e^2}{4\pi\epsilon_0 mc^2}\right) E \cdot \ln\frac{183}{Z^{1/3}} \tag{4.34}$$

with α being the fine structure constant.

4.2.2. Signal Evolution in a Multiwire-Proportional-Chamber

The electric potential between cathode and anode is set such that the primary electron ion pairs are separated. The electrons will drift along field lines until they reach the high field region (amplification region), very close to the anode wires, where avalanche multiplication can occur depending on the applied anode voltage (see figure 4.11). A

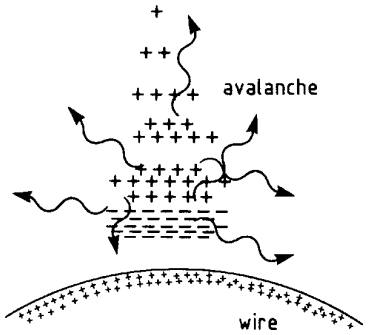

Fig. 4.11: Schematic development of the proportional wire avalanche [BRR08].

typical drop-like avalanche develops with all electrons in the front and ions behind. The avalanche surrounds the wire depending the operational mode (compare to figure 4.14) because of lateral diffusion and the small radius of the anode wire (see figure 4.12). In the proportional mode the avalanche in $ArCH_4$ (90/10) with a wire diameter of 25 μm has been observed to occupy only 100° in azimuth (FWHM), while the avalanche started to surround the anode wire when voltage was raised [OFRW79]. The negative signal is given

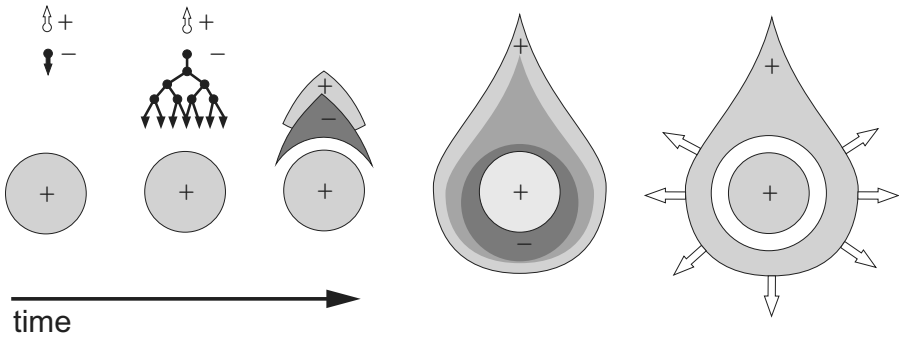

Fig. 4.12: Time development of an avalanche in a proportional counter. A single primary electron proceeds towards the anode wire, in regions of increasingly high fields, experiencing ionizing collisions; due to the lateral diffusion, a drop-like avalanche, surrounding the wire, develops. Electrons are collected in a very short time (about 1 nsec) and a cloud of positive ions is left, slowly migrating towards the cathode [Sau77].

by the electron avalanche which is collected by the wires within a fraction of a nanosecond [BRR08]. The positive ions are left over in the trail of the electron avalanche due to their lower drift speed. The drift speed depends on the charge to weight fraction and their higher cross section. These positive ions are moving away from the wire at relatively

low speed. With a mobility of a few cm/s per V/cm, a typical speed near the thin wire would be several 10^5 cm/s, and a hundred times less at a hundred times the radius. For a continuous particle flow with a much higher frequency than the corresponding ion travel time, a stationary situation develops. The traveling ions build up a stationary space charge density in the chamber volume. This reduces the electric field close to the wire and therefore the gas gain, which poses a fundamental limitation on the rate capability of any wire chamber [BRR08].
The ions induce image charges in all surrounding electrodes and these result in a positive signal on the wire behind the electron peak depending on the avalanche's position. The neighboring wires are also affected, however, the signals induced here are of reverse polarity and have a smaller amplitude. In a similar manner, a positive signal is induced on the cathode plane, if the cathode is grounded and positive voltage is applied to the anode wires. The signal from one cathode plane does not give information on the position of the avalanche. One can obtain the coordinate of the induced charge by a subdivision of the cathode into read-out pads perpendicular to the anode wire direction. A sketch of a symmetric MWPC with anode and cathode read-out is shown in figure 4.13. The

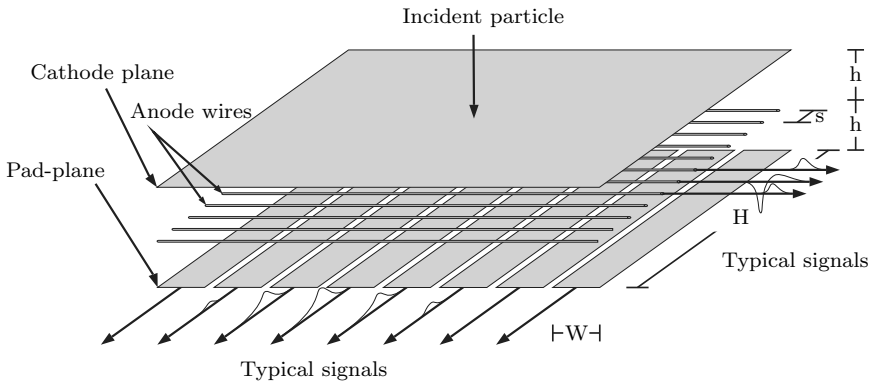

Fig. 4.13: Sketch of a MWPC with anode signal read-out based on [Leo87] and cathode signal read-out based on [GLO+79].

induced charge distribution should be shared between two or three adjacent pads in order to obtain the best possible position resolution and signal to noise ratio (S/N). The signal to noise ratio decreases as well as occupancy increases, if the charge signal is shared by more than three pads. When the induced charge is measured only by one pad (one-pad clusters), the position resolution is given by $1/\sqrt{12}$ times the pad width W. Therefore, a proper matching of the pad width W to the width of the induced charge distribution is required.
There are three known working types of gaseous ionization detectors: the *ionization chamber*, the *proportional counter*, and the *Geiger-Müller counter* (see figure 4.14). They can be characterized by the different applied voltages. If there is no potential difference between cathode and anode or both are set to ground potential (I), the electron-ion pairs recombine under their own electrical attraction and no charge is collected at the anode or cathode. As the potential difference is raised, the recombination is reduced and the current begins to increase. In the operating region of the *ionization chamber* (II), all primary electron-ion pairs are separated and collected. A further increase of the voltage has no effect on the output current. After further increasing the voltage above a certain threshold, the current increases again. This is due to the increasing kinetic energy of the electrons. They can create secondary electron-ion pairs by themselves

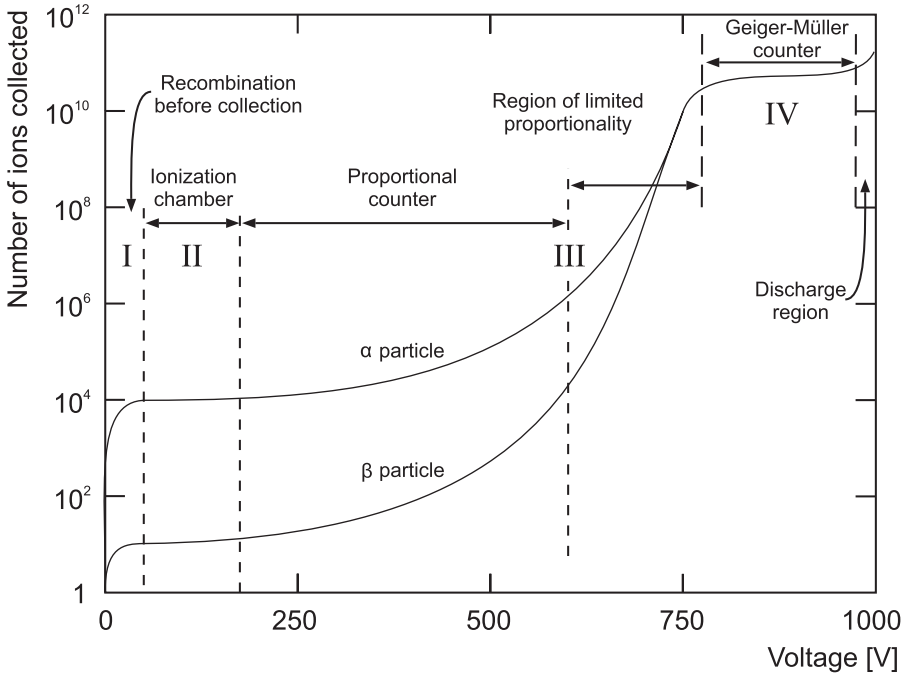

Fig. 4.14: Gain-voltage characteristic for a proportional counter, showing the different regions of operation [Sau77].

during avalanche multiplication (see figure 4.12). The number of electron-ion pairs in the avalanche is proportional to the number of primary electrons. This gives a proportional amplification of the signal. The multiplication factor depends on the working voltage, the gas mixture, temperature, gas pressure and the chamber geometry. This so-called *proportional counter* (III) region is the operating condition for MWPCs. A discharge occurs in the gas, if the anode voltage is raised beyond the proportional region. Instead of a single, localized avalanche, a chain reaction of many avalanches is triggered. The output current becomes completely saturated, always giving the same amplitude which depends no longer on the energy of the initial event. *Geiger-Müller counters* (IV) are working in this voltage region. The description above is also true for asymmetric or drift-MWPCs. This drift-wire-grid elongates the area of parallel field lines where electrons and ions have individual constant drift velocity. This allows to study the time evolution of the signal. It also allows to choose the optimal width of cathode pads, independent of the total gas thickness of the MWPC (see chapter 4.3).

4.3. Position Reconstruction

The induced charge distribution on the cathode plane can be described by the empirical formula proposed by Mathieson in 1988 [Mat88]

$$\rho(d/h) = q_a \cdot \frac{\frac{\pi}{2} \cdot \left(1 - \frac{\sqrt{K_3}}{2}\right) \sqrt{K_3}}{4 \arctan\left(\sqrt{K_3}\right)} \cdot \frac{1 - \tanh^2\left(\frac{\pi}{2} \cdot \left(1 - \frac{\sqrt{K_3}}{2}\right) \frac{d}{h}\right)}{1 + K_3 \tanh^2\left(\frac{\pi}{2} \cdot \left(1 - \frac{\sqrt{K_3}}{2}\right) \frac{d}{h}\right)}. \tag{4.35}$$

This formula depends on the chamber geometry parameter K_3, the pad width W perpendicular to the anode wire direction (or respectively pad height H parallel to the anode wire direction), the displacement d of the particle track with respect to the closest pad center and the pad-plane to anode wire plane distance h. Values of K_3 have

been presented [Mat88] as function of characteristic chamber parameters like the anode wire radius r_a, anode-cathode separation h, and the anode wire pitch s (see figure 4.15). From equation 4.35, one can calculate the charge ratio distribution or so called Pad

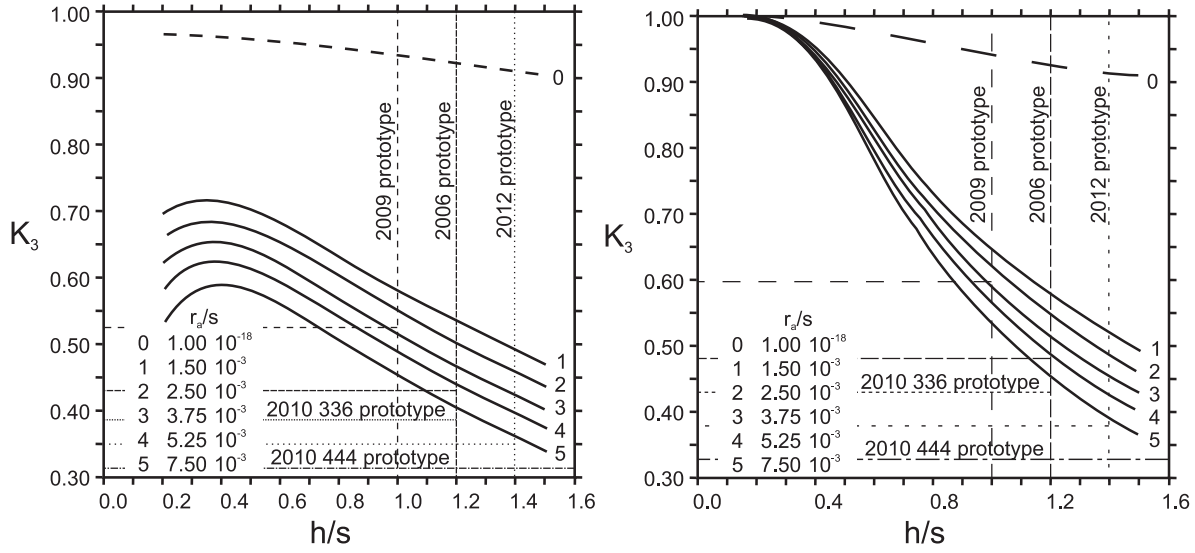

Fig. 4.15: Values of K_3 as function of h/s depending on r_a/s parallel (left) and perpendicular (right) to the anode wire direction based on [Mat88] realized for CBM TRD MWPC prototypes built since 2006.
2010/11 MS336:
$h = 3.0\,\text{mm}$, $s = 2.5\,\text{mm}$, $h/s = 1.2$, $r_a = 20\,\mu\text{m}$, $K_{3,\parallel} \approx 0.38$ and $K_{3,\perp} \approx 0.43$
2010/11 MS444:
$h = 4.0\,\text{mm}$, $s = 2.5\,\text{mm}$, $h/s = 1.6$, $r_a = 20\,\mu\text{m}$, $K_{3,\parallel} \approx 0.31$ and $K_{3,\perp} \approx 0.32$
2012 MS3.5/3.5/5.0:
$h = 3.5\,\text{mm}$, $s = 2.5\,\text{mm}$, $h/s = 1.4$, $r_a = 20\,\mu\text{m}$, $K_{3,\parallel} \approx 0.35$ and $K_{3,\perp} \approx 0.38$

Response Function (PRF) by calculating the integral of $\rho(d/h)$ assuming $q_a = 1$.

$$\begin{aligned} PRF(d/h) &= \int_{d/h-W/2}^{d/h+W/2} \rho(d'/h)\; d(d'/h) \\ &= -\frac{\arctan\left(\sqrt{K_3}\tanh\left(\pi(\sqrt{K_3}-2)\cdot\dfrac{W-2\cdot d}{8h}\right)\right)}{2\arctan(\sqrt{K_3})} \\ &\quad -\frac{\arctan\left(\sqrt{K_3}\tanh\left(\pi(\sqrt{K_3}-2)\cdot\dfrac{W+2\cdot d}{8h}\right)\right)}{2\arctan(\sqrt{K_3})}. \end{aligned} \tag{4.36}$$

This equation can be used to reconstruct the hit position of a measured charge (ratio) distribution or in order to simulate a realistic detector response to a given simulated track. It can also be used to fit a measured PRF to estimate for example the distance between the pad-plane and the anode wire plane one has to approximate the histogram presented in figure 4.15 for a known (r_a/s) ratio or as function of h and (r_a/s). The datasets 1 to 5 can be approximated linearly between 0.4 and 1.5 h/s (which means h between 1.25 and 4.0 mm in case of the 2012 prototypes) and for (r_a/s) ratios between 0.0015 and 0.0075 as presented in figure 4.16. Since the values presented in figure 4.15 are not listed they are read from the histogram their uncertainty (of the ordinate) is

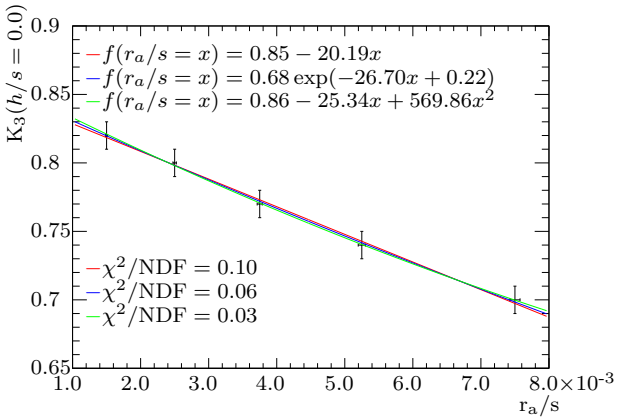

Fig. 4.16: Values of $K_{3,\parallel}$ at $h/s = 0.0$ as function of r_a/s linearly extrapolated based on the data between $h/s = 0.4$ and 1.5 for datasets 1 to 5. The error bars represent an estimated read out uncertainty of 0.01 of the values presented in figure 4.15. Three different fit functions have been tested; a polynomial of first and second order and an exponential function. The χ^2/NDF (Number of Degrees of Freedom) is also presented.

assumed to be 0.01. In absence of a theoretical model describing the relation between (r_a/s) and $K_{3,\parallel}$ a linear, exponential and second order polynomial fit functions have been tested with the following results

$$\begin{aligned} K_{3,\parallel}(h, r_a, s) &= -0.245 \cdot h/s + (-20.19 \cdot (r_a/s) + 0.85) \text{ or} \\ K_{3,\parallel}(h, r_a, s) &= -0.245 \cdot h/s + (0.68 \cdot \exp(-26.70 \cdot (r_a/s) + 0.22)) \text{ or} \\ K_{3,\parallel}(h, r_a, s) &= -0.245 \cdot h/s + (0.86 - 25.34 \cdot (r_a/s) + 569.86 \cdot (r_a/s)^2). \end{aligned} \tag{4.37}$$

The χ^2/NDF of the three fits suggest that the assumed extraction uncertainty is chosen too high.
$K_{3,\perp}$ is approximated by a more complex approach in the parameter ranges of (h/s) between 0.2 and 1.4 and (r_a/s) between 0.0015 and 0.0075. The correlation between $K_{3,\perp}$ and (h/s) is fitted to a polynomial of degree four for each (r_a/s) ratio (13 values per curve). The resulting parameter sets are fitted to a polynomial with degree three as function of (r_a/s). The resulting functional dependence are listed below:

$$\begin{aligned} &K_{3,\perp}(h, r_a, s) = \\ &\quad \left[0.89 + 22.15(r_a/s) - 3769.00(r_a/s)^2 + 118932.90(r_a/s)^3\right] \\ &\quad + \left[1.16 - 216.68(r_a/s) + 48178.04(r_a/s)^2 - 2447137.05(r_a/s)^3\right](h/s) \\ &\quad + \left[-3.49 + 569.45(r_a/s) - 154406.27(r_a/s)^2 + 9295879.37(r_a/s)^3\right](h/s)^2 \\ &\quad + \left[3.01 - 659.90(r_a/s) + 178653.38(r_a/s)^2 - 11385860.38(r_a/s)^3\right](h/s)^3 \\ &\quad + \left[-0.88 + 241.10(r_a/s) - 64171.15(r_a/s)^2 + 4194790.72(r_a/s)^3\right](h/s)^4 \end{aligned} \tag{4.38}$$

It has to mentioned that there is no way to quantify the accuracy of this model beyond the parameter space defined by the curves shown in figure 4.15. Especially the parameters of prototype 2010/11 (4.0+4.0+4.0) are not included in this parameter range. A more detailed description can be found in appendix F.
Based on these results and equation 4.36, the optimal pad width W to h matching can be estimated. The induced charge fraction on the central pad as function of pad width and pad-plane to anode wire plane distance is shown in figure 4.17 for constant $K_{3,\parallel}$ and linear fitted values of $K_{3,\parallel}$ for $s = 2.5\,\text{mm}$ and $r_a = 20\,\mu\text{m}$. The best signal to noise

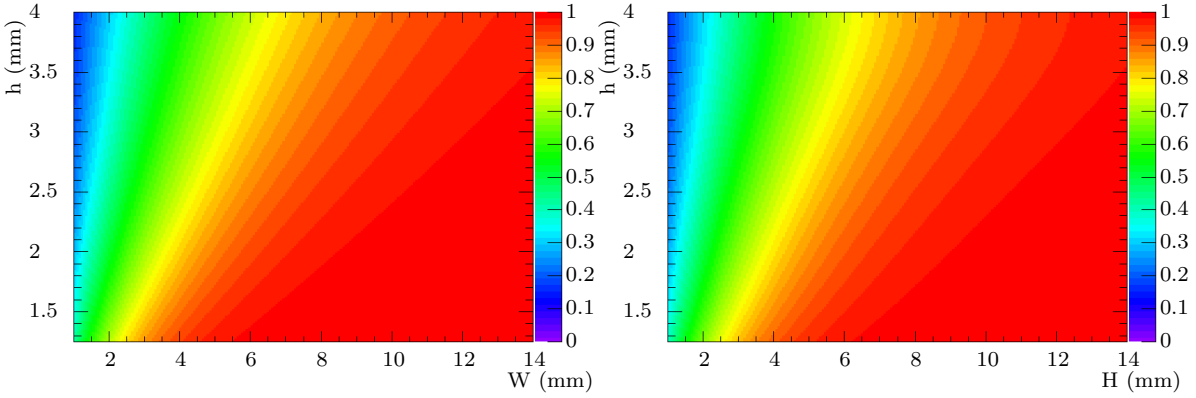

Fig. 4.17: Percentage of charge on the central pad for a track through the center of the central pad for fitted $K_{3,\parallel}$ (left) and fitted $K_{3,\perp}$ (right) for s=2.5 mm, r_a=20 μm.

ratio and therefore best position resolution performance is assumed for a charge fraction of 75-85% on the central pad, corresponding to an average cluster width of 2.4-2.6 channels. The calculated PRF for prototypes from 2010, 2011 and 2012 are shown in figure 4.18 (parameters listed in table 4.1). From this calculation it can be seen that a

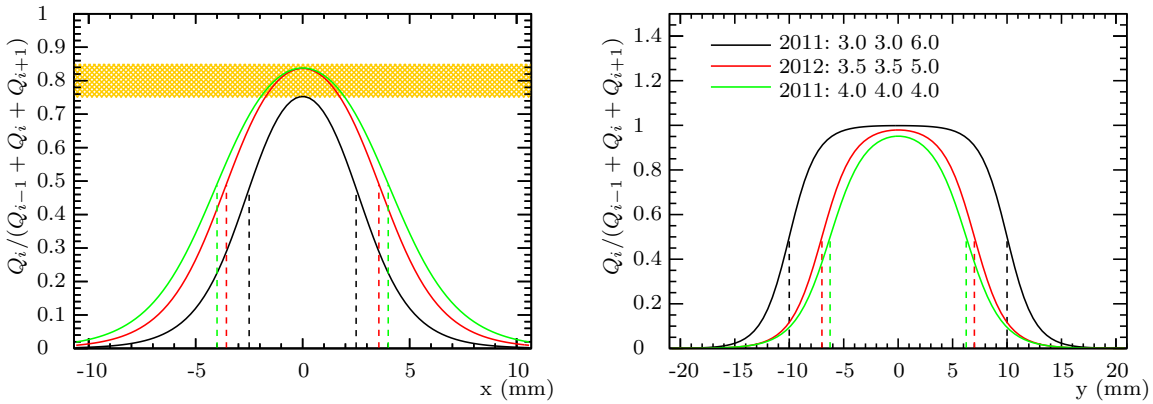

Fig. 4.18: Pad response function calculated for different geometrical chamber parameters like pad width (W), pad height (H), distance between anode wire grid and pad-plane (h) using a $K_{3,\parallel}$ (left) and $K_{3,\perp}$ (right) value (compare to figure 4.16). The optimal signal fraction with respect to S/N and position reconstruction is given by the orange area. The black and green lines correspond to the prototype geometry from 2010 and 2011 (MS336 and MS444). The red line was calculated for the 2012 chamber geometry. The dashed, colored lines indicate the crossover to the adjacent pad on the left and right side.

Tab. 4.1: Geometrical parameters of Münster multi-wire-proportional chamber prototypes between 2012 and 2012 including $K_{3,\parallel}$ and $K_{3,\perp}$ based on equation 4.37 and 4.38.

Year	W (mm)	H (mm)	h (mm)	drift (mm)	r_a (μm)	s (mm)	$K_{3,\parallel}$	$K_{3,\perp}$
2010/11	5.000	20.0	3.0	6.0	20.0	2.5	0.39	0.43
2010/11	8.000	12.5	4.0	4.0	20.0	2.5	0.30	0.21
2012	7.125	14.0	3.5	5.0	20.0	2.5	0.35	0.35

two dimensional position reconstruction is feasible for rectangular pad geometries within certain limitations. First, the position perpendicular to the anode wire direction can only

be reconstructed at wire positions, since the primary electrons are guided towards the wires by the electrical field and the avalanche is located around the anode wire (compare to chapter 4.2.2). Second, the signal on the adjacent pad row has to be significant above the noise level. Keeping this in mind, it is clear that prototypes from 2010/11 (3.0 3.0 6.0) are only position sensitive at ±5 mm with respect to the pad border (see black curve plateau in figure 4.18 right side). While a sufficient position sensitivity is reached for the two other prototype geometries (2010/11 (4.0 4.0 4.0) and 2012 (3.5 3.5 5.0)). A comparable two dimensional track position reconstruction has been performed for a previous double-sided prototype generation with rectangular pad geometry. Based on test beam data from 2006 [Ber09], both coordinates could be reconstructed for avalanches located up to the third anode wire (7.5 mm) next to the pad row border. The pads of this prototype had an aspect ratio of $5 \times 10\,\mathrm{mm}^2$ with h=3 mm, s=2.5 mm. For the given prototype geometry this resulted in a good two-dimensional reconstruction efficiency across the entire surface of the rectangular pads.
In general a track position can be reconstructed in different ways: for example fitting the measured charge distribution to the PRF, using a so called weighted center of gravity method, general charge ratio algorithm, hyperbolic secant squared (SECHS) approach or a Gaussian approximation of the charge distribution. The main difference of these algorithms are systematic deviations between the true track position and the reconstructed one, which will be discussed later based on in beam test data.
For a track at a position d, a charge fraction on the pad with maximum charge (i), left pad ($i-1$), and right pad ($i+1$) will be measured. The charge fraction can be expressed in terms of function values of the PRF assuming the PRF can be approximated by a Gaussian distribution, where W denotes the pad width:

$$\frac{Q_i}{Q_{i-1}+Q_i+Q_{i+1}} = A \cdot \exp\left(-\frac{d^2}{2\sigma^2}\right), \tag{4.39}$$

$$\frac{Q_{i-1}}{Q_{i-1}+Q_i+Q_{i+1}} = A \cdot \exp\left(-\frac{(d+W)^2}{2\sigma^2}\right), \tag{4.40}$$

$$\frac{Q_{i+1}}{Q_{i-1}+Q_i+Q_{i+1}} = A \cdot \exp\left(-\frac{(d-W)^2}{2\sigma^2}\right). \tag{4.41}$$

To derive an equation to get d, equation 4.39 is divided by equation 4.40:

$$\frac{Q_i}{Q_{i-1}} = \exp\left(\frac{2dW+W^2}{2\sigma^2}\right). \tag{4.42}$$

Now equation 4.41 is divided by equation 4.39

$$\frac{Q_{i+1}}{Q_i} = \exp\left(\frac{2dW-W^2}{2\sigma^2}\right), \tag{4.43}$$

and equation 4.43 is multiplied with equation 4.42

$$\frac{Q_{i+1}}{Q_{i-1}} = \exp\left(\frac{2dW^2}{2\sigma^2}\right), \tag{4.44}$$

and equation 4.42 divided by equation 4.43

$$\frac{Q_i^2}{Q_{i-1}\cdot Q_{i+1}} = \exp\left(\frac{W^2}{\sigma^2}\right). \tag{4.45}$$

Solved for d, the result is

$$d = \frac{W}{2} \cdot \frac{\ln\left(\frac{Q_{i+1}}{Q_{i-1}}\right)}{\ln\left(\frac{Q_i^2}{Q_{i-1} \cdot Q_{i+1}}\right)}. \tag{4.46}$$

Once the PRF is measured, the track position relative to the center of the pad with maximum charge can be calculated by using equation 4.42 solved for d. Therefore, the knowledge of the charge on pad i and $i-1$ is needed

$$d = \frac{\sigma^2}{W} \cdot \ln\left(\frac{Q_i}{Q_{i-1}}\right) - \frac{W}{2} \tag{4.47}$$

or the charge on pad i and $i+1$

$$d = \frac{\sigma^2}{W} \cdot \ln\left(\frac{Q_{i+1}}{Q_i}\right) + \frac{W}{2}. \tag{4.48}$$

The best results are obtained by combining these two equations to a weighted average of both displacements d, if the assumption of the Gaussian shape of the PRF is realistic. Since the errors of charge measurement are approximately inverse to the measured charge which is induced on the pad, the error of the calculated displacement can be minimized by choosing the weights as Q_{i-1}^2 and Q_{i+1}^2 [BR94]:

$$\begin{aligned} d = & \frac{1}{Q_{i-1}^2 + Q_{i+1}^2} \cdot \\ & \left[Q_{i-1}^2 \left(\frac{\sigma^2}{W} \ln\left(\frac{Q_i}{Q_{i-1}}\right) - \frac{W}{2} \right) + Q_{i+1}^2 \left(\frac{\sigma^2}{W} \ln\left(\frac{Q_{i+1}}{Q_i}\right) + \frac{W}{2} \right) \right]. \end{aligned} \tag{4.49}$$

But it has to be mentioned that this algorithm tends to overestimate the probability of central hit positions. There is always a peak around very small displacements relative to the center of the maximum pad and dilution at the outer regions which has to be compensated. There are other algorithms available which will be shortly introduced in the following but not derived from theory. A rather simple approach is the charge ratio method:

$$d = \left(\frac{Q_{i+1} - Q_{i-1}}{Q_i - Q_{i-1}}\right) \cdot \frac{W}{2} \tag{4.50}$$

[SOF12] which can be written more generally as general charge ratio algorithm

$$d = \frac{\arctan\left(1.65 \cdot \left(\arctan\left(\frac{(1 - Q_{i-1}/Q_i)}{(1 - Q_{i+1}/Q_i)}\right) - \frac{\pi}{4}\right)\right)}{\arctan\left(1.65\frac{\pi}{4}\right)} \cdot \frac{W}{2} \tag{4.51}$$

proposed by [C+83] and [LP95]. Nevertheless, the hyperbolic secant squared (SECHS) method

$$d = \frac{a_3}{\pi} \tanh^{-1}\left(\frac{\sqrt{Q_i/Q_{i-1}} - \sqrt{Q_i/Q_{i+1}}}{2\sinh((\pi W)/a_3)}\right) \tag{4.52}$$

with

$$a_3 = \frac{\pi W}{\cosh^{-1}\left(0.5 \cdot \left(\sqrt{Q_i/Q_{i-1}} + \sqrt{Q_i/Q_{i+1}}\right)\right)} \tag{4.53}$$

as proposed by [LP95], [LST72], [B$^+$85] and [OH$^+$99] showed the lowest systematic deviation of the reconstructed position which can only be reached by using the PRF to fit the charge fraction distribution event by event with two bound parameters K_3 [0.1, 0.9] and d [$-0.5W$, $0.5W$]. The ranges were estimated by an iterative optimization procedure. The reconstruction algorithm for overflow signal on central channel

$$d = a \cdot \log\left(\frac{Q_{i-1}}{Q_{i+1}}\right) + \frac{W}{2} \tag{4.54}$$

where a is a parameter of applied anode voltage applied to the presented chamber geometry; -0.10 at 950 V and -0.13 at 1200 V which has to be determined by a GARFIELD simulation for each given chamber geometry as proposed at the SOFIA Collaboration meeting 2012 [SOF12].

4.4. Particle Identification

There are different statistical methods known to perform particle identification/separation based on TRD-data like one or multidimensional (logarithmic) likelihoods, weighted decision trees, Neural Network (NN) and several more. Likelihood ratios are often used to identify the particle identity of reconstructed tracks. In this case, there is a discrete set of hypotheses, but the data may or may not discriminate between them. The focus of this thesis will be the electron-pion-separation using likelihood on total charge (Q-likelihood).

4.4.1. Probability Density Functions

The probability density function (PDF) describes the response of a detector to each particle species. The PDF, written as $\mathcal{P}(x|H)$ denotes to the probability for a particle track of species H leaving a signature x described by a vector of measurements. $\mathcal{P}(x|H)dx$ is the probability for the detector to respond to a track of type H with a measurement in the range $(x, x + dx)$. As with any PDF, the integral over all possible values is unity. The vector x may describe a single measurement in one detector, several measurements in one detector, or several measurements in several detectors. In many cases of interest the correlations of x will be reasonably small and the overall PDF can be determined as a product of the PDFs for individual detectors.

4.4.2. Likelihood

For given relevant PDFs, the likelihood that a track with measurement vector x is a particle of species H is denoted by $\mathcal{L}(H|x)$. The functional forms of PDFs and the corresponding likelihood functions are the same:

$$\mathcal{L}(H|x) \equiv \mathcal{P}(x|H). \tag{4.55}$$

The difference between $\mathcal{L}(H|x)$ and $\mathcal{P}(x|H)$ is a function of the measurable quantities (x) for a fixed hypothesis (H). Likelihood is a function of the particle type (H) for the measured value (x). Therefore, an observed track for which x has been measured has a likelihood for each particle type. Competing particle type hypotheses should be compared using the ratio of their likelihoods. Other variables having an 1-to-1 mapping onto the likelihood ratio are equivalent. Two commonly used mappings of the likelihood ratio are the difference of log-likelihoods and a normalized likelihood ratio, sometimes called

likelihood fraction [B+02]. For example, to distinguish between the π and e hypotheses for a track with measurements x both hypotheses with the same probability, the ratio of their likelihood is written as:

$$\mathcal{F}(e|x) = \frac{\mathcal{L}(e|x)}{\mathcal{L}(\pi|x)}. \tag{4.56}$$

It can be shown rigorously that the likelihood ratio (equation 4.56) and its equivalent

$$\mathcal{F}(e|x) = \ln\left(\mathcal{L}(e|x)\right) - \ln\left(\mathcal{L}(\pi|x)\right) \tag{4.57}$$

and

$$\mathcal{F}(e|x) = \frac{\mathcal{L}(e|x)}{(\mathcal{L}(e|x) + \mathcal{L}(\pi|x))} \tag{4.58}$$

and any other 1-to-1 mapping discriminate between hypotheses most powerfully [B+02]. For any particular cut on the likelihood ratio there exists no other set of cuts or selection procedure which gives a higher signal efficiency for the same background rejection. In the case (such as particle identification) where the probabilities of the competing hypotheses are known numbers, $\mathcal{P}_{\mathcal{A}}(H)$, likelihoods can be used to calculate the expected purities of given selections. Considering the case, seven pions are produced for each electron, then the fraction of electrons in a sample with measurement vector x is:

$$\begin{aligned}\mathcal{F}(e|x) &= \frac{\mathcal{L}(e|x)\cdot\mathcal{P}_{\mathcal{A}}(e)}{\mathcal{L}(\pi|x)\cdot\mathcal{P}_{\mathcal{A}}(\pi) + \mathcal{L}(e|x)\cdot\mathcal{P}_{\mathcal{A}}(e)} \\ &= \frac{\mathcal{L}(e|x)}{\mathcal{L}(\pi|x)\cdot 7 + \mathcal{L}(e|x)}.\end{aligned} \tag{4.59}$$

This can be considered as a weighted likelihood ratio where the weighting factors $\mathcal{P}_{\mathcal{A}}$ are probabilities. The $\mathcal{F}(e|x)$ are also called posteriori probabilities, relative probabilities, or conditional probabilities, and their calculation according to equation 4.59 is an application of Bayes' theorem. By construction $\mathcal{F}(e|x) + \mathcal{F}(\pi|x) = 1$. The purity, i.e., the fraction of pions in a sample selected with, say, $\mathcal{F}(e|x) > 0.9$, is determined by calculating the number of pions observed in the relevant range of values of $\mathcal{F}$ and normalizing to the total number of tracks observed there.

There has been an implicit assumption made so far that there is perfect knowledge of the PDF describing the detector. In the real world, there are often tails on distributions due to track confusion, nonlinearities in detector response, and many other experimental sources which are imperfectly described in PDFs. While deviations from the expected distribution can be determined from control samples of real data and thereby taken into account correctly, the tails of these distributions are often associated with fake or badly reconstructed tracks. This is one reason why experimentalists should include an additional consistency test. For a device measuring a single quantity and a Gaussian response function, a track is said to be consistent with hypothesis at the 31.7% (45.5%) significance level if the measurement falls within 1 (2) σ of the peak value. If the PDF is an univariate Gaussian,

$$\mathcal{P}(x|H) = \frac{1}{\sqrt{2\pi}\sigma(H)} \exp\left[-0.5\left(\frac{(x-\mu(H))}{\sigma(H)}\right)^2\right], \tag{4.60}$$

the significance level (SL) for hypothesis H of a measured track with $x = x_{obs}$ is defined by

$$SL(x_{obs}|H) \equiv 1 - \int_{\mu H - x_{obs}}^{\mu H + x_{obs}} \mathcal{P}(x|H)dx. \tag{4.61}$$

Notice that the integration interval is defined to have symmetric limits around the central value. This is an example of a two-sided test. This definition is equally sensible for other symmetric PDFs with a single maximum. For non Gaussian, non monotonic or asymmetric PDFs (e.g. ionization measurements) a particularly useful generalization of the significance level of an observation x_{obs} given the hypothesis H is defined as

$$SL(x_{obs}|H) = 1 - \int\limits_{\mathcal{P}(x|H)>\mathcal{P}(x_{obs}|H)} \mathcal{P}(x|H)dx. \tag{4.62}$$

Although we define the consistency in terms of an integral over the PDF of x, note that the range(s) is(are) specified in terms of the PDF, not in terms of x. This allows a physically meaningful definition. All significance levels derived from smooth distributions of the true hypothesis are uniformly distributed between 0 and 1 (as are confidence levels). This can be used to test the correctness of the underlying PDF using a pure control sample.

4.4.3. Likelihood on Total Charge

The likelihood on total charge (LQ) is used to separate reconstructed particle tracks of different species (in case of CBM TRD electrons and pions) based on the characteristic charge deposition within the detector (MWPC). For momenta between 2 and 10 GeV/c electrons loose energy by ionization plus TR whereas other particles like pions loose energy only by ionization. Pions of some GeV/c are minimum ionizing particles in contrast to electrons, which are already in the Fermi plateau (compare to figure 4.9). Therefore, the average electron signal in this momentum region is larger than the pion signal, irrespective of the detector. As introduced in chapter 4.4 a simulated or measured energy loss spectrum for electrons and pions can be used as input PDF. The pion rejection approximation procedure will be illustrated in the following based on simulated data. Electrons and pions have a probability $\mathcal{P}(E|H)$ equivalent to the normalized count $C(E)$ to deposit the energy E in one detector. Assuming that the measurements of TRDs with equivalent geometrical properties are independent, the pion-rejection factor can be extrapolated to m detector layers based on the simulated normalized charge distributions of one chamber. This estimation is valid under the assumption that all detector layers have a geometrical acceptance of 100%, perfect detector efficiency and only TR-photons are absorbed within the detector produced within the associated radiator. The measurement vectors are E^e and E^π which are m times randomly sampled energy losses for electrons and pions according to the simulated charge-loss spectra. The probabilities of the hypotheses to produce an electron $\mathcal{P}_\mathcal{A}(e)$ or a pion $\mathcal{P}_\mathcal{A}(\pi)$ are assumed to be equal to 1. The probability for an electron or a pion to deposit the energy E_n in detector layer n is $\mathcal{P}_n(E_n^e \,|\, e)$ respectively $\mathcal{P}_n(E_n^\pi \,|\, \pi)$. The likelihood $\mathcal{L}(e|E^e)$ for an electron to produce a vector of energy losses $E^e = \{E_1^e, ..., E_m^e\}$ within m detector layers is

$$\mathcal{L}(e|E^e) = \mathcal{P}(E^e \,|\, e) = \prod_{n=1}^{m} \mathcal{P}_n(E_n^e \,|\, e) \quad \text{with} \;\; 0 < \mathcal{P}_n(E_n^e|e) < 1 \tag{4.63}$$

[Wil04] under the assumption of 100% detector efficiency and acceptance. The likelihood for pions $\mathcal{L}(\pi|E^\pi)$ can be calculated analogical:

$$\mathcal{L}(\pi|E^\pi) = \mathcal{P}(E^\pi \,|\, \pi) = \prod_{n=1}^{m} \mathcal{P}_n(E_n^\pi \,|\, \pi) \quad \text{with} \;\; 0 < \mathcal{P}_n(E_n^e|\pi) < 1. \tag{4.64}$$

The likelihood ratio $\mathcal{F}(e|E^e)$ for a single track to be an electron can be calculated according to:

$$\mathcal{F}(e|E^e) = \frac{\mathcal{L}(e|E^e)}{\mathcal{L}(e|E^e) + \mathcal{L}(\pi|E^e)}, \qquad \text{with } 0 < \mathcal{L}(H|E^e) < 1. \tag{4.65}$$

The likelihood ratio for a single track to be a pion identified as an electron is:

$$\mathcal{F}(e|E^\pi) = \frac{\mathcal{L}(e|E^\pi)}{\mathcal{L}(e|E^\pi) + \mathcal{L}(\pi|E^\pi)}, \qquad \text{with } 0 < \mathcal{L}(H|E^\pi) < 1 \tag{4.66}$$

or

$$\mathcal{F}(e|E^\pi) = 1 - \mathcal{F}(\pi|E^\pi). \tag{4.67}$$

4.4.4. Electron and Pion Efficiency

In order to determine the pion rejection a large number (> 1000 tracks/likelihood ratio bin) of tracks are required. The ratios $\mathcal{F}(e|E^e)$ and $\mathcal{F}(e|E^\pi)$ for each track are filled to two histograms as presented in figure 4.19. In case of the total ratio (equation 4.58) all

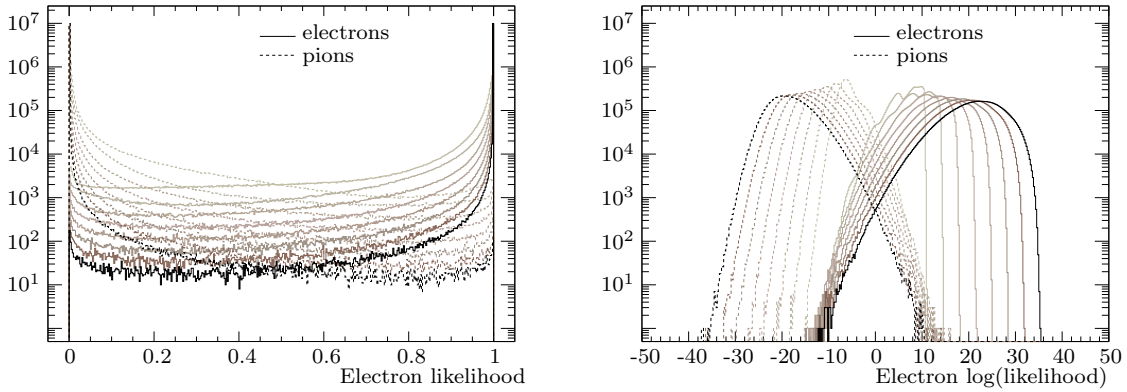

Fig. 4.19: Likelihood ratio distribution (left) and logarithm of likelihood ratio distribution (right) of electrons (solid line) and pions (dashed line) at 3.125 GeV/c in 12 mm Xe/CO_2 (80/20) with POKALON radiator B++ (parameters can be found in table 6.2) at 65% photon efficiency (compare to equation 4.13) . Likelihood distributions are calculated for 3 to 10 detector hits. Increasing darker color indicates increasing number of detector hits. Both distributions include $1 \cdot 10^7$ simulated tracks.

values are by definition between 0 and 1 where the distribution range has to be adapted for each analysis in case of the logarithmic ratio (equation 4.57). The total ratios increase exponentially towards 1 ($\mathcal{F}(e|E^e)$) respectively 0 ($\mathcal{F}(e|E^\pi)$) for increasing measurement vector dimensions (simulated detector layers). In contrast the upper limit of the $\mathcal{F}(e|E^e)$ distribution and the lower limit of the $\mathcal{F}(e|E^\pi)$ moves linear with increasing measurement vector dimensions. The electron efficiency (eE) ϵ_e gives the fraction of identified electrons. The number of misidentified pions at a given ϵ_e is defined to be the pion efficiency (pE). The pion suppression is given by $1/\epsilon_\pi$. Typically, an ϵ_e of 90% is used. The likelihood ratio distribution of electrons f^e is integrated until the integral includes 90% of the best electron candidates:

$$0.9 = \int_{\epsilon_e=0.9}^{1} f^e(\mathcal{F}(e|E^e))/\int_{0}^{1} f^e(\mathcal{F}(e|E^e)) \leq \sum_{\epsilon_e \geq 0.9}^{1} f^e(\mathcal{F}(e|E^e))/\sum_{0}^{1} f^e(\mathcal{F}(e|E^e)), \tag{4.68}$$

The pion efficiency is usually defined as the fraction of pions included by the integration limits for 90% of the electrons relative to all included particles:

$$\begin{aligned}\epsilon_\pi &= \int_{\epsilon_e=0.9}^{1} f^\pi(\mathcal{F}(e|E^\pi))/\left(\int_{\epsilon_e=0.9}^{1} f^e(\mathcal{F}(e|E^e)) + \int_{\epsilon_e=0.9}^{1} f^\pi(\mathcal{F}(e|E^e))\right) \\ &\leq \sum_{\epsilon_e\geq 0.9}^{1} f^\pi(\mathcal{F}(e|E^e))/\left(\sum_{\epsilon_e\geq 0.9}^{L_e=1} f^\pi(\mathcal{F}(e|E^e)) + \sum_{\geq 0.9}^{1} f^e(\mathcal{F}(e|E^e))\right).\end{aligned} \tag{4.69}$$

There is another definition of the pion efficiency which is often used. It is the included pion fraction relative to all pions in the likelihood distribution. The choice of definition strongly depends on the definition of signal purity. In a particular case, is the demanded quantity the number of pions which are misidentified as electron within all accepted electron tracks or the fraction of pions relative to all available pion tracks. For a final answer one has to take into account the average relative production ratio of electrons $\mathcal{P}_\mathcal{A}(e)$ and pions $\mathcal{P}_\mathcal{A}(\pi)$ per event as already mentioned. The second definition has the big advantage that the normalization is done with a constant value, namely all simulated pion tracks included in the pion likelihood distribution. On the other side the first definition is closer to the real measurement or experimental use case. During the experiment it is of interest how large the contamination of a given sample of n accepted tracks is and not how many misidentified tracks are within the sample relative to all possible tracks which could have been misidentified.
The pion efficiency as function of detector hits at 3.0 GeV/c in 12 mm Xe/CO_2 (80/20) with POKALON radiator based on equation 4.58 and 4.57 is presented in figure 4.20. The pion efficiency has an exponential falling tendency towards increasing number of

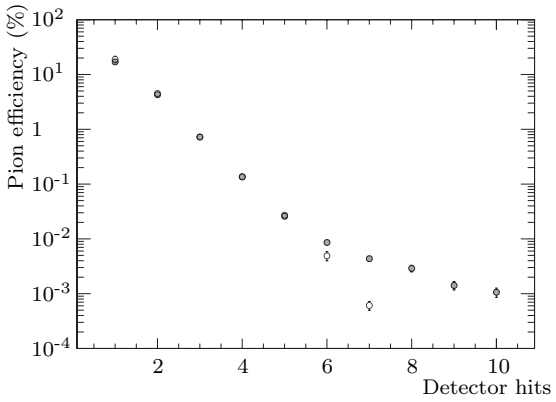

Fig. 4.20: Pion efficiency (gray: likelihood ratio equation 4.58; white: log. likelihood ratio equation 4.57) as function of detector hits at 3.0 GeV/c in 12 mm Xe/CO_2 (80/20) with POKALON radiator B++ (parameters can be found in table 6.2). The exponential tendency breaks at 6 detector hits since at least 90% of all electrons in the likelihood distribution are within the first bin in case of linear likelihood (compare to figure 4.19).

detector hits. Both results are in good agreement up to 5 detector hits. This tendency breaks at a certain detector hit number since at least 90% of all electrons in the total likelihood ratio distribution is included within the first bin (compare to figure 4.19). Therefor, the pion fraction included in this bin is dominated by statistical fluctuations and always over estimated. This saturation effect can only be avoided with higher likelihood distribution granularity and increased simulated track statistic in parallel leading

to exponentially increasing simulation effort. This effect can not be seen in case of logarithmic likelihood ratio. There is just no longer an intersection between the distribution of $\mathcal{F}(e|E^e)$ and $\mathcal{F}(e|E^\pi)$ due to statistic at a measurement vector dimension above 7. The conclusion is, that the integration uncertainty is lower in case of logarithmic likelihood ratio but several orders of magnitude higher simulated track statistic is needed for the same measurement vector dimension.
Another important effect is correlated to the binning of the input PDF and the simulated track statistic which is illustrated in figure 4.21 at constant measurement vector dimension of 10 and constant track statistic of 10^7 tracks. It can be observed that the

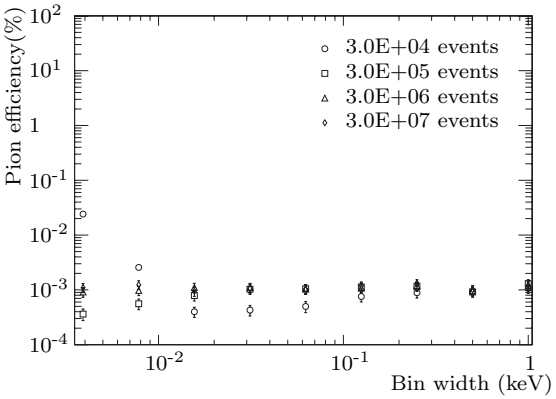

Fig. 4.21: Simulated pion efficiency at 90% electron efficiency in 12 mm Xe/CO_2 (80/20) with POKALON radiator B++ (parameters can be found in table 6.2)as function of the bin width at $3 \cdot 10^4$, $3 \cdot 10^5$, $3 \cdot 10^6$ and $3 \cdot 10^7$ events per PDF and a spectrum energy loss range between 0 and 100 keV. Approximation for 10 detector hits.

pion efficiency suffers from too low input PDF statistic (3000 events per PDF) at too high bin granularity (<0.01 keV/bin). Such a PDF is dominated by empty bins which are excluded from the likelihood estimation by definition (see equation 4.63 and 4.64). A clearly visible minimum in pion efficiency can be seen at a bin width of 0.01 to 0.02 keV for 30000 simulated events in the input PDFs. The minimum moves towards smaller bin width <0.004 keV if the PDF event statistic is increased by one order of magnitude. Above $3 \cdot 10^6$ events in each PDF there are no minima visible in the observed bin width range. The pion efficiency for all PDF statistic settings saturates at 0.001 between 0.1 and 1 keV bin width.
Since the described integration is carried out with histograms providing a finite bin granularity this is leading to an electron integral uncertainty (see equation 4.68 and 4.69) this error has to be taken into account. The deviation of the electron integral relative to 90% is assumed to be the systematic error of the pion integral in the following analysis. For example, the electron integral includes 96.7% of all electrons, the over shoot of 6.7% corresponds to 37% of the bin content of the last added electron likelihood bins. The systematic error on the pion integral is assumed to be 37% of the last added pion likelihood bin.
Based on the previous discussed topics the influence of a first detector design parameter defining the PID performance of the CBM TRD can be simulated; the thickness of the active gas volume as presented in figure 4.22. The absorption probability increases for thicker gas volumes towards higher photon energies at a constant radiator emission spectrum. Therefore the average total energy deposit per electron is enhanced in addition to the increasing energy loss due to ionization. This leads to an increase in pion rejection

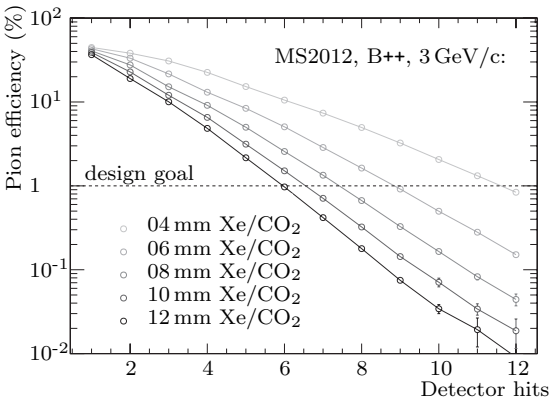

Fig. 4.22: Simulated pion efficiency at 90% electron efficiency in 12 mm Xe/CO_2 (80/20) with POKALON radiator B++ (parameters can be found in table 6.2) at 3.0 GeV/c as function of number of detector hits for different Xe/CO_2 (80/20) thicknesses.

at a constant number of simulated hits per track.

4.5. Double Hit Identification

Double hits can be a major limiting factor on position resolution and particle identification in a high counting rate/occupancy environment. A reliable double hit identification algorithm with a minimum single hit misidentification plays, in this case, a key role. In absence of MC-truth, only the measured charge can be used to separate double- from single hits. There are different approaches like 2-dim fitting with one or two Gaussian respectively Mathieson distributions, cluster sizes or cuts on charge ratios as presented in [WBW96]. All algorithms have to be tested very carefully using MC-truth in order to find the best solution for a given problem or pad-plane geometry. The notation which will be used in the following indicates the separation of pads in x- and y-direction (x, y). Following this, (0,0) denotes two hits on the same pad, (1,0) for two hits on two adjacent pads in the same row, (0,1) for hits on adjacent pads in one column. Nearby located double hits may not be separated by the measurement of the total charge in the cluster, because the pulse height can be very different even for the same particle type due to the long Landau tails in the energy loss distribution.
The only clear information can be extracted from the width of the observed charge measurement or unusual charge ratios of adjacent pads. However, the width can only be determined with some uncertainty due to noise and the low number of involved pads in each cluster. Therefore, some double hits can not be differentiated from single hits, in case they are very close to each other or the energy loss is very different. Thus the smaller signal disappears in the tail of a large peak.
All algorithms were compared in a simulation. A pad-plane of 9×9 pads with a pad width W of 7.125 mm and a height H of 14 mm was assumed. The charge sharing was simulated based on the PRF (equation 4.36) in both dimensions. The resulting charge fraction per channel distribution was multiplied with random energy loss corresponding to the simulated energy loss spectrum of 3 GeV/c pions in a 12 mm thick Xe/CO_2 (80/20) mixture. A common noise with a Gaussian distribution width $\sigma = 0.1$ keV was added to each channel. The first hit was uniformly, randomly positioned on the central pad $[x, y]$ and the second one was positioned randomly, uniformly on the central 5×5 pads. It was ensured that on the central pad the largest signal fraction was induced. Two ap-

proaches will be presented in more detail; The identification based on the (A) horizontal charge ratio $Q_{[x-1,y]}/Q_{[x,y]}$ vs. $Q_{[x+1,y]}/Q_{[x,y]}$, (B) vertical charge ratio $Q_{[x,y-1]}/Q_{[x,y]}$ vs. $Q_{[x,y+1]}/Q_{[x,y]}$ as well as on (C) cluster size vs. $(Q_{[x-1,y]} + Q_{[x,y-1]})/Q_{[x,y]}$, where the first hit with the largest signal fraction is on pad $[x, y]$. The cluster size is evaluated based on a minimum charge threshold of 0.45 keV. The characteristic distributions of single hits are presented in figure 4.23. The double hit identification cut values are evaluated

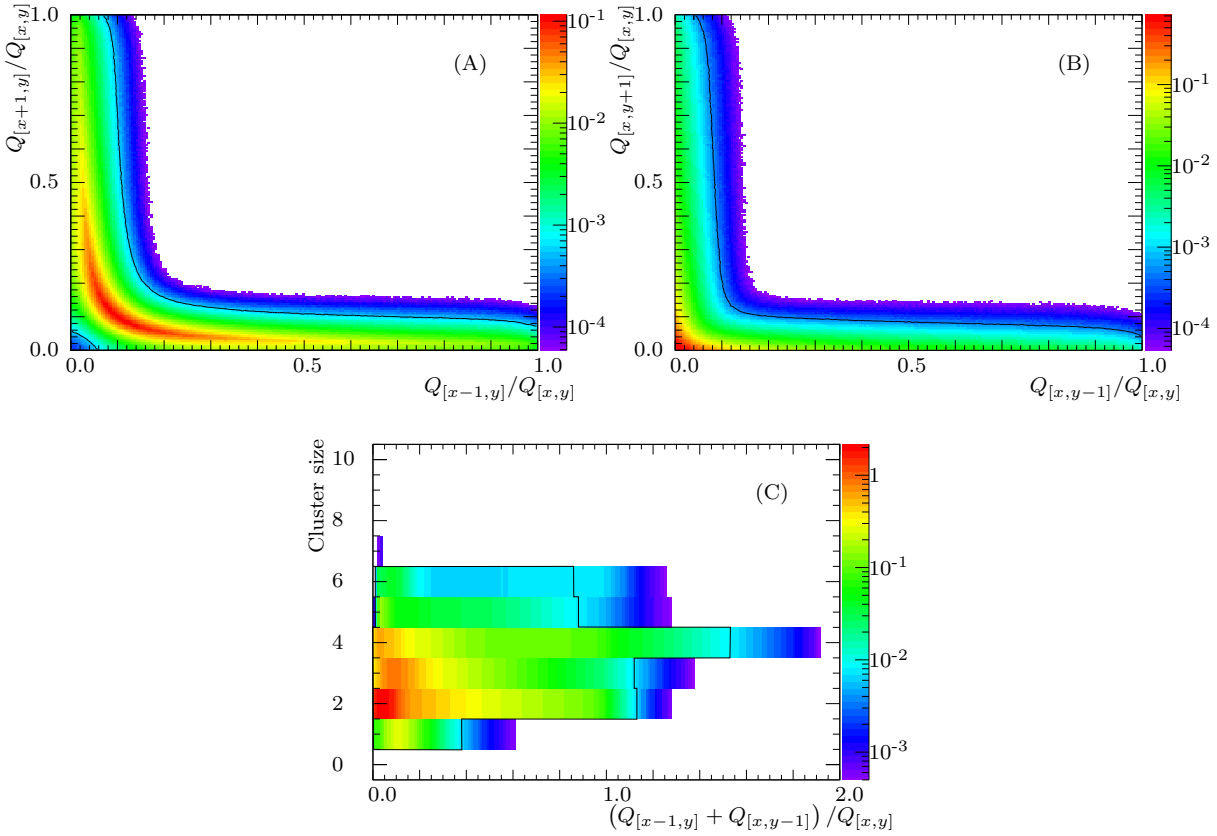

Fig. 4.23: Single hit distributions of (A) horizontal charge ratio, (B) vertical charge ratio and (C) cluster size vs. $(Q_{[x-1,y]} + Q_{[x,y-1]})/Q_{[x,y]}$ with cut values for 1% single hit misidentification (black line). The double hit distributions are presented in appendix G.

based on the shape of the accumulation area of the single hit distributions to ensure a single hit misidentification of 1% at maximum double hit identification performance. The resulting double hit recognition performances of the three presented approaches are presented in table 4.2 and appendix G respectively. It is obvious that one single

Tab. 4.2: Double hit identification efficiency given in % at 1% single hit misidentification probability for nine different double hit classes (x, y).

	(0,0)	(0,1)	(0,2)	(1,0)	(1,1)	(1,2)	(2,0)	(2,1)	(2,2)
(A)	5.06	26.70	5.17	1.68	9.36	1.78	0.98	1.01	1.01
(B)	15.78	2.36	1.00	51.98	8.71	1.01	17.59	2.43	1.02
(C)	4.05	20.67	23.69	14.66	19.58	23.99	22.28	23.84	23.76

algorithm is not sufficient to identify all different double hit classes. The highest global identification performance at 1% misidentification of single hits is obtained by a combination of charge ratio and total cluster size (C). The impact of unidentified double hits on tracking as well as PID performance has to be further investigated.

5. MWPC Detector Prototypes

When designing TRD prototypes for the CBM experiment, a compromise between PID performance and high rate capability has to be found, since these are opposing 'features' of a MWPC based TRD as mentioned before. The PID performance scales with the gas thickness (absorption probability of the TR-photons), where the read-out speed decreases when signal collection time increases with the gas thickness. The first step is to get an estimation on maximum hit rate distribution, which is the limiting parameter for the maximum signal collection time depending on the MWPC geometry and gas thickness, defining the corresponding PID performance. This development path and the used frameworks and tools will be described in the following section.

5.1. The CbmRoot Simulation Framework

The ROOT C++ object-oriented program and library developed at CERN [BR97] is the basis of the CbmRoot framework. CbmRoot supports several external particle generators and transport algorithms as GEometry ANd Tracking (GEANT) 3, GEANT4 [A+03b] or FLUktuierende KAskade FLUKA (German: Fluctuating Cascade) [B+07], without changing the user code. The detector response is supported by the framework as well as physics analysis. The flow chart in figure 5.1 visualizes the simulation and reconstruction hierarchy and the internal data processing within CbmRoot. As standard event gene-

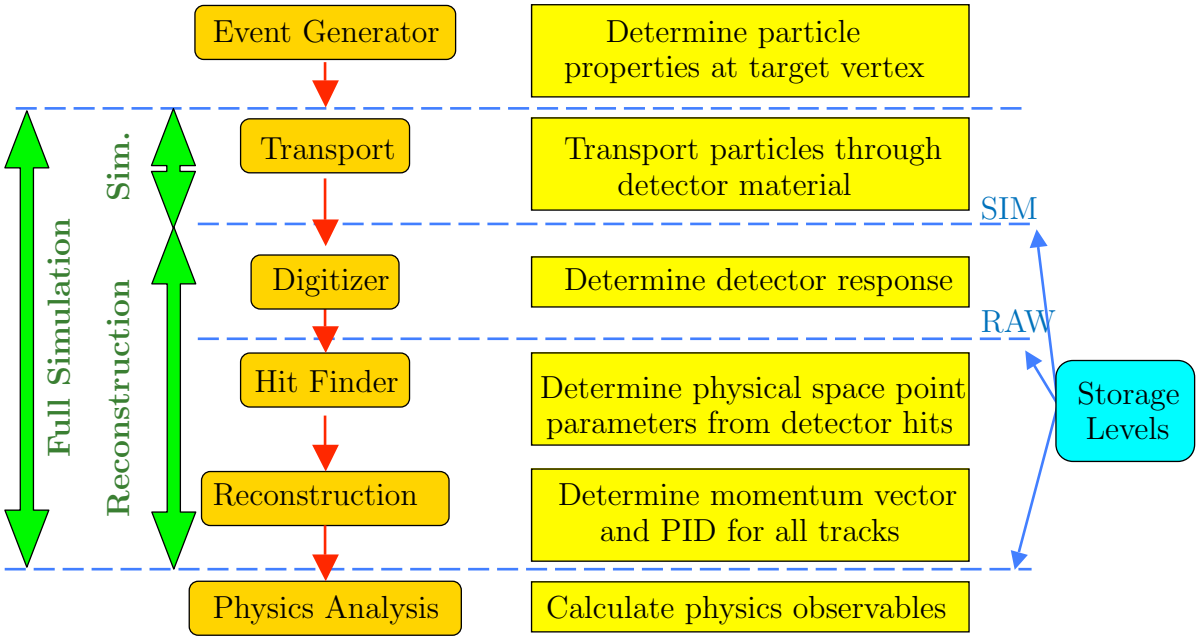

Fig. 5.1: CbmRoot simulation framework structure [ATBUK08]. The simulation step begins with the pure event generator feeding the particles to the transport algorithm GEANT3. The reconstruction step includes digitization (detector and read-out electronic response) followed by the hit finder. The last step is the reconstruction comprising track-fitting and particle identification. The resulting output is used afterwards for physics analysis.

rator the Ultra-Relativistic Quantum Molecular Dynamics (UrQMD) [BBB+98] code is used. The UrQMD model is a microscopic model designed to simulate ultra-relativistic heavy-ion collisions in the energy range from 1 AGeV up to 200 AGeV. UrQMD is a multi-purpose tool for studying a wide variety of heavy-ion reaction mechanisms like

multi-fragmentation and collective flow. Since rare probes, such as vector mesons and charmed hadrons, are not included in UrQMD, the results of different models are embedded into the events. In case of the dilepton simulation the PLUTO [F+07] model is used as thermal source and multiplicities are taken from Hadron-String Dynamics (HSD) [EC96]. HSD multiplicities are also used in case of charm production together with a PYTHIA [SMS06] decayer. In the following studies the particles are propagated through the CBM detector model using the transport code GEANT3 focusing on the detector response as well as on detector occupancy.

5.2. TRD Geometries

The CBM TRD geometry is subject to influence of ongoing developments. The detector models of v12f geometry as presented in figure 5.2 are based on the detector prototypes from Münster tested in beam 2012 at CERN Proton Synchrotron (PS) (see chapter 8.2 and A.1). The detector modules are scaled to two sizes, $60 \times 60\,\mathrm{cm}^2$ and $100 \times 100\,\mathrm{cm}^2$.

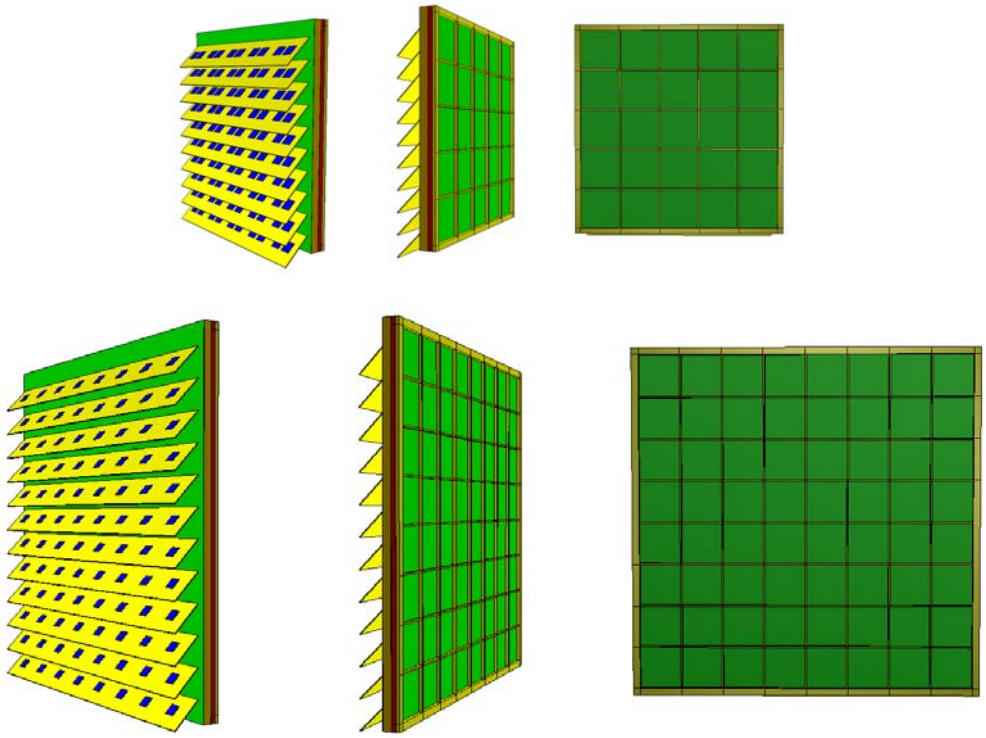

Fig. 5.2: Two basic chamber modules with highest pad-plane granularity implemented in CbmRoot [Ems13a]. Modules used in the outer part with a size of $100 \times 100\,\mathrm{cm}^2$ are presented in the lower row and detectors foreseen for the inner part with a size of $60 \times 60\,\mathrm{cm}^2$ are shown in the upper row.

The modules have an active gas volume thickness of 12 mm enclosed by a 25 μm Kapton foil supported by a G11 (glass-reinforced epoxy laminate) support grid (small chamber: $0.4 \times 0.4 \times 1.5$ cm; big chamber: $0.4 \times 0.4 \times 2.0$ cm) on the front side and a 360 μm thick FR4 pad-plane covered by a 25 μm thick segmented copper layer on the back. The pad-plane is mechanically supported by a 23 mm honeycomb, carbon-fiber ($2 \times 190\,\mu$m) sandwich. The Front-End-Boards (FEBs) are modeled of 2.5 mm thick and 100 mm wide FR4 sheets. The FEBs have the same length as the correspondent detector modules.

The number of FEBs per chamber are derived from the pad-plane granularity and the number of channels per Application-Specific Integrated Circuit (ASIC) reading data from 2-6 pad rows (in anode wire direction). Gas supply, low voltage or high voltage as well as other services or mechanical support of the individual modules are not yet implemented. To avoid unnecessary complex and small structures within the transport model also anode-, drift-wires and the thin aluminum sheet on the entrance window are excluded from the geometry.
The modules are arranged in four (SIS100) respectively 10 layers (SIS300). The layers within the same station are built identically. The first layer of each station is presented in figure 5.3. The pad granularity decreases as function of the distance to the beam-pipe

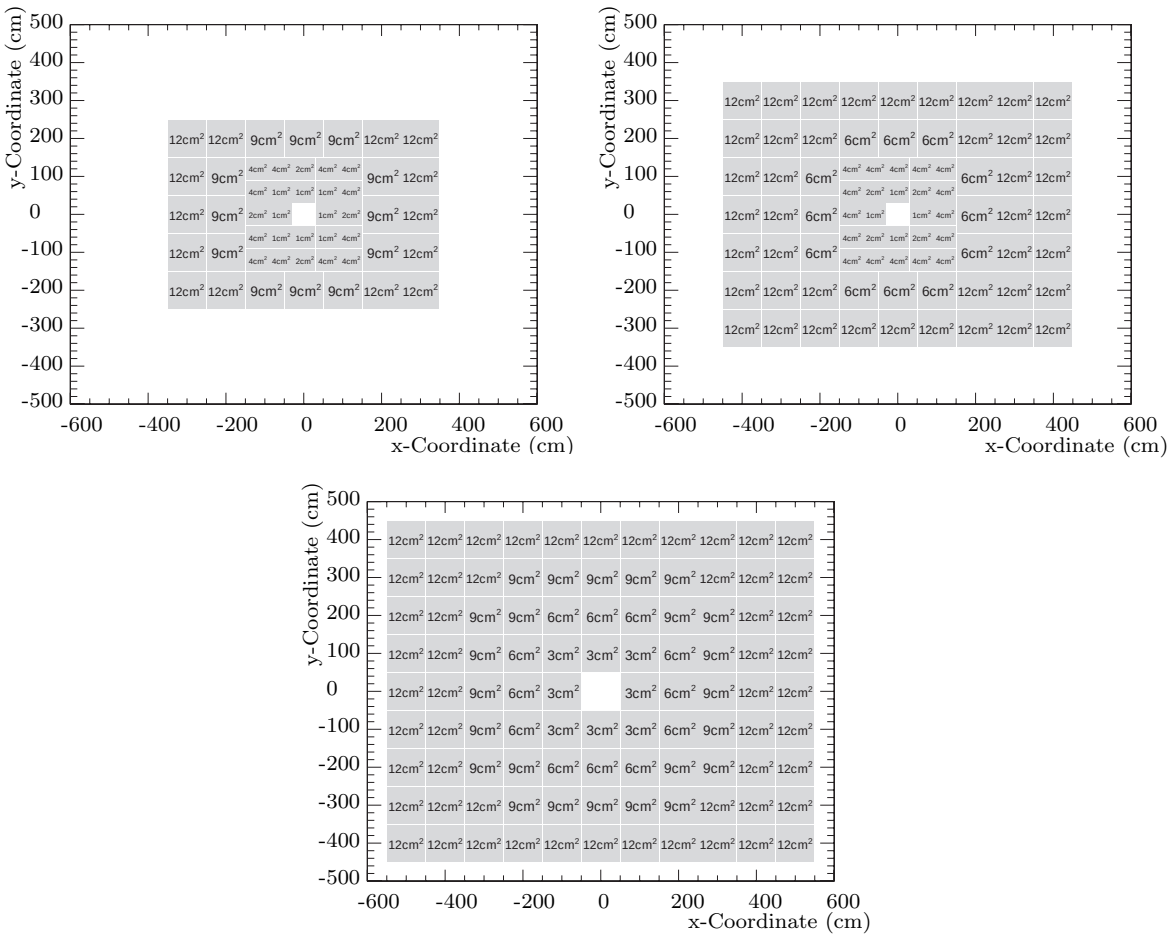

Fig. 5.3: CBM TRD pad-plane layout geometry $v12f$ [Ems13a]. Here are only the first layer of each station are presented, since the pad-plane layout of different layers within the same station does not differ. It has to be mentioned that all even layer numbers are rotated by 90 deg around z with respect to the odd ones. The number corresponds to the average pad area at a pad width of 0.7125 cm.

to match the decreasing average charged particle track rate. Since the optimal pad width of 7.125 mm ($v12f$) (in anode wire direction) is given by the distance of the anode wire grid to the pad-plane, there is only one parameter left. The pad height (perpendicular to the anode wire direction) can be varied in integer multiples of the anode wire spacing. This parameter was chosen to limit the maximum hit rate in the inner part of the TRD to 100 kHz (corresponding to 10 μs average signal delay) and 10% average detector occupancy. The pad-planes are subdivided into three sectors of equal pad area and pad height within each individual sector. The outer sectors are identical. The difference

between outer and inner sector is rather small and introduced to realize pad heights of integer multiples of the anode wire spacing, e.g. $8 \times 2.75 + 4 \times 2.5 + 8 \times 2.75 = 54$. The different layer types are mounted in the same support structure per type. The mounting chassis are composed of IPB 400 aluminum profiles, 30×40 cm in size with 2 cm wall thickness. This mounting structure defines the so called station. The first four identical layers sharing the same support structure are merged to station 1. The following four identical layers are arranged in a second support cage. The two last layers with the largest active area per layer are supported by a last support frame. The first station is supposed to be used as SIS100 TRD in the first CBM startup version.

5.3. Ideal Detector Response

The fundamental processes included in the signal creation/evolution within a TRD are described in detail in chapter 4.2.2. It is possible to include all these details within a Monte Carlo(MC)-detector-response-simulation framework, but at the price of a relative high time consumption. To have a sufficient compromise between a detailed physics simulation and an efficient detector response, both parts are decoupled in the CbmRoot simulation framework. The particle production and transport as well as all relevant energy loss effects except TR-photon production are calculated within the *simulation*. Only the total energy loss per active detector volume is stored. The detector response, Data AcQuisition (DAQ), data transport, event building and the physics analysis is done in the second step, the *reconstruction*. The output of the simulation is pure MC-information, like the ionization energy loss or the entrance and exit points of particle trajectories crossing active detector volumes. In order to get a detailed and efficient detector response, this information has to be processed to 'restore' the essential features of the detector and add missing processes (e.g. TR-production) as illustrated in figure 5.4.

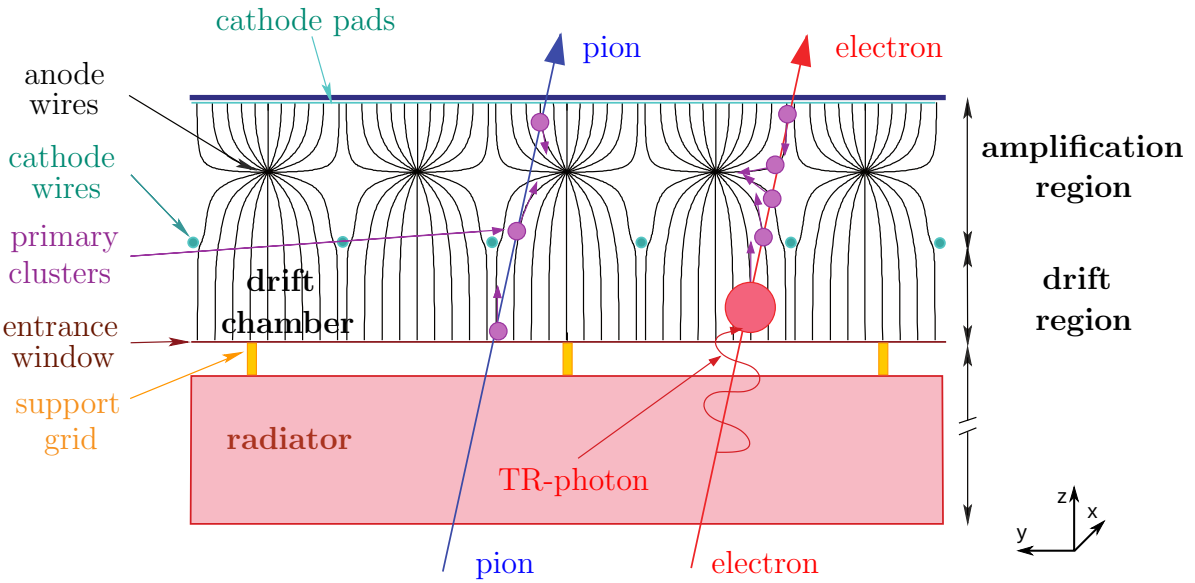

Fig. 5.4: Schematic view of the ideal detector response of the CBM TRD. This figure includes primary ionization clusters as well as TR-photon creation. The primary clusters drift along the electric field lines towards the anode wires. The material budget includes radiator, entrance window, wires the pad-plane, and the back-panel (not shown in this figure).

5.4. Simulation

The simulation step covers the event generation as well as the particle transport and the calculation and storage of the energy loss of these particles traversing the active detector volumes and support (non-active) volumes. The MC-energy loss by ionization as delivered by GEANT3 within the active detection volumes is summed up and stored in the so called *CbmTrdPoint* container, together with the entrance and exit point coordinates and other informations on the MC-level, like an unique track ID, active volume ID, momentum at the entrance and exit point, time of flight and total track length. This is illustrated in figure 5.5. Since the detector/radiator combination is not finally fixed,

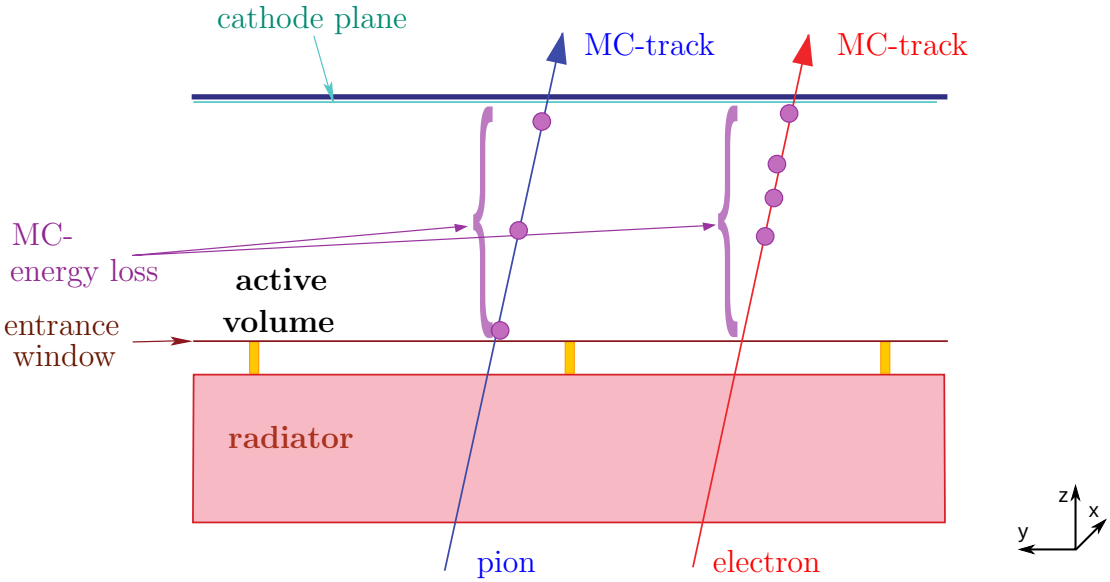

Fig. 5.5: Schematic view of the CBM TRD as implemented in CbmRoot simulation step. The particles from the UrQMD events are propagated through the detector setup by GEANT3. The total MC-energy loss is stored as well as the entrance an exit point of the MC-track.

the TR-photon production by the radiator is simulated in the reconstruction step. This is the first part of the reconstruction, independent of the detector response flavor used later on.

5.5. Reconstruction

The second step the *reconstruction* covers or will cover radiator simulation, MWPC-detector and Front-End-Electronic (FEE) response, Data AcQuisition (DAQ), data transport, event building and the physics analysis.

5.5.1. TRD Radiator Simulation

The simulation of the TR-photon production is done based on formula 4.9 as described in chapter 4.1.1. The self-absorption of the radiator is taken into account as well as the absorption of the aluminized entrance window and the active gas volume. Loss due to TR-photon absorption within the G11 support grid between the radiator and the entrance window foil are not yet implemented. The final energy loss due to TR-photon absorption within the sensitive gas volume is added to the ionization energy loss coming from the simulation part. The radiator task has to be called in the reconstruction macro

before the digitizer, where the TR-photon simulation itself is done within the digitizer task.

5.5.2. TRD MWPC-Detector Response

Up to now there are four reconstruction chains available for the CBM TRD: *CbmTrdHitProducerIdeal* (Ideal), *CbmTrdHitProducerSmearing* (Smearing), *CbmTrdDigitizer* (Digitizer), and *CbmTrdClusterizer* & *CbmTrdClusterFinderFast* & *CbmTrdHitProducerCluster* (Clusterizer). A chain can consist of up to three steps; a digitizer, clusterizer (cluster finder) and hitproducer. The different flavors result from a consistent development starting with the pure MC-information (Ideal) towards a gradually more and more realistic detector response and reconstruction algorithms. All reconstruction flavors are very useful to investigate on different detector and reconstruction algorithm features. The present algorithms will be shortly introduced in the following chapters in an order of increasing number of detector response features. The input information of all different reconstruction flavors are collected in the so called *CbmTrdPoint*. This class contains the full MC-information. Towards different subclasses this information is processed to include detector features which result in the end in so called *CbmTrdHits*. This class is afterwards used for tracking and higher analysis. A detailed performance analysis with respect to tracking and particle identification will be shown in chapter 8.

5.5.2.1. Ideal Reconstruction Chain The Ideal reconstruction chain uses just the pure MC-information provided by the *CbmTrdPoint* and copies these informations to the data class members of the *CbmTrdHit*. The hit position is associated with the MC-exit point. There is no detector response or features like pad-plane granularity or charge sharing between adjacent pads are included.

5.5.2.2. Smearing Reconstruction Chain The Smearing reconstruction chain smears the central position between the MC-impact point and the exit point within a Gaussian distribution representing the measured position resolution of prototypes built by the groups in Bucharest and Münster tested in beam. This takes also into account that rectangular pads provide different position resolution in the short and long pad size direction (compare to figure 5.6). The error of the reconstructed hit position is the absolute distance between the MC-exit point and the smeared reconstructed hit position. The energy loss is copied to the hit level. Nevertheless there are still features like charge sharing and finite detector granularity missing. Cluster merging due to a too short distance between two or more hits was implemented. The minimum distance between two hits which can be separated is represented by the variable fMinDist (in cm). This allows to investigate on tracking efficiency as function of the detector hit resolution without a dedicated pad granularity. Nevertheless this reconstruction flavor is still the default version for all global CbmRoot based simulations and physics analysis. A benchmark can be found in [LHLO12].

5.5.2.3. Digi Reconstruction Chain Here the central position between the MC-impact point and the exit point is projected to the pad-plane and moved towards the closest pad center. This position is transfered through the *CbmTrdDigi* level to the *CbmTrdHit*. The error of the reconstructed hit position is half of the corresponding pad dimension. The algorithm is illustrated in figure 5.7. The signal of channels with the same address which are fired within the same event by different MC-tracks are merged (signal is summed

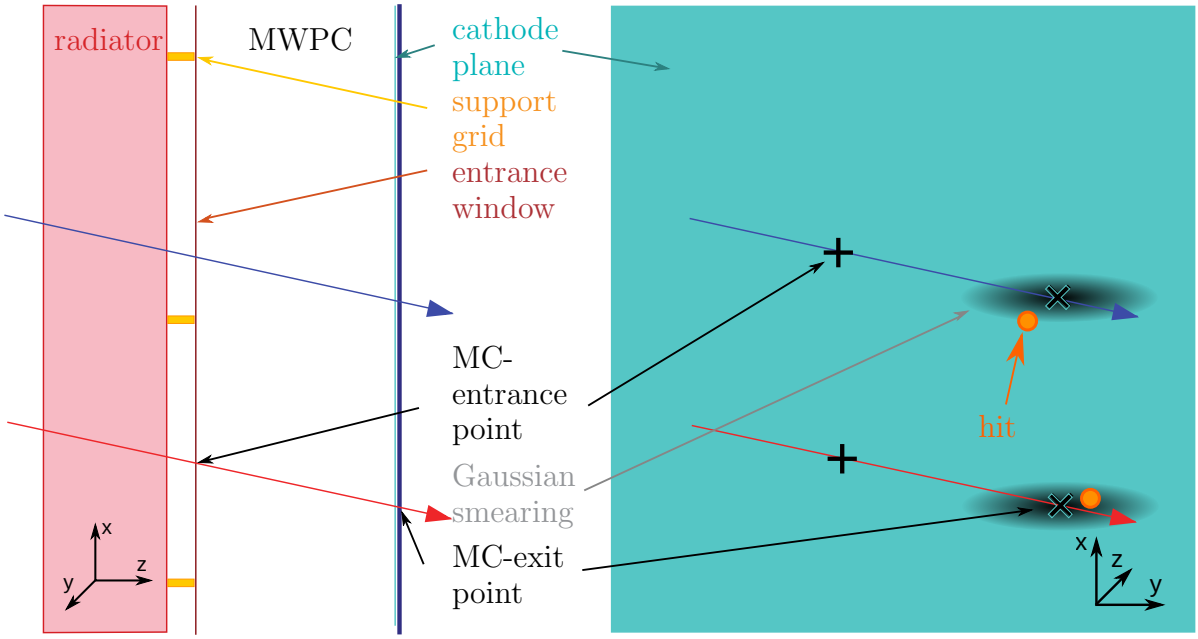

Fig. 5.6: Schematic view of the CBM TRD as implemented in CbmRoot reconstruction step using smearing hitproducer. The hitproducer smearing is based on the ideal hitproducer. The entrance point of the MC-particle (red and blue arrow) is marked by a (+). The reconstructed hit position (orange point) is associated to the smeared exit point of the MC-track (×). The smearing is done according to a Gaussian-distribution which is individually defined for the x- and y-coordinate for each detector layer.

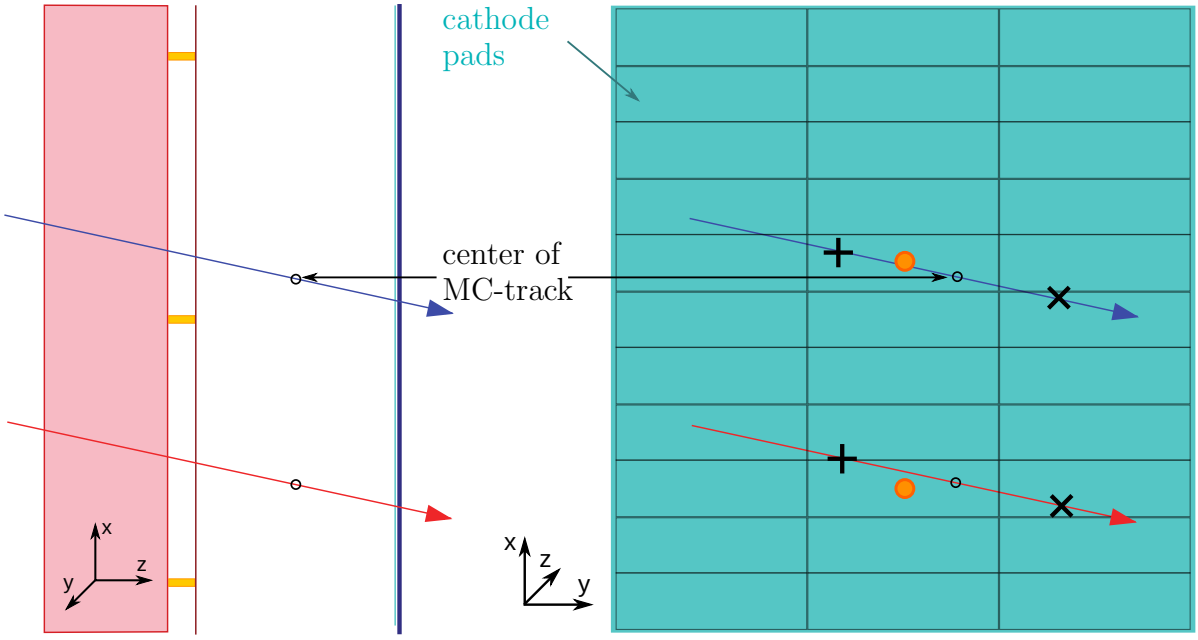

Fig. 5.7: Schematic view of the CBM TRD as implemented in CbmRoot reconstruction step using digi hitproducer. The algorithm of the digi hitproducer is also based on the ideal hitproducer. The pad granularity is considered for the first time. The central point between the entrance and exit point are projected to the pad-plane and the center of the underlying pad is associated with the hit position.

up). This allows for hit merging on the digi level as well as for occupancy studies for the first time. Therefore the number of MC-exit points and reconstructed hits is not equivalent by definition. The position resolution of the chamber is no longer included

and features like charge sharing are still missing.

5.5.2.4. Cluster Reconstruction Chain This algorithm was developed and implemented as part of this thesis. Charge sharing and finite detector granularity are the starting point of the cluster reconstruction algorithm. The basic features of this algorithm are presented in figure 5.8. The 1-dimensional induced charge density distribution on the

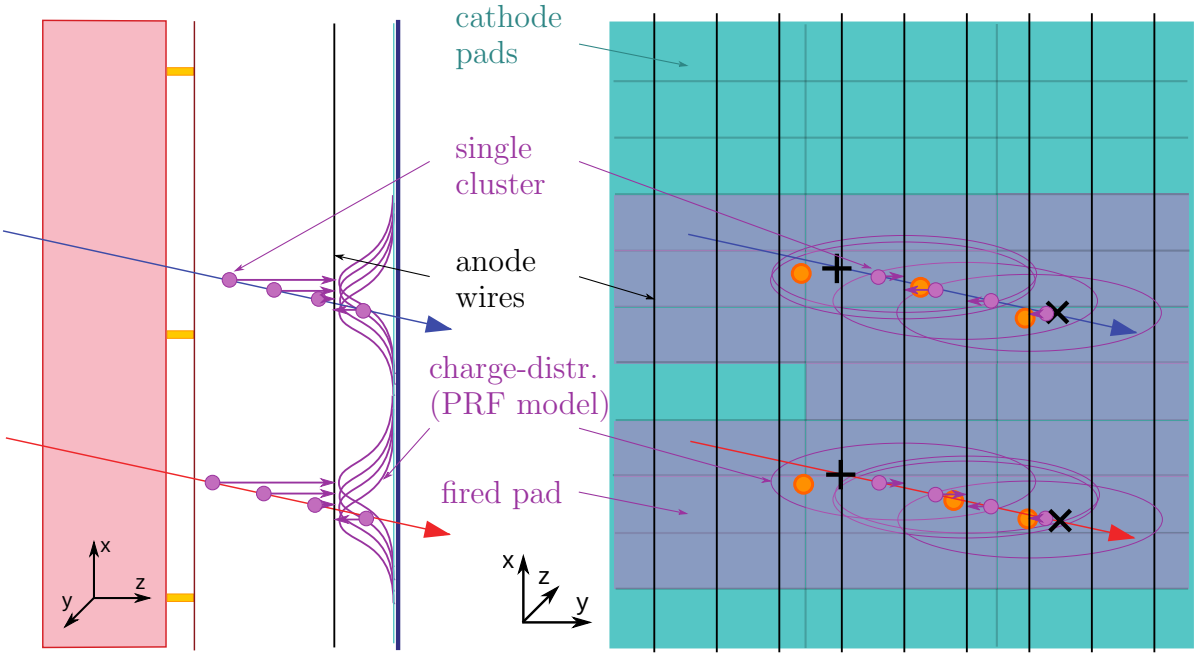

Fig. 5.8: Schematic view of the CBM TRD as implemented in CbmRoot reconstruction step using cluster hitproducer. This algorithm splits the total MC-energy-loss into several equal single clusters per unit track length inside the active detector volume. These single clusters are transported towards the closest anode wire position. The induced charge fraction as function of the displacement of the single cluster position with respect to the center of the underlying pad is calculated in x- and y-direction based on the PRF model (equation 4.36). The product of the x and y charge fraction per pad is multiplied with the single cluster charge to evaluate the induced charge on each pad. The signal of two or more single clusters of the same or different MC-tracks within the same event are summed up. The resulting signal distribution on the pad-plane is clustered into groups of three adjacent channels along the anode wire direction if the central channel has a signal above a certain threshold and corresponds to a local signal maximum of the collection. The two neighboring channels do not need to have a signal above the threshold in order to be clustered. The hit position of each cluster is reconstructed with a center of gravity algorithm. This leads to a higher number of reconstructed hits compared to the number of MC-tracks, since the algorithm reconstructs one hit per pad row seeing a signal above a certain threshold.

pad-plane in a MWPC is theoretically well understood and predicted by the so called Mathieson-formula (see chapter 4.3 and equation 4.35) as function of one global parameter K_3, pad width and the orientation of the wires. K_3 depends on different chamber parameters and can be evaluated from in beam prototype tests. The integral of the Mathieson-formula is called Pad Response Function (PRF). The PRF represents the percentage accumulated charge as function of the event displacement with respect to the center of the closest pad. The sum along a pad row (anode wire direction) converges to one. By just multiplying the induced charge percentage on each pad with the energy-loss provided by the *CbmTrdPoint* one gets a realistic charge sharing in one dimension. To have also a realistic charge sharing perpendicular to this row, one can multiply the induced charge percentage on each pad of this row with the induced charge percentage

given by the PRF using the pad height instead of the pad width. Since we have not measured the charge distribution on more than two adjacent pad rows, we could not fit a realistic K_3 value for this direction. Therefore we use the same value for both directions, knowing that there will be a deformation of the charge distribution in the long pad size direction. This procedure is done for each single cluster and each MC-track for all individual modules within the same event. The resulting signal distributions are summed up to create a realistic digi collection. This data collection is afterwards used by the clustering algorithm to create so called *CbmTrdCluster*. A *CbmTrdCluster* represents a digi accumulation in space and time. This can be done in different ways. The accumulation in time is guaranteed to be within the same event. Overlapping events within the detector's characteristic time resolution are not yet considered. The spatial clustering is done with a sorting algorithm making use of the unique channel address in combination with an artificial dummy column (perpendicular to anode wire direction) to separate channels from adjacent rows. The highest local signal channel above a software trigger level, within a continuous collection of adjacent digis in the same row, is used as cluster seed to create three pad cluster. The channel on the left and right side of the seed do not have to have a signal above the threshold. This represents the neighbor channel trigger read-out which is a feature of the SPADICv1.0. The limitation of the cluster size is done to reduce charge sharing between neighboring clusters. The used cluster definition allows for multiple clusters in a continuous collection of adjacent digis separated by local signal minima. The hit position of each three channel cluster is calculated with a center of gravity approach assuming a Gaussian charge distribution (equation 4.36) resulting in an average deviation of the reconstructed *CbmTrdHit* from the next *CbmTrdPoint* of 0.122 mm (depending on the TRD geometry) in the short pad size direction. It represents the charge sharing between adjacent clusters sitting on top of combinatorial background and systematic errors of the reconstruction algorithm. Since a cluster can only contain digis of the same row, artificial cluster splitting leads to a high number of ghost clusters and has to be compensated. This can be done (but is not yet implemented) in a more efficient way on the hit level based on the distance between the reconstructed hit positions in adjacent rows. The separation between ghost and real hits is done by the tracking algorithm based on the quality of fit. For the first time detector features like charge sharing between adjacent charge clusters and cluster merging are implemented. There is no longer an 1-to-1 correlation between the number of input *CbmTrdPoints* and the *CbmTrdHits*. The *CbmTrdPoint* with the shortest distance below a maximum distance threshold to the reconstructed hit are associated. Additional tracking information is not taken into account for this benchmark. An estimation on the efficiency of the point to hit combining approach as function of the opening angle $\alpha = \arctan(\sqrt{x^2+y^2}/z)$ or radial position relative to the beam-pipe ($r = \sqrt{x^2+y^2}$) based on $v12f$ geometry is presented in figure 5.9. Lost points are points without associated hits. Ghost hits are hits without corresponding MC points. The ghost hit fraction was significantly reduced to almost zero in geometry $v13p\_3e$ due to a parallel pad-plane granularity and clustering algorithm optimization while keeping the reconstruction efficiency at 90%. Most of the lost MC-points correspond to merged clusters of electron positron pairs from conversions outside of the magnetic field within the detector material of RICH or TRD. Such particle tracks would nevertheless not contribute to the physics analysis due to the missing measurement of the particle momentum. To get a more detailed view on the limitations of the cluster reconstruction chain the average hit efficiency, ghost rate and loss fraction are presented in appendix E for each module per layer. Since the cluster reconstruction chain is the most advanced and the most realistic detector response model it will be

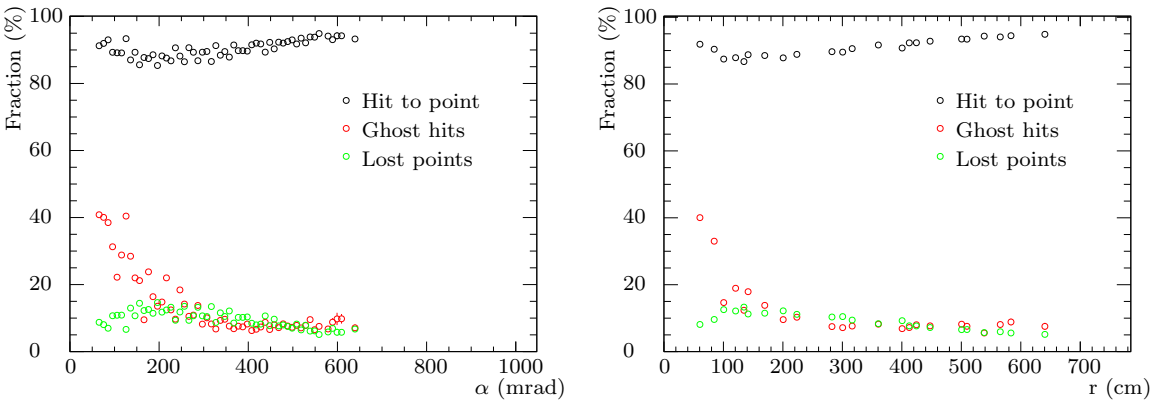

Fig. 5.9: Found hits, ghost and lost for 100 AuAu events at 25 AGeV based on $v12f$ geometry. Identification criteria for a point hit pair is a maximum distance radius of one pad diagonal and both are located on the same pad. Lost points are points without hits. Ghost hits are hits without associated points.

used for all following simulations, if a detector response is needed e.g. during detector occupancy studies.

5.6. CbmRoot Based Detector Optimization

The CbmRoot Framework was chosen to determine effects arising from pad-plane granularity and charged particle hit rate distribution. Pad-plane granularity limiting parameters are the maximum data read-out speed of the final SPADIC ASIC of 100.000 events per second and channel as well as a maximum tolerated average detector occupancy of 10%. Since the CbmRoot framework does not contain a detailed ASIC response implementation, these effects will be neglected in the following part, but covered by a separate simulation using the Garfield framework and an independent MC.

5.6.1. Charged Particle Hit Rate Distribution

The first step is the estimation of the expected most demanding running scenario (SIS300) conditions. The charged particle rate distribution is given by the beam intensity, target material and thickness as well as the magnetic field configuration. A large event number of simulated events is needed to estimate this distribution. A parametrization of an already existing simulation with a sufficient number of events has been chosen for the optimization of the TRD geometry to allow for more frequent iterations, since a full simulation is rather time consuming. The particle rate distribution was parametrized to results presented in the Technical Status Report January 2005, chapter 12 (Experimental conditions), page 285 ff. [Col05] (see figure 5.10) as function of z-position and emission angle. The hit densities refer to charged primary and secondary particles emitted in central Au+Au collisions at 25 AGeV, calculated based on the standard event generator, the Ultra-Relativistic Quantum Molecular Dynamics (UrQMD) [BBB+98]. The rates are calculated for 10 MHz minimum bias Au+Au collisions at 25 AGeV and the default magnetic field of 2005 [Col05]. Secondary particles are regarded at the station level but the increase in secondary particles within one station between two layers are not taken into account separately as well as increase of secondaries due to an increase of detector material in the simulation and can also not be included in the *CbmTrdHitRateQa* class. The hit rate per area was empirically parametrized in z-direction for different

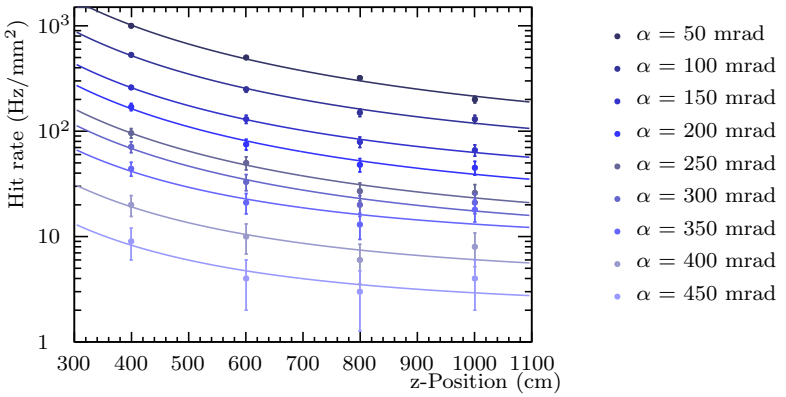

Fig. 5.10: The particle rate per emission angle (α) vs. z-position are fitted to equation 5.1

emission angle bins

$$f(z) = a(\alpha) + \frac{b(\alpha)}{z^2} \tag{5.1}$$

with:

$$\begin{aligned} a(\alpha) &= \exp(c + d \cdot \alpha) \\ b(\alpha) &= \exp(e + g \cdot \alpha) \end{aligned} \tag{5.2}$$

as shown in figure 5.10. The evaluated parameters a and b are afterwards fitted to exponential functions as presented in equation 5.1. The results are shown in figure 5.11. This approximation does not take into account asymmetries corresponding to different production rates of positive and negative charged particles, since it reflects only an overall average rate of charged particles as visible in figure 5.12. The presented parametriza-

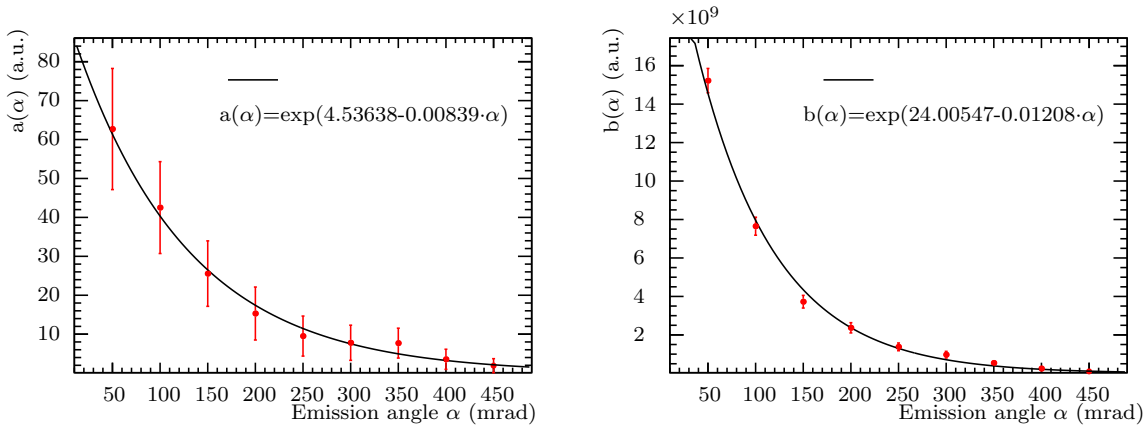

Fig. 5.11: The fit parameters a and b are fitted to an exponential function to evaluate a function describing the hit rate as function of r ($r = \sqrt{(x^2 + y^2)} = \tan(\alpha) \cdot z$) and z.

tion allows for fast hit rate approximations for different TRD geometries without time intensive MC-simulations. This tool is used during optimization of the pad-plane layout with respect to the maximum number of 100.000 signals per second, which can be processed by the SPADIC in the final version. The hit rate per channel distribution, which is estimated based on the presented approximation, is shown in figure 5.12. The average maximum hit per pad distribution is not reached anywhere in the TRD. The radially increasing pad length (perpendicular to the anode wire direction) is visible as well as

the three sectors of different pad length within each chamber. The sector borders are visualized by gray dashed lines. These zones of different pad areas are needed to subdivide the active area into an integer multiple of the anode wire spacing. The average pad area of each module can be found in figure 5.3.

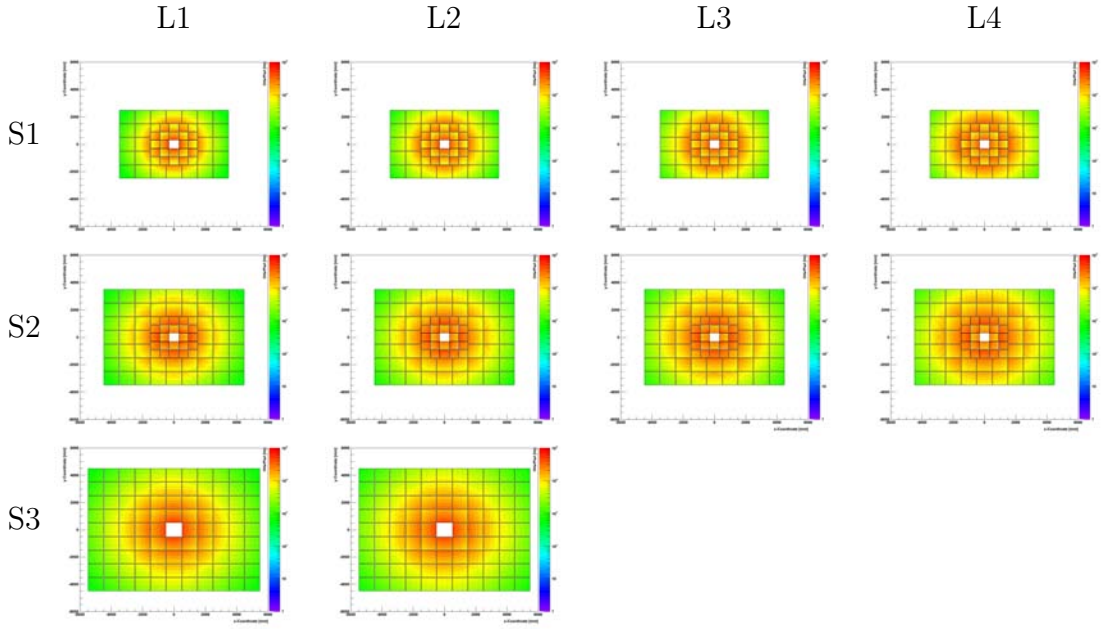

Fig. 5.12: Hit rate per pad (channel) distribution for geometry $v12f$ based on equation 5.1 and 5.2. The order is from left to right, layer (L) 1, 2, 3, 4 where the row corresponds to station (S) from 1 to 3. The histograms cover a range of ±6.0 m in x- and y-direction each. The z-axis (color scale) is fixed to the range between 1 and 10^5 Hz/pad. The pad-plane is subdivided into three sectors differing in pad height but with same pad width. The sector borders are marked by the dashed lines.

Based on this optimization of the hit rate distribution with respect to the maximum data read-out speed and the developed toolkits, the detector geometry can be further evolved. Detector parameters which are directly correlated to the maximum hit rate are the maximum anode wire length, pad-plane granularity, signal collection time and the signal read-out-parameters.

5.6.2. Occupancy and Pad-Plane Granularity

The detector has to cope with high counting rate environment without external trigger signal. To keep the data volume at the lower limit, it is useful to limit the average signal size at 2.5-3 channels per single event. The signal to noise ratio is also higher for smaller signal distributions. Using the information of more than two channels per event, a center of gravity algorithm can be used to determine the hit position with a position resolution better than the pad width. Different detector geometries have been considered during this optimization process. The theoretically predicted charge sharing given by the PRF as function of pad width and anode-wire plane to pad-plane distance is shown in figure 4.17. The cluster reconstruction chain (see chapter 5.5.2.4) was used to describe the detector response since it is based on the theoretical prediction of the PRF. A fixed ASIC trigger threshold of 1.0 keV/Channel and neighbor channel triggered read-out in anode wire direction are included in this simulation. Effects arising from the overlapping of different events (collisions) in time and due to the detector signal collection time can not be taken into account by an event based simulation using CbmRoot.

The implementation of time-based CbmRoot simulation flavor has been started but has not been finished up to now. The prototype pad-planes, as well as the CbmRoot geometries ($v12f$ is presented in figure 5.3) , have been designed in collaboration with Dr. David Emschermann [Ems13a], in order to find the optimum pad width for each detector concept: MS336, MS444 and MS3.5/3.5/5.0 to study effects arising from the aspect ratio of the pads like cross talk, charge sharing and several others. An average detector occupancy of below 10% is intended. The average occupancy was calculated using 100 central UrQMD Au+Au events for 25 AGeV (SIS300) and 10 AGeV (SIS100) as well as 500 minimum bias (MB) UrQMD Au+Au events for 25 AGeV (SIS300) and 10 AGeV (SIS100) based on geometry $v12f$. The occupancy distributions of a single TRD module of the inner region is shown in figure 5.13. The difference between central and MB events

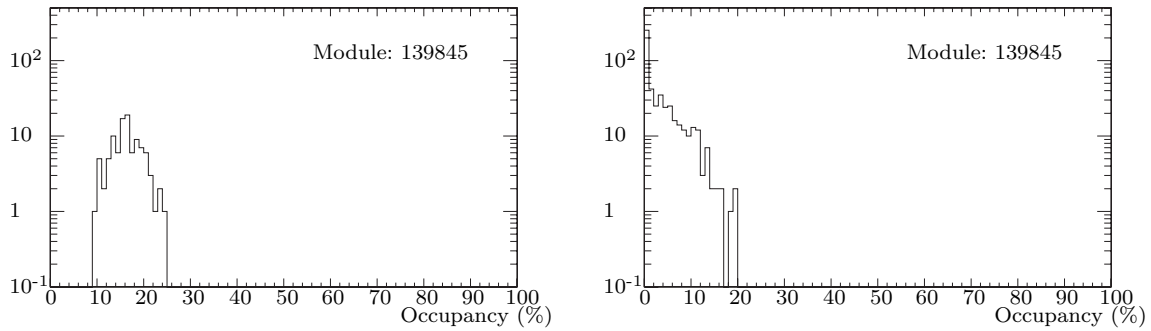

Fig. 5.13: Occupancy distribution of module 139845 geometry $v12f$ for 500 Au+Au central events (left) and 500 Au+Au minimum bias events at 25 AGeV (right).

is clearly visible. The occupancy distribution for single modules is more or less Gaussian distributed (see figure 5.13, left side). The occupancy distribution of MB events for single modules is exponentially decreasing towards higher values corresponding to the centrality distribution (see figure 5.13, right side). It can also be seen that approximately 10% of all MB events would result in an occupancy above the limit where at least all central events would lead to an occupancy above the maximum excepted occupancy of 10%. The mean occupancy for central events could be reduced for all modules below 10% at 25 AGeV by a systematic improvement of the pad-plane granularity resulting in the TRD geometries $v13p\_3e$ and $v13p\_1e$. The results for the complete TRD setup $v12f$ are presented in figure 5.14. The central events are used to determine the scenario with the highest occupancy which can occur whereas the MB events (distributions are not presented) represent a realistic run scenario. Here the asymmetry between the production rate of positive and negative charged particles due to δ-electron production within the magnet is clearly visible. The occupancy can be modified by scaling the pad height (perpendicular to the anode wire direction) in steps of integer multiples of the anode wire spacing. Scaling of the pad width has to be avoided if possible since the total number of channels per row should be a multiple of the channel per ASIC (depending on the read-out schema). Adding or removing of an ASIC is leading to modifications of the complete chamber geometry to keep the average cluster size within the optimal range with respect to the self triggered read-out electronic. This optimization is needed to produce a minimum amount of data and optimize the signal to noise ratio. Such a modification would require different FEB layouts, which would dramatically increase the overall production costs.

Since the occupancy study was done on the event base without δ-electron production within the target, but including δ-electron production within all other detector components,

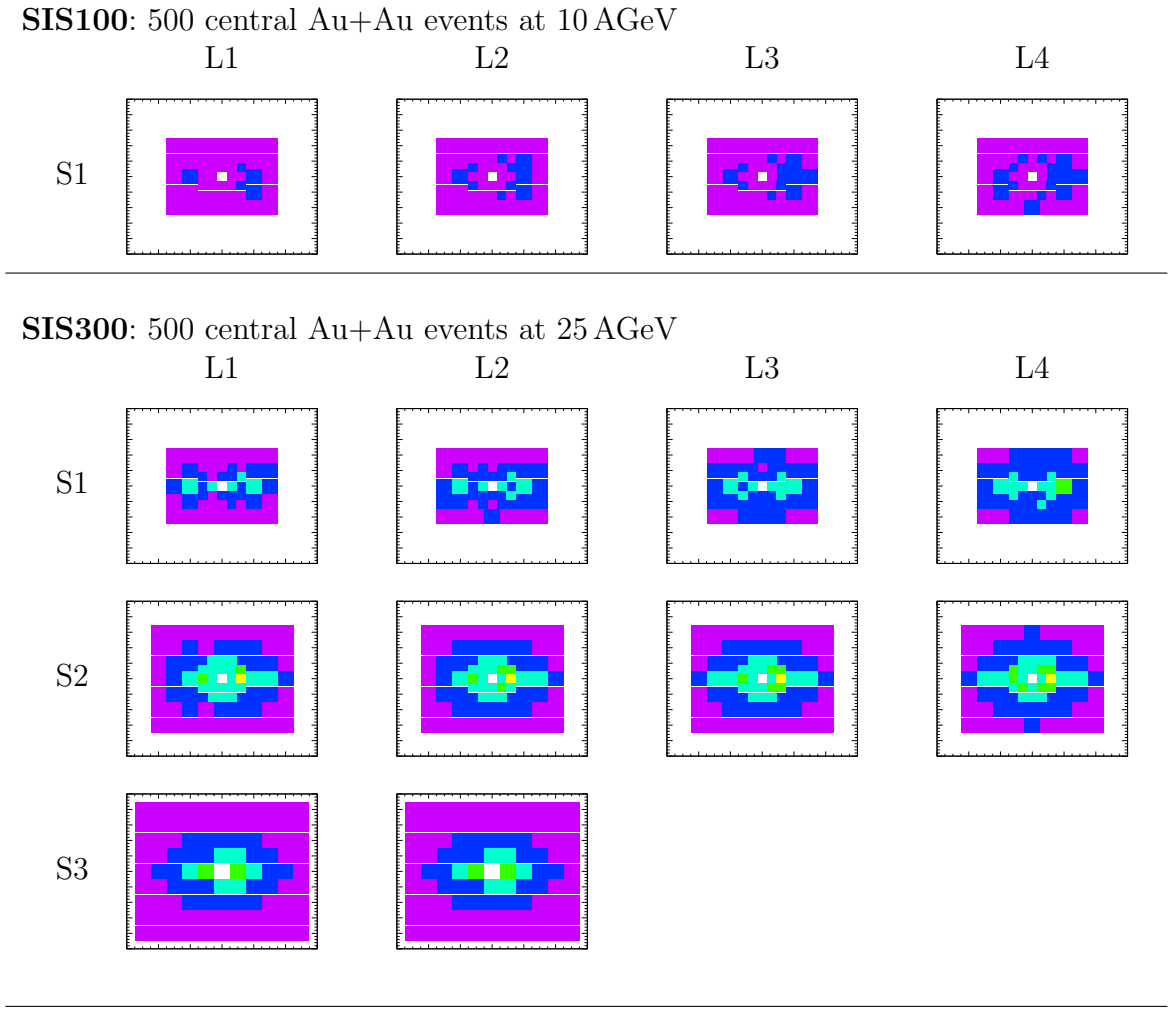

Fig. 5.14: Average occupancy for 500 Au+Au central events at 10 AGeV and average occupancy for 500 Au+Au central events at 25 AGeV. The order is from left to right, layer (L) 1, 2, 3, 4 where the row corresponds to station (S) from 1 to 3. The last station has only 2 layers in the geometry $v12f$, which gives 10 layers in total. The coordinate system covers a range of ± 6 m in x- and ± 5 m in y-direction. The color scale represents the mean occupancy and is: purple $< 5\%$, blue $< 10\%$, cyan $< 15\%$, green $< 20\%$, and yellow $< 25\%$.

the shown results are lower limits. The δ-electron production is strongly correlated to the material budget of the sub-detector systems in front of the TRD and also to the material budget of the TRD itself. The simulation is based on the $v12f$ geometry including a realistic foam radiator of 30 cm thickness, but without any mechanical support structure keeping the detector modules in position, slow controls, gas system, low and high voltage supply or any realistic read-out-electronic on the back-sides of the modules. Due to these reasons this simulation has to be redone after each geometry iteration. The pad granularity of the $v12f$ geometry would be sufficient for the SIS100 scenario, but is already at the limit for SIS300 in the inner region and pure central events. A final estimation on this topic can only be made based on a time-based simulation taking into account the interaction rate, beam structure and detector signal collection time. The time overlap of two or more events will significantly increase the average occupancy.

5.7. Garfield Based Detector Simulations

Garfield [Vee10] is a computer program for the detailed simulation of drift chambers in two- and three-dimensions. The program was developed for two-dimensional chambers composed of wires and planes, such as drift chambers, TPCs and MWPCs. For many of these two-dimensional configurations, exact fields are known. This is not the case for three-dimensional configurations, not even for rather simple arrangements. Furthermore, dielectric media and complex electrode shapes are difficult or even impossible to handle with analytic techniques. To handle such increasingly popular detectors, Garfield is interfaced with the nearly exact Boundary Element Method (neBEM) program provided by CERN. Garfield also accepts two- and three-dimensional field maps computed by commercial or open finite element programs such as Ansys, Maxwell, Tosca, QuickField and FEMLAB as basic simulation input. The electron transport properties in nearly arbitrary gas mixtures are covered by an interface to the Magboltz program.The ionization of gas molecules by particles traversing the chamber is integrated by an interface with the Heed program. Particle transport, including diffusion, avalanches and current induction is treated in three dimensions independent of the technique used to compute the fields. The advantage of the finite element technique is, that it can handle nearly arbitrary electrode shapes as well as dielectrics. The program can be used to calculate field maps, contour plots and 3-dimensional impressions, the wire sag that results from electrostatic and gravitational forces, visualization of electron and ion drift lines, drift time tables and arrival time distributions as well as signals induced by charged particles traversing a chamber, taking both electron pulse and ion tail into account [Vee10]. Since the CbmRoot framework does not contain a detailed ASIC response implementation, this part will be covered by simulations using the Garfield framework to produce input data for a separate MC tool. The SPADIC v0.3 has an sampling rate of 25 MHz collecting 45 samples with a total maximum signal length of 1.8 μs.

5.7.1. Signal Collection Time

The maximum tolerable signal collection time is limited by the maximum particle rate in the inner part of the detector of 100 kHz/cm^2 at an average interaction rate of 10 MHz and in second order by the time resolution and shaping order of the ASIC. Therefore the minimum distance in time between two signals measured on the same channel of the read-out electronic has to be estimated. The simulated signal collection time as function of different drift length and drift voltages for Xe/CO_2 and Ar/CO_2 based on Garfield is shown in figure 5.15. An Argon based MWPC is two times faster compared to the Xenon based model, but has to be several times thicker to reach the same TR-photon absorption probability (see chapter 5.8.2). Therefore, MWPCs operated with Xenon are the favored option for CBM TRD to keep the detector thin and relatively fast at the same time. The biggest effect of an increasing drift voltage is found between 10 and 100 V/mm where an exponential dependence is observed. A further increase is only leading to several percent higher signal collection times. A compromise between maximum tolerable signal collection time and minimum gas thickness with regard to a sufficient TR-photon absorption probability (see chapter 5.8.1 and 5.9) has to be found. The minimal signal collection time for a 12 mm thick MWPC is of the order of 200 ns. This will enhance the occupancy and therefore the probability of double hits. This was investigated based on a second, detailed Garfield simulation.

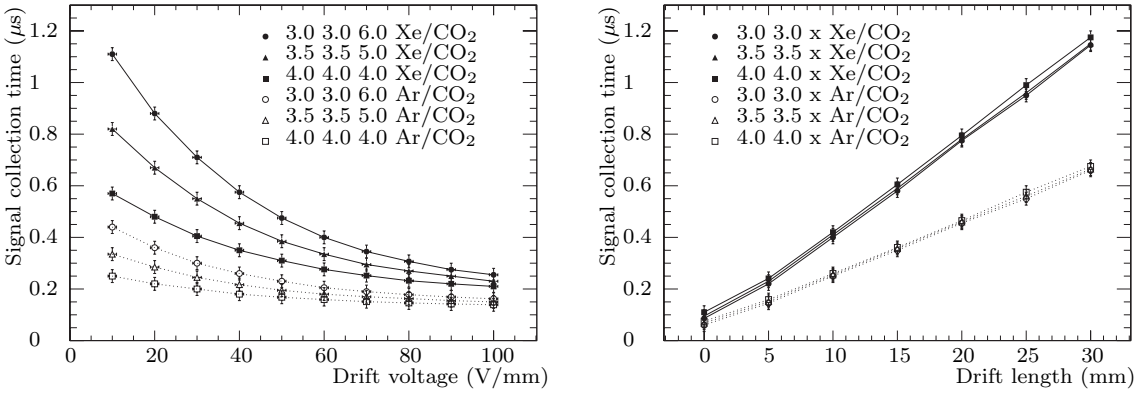

Fig. 5.15: Signal collection time for a simulated electron signal in Xe/CO_2 (80/20) represented by filled symbols and Ar/CO_2 (80/20) by open symbols. An anode voltage of 1675 V is applied for 3.0 3.0 x geometries, 1800 V for 3.5 3.5 x geometries, and 1925 V for 4.0 4.0 x geometries. The drift voltage scan is shown on the left side and the drift length scan at 100 V/mm on the right side.

5.7.2. Average Pulse Shape

The chamber response to 500 electron, pion and photon events was simulated using Garfield which gives the output current measured on an unsegmented planar cathode as a function of time. The TR-photon signal is obtained from Garfield simulated mono-energetic 8 keV photons. The mean number of photons per electron is given by the integral of the simulated TR-yield spectrum for radiator prototype (D) which was scaled to 45% to fit in beam test results from 2011. A Poisson distributed random number of photons per electron is assumed to be produced by the radiator. The energy of single photons is scaled to random energies following the shape of the simulated TR-spectrum. The photon signals are summed up to get the total photon signal per electron. This method will be described in more detail in section 6. The average signals for different drift region thicknesses at a constant amplification region geometry of 3.5+3.5 mm with an anode wire pitch of 2.5 mm and a staggered cathode wire plane with the same wire pitch are shown in figure 5.16. These average pulse shapes include exponential ion tails and are therefore longer than the presented electron signal collection times presented in figure 5.15. Neglecting cross talk due to the ion tail signal (which we hope to cancel using digital filters [Kri11]), space charge in a high counting rate environment and signal elongation due to the shaper response of the read-out electronic, two chamber signals are identifiable with a minimum time delay of the electron signal collection time of approximately 150 ns without drift region. This minimum time delay increases up to 250 to 300 ns with a drift length of 5 mm as chosen for the 2012 prototypes. Since there is a signal elongation due to the shaper response, this has also to be taken into account to consider the minimum time delay of two separate signals. The average time response of the read-out electronic is calculated by convolving the individual Garfield pulses to a simplified SPADIC response function $h(t)$ of the shaper [Kri11]

$$h(t) = (t/T)^2 \exp(-t/T) \tag{5.3}$$

with a shaping time of $T = 90$ ns. The transfer function $y(t)$ is given with

$$y(t) = \int_{\lambda=-\infty}^{\infty} x(t-\lambda) \cdot h(\lambda) d\lambda. \tag{5.4}$$

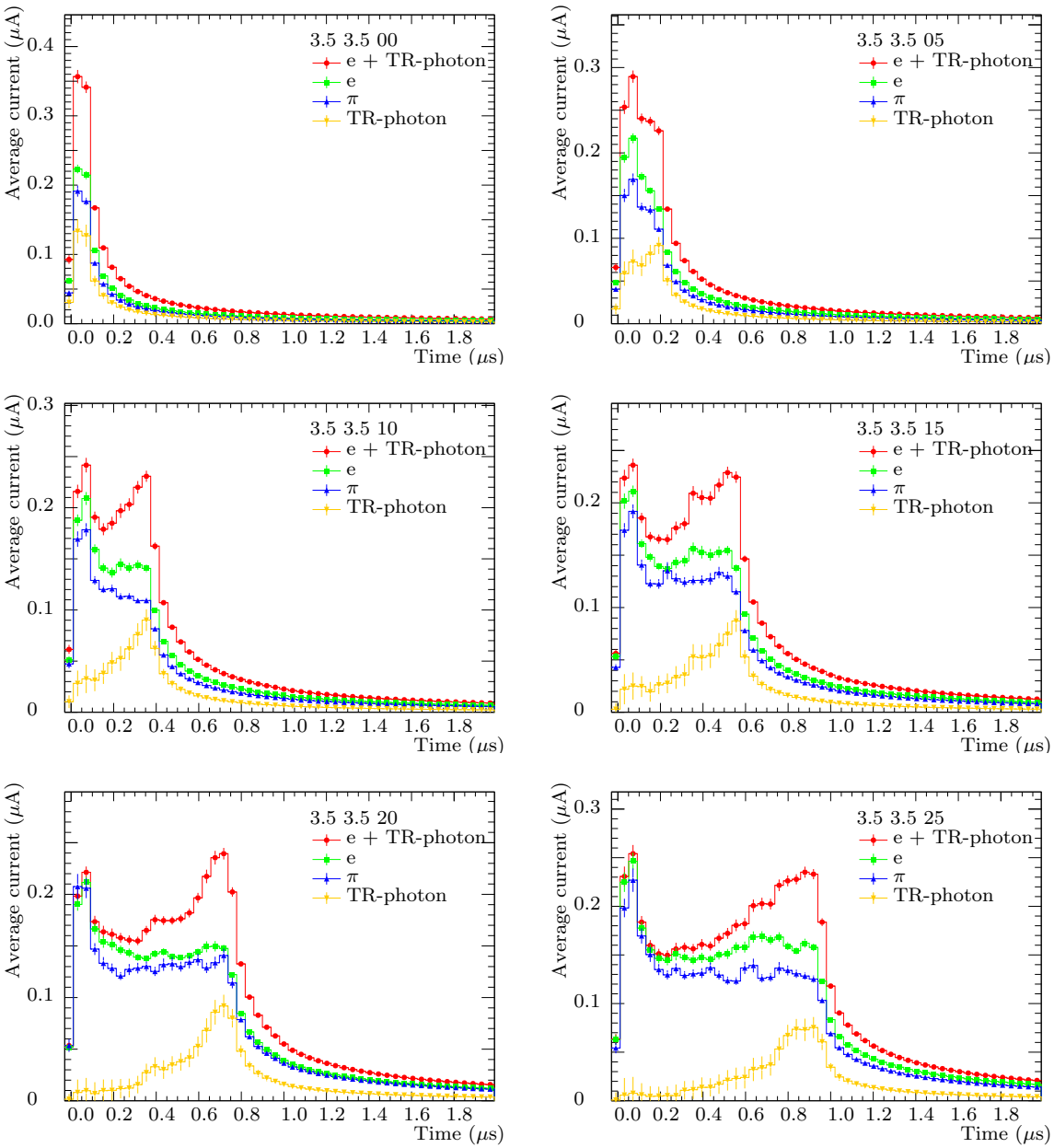

Fig. 5.16: Garfield average pulse shape for 500 events with an amplification region of 3.5 + 3.5 mm with a drift region between 0 and 25 mm with an applied drift voltage of 100 V/mm using Xe/CO_2 (80/20). Pure Garfield output for electrons and pions at 3 GeV/c. The TR signal is obtained from simulated 8 keV photons integral normalized to simulated TR-spectra. The mean number of photons per electron is given by the integral of the simulated TR-yield spectrum for a Polypropylene based foil radiator with $N_f = 100$, $l_1 = 15\,\mu$m, $l_2 = 700\,\mu$m, 45% photon scaling ($a = 0.45$), chamber absorption probability distribution included to fit in beam test results from 2011. The number of produced photons per electron is assumed to be Poisson distributed.

The integral becomes a sum for time discrete input signals

$$y(t) = \sum_{i=-\infty}^{\infty} T_0 \cdot x(iT_0) \cdot h(t - iT_0) \tag{5.5}$$

with T_0 being the width of one time slice. The resulting average pulse shapes can be seen in figure 5.17. The pulse shape length extends with increasing drift length. The average

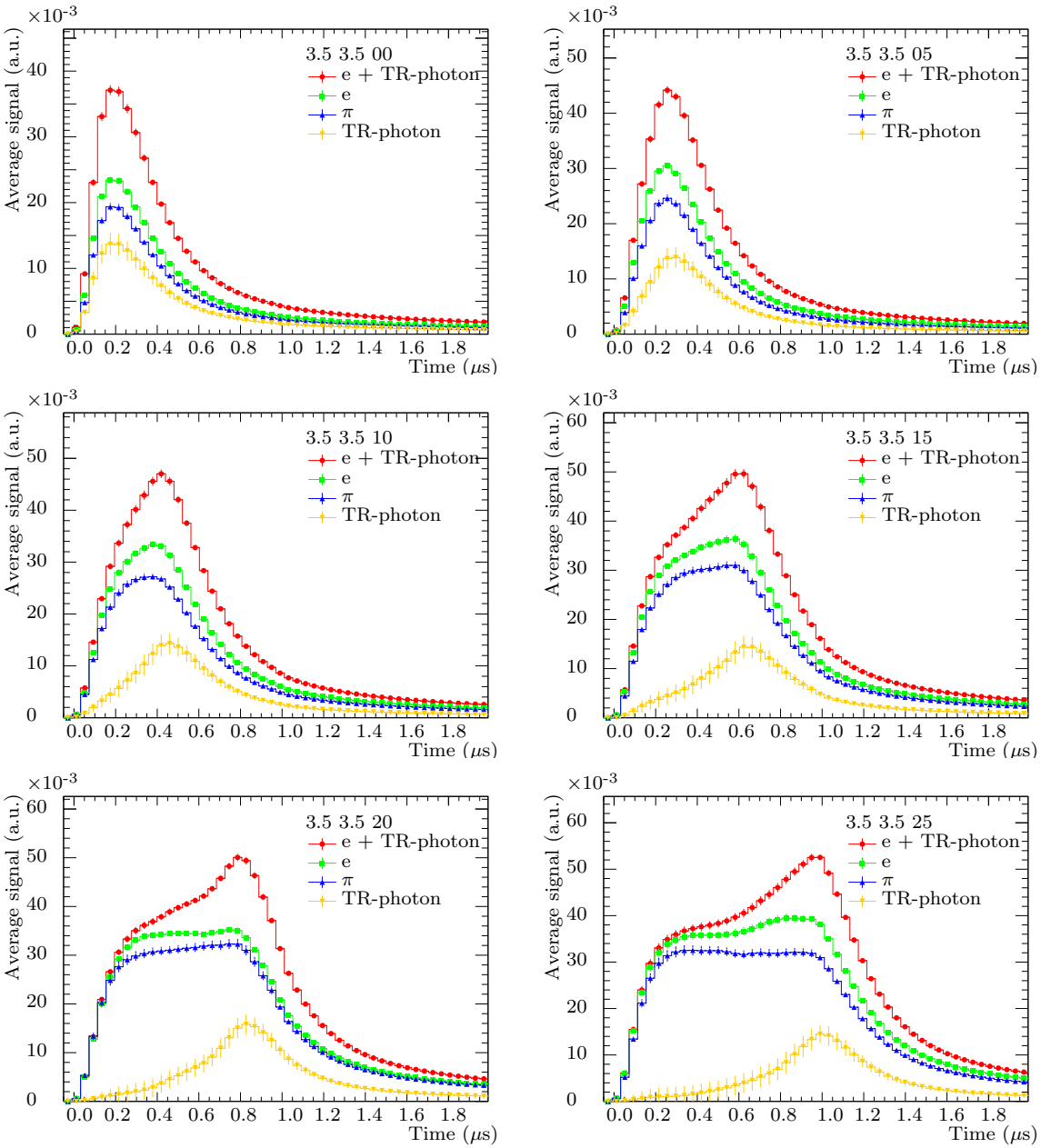

Fig. 5.17: SPADIC average pulse shape (transfer function presented in equation 5.3) for 500 events and chamber geometries with 3.5 3.5 (00-25), 100 V/mm drift voltage, Xe/CO_2 (80/20), and 3 Gev/c.

electron including TR-photons and pion pulses can be separated by the shape beginning at a drift length of 10 mm. A particle separation based on the average pulse shape is not feasible below a total Xe/CO_2 (80/20) gas thickness of 17 mm, since the TR-photons are homogeneously absorbed in the gas volume. Since the maximum tolerable signal collection time, as discussed in the previous section, is reached for a 12 mm thick Xenon based MWPC, a particle identification based on the average signal shape will not be technically enforceable for the CBM TRD.

5.8. Photon Transition Probability and Radiation Length

The amount of material traversed by a particle is also dependent on the angle and the origin of the particle. The radiation length calculated in this section is however only

given for a particle which traverses the detector perpendicular to its plane (z-direction in the CBM coordinate system) [Adl06]. The radiation length was calculated with the formula from Tsai [TYS74] as described in [E$^+$04] for elements heavier than Beryllium:

$$\frac{1}{X_0} = 4\alpha {r_e}^2 \frac{N_A}{A} \left\{ Z^2 \left[L_{rad} - f(Z) \right] + Z L'_{rad} \right\}. \tag{5.6}$$

For A=1 g/mol, $(4\alpha {r_e}^2 N_A)/A$=$(716.408\,\mathrm{g/cm^2})^{-1}$ L_{rad} and L'_{rad} are given by

$$L_{rad} = \ln\left(184.15 \cdot Z^{-1/3}\right) \tag{5.7}$$

and

$$L'_{rad} = \ln\left(1194 \cdot Z^{-2/3}\right). \tag{5.8}$$

The function $f(Z)$ is an infinite sum, but for elements up to uranium it can be represented by

$$f(Z) = a^2 \left[\left(1 + a^2\right)^{-1} + 0.20206 - 0.0369a^2 + 0.0083a^4 - 0.002a^6 \right] \tag{5.9}$$

with

$$a = \alpha Z. \tag{5.10}$$

Since most parts of the TRD are made of composite materials the radiation length of those has to be approximated. This is done according to

$$\frac{1}{X_0} = \sum_i \frac{\omega_i}{X_i}, \tag{5.11}$$

where ω_i and X_i are the fraction by weight and the radiation length for the ith element [E$^+$04]. The radiation length for elements and components used in the CBM-TRD prototypes calculated based on equation 5.11 are listed in table 5.1 and 6.1.

Tab. 5.1: Material components and Elements [Adl06], densities and radiation length X_0 of the CBM TRD prototypes calculated with the formula of Tsai at STP (101.325 kPa and 273.15 K).

Element/Material	Chemical formula		ρ (g/cm^3)	X_0 (g/cm^2)	X_0 (mm)
Hydrogen	H		8.9E-05	67.6	7.5E06
Carbon	C		2.3	42.7	188.9
Nitrogen	N		0.0013	38.0	0.3E06
Oxygen	O		0.0014	34.2	0.2E06
Aluminum	Al		2.7	24.0	88.9
Silicon	Si		2.3	21.8	93.7
Copper	Cu		8.9	12.9	14.4
Argon	Ar		0.0018	19.5	110.0E03
Xenon	Xe		0.0059	8.5	14.4E03
Mylar	$(C_{10}H_8O_4)_n$		1.0	40.1	400.1
Epoxy	$C_2H_4N_1$		1.2	42.5	354.6
Carbon fibers	$C + C_2H_4N_1$	(60.0/40.0)	1.8	42.7	237.2
Rohacell HF71	$(C_5H_8O_2)_n$		0.075	40.8	5437.6
Kapton	$(C_{22}H_{10}N_2O_5)_n$		1.43	40.7	284.3
Honeycomb	$(C_{14}H_{10}N_2O_2)_n$		0.032	41.4	12941.7
Air	$N_2 + O_2$	(76.6/23.3)	0.0012	37.1	309166.7

Element/Material	Chemical formula		ρ (g/cm^3)	X_0 (g/cm^2)	X_0 (mm)
FR4/G11	SiO_2+$C_2H_4N_1$	(61.0/39.0)	2.0	31.9	159.2
Polyethylene foil	$(C_2H_4)_n$		0.900	45.2	502.6
Polyethylene foam	Air+$(C_2H_4)_n$	(97.9/2.1)	0.020	45.2	22615.8
Polyethylene foam	Air+$(C_2H_4)_n$	(90.0/10.0)	0.091	45.2	4970.5
Polypropylene foil	$(C_3H_6)_n$		0.900	45.2	502.6
Polypropylene fiber	Air+$(C_3H_6)_n$	(93.0/7.0)	0.064	45.2	7067.4
Polypropylene fiber	Air+$(C_3H_6)_n$	(91.9/8.1)	0.074	45.2	6112.4
POKALON N470	$(C_{16}H_{14}O_3)_n$		1.150	41.7	362.3

The total radiation length of the TRD has to be minimized in order to keep the scattering probability as low as possible. The radiation length and photon cross-section of the entrance window are of special interest. The PID performance of the detector is directly correlated to the additional energy deposit by TR-photons absorbed in the active gas volume. The approximated radiation length for different TRD prototype components and the photon transmission probability as function of the photon energy are presented in the following sections.

5.8.1. Front-Panel and Gas Window

Three different front-panel (gas window) flavors were built between 2010 and 2012. The first design in 2010 was based on the ALICE TRD geometry optimized for mechanical stability and characterization of different radiator prototypes on the same chamber. Therefore the ALICE fiber radiator material was removed and the two Rohacell HF71 sheets of 8 mm thickness each were glued together. Two aluminized (3 μm aluminum on one side per foil) Mylar foils (12 μm each) on top of two carbon fiber sheets (0.2 mm each) on the bottom and top of the Rohacell sandwich are used as drift electrode to ensure gas leak tightness and avoid at the same time mechanical deformation due to hygroscopic properties of the Rohacell. Due to the high photon absorption probability in the favored TR energy region, the entrance window material budget was reduced to a minimum. Therefore the central area of the sandwich structure was milled down to the last millimeter of Rohacell in front of the inner carbon fiber sheet in 2011 . A minimal amount of material between radiator and active gas volume was reached in 2012 by exchanging the Rohacell, carbon fiber sheet and Mylar foil by a single Kapton foil, stabilized by a G11 support grid. The resulting radiation lengths are presented in table 5.2.

Tab. 5.2: Front panel component radiation length from 2010 to 2012 prototypes

Material	Thickness (μm)	X/X_0 (%)
2010		
Aluminium	2×3	0.007
Mylar	2×12	0.006
Epoxy	5×100	0.141
Carbon fiber sheet	2×200	0.168
Rohacell HF71	2×8000	0.295
Sum		**0.617**

Material	Thickness (μm)		X/X_0 (%)
2011			
Aluminium	3		0.003
Mylar	12		0.003
Epoxy	100		0.028
Carbon fiber sheet	200		0.084
Rohacell HF71	1000		0.018
Sum			**0.136**
2012			
Aluminium	3		0.003
Kapton	25		0.009
G11	10000		(6.280)
Sum			**0.012**
		Support grid	+6.280

5.8.2. Gas Volume

The second important component affecting the PID performance is the length of the active gas volume and the used gas mixture. The two noble gas mixtures which come into consideration are Xenon and Argon based as discussed in chapter 4.1.3. The transmission probability of these mixtures (85% noble gas and 15% CO_2) at different thickness are presented in figure 5.18. The most probable counting gas mixture which will be used

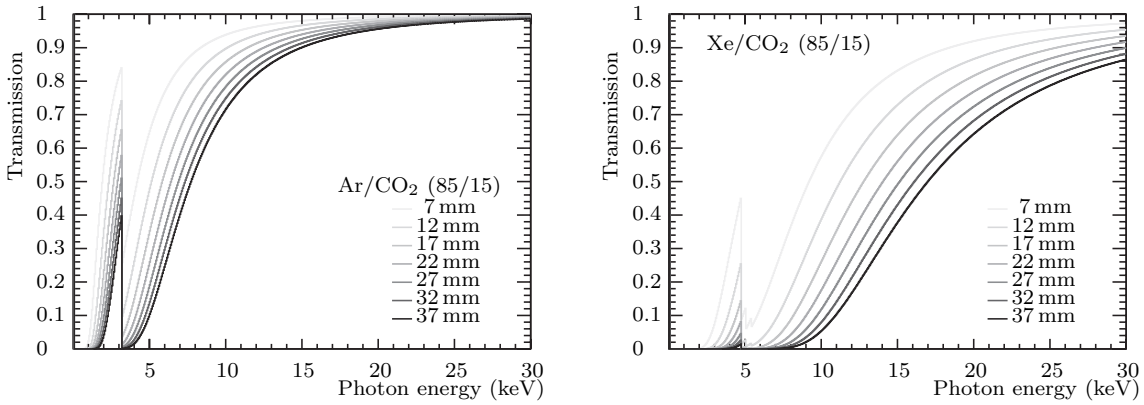

Fig. 5.18: Transmission probability for Argon (left) and Xenon (right) based mixtures (85% noble gas and 15% CO_2) of different gas thicknesses: 7, 12, 17, 22, 27, 32, 37 mm.

in the CBM TRD is Xe/CO_2 (85/15) due to the higher TR-photon absorption cross section, where a (80/20) mixture is used for the test beams to reduce the costs. A total gas mixture thickness of 12 mm under operating conditions contributes a radiation length of $X/X_0 = 0.065\%$.

5.8.3. Back-Panel and Pad-Plane

The same back-panel components including the pad-plane have been used for all prototypes between 2010 and 2012 where the size has been scaled from $26\times26\,\mathrm{cm}^2$ to $59\times59\,\mathrm{cm}^2$. This scaling of the surface does not effect the radiation length since the material budget is estimated for trajectories perpendicular to the front-panel. The radiation length for each subcomponent as well as the total radiation length are listed in table 5.3. The hig-

Tab. 5.3: Back-panel and pad-lane component radiation length.

Material	Thickness (μm)	X/X_0 (%)
Honeycomb	22000	0.170
Air	22000	0.007
Epoxy	100	0.028
Carbon fiber sheet	2×300	0.253
FR4	360	0.226
Cu	25	0.174
Sum		**0.858**

hest contribution to the total material budget (sum of gas window, gas and back-panel) of 1.540-0.093% X/X_0 of all prototypes, neglecting the support grid (10 mm thick G11: $X/X_0 = 6.280\%$) and chamber frame (22 mm thick G11: $X/X_0 = 13.817\%$), is due to the back-panel.

5.9. Photon Absorption Probability

Predictions on the photon absorption probability in the gas volume can be made based on the previous simulation results. The transmission probability of the passive components between the radiator and the active gas volume of 12 mm thickness is multiplied with the absorption probability of the gas volume. Different entrance window options have been simulated and are presented in figure 5.19. The highest integrated photon absorption

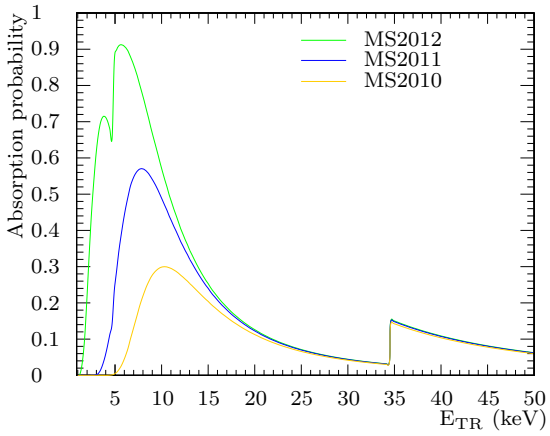

Fig. 5.19: Effective photon detection spectrum including transmission of the front panel components are shown. Approximation was done using values taken from [HGD93] for $Xe/CO_2(85/15)$.
MS2010: Absorption maximum at 10.33 keV, intg. probability [0,50]: (10.6%),
MS2011: Absorption maximum at 7.88 keV, intg. probability [0,50]: (15.7%),
MS2012: Absorption maximum at 5.66 keV, intg. probability [0,50]: (22.7%).

probability can be realized with a single foil Kapton entrance window. Homogeneously distributed support materials like 16 mm Rohacell (2010 prototypes) increase the total photon absorption probability by more than a factor two compared to the gas window built in MS2012 open (2012 prototypes 3.5 3.5 5.0). Depending on the emitted TR-spectrum this leads to an increase in PID performance. The difference in PID performance due to homogeneous support structures in comparison to inhomogeneous support structures like the 2012 G11 support grid on the full surface have to be investigated in a detailed simulation including the full CBM setup.

5.10. Prototype Components, Assembly and Characterization

5.10.1. Prototypes 2011

There are two different chamber geometries called MS336 and MS444. The numbers denote the wire grid distances (see figure 5.20); e.g. 3 mm between pad-plane and anode wire grid followed by 3 mm from the anode wires to the cathode wire plane and 6 mm drift region thickness in case of the MS336 prototypes. The outer dimensions are

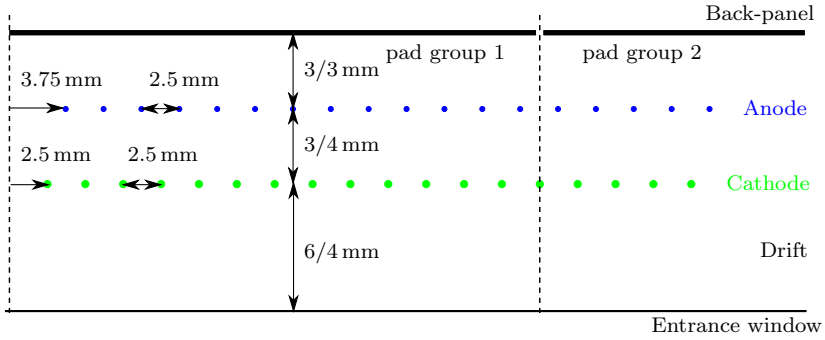

Fig. 5.20: A schematic drawing of the anode and cathode wire grid position relative to the pad-plane based on is shown [Ems13c]

$26 \times 26\,\mathrm{cm}^2$ with a common pad-plane. The pad-plane consists of one half with 5 mm pad width, where the pads on the other half are 8 mm wide to get an optimal charge charing (10/80/10). The chamber design is derived from the ALICE TRD modules [ALI01] as well as the assembly procedure [Adl05]. Four Wacosit profile parts are cleaned and glued together with Araldite AW 106 and screwed together. In parallel two 8 mm thick Rohacell/carbon-fiber/Mylar plates are glued together with the Rohacell sides in the middle to build the front-panel (see figure 5.21). After hardening of the glue a thin band of AW 106 is applied to the ledge of the frame profiles. If glue is polymerized to an

Fig. 5.21: The front-panel built from two Rohacell/carbon-fiber/Mylar plates (8 mm thickness) is glued together (left) and afterwards applied to the chamber body made from four Wacosit profile parts (right).

extent where it will not flow away anymore the gap between the body-frame and the front-panel is filled with AW 116. After glue hardening the drift cable feedtrough is drilled into the chamber body and the Mylar foil is removed in an area of about $1\,\mathrm{cm}^2$ from the carbon-fiber as shown in figure 5.22. A copper strip is cut to fit the contact area on the carbon-fiber plate. The copper strip is glued to the exposed carbon-fiber area using conductive silver epoxy. The drift cable is pushed through the hole, glued to the body, soldered to the copper strip and the outer edge of the copper strip is covered with a thin

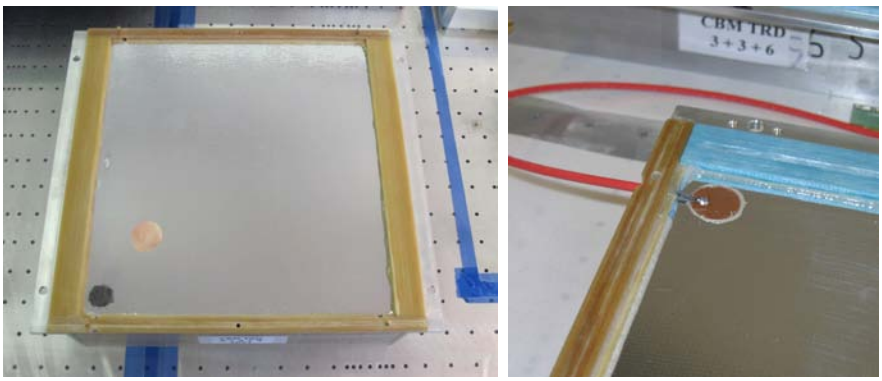

Fig. 5.22: Preparation and connection of the drift electrode.

line of AW 106 to avoid sparks between the sharp copper strip edge and the cathode wires. The back-panel is built from an aluminum frame and a honey-comb carbon-fiber sandwich like in the ALICE TRD. The 23 mm thick honeycomb carbon-fiber-sandwich is glued to this frame using Araldite AW 106 and the gap is filled by AW 116. Overlaying glue is milled in the next step to get a perfect down surface to which the pad-plane is glued. The next step is the preparation of the pad-plane. The read-out cable connectors are soldered to the back side and filled with short-cut copper strips to keep the connectors free of glue. The front side is cleaned with isopropanol and covered with adhesion foil. The pad-plane is put with the connectors upside to the vacuum table and fixed in position using two dowel pins. The gas tightness is ensured using traceless adhesion tape (blue) between the pad-plane and the vacuum-table (see figure 5.23). A thin ho-

Fig. 5.23: Gluing of the back-panel to the pad-plane.

mogeneous layer of AW 116 (350-400 g/m^2 Araldite AW 116 [Adl05]) is distributed to the pad-plane leaving the area around the connectors out. The back-panel is put upside down (honeycomb side facing up) and the outermost row of honeycomb is covered with glue to ensure maximum mechanical connection between pad-plane and back-panel. The panel is turned around and lowered until it sits on the pad-plane. Aluminum bricks are put all along the edge of the panel to ensure a perfect interconnection. After hardening of the glue and drilling of the missing reamed holes, the pad side is cleaned with isopropanol after removal of the adhesion foil. Coming back to the chamber-body the cathode wire application is prepared. The chamber-body is prepared with a 2.5 mm wide copper adhesive tape glued to the 0.2 mm deep groove on the top side as shown in figure 5.24. The cathode wires (75 μm Cu-Be wire) are winded to an ALICE wire transfer frame with a pitch of 2.5 mm and a tension of 100 cN. Technicoll is used to fix wires in position on the frame before dividing the frame in two halfs. The wire grid is positioned and lowered to the chamber-body until the wires rest on top of the ledges. A thin film of AW 106 is applied, a wire ledge of 4 mm (3 mm) is put on top to keep the wires in position.

Fig. 5.24: Application of the cathode wire plane.

The ledges are connected to the chamber-body using copper aligning pins to adjust a precise distance of 6 mm respectively 4 mm distance between the cathode electrode and the drift wires. The wires are soldered to the copper strip, which is connected by the cathode cable through a hole in the chamber-body. The cathode wires are cut off the transfer-frame afterwards. The anode wires (20 μm Au-plated W wire) are winded to a transfer frame with a pitch of 2.5 mm and a tension of 50-55 cN. A schematic drawing of the anode and cathode wire grid position relative to the pad-plane is presented in figure 5.20. The anodes are positioned staggered to the cathode wires on the wire ledges. After positioning the wires are fixed using another thin film of AW 106. The wires are soldered to the copper strip which is subdivided into eight sectors. The wires are cut off the transfer frame. The anode cables are feed through the anode cable ledge which is glued to the frame close the the anode wire distance ledge with the copper strip. The anode cables are soldered to the copper strip to apply electrical connection as depicted in figure 5.25 right. The outer frame is completed by two frame ledges with two gas holes each. The

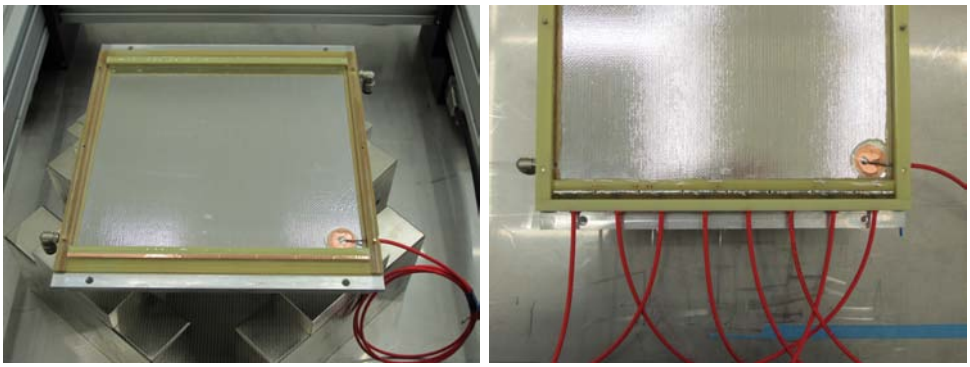

Fig. 5.25: Mounting of the anode wire plane (left) and soldering of the anode connectors (right).

ledges are glued to the frame with AW 106 and positioned using four short and two long copper dowel pins. The gas ports are screwed to the frame applying a thin film of glue on the winding. The long pins are used in the following step to position the back-panel on the chamber body. The two parts are glued together using a thin film of AW 106. The weight of four aluminum blocks is used to get a good mechanical interconnection and gas tightness.The fully mounted chamber including HV-filter-board on the back side of the copper base plate and two SPADIC/SUSIBO read-out units is presented in figure 5.26. The front-panel (entrance window) has been milled down to 1 mm thickness in order to enhance the TR efficiency. The effect on the photon transmission probability presented in figure 5.27 was tested by a rate measurement as function of the Rohacell HF71 front

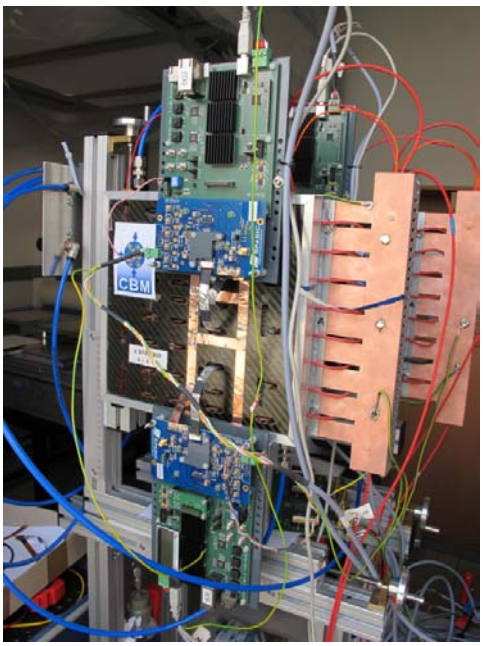

Fig. 5.26: Mounted MWPCs on the beam test setup in the lab.

panel thickness using an ^{55}Fe source (10 MBq) at a distance of 5 cm collimated to a diameter of 1 mm. The first in lab test has been performed with a collimated ^{55}Fe source

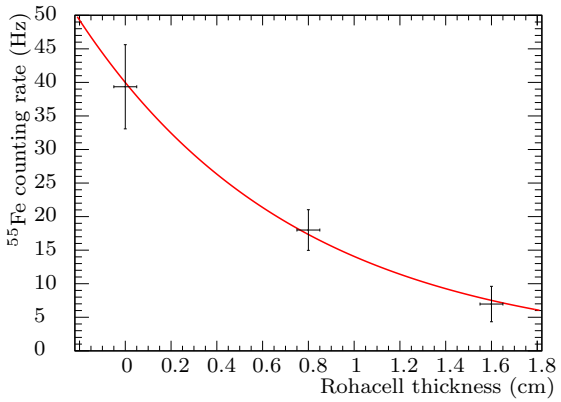

Fig. 5.27: Rate measured as function of the Rohacell HF71 front panel thickness with MS336 with reduced front panel (1 mm Rohacell HF71 and 1 aluminized Mylar carbon fiber layer) using a ^{55}Fe source (10 MBq) at a distance of 5 cm, collimated to a diameter of 1 mm.

and Ar/CO_2 (82/18) gas mixture to find the optimal gas gain for the fixed ASIC gain. The spectrum of the iron source is ideal to test MWPC prototypes, specially TRDs. The emitted photon spectrum has a peak at 5.9 keV. This value matches the mean photon energy of most radiators. The spectrum can be calibrated due to the K_α and K_β escape peak at 2.94 keV and 2.71 keV. The usual MWPC energy resolution of around 10% σ/μ is not sufficient to separate these two peaks, leading to a broad single escape peak at an intermediate energy.The energy resolution is presented as ratio of the two Gaussian fit parameters σ/μ estimated for the 5.9 keV peak. The results are presented in figure 5.28. It was found that the optimal anode voltage for the MS336 prototype working with an argon based gas mixture is between 1650 and 1700 V, resulting in an energy resolution of 10-11%, where the MS444 prototypes are showing best results between 1900 and 1950 V at an energy resolution of 11-12%. The further enhancement in the energy resolution

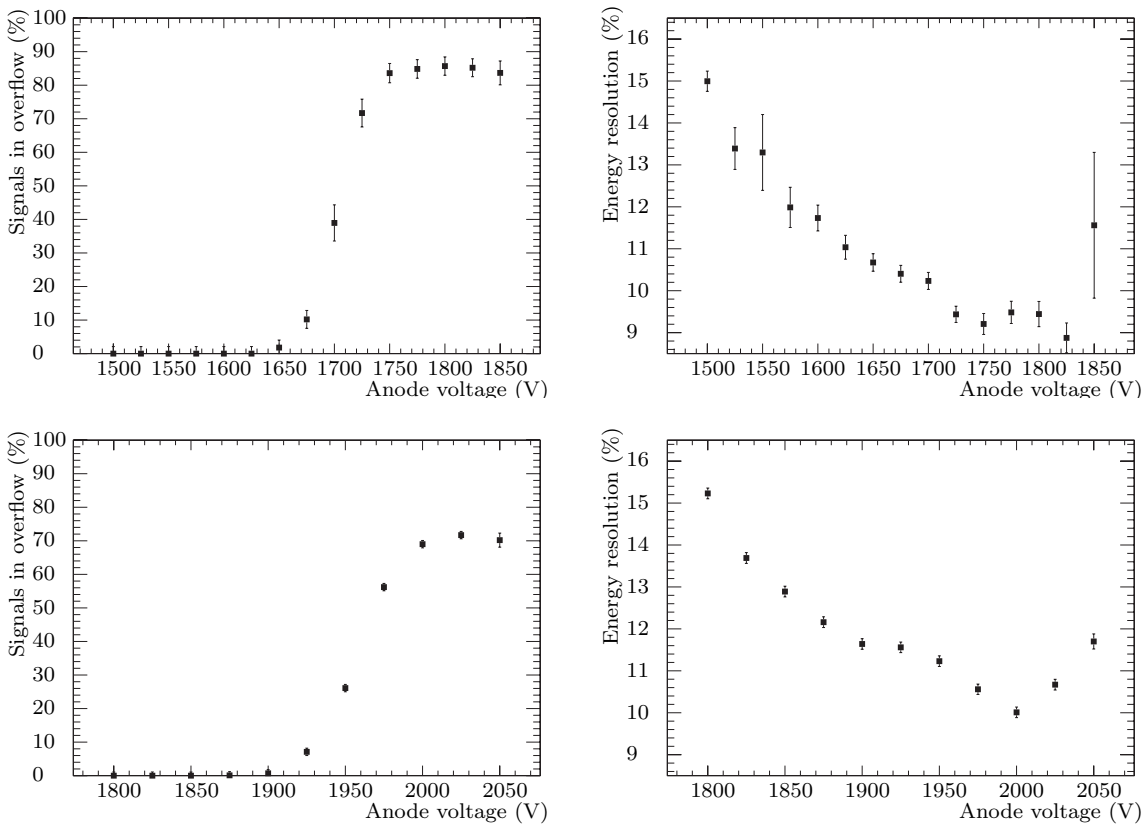

Fig. 5.28: 2011 MS336 (**upper row**) and MS444 (**lower row**) operated with Ar/CO_2 (82/18) and a collimated ^{55}Fe source (10 MBq). The signal in overflow fraction as function of anode voltage is presented on the left and the energy resolution as function of anode voltage on the right. The presented errors include uncertainties arising from the energy calibration of the individual spectra, Gaussian fitting procedure, and fluctuation between different measurements (in case of MS336).

is a result of the increasing fraction of fragmented signals leading to a compression of energy loss spectrum at highest values. The full energy peak width decreases leading to an unphysical energy resolution.

5.10.2. Prototypes 2012

In order to get a detector with a minimum amount of material budget, but highest mechanical stability one has to define. Such a deformation causes field line deformations especially in the drift region and a shift of the zero potential line which has been simulated with Garfield (see figure 5.29). The amplification field is slightly reduced on the drift side and becomes inhomogeneous on the percentage level. Therefore a deformation of up to 1 mm seems to be tolerable. It has to be kept in mind that there are pressure differences which can not be compensated by an external gas system like hydrostatic pressure of the counting gas. For pure Xe the density is $0.0058982\,g/cm^3$, where air has a density of $0.001225\,g/cm^3$. The density difference between the chamber volume and the surrounding air is $0.0046732\,g/cm^3$. The overpressure at the bottom of a 2012 prototype of 59 cm height is 0.27 mbar (0.46 mbar/m). These pressure differences come always in addition to instabilities within the gas control system which are assumed to be controllable in the range of below 1 mbar.
The gas window was optimized to get a minimum of absorption between the radiator

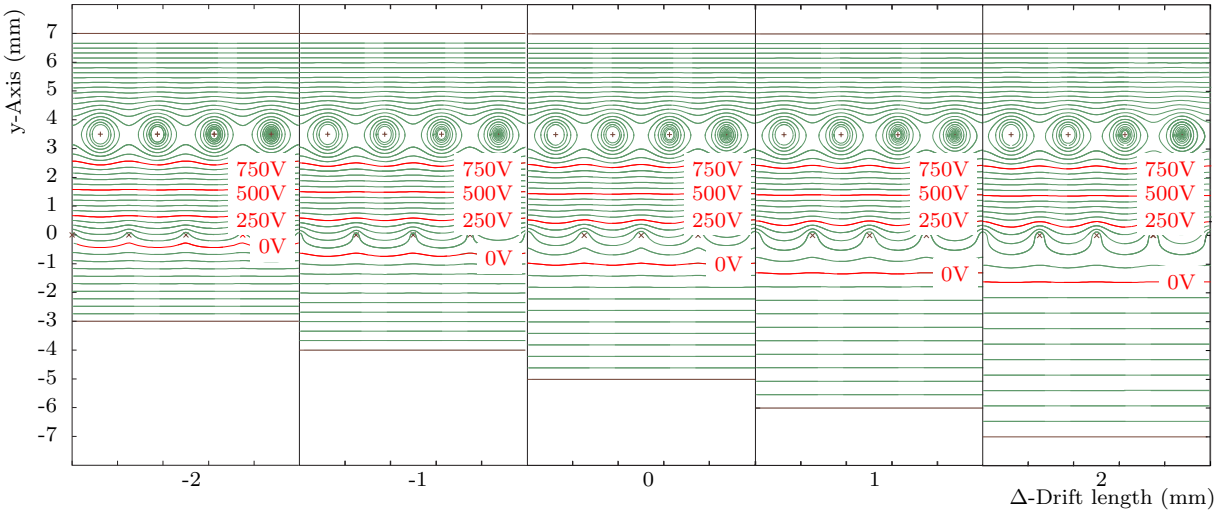

Fig. 5.29: Garfield drift field scan for deformed gas window of ±1 and ±2 mm for constant drift voltage of 500 V. Nominal MS2012 geometry is 3.5 + 3.5 + 5 mm (central slice). The potential lines for 0, 250, 500, and 750 V between the anode and cathode wire plane are highlighted in red.

and the active gas volume. Therefore, a foil window (54×54 cm) of 25 μm Kapton with 0.05 μm aluminum on one side was chosen. The foil was stretched by the thermal expansion of a plexiglas, PMMA (PolyMethylMethAcrylate), frame from 20 °C to 50 °C [Hal07]. The foil prepositioning is done using Kapton adhesive tape. The foil is fixated in the frame by 52 screws, which are tightened with 20 Nm per screw. The thermal expansion coefficient α at 25 °C is 82.8E-06 K^{-1} [Bre06] for PMMA. The heat deflection temperature of PMMA is between 65-105 °C which gives the upper temperature limit for this procedure. The length ℓ of a solid structure after heating up by ΔT with an initial length ℓ_0 can be approximated with

$$\ell = \ell_0 + \Delta\ell = \ell_0(1 + \alpha \cdot \Delta T). \tag{5.12}$$

The total expansion of the frame (69.0±0.1 × 69.0±0.1 cm^2 at 20±1 °C) from 20 °C to 50 °C (see figure 5.30) is calculated to 0.17±0.01 cm (0.207±0.009%) using equation 5.12. The Kapton foil has a thermal expansion coefficient of 20.0E-06 K^{-1} [DuP11]. The Kapton foil itself expands about 0.04±0.01 cm (0.06±0.002%). The difference between both materials gives the elongation of the Kapton foil. The first gas window without any additional support structure is shown in figure 5.31. The deformation of the window was characterized in an overpressure test, which has been performed on the PMMA frame with a plug fitting on the bottom side. This fitting was connected by a T-fitting to a gas bottle and a bubble counter used as overpressure control valve. The differential height of the Diffelen oil ($\rho = 1.07\,g/cm^3$ [VAC10]) within the bubble counter above the end of the gas inlet defines the maximum overpressure in the system. First tests were done with 2 mm Diffelen, which corresponds to a static pressure of $p(h) = 0.21$ mbar $= g \cdot \rho \cdot h + p(0)$ with $p(0) = 0$ leading to a deformation of 6.4 mm in the center of the gas window. An oil height of 12 mm (1.26 mbar) leads to a deformation of 12.2 mm. This type of entrance window is highly sensitive to differential pressure variations. The maximum deformation d of a quadratic membrane fixed at all edges with dimension $a = b$ and a thickness h is in first order proportional to a^4/h^3 [Wie96]. There are two ways to limit the deformation, first the aspect ratio of the foil can be reduced (inhomogeneous support structure) or the thickness of the support structure has to be enhanced (homogeneous structure). Several mechanical support structures are considered to keep the mechanical deformations of

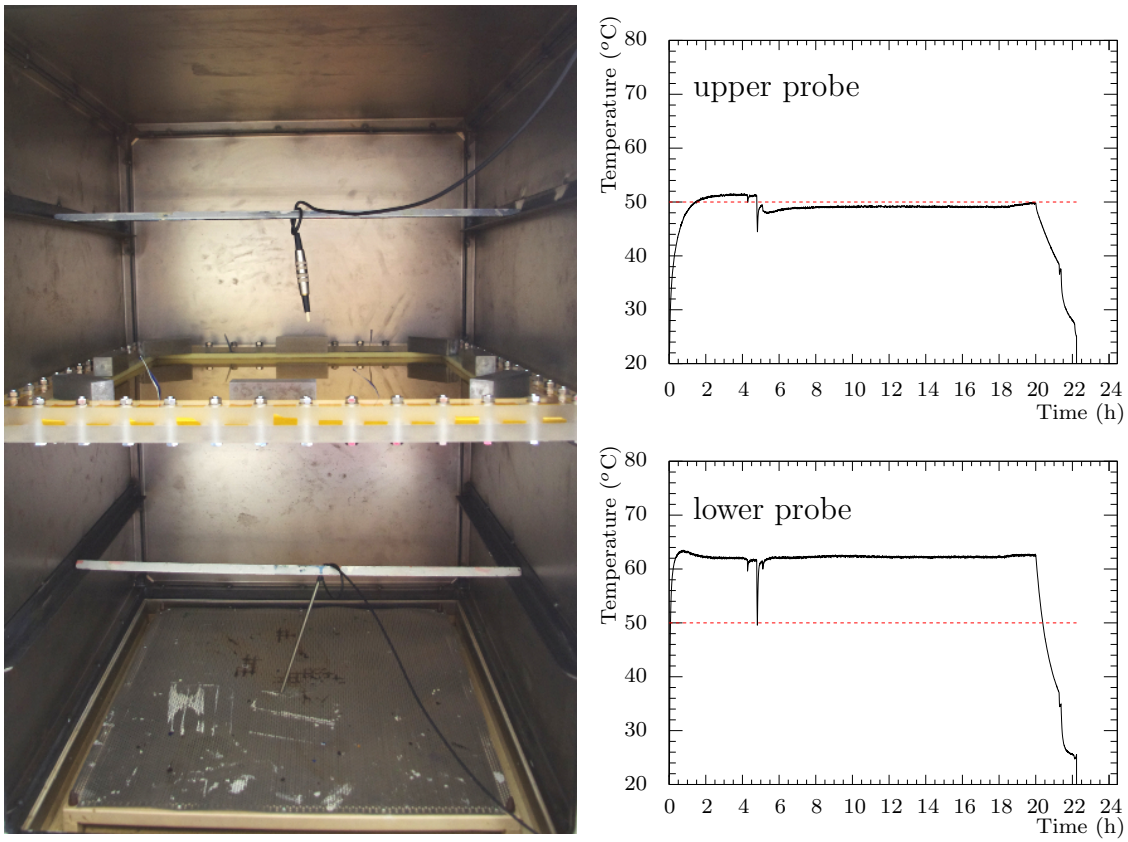

Fig. 5.30: Left: Stretched foil within PMMA frame with two temperature probes. Right: Temperature measured by the lower probe (RMS of 0.06 °C) and temperature measured by the upper probe (RMS of 0.05 °C). The foil within the PMMA frame is heated 4.5 h until the frame has reached a stable temperature of 50 °C. It is assumed that the temperature measured by the upper probe is equivalent to the temperature of the foil and the PMMA frame. The G11 frame with Araldit AW 106 on one side is put on the kapton side of the stretched foil leading to a spike in the temperature trend. Afterwards, the glue needs at least 4 h for hardening. In order to avoid mechanical stress before finishing the hardening process a temperature of 50 °C is kept for 15 h.

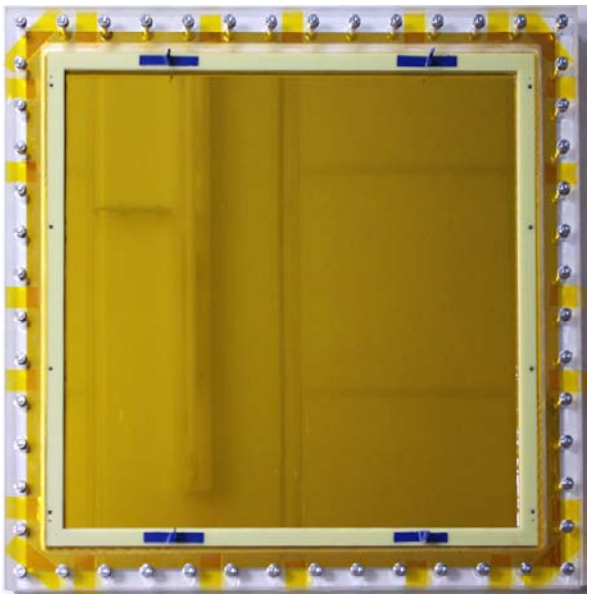

Fig. 5.31: Kapton foil window for the open TRD geometry is shown, after stretching in the oven.

the TR-entrance foil window within the limits of ±1 mm. The advantage of a homogeneous additional support structure is the remaining of an equable PID performance on the complete active detector surface. The inhomogeneous support gains from the high performance in areas without additional support structure. By positioning the additional material budget above pad boundaries one can limit the disadvantages to a minimum.

5.10.2.1. Homogeneous Support Structures Rohacell HF71 ($\rho = 0.075\,\mathrm{g/cm^3}$) was used to build a first homogeneous structure based on the experience of the ALICE collaboration. A 6 mm thick Rohacell HF71 sheet was glued using Araldit 116 to the G11 frame (see figure 5.32). The gas foil window had a maximum deformation of (6.1±0.5) mm

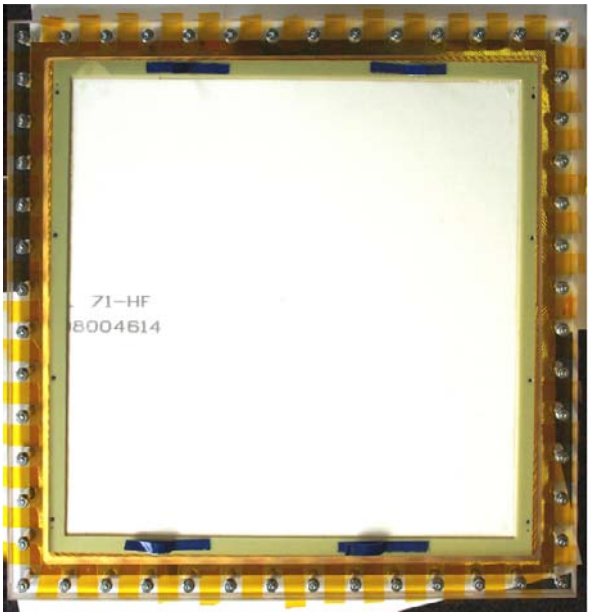

Fig. 5.32: Gas foil window supported with 6 mm Rohacell HF71 sheet.

at the foil center at an overpressure of 1.0 mbar. The uncertainty of the measurement is dominated by the roughness of the foam surface. The maximum deformation was reduced by approximately 50% by the homogeneous support structure compared to the deformation of the pure foil window as presented in figure 5.33. It was shown that the stiffness of the entrance window could be increased by an additional Rohacell support structure, but the maximum deflection of the entrance window due to differential overpressure is still above 1 mm. The mechanical stability can be enhanced by using a Rohacell plate of at least 11 mm ($h_{min} = (6.1\,\mathrm{mm} \cdot (6\,\mathrm{mm})^3/(1\,\mathrm{mm}))^{(1/3)} = 11\,\mathrm{mm}$) which increases the TR-photon absorption probability (approximated using figure 5.27) to 75% for a 11 mm and 47% for a 6 mm Rohacell structure. Another option could be an ALICE like radiator box structure [ALI01]. It was shown that the maximum deformation due to 1 mbar overpressure of a $(120 \times 120)\,\mathrm{cm^2}$ radiator model could be limited to 0.9-3.25 mm depending on the reinforcement. This option would result in a mechanical union of radiator and MWPC and eliminate a possible radiator exchange and some radiator options.

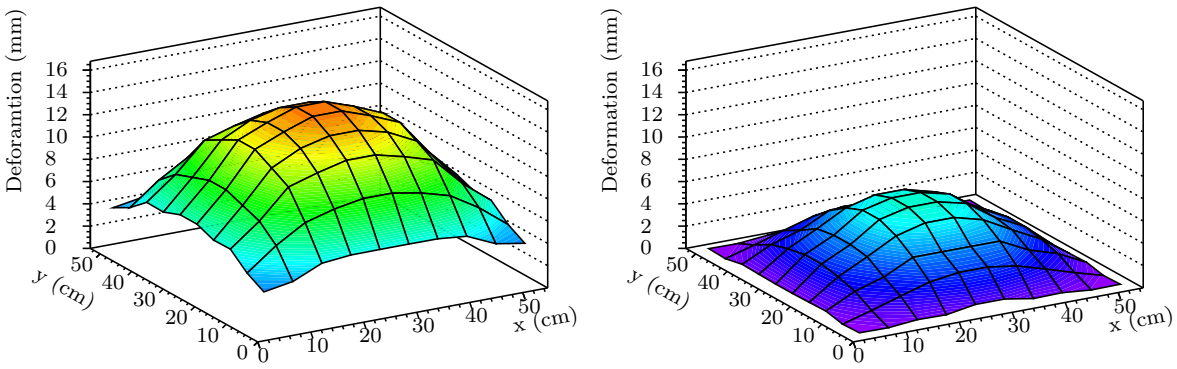

Fig. 5.33: Entrance window deformation of the Kapton foil (left) and 6 mm Rohacell HF71 (right) at 1 mbar overpressure. The maximum deformation of the pure foil window is (14.3±0.4) mm where the entrance window with a homogeneous mechanical Rohacell support has a maximum deflection of (6.1±0.5) mm.

5.10.2.2. Inhomogeneous Support Structures To avoid additional material budget between radiator and active gas volume on most of the surface an inhomogeneous support structure was considered. The largest 25 μm Kapton foil dimension with a maximum deformation of 1 mm at a pressure difference of 1 mbar was estimated in a pre-test to be $(10 \times 10)\,\mathrm{cm}^2$. The resulting support structure called support grid is presented in figure A.2 and figure 5.34 and made from 10 mm thick G11. The deformation of the support

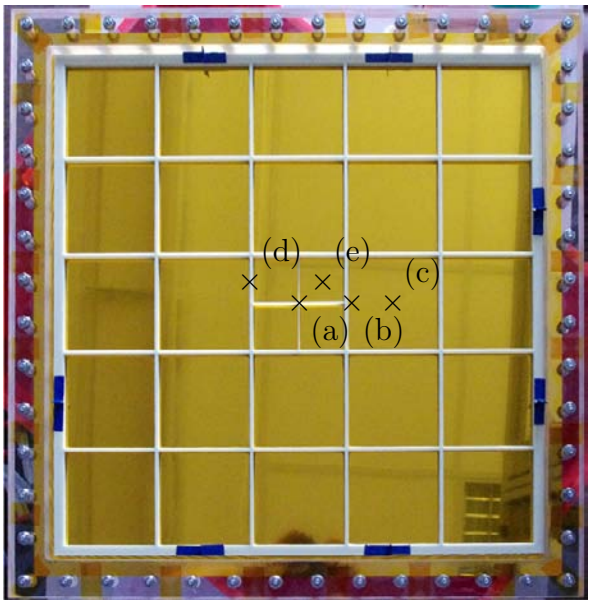

Fig. 5.34: Gas foil window supported with 10 mm G11 lattice window support structure with small lattice center. The relative deformations have been measured at five different positions; (a) on top of the crossing of the small support grid, (b) at the base contact between foil and lattice frame of one big square, (c) foil deformation at the center of one big square, (d) at the base contact between foil and lattice frame of one small lattice and (e) the foil deformation at the center of one small square. The maximum deformation of the support grid is 0.2 mm at position (b). The additional maximum foil deflection at the center of a big square is 0.4 mm (c-b) and 0.2 mm (e-d) for the small square. The deformation was estimated for an over pressure of 1.0 mbar equivalent to 1 cm fluid height.

grid and the foil has been determined at an overpressure of 1.0 mbar at five different positions. The maximum deformation of the support grid itself is 0.2 mm at position

(b). It is assumed that the maximum foil deflection within a single square is independent of the grid position and only influenced by the lattice dimensions. The maximum foil deflection at a center of a big square is 0.4 mm (c) and 0.2 mm (e) for the small square. The total maximum deflection of the foil center in the central square (without small cross structure) is 0.6 mm, which is below the limit of 1 mm. The inhomogeneous lattice influences the PID performance in a negative way, since the parts of the active gas volume which are shadowed have a lower probability to be reached by TR-photons. This effect is the lowest for particles with an impact angle of 0 ° where the shadowed fraction of the total surface is around 5%. The shadowed area increases with increasing impact angle to up to 11% as shown in figure 5.35. The covered surface fraction can be

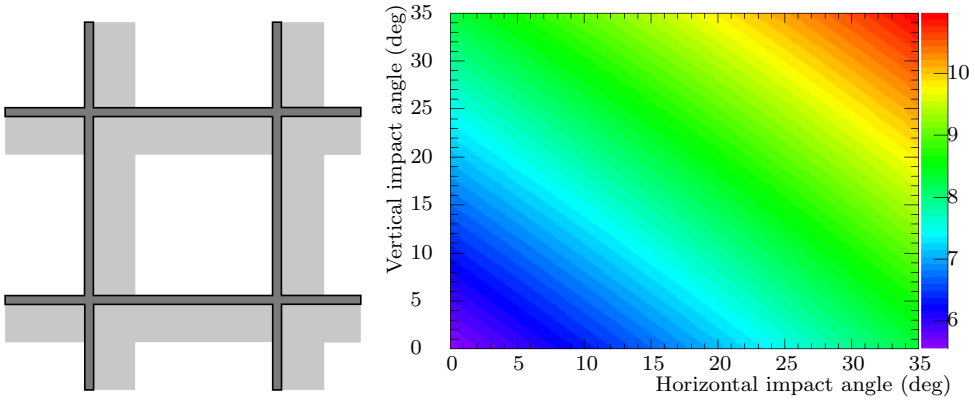

Fig. 5.35: A schematic drawing of a support grid part on the left side. The dark gray area is covered by the lattice itself where the light gray area is the additional shadowed area seen by particles coming from the upper left side. The light gray area varies with as a function of the horizontal and vertical impact angle of the particle relative to the chamber surface. The shadowed active area fraction in percent calculated for one TRD module of 570×570 mm^2 with 4×4 lattice rips of 4 mm width and a rip height of 10 mm as function of the horizontal and vertical impact angle is presented on the right side. The covered area is 5.5% where the additional shadowed area fraction at maximum impact angels is 11%.

further reduced by using a lattice rip width as thin as 1 mm. The mechanical stability of the entrance window is not affected since the stiffness perpendicular to the foil surface scales with rip height which is still 10 mm. The resulting surface coverage would be of the order of 1%. The maximum shadowed area for particle tracks with a maximum impact angle of 35^o would be approximately 7%.
Nevertheless an inhomogeneous support structure has been chosen for the 2012 prototypes to have optimal radiator test conditions with a minimum material budget between radiator and detector.
The chamber construction is derived from the ALICE Time Projection Chamber (TPC). A schematic crosscut of the 2012 prototypes is presented in figure 5.36. In most cases the wire tension is compensated by the 'front-panel', the 'back-panel' while (pad-plane shown in figure A.1 and its mechanical supports) the last part glued to the chamber body already carrying the wires. This concept is turned around for the CBM TRD 2012 prototypes. The detector assembly starts with the aluminum back-panel support frame (figure A.3). An ALICE TRD 23 mm thick honeycomb carbon-fiber-sandwich [ALI01] (figure A.4) is glued to this frame using Araldite AW 106 and the gap is filled by AW 116. This combination will give the mechanical stability to the chamber and compensate the wire tension from the anode as well as the cathode wires. The back-panel is built in the same way as it was done for the 2010/11 prototypes. After hardening of the back-panel,

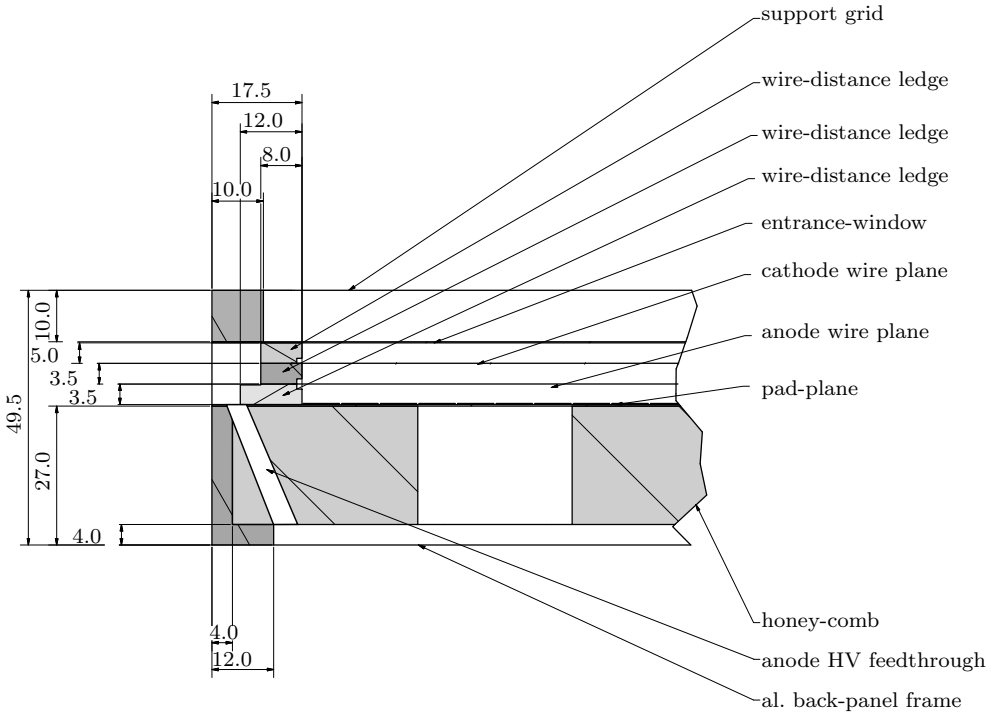

Fig. 5.36: Crosscut of a 2012 prototype [Ver13]. All presented length are given in millimeter. Parts from top to bottom: support grid (figure A.2), entrance window, wire-distance ledge (figure A.10), cathode wire plane, wire-distance ledge (figure A.9), anode wire plane, wire-distance ledge (figure A.7), pad-plane (figure A.1), honey-comb (figure A.3), aluminum back-panel frame (figure A.4).

pad-plane sandwich the missing reamed holes (master plate is presented in figure A.5) for the wire distance ledges and the eight anode HV cable feedthroughs are drilled next to the wire distance ledge position in regular spacing through the pad-plane back-panel (see left figure 5.37). The pad side of the pad-plane back-panel sandwich is finally clea-

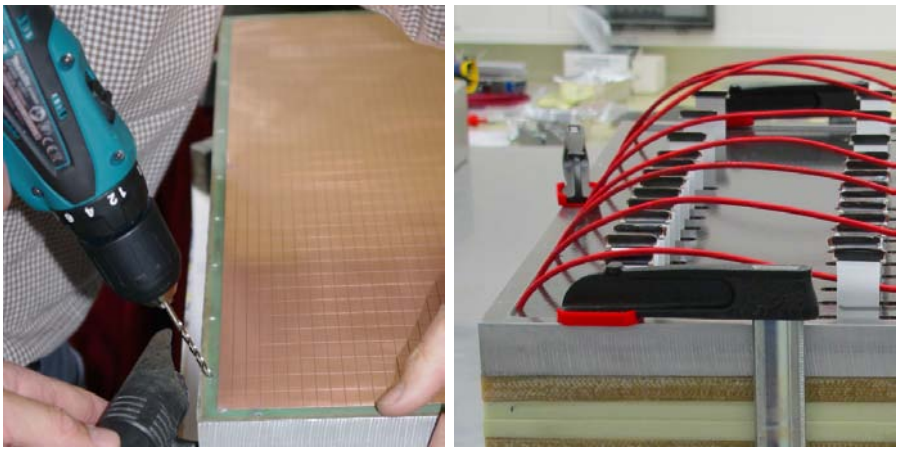

Fig. 5.37: Drilling of the anode HV cable feedthroughs (left) and gluing of the anode HV cable feedthroughs (right).

ned with isopropanol. The wire distance ledges (figure A.8) are prepared with a 2.5 mm copper adhesive tape glued to the 0.2 mm deep groove on the top side. The ledges are connected to the back-panel using AW 106 and nylon aligning pin parallel to long pad size direction to adjust a precise distance of 3.5 mm between the pad-plane and the anode wires. The anode wires (20 μm Au-plated W wire) are winded to an ALICE wire

transfer frame with a pitch of 2.5 mm and a tension of 50-55 cN. Technicoll is used to fix wires in position on the frame before dividing the frame in half. The wire grid is positioned and lowered to the wire ledges until the wires rest on top of the ledges. A schematic drawing of the anode and cathode wire grid position relative to the pad-plane is presented in figure 5.38. The anode wire copper strip is subdivided into eight equal

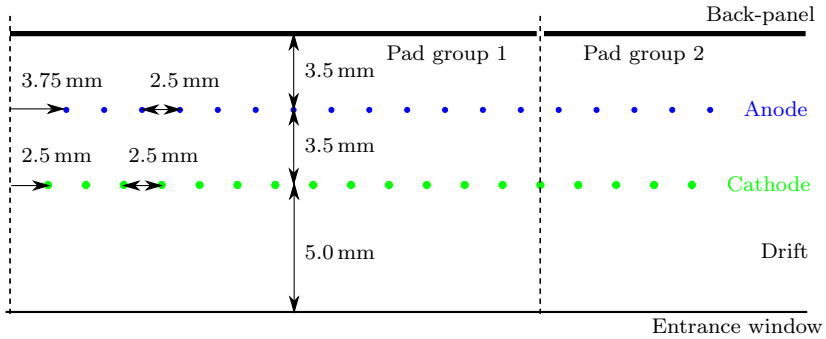

Fig. 5.38: A schematic drawing of the anode and cathode wire grid position relative to the pad-plane based on [Ems13c] is shown.

anode sectors. A thin film of AW 106 is applied on top of the wire ledges and a second wire ledge (figure A.9) of 3.5 mm thickness is put on top of this film to keep the wires in position. The second distance ledge on the opposite side of the anode wire copper strip is prepared with another copper strip to connect the cathode wires later. After hardening of the glue the wires are soldered to the copper strip and cut off the transfer frame. The anode HV cables are coated with a thin Technicoll film and pitched through the back-panel feedthroughs (see right figure 5.37). The glue film ensures gas tightness and mechanical load removal from the soldering point on the copper strip, to which the anode HV cables are soldered. The cathode wires (75 μm Cu-Be) are winded with the same spacing and a tension of 100 cN. The second wire plane is positioned staggered relative to the anode wire grid. The gluing procedure is analog to the anode procedure. A last wire distance ledge (figure A.10) of 5.0 mm thickness is put on top of the glue film. The cathode wires are cut off the transfer frame after hardening of the glue and soldered to the copper strip on the opposite side of the wire ledge, to which the anode wires have been soldered previously. The cathode cable is soldered to the copper strip. The open sides are completed by the so called end strip (figure A.6) which is adjusted by another set of nylon aligning pins as illustrated in figure 5.39. The electrical connection

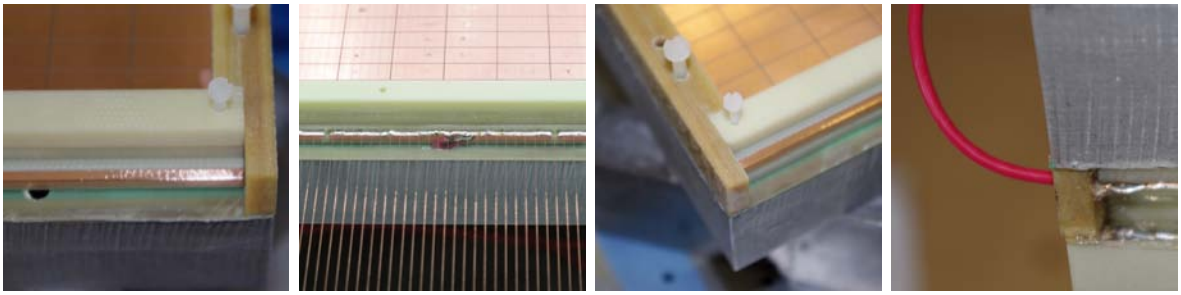

(a) **(b)** **(c)** **(d)**

Fig. 5.39: Anode wire connection side with open anode HV cable feedthrough (a and b) and cathode wire soldering side (c) with three applied wire distance ledges and end strips with open gas supply feedthrough. The cathode cable soldered to the copper connection strip is shown in figure d.

to the aluminized Kapton gas window is realized by an overlapping part of the Kapton foil crimped over a copper strip covered on both sides with silver glue as presented in figure 5.40. The drift HV-cable is soldered to this copper strip after hardening. The cop-

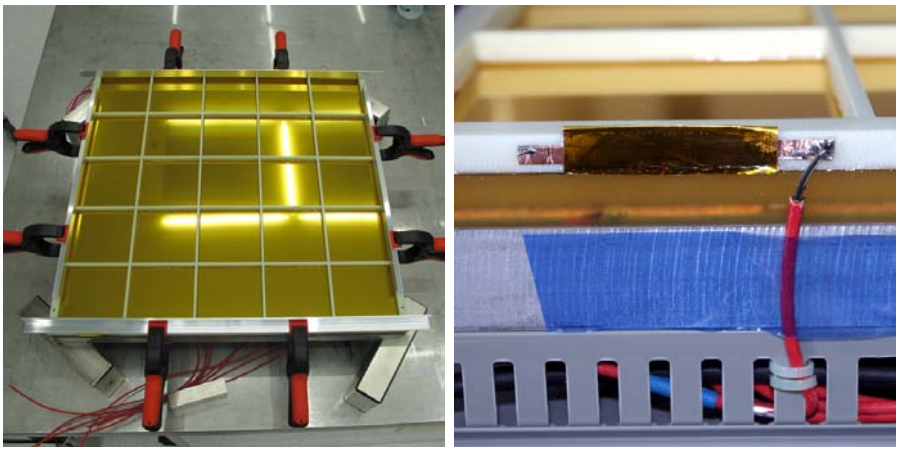

Fig. 5.40: Closure of the chamber body (left) and gas window connection to filter-board are shown (right).

per strip is afterwards covered by a Kapton adhesive tape to ensure electrical isolation to the outside. The chamber is closed by gluing the support grid gas window on top of the active detector volume. The gaps on the two wire ledge stack sides are filled with AW 106 to ensure gas tightness and increase mechanical stability. The anode, cathode and drift cables are soldered to the HV-filter board (A.14), one first order low-pass pre-filter (1 MΩ resistor and 4.7 nF/3kV capacitor) followed by eight channel individual first order low-pass filter (1 MΩ resistor and 2.2 nF/3kV capacitor) on the anode section and one first order low-pass filter (1 MΩ resistor and 4.7 nF/3kV capacitor) for the drift HV. The common ground potential bar for the drift and anode filter sections is connected via one 1 kΩ resistor on each side to the floating ground of each HV-power supply. The filter board is mounted on the back-side of the back-panel inside of a cable shaft.
A first lab test of the prototype characteristics is the estimation of the energy resolution, which was done with an Ar/CO_2(82/18) mixture and a collimated ^{55}Fe source.The energy resolution is presented as ratio of the two Gaussian fit parameters σ/μ of the 5.9 keV peak in figure 5.41.

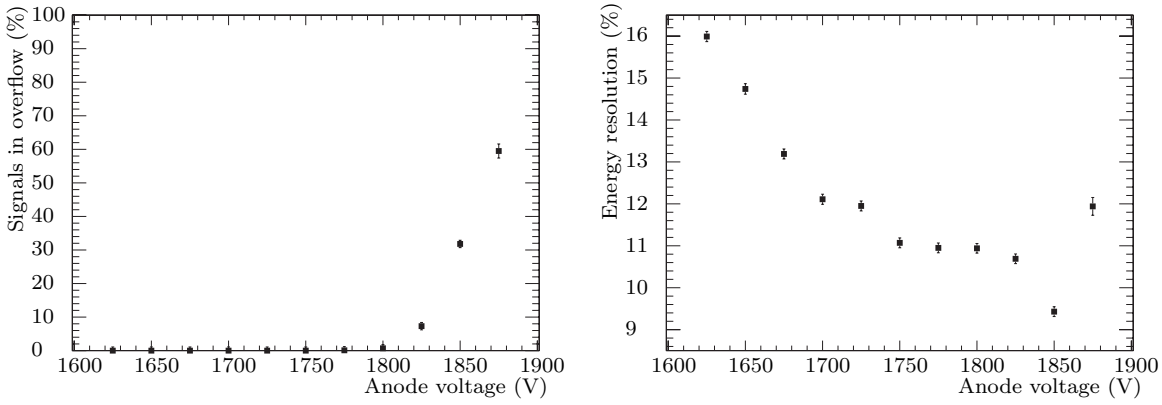

Fig. 5.41: 2012 MS35355 operated with Ar/CO_2 (82/18) and an ^{55}Fe source. **Left:** Fraction of signals in overflow as function of anode voltage **Right:** Energy resolution as function of anode voltage. The presented errors include uncertainties arising from the energy calibration of the individual spectra and Gaussian fitting procedure.

Another interesting quantity is the matching of the read-out electronic gain to the chamber gain. Since the ASIC gain is fixed the chamber gain has been varied in order to find the optimal anode voltage setting at minimum energy resolution (see right side of figure 5.41). This optimal working point has been determined at 1800 V for the argon based gas mixture. The iron spectrum shape is modified by a further increase of the chamber gain due an increasing fraction of signals in overflow as previously discussed for the 2011 MWPC prototypes.

6. Radiator Prototypes

To increase the particle identification performance of MWPCs one can use the superposition two parallel energy loss processes in; electromagnetic interaction described by the Bethe-Bloch-Formula and conversion of Transition Radiation (TR). Radiators produce TR-photons emitted at material boundaries between materials with different dielectric constants ϵ. Considering the different types of boundaries they can be classified as regular foil, foam and fiber radiators. The absorption probability of different detectors varies over a wide range. Therefore, it is advantageous to optimize the radiator photon emission spectrum described by equation 4.9 to the detector absorption probability spectrum. This was done for our prototypes (MS336 and MS444). Since both prototypes consist of the same components with an equivalent active gas volume thickness (12 mm) and composition (Xe/CO_2 (80/20)), we assume the same absorption probability within the gas. The incoming TR-spectrum is reduced by the absorption in the MWPC components of the window between the radiator and the gas volume. These are in our case 1 mm Rohacell, 200 μm Epoxy, 300 μm Carbon fibers and 12 μm single sided aluminized Mylar foil (3 μm Al). The usable spectrum is also narrowed by the absorption inefficiency due to decreasing photon cross section of the active gas for increasing photon energy. The resulting effective detector spectrum is shown in figure 5.19. The photon emission spectrum matches chamber effective detector spectrum best if both maxima are at the same energy. It is essential to understand the influence of radiator parameters like material, number of foils, foil and gap thickness to optimize the TR-yield to the chamber effective detector spectrum. This will be shown for a material collection which can be used as radiator material. The materials have different properties like stability, conductivity, density, and photon cross section. The following optimization aims to find a cost efficient, light weight, high performance radiator with a minimal radiation length. The material properties, which are essential for this optimization, are shown in table 6.1 and figure 6.1.

Tab. 6.1: Gap and foil material properties: Z, A, ρ and ω_P at 101.325 kPa and 293.15 K. The properties of mixed materials are not presented in case of foams or fibers. The gaseous and solid components are presented separately within the first part of the table and are used as simulation input.

Material	Z	A	ρ (g/cm^3)	ω_P (eV)
Air	14.49	29.02	1.20E-03	0.71
Hydrogen	1.00	1.01	8.38E-05	0.27
Helium	2.00	4.00	1.70E-04	0.27
Neon	10.00	20.18	8.40E-04	0.59
Nitrogen	7.00	14.01	1.17E-03	0.70
Oxygen	8.00	16.00	1.33E-03	0.74
Carbon dioxide	7.33	14.67	1.83E-03	0.91
Argon	18.39	39.95	1.66E-03	0.79
Xenon	54.00	131.30	5.46E-03	1.37
Mylar	4.55	8.73	1.393	24.53
POKALON N470	4.06	7.71	1.150	22.43
POKALON N331	3.90	7.36	1.150	22.50
ARYPHAN N681	4.18	7.96	1.210	22.96
TACPHAN OG863	4.53	8.65	1.300	23.76
Polyethylene (PE)	2.67	4.68	0.900	20.65
Polypropylene (PP)	2.67	4.68	0.900	20.65

Material	Z	A	ρ (g/cm^3)	ω_P (eV)
Polyvenylchlorid (PVC)	5.33	10.42	1.300	23.51
Polyoxymethylene (POM)	4.00	7.51	1.400	24.89
Kapton	5.03	9.80	1.430	24.67
Cellulose paper	4.00	7.51	1.200	23.04
Polystyrene (PS)	3.50	6.51	1.100	22.16
Polymethylmethacrylate (PMMA)	3.18	5.89	1.180	22.99
Aluminum	13.00	26.98	2.700	32.87
Lithium	3.00	6.94	0.534	13.85
Beryllium	4.00	9.01	1.848	26.10
Sodium	11.00	22.99	0.971	19.64
Magnesium	12.00	24.31	1.738	26.69

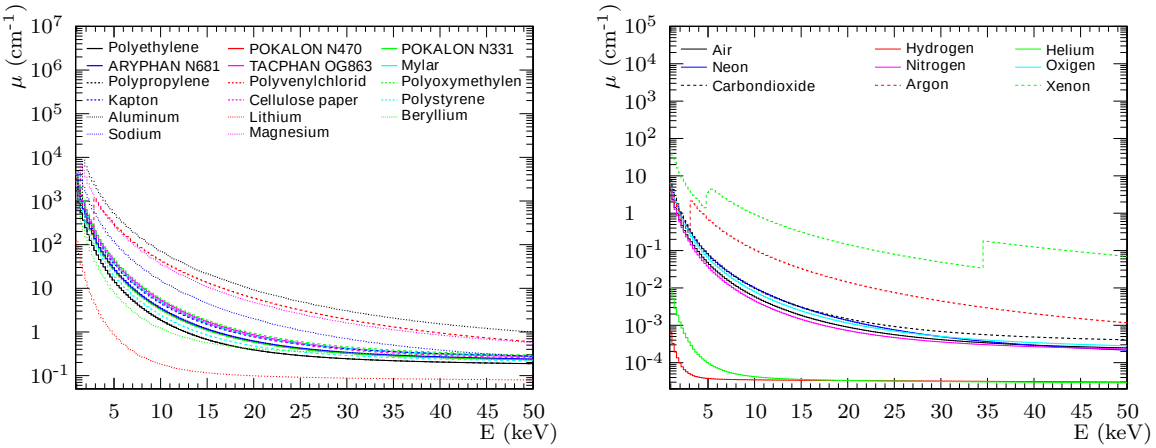

Fig. 6.1: Attenuation coefficients μ as function of photon energy E for different foil (left) and gap (right) materials presented in table 6.1. Values of mass attenuation coefficients μ/ρ are taken from XCOM: Photon Cross Sections Database and multiplied by the material density ρ.

The different materials are chosen to study different common/usable plastics and metals over a wide range of properties like density and plasma frequency. The metals were included, since first radiator prototypes were built from Lithium and Beryllium foils in the 1980th and showed good performance. The production of such radiators in scales needed for CBM would be too expensive, they are calculated for comparison. The different gases, which can be used as gap material, are calculated for the same reason. Apart from the material question there are in addition different ways to position the foil/solid material with more or less regular spacing. Also, there are mixtures between regular and irregular spacing possible or spacing due to a substructure of the foil material itself. For example, the perforated and unperforated PE foam foil can be used in addition to build irregular radiators and to adjust the gap thickness. These questions will be addressed by special prototype designs presented in section 6.3.3 and 6.3.2.

6.1. Foil Radiator Parameters

The correlation of the different radiator parameters like foil thickness l_1, gap thickness l_2, number of foils N_f, and gap material will be shown for one example radiator made from polyethylene ($(C_2H_4)_n$) foil ($N_f = 100$; $l_1 = 15\,\mu$m) and air ($l_2 = 300\,\mu$m) at particle momenta of 2 GeV/c. The input material photon cross sections are taken from XCOM:

Photon Cross Sections Database. An optimization procedure will be shown, based on the found parameter correlations, leading to best performance matching of a radiator to a given chamber design.

6.1.1. Material Density

The material density is one of the most important sources of uncertainty. It influences the plasma frequency and self-absorption. This first parameter scan is used to estimate the influence of solid and gaseous material density uncertainty on the total TR-spectrum uncertainty. A systematic variation of the air density (ρ_2) and a parameter scan of the polyethylene foil density (ρ_1) are shown in figure 6.2. The influence of the gas density

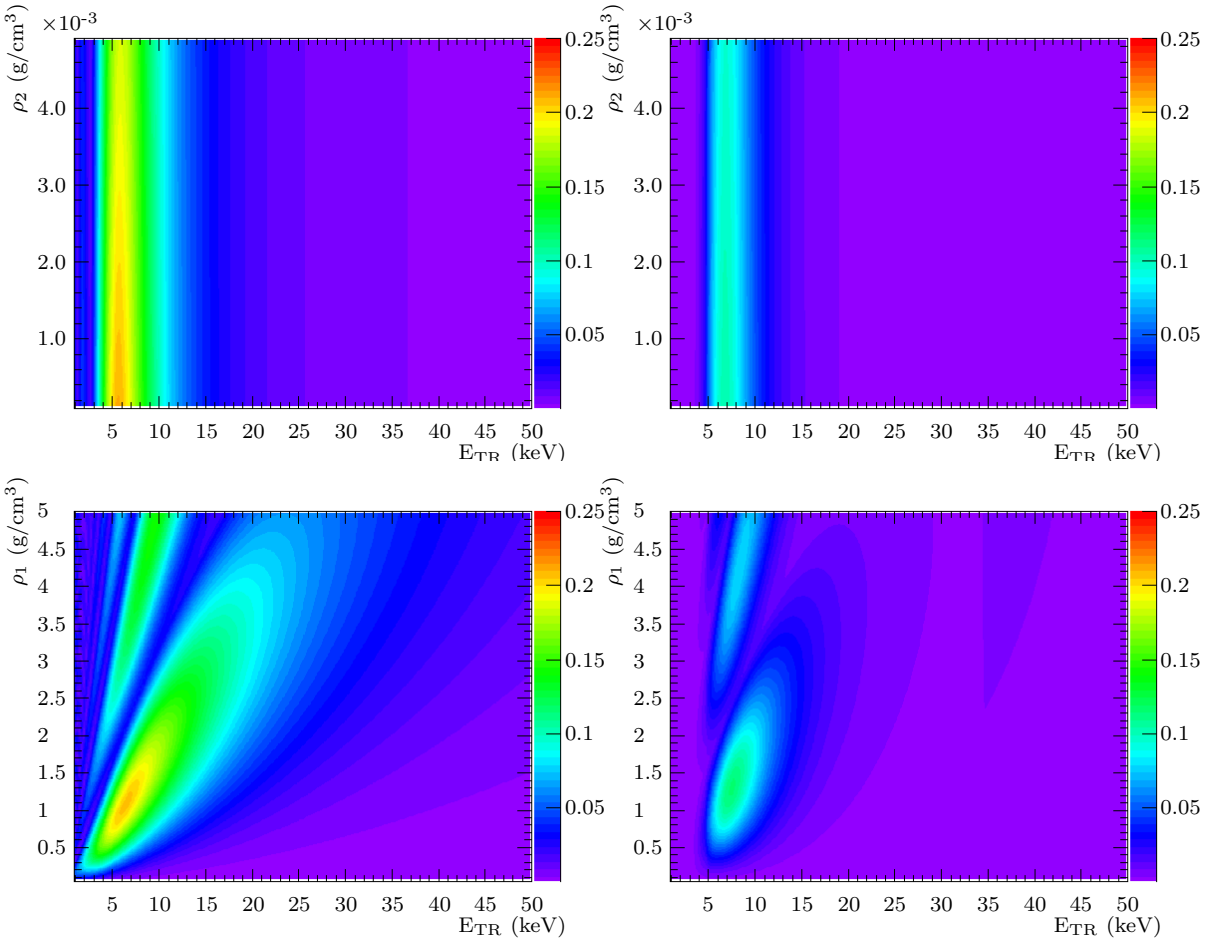

Fig. 6.2: TR-yield emission spectrum (left) and spectrum of photons deposited within the 2011 detector (right) calculated for foils ($N_f = 100$; $l_1 = 15\,\mu$m) and air ($l_2 = 300\,\mu$m) as function of gas density ρ_2 (upper row) and as function of foil density ρ_1 (lower row) at 2.0 GeV/c. The theoretical value of ρ_2 for air is 1.2E-03 g/cm^3 and of ρ_1 for Polyethylene is 0.9 g/cm^3.

on the TR-photon emission spectrum is relatively small, since the absolute density is three orders of magnitude smaller compared to solid materials as presented in table 6.1. Therefore the self-absorption due to the gaseous radiator component is very small. The shape of the spectrum is not modified but the total TR-yield decreases for increasing gas density for constant foil material density. This is due to the $1/\rho$ proportionality of ω_P of the gas. Since the self-absorption of the solid parts of the radiator are dominant, there are two effects in parallel visible in figure 6.2. The self-absorption increases with rising foil density and the TR-yield suffers from the decreasing difference between the two

plasma frequencies. The shape of the TR-spectrum is modified with a clear maximum between 0.9-1.4 g/cm^3 density and 5-8 keV. The influence of the density uncertainty on the overall uncertainty of this simulation can be demonstrated with a short example. The calculated value for the plasma frequency for polyethylene at 0.9 g/cm^3 is 20.65 eV. Lets assume an uncertainty of the density of the order of 10%. This would result in an systematic error of $\Delta\omega_P = \pm(\Delta\rho L)/(2\sqrt{L\rho})$ with $L = 4\pi\alpha\hbar c/(m_e/c^2)$ of 0.05 eV or 0.24%.

6.1.2. Lorentz Factor

A variation of the Lorentz factor γ ($\gamma = \sqrt{1+(p/m_0c)^2}$) of electrons for constant radiator parameters ($N_f = 100$; $l_1 = 15\,\mu$m and $l_2 = 300\,\mu$m) built from polyethylene foil and air is shown in figure 6.3. It can be seen that the position of the TR-yield maximum

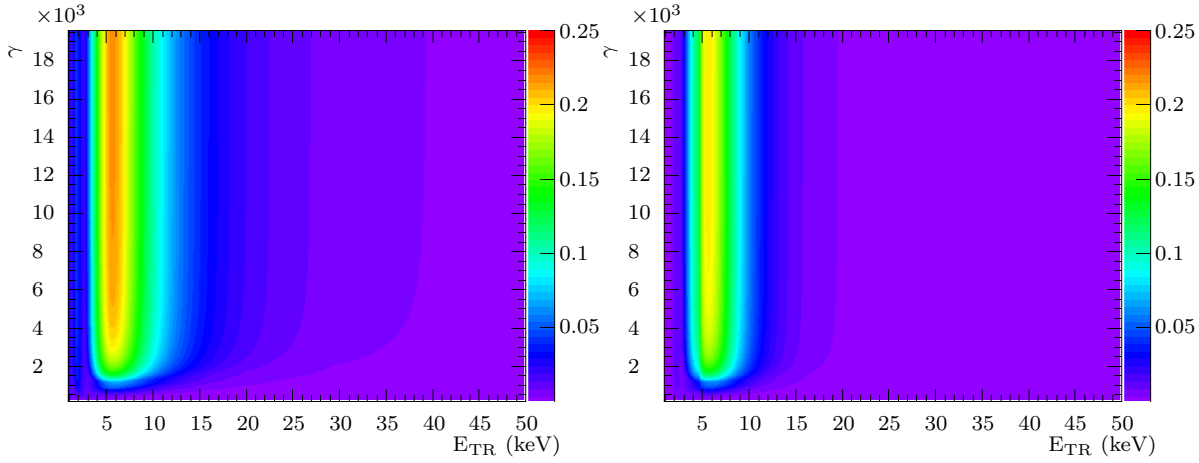

Fig. 6.3: TR-yield emission spectrum (left) and spectrum of photons deposited within the 2011 detector (right) calculated for polyethylene foil ($N_f = 100$; $l_1 = 15\,\mu$m) and air ($l_2 = 300\,\mu$m) as function of γ ($\gamma = \sqrt{1+(p/m_ec)^2}$)

has a fixed position between 5 and 6 keV for different Lorentz factors γ. The total yield increase begins at a threshold $\gamma_{th.}$ presented in equation 4.14. The maximum TR-emission probability increases slightly as well as the width of the spectrum for increasing Lorentz factor for constant radiator parameters. Therefore, an uncertainty of the particle momentum has only low influence on the total TR-yield uncertainty and will be neglected in the later on in the in beam test analysis.

6.1.3. Foil Thickness

The TR-spectrum as function of the foil thickness l_1 is calculated for a radiator made from polyethylene foil ($N_f = 100$) and air ($l_2 = 300\,\mu$m) and 2.0 GeV/c electrons (see figure 6.4). The foil thickness is directly correlated to the position and number of the interference maxima of the TR-spectrum. The position of the highest maximum can be approximated by using equation 4.16. The emission spectrum is dominated by the self-absorption due to the solid component of the radiator for foil thickness larger than 100 μm for a given gap diameter. The highest emission probability is reached for a foil thickness between 9 and 18 μm at an photon energy of 4-6 keV. An uncertainty of the foil thickness of 1 μm in the range between 9 and 18 μm is leading to a rather large modification of the spectrum shape compared to the previously discussed parameters.

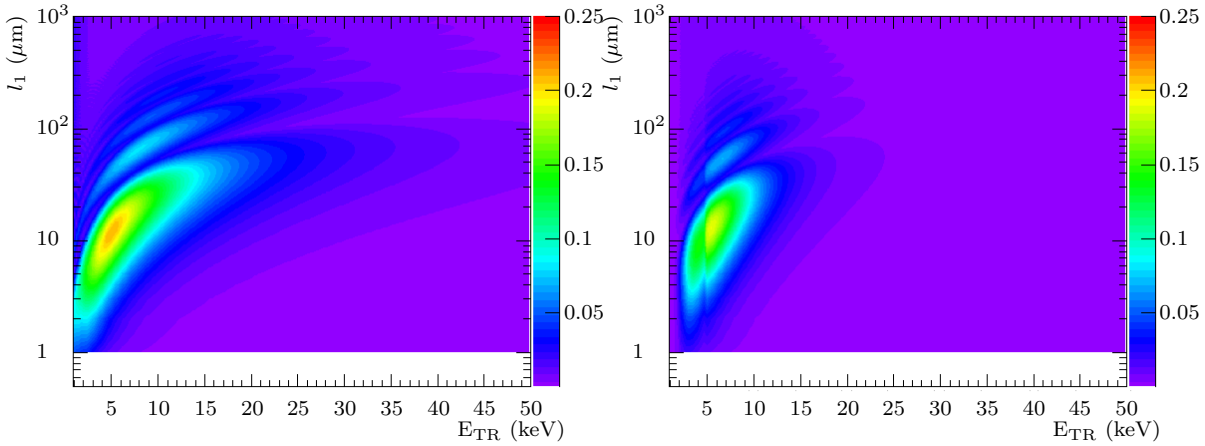

Fig. 6.4: TR-yield emission spectrum (left) and spectrum of photons deposited within the 2011 detector (right) calculated for polyethylene foil ($N_f = 100$) and air ($l_2 = 300\,\mu$m) as function of foil thickness l_1 for 2.0 GeV/c electrons

6.1.4. Gap Thickness

The influence of the gap thickness l_2 on the TR-spectrum is shown in figure 6.5. The total

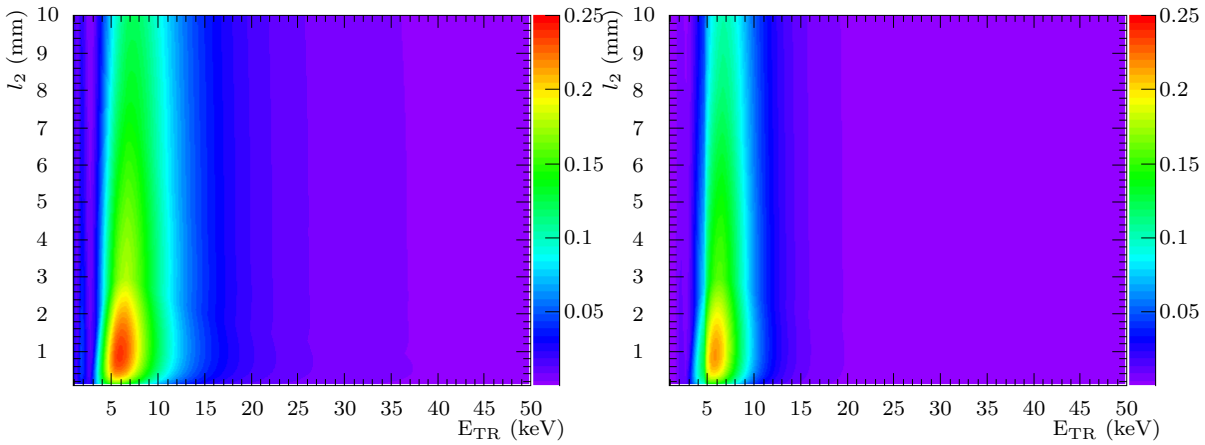

Fig. 6.5: TR-yield emission spectrum (left) and spectrum of photons deposited within the 2011 detector (right) calculated for polyethylene foil ($N_f = 100; l_1 = 15\,\mu$m) and air as function of gap thickness l_2 for 2.0 GeV/c electrons

TR-yield can be increased up to a maximum by increasing gap thickness. The maximum of the emitted photon spectrum is slightly shifted to higher energies of 5-8 keV for a constant foil thickness of 15 μm. The maximum yield is reached between 700 and 1200 μm. The yield decreases after the first maximum, if the thickness is further increased. The spectrum width decreases also with increasing gap size slightly due to the increasing self-absorption of the gap material. The effect is rather small, since the density of the gap material (air) is three orders of magnitude lower compared to the foil material. The uncertainty arising from a variation of several hundred microns in the range between 700 and 1200 μm is small compared to the impact of several microns difference in foil thickness. This is partly due to the density difference between solid foils and the gas gaps.

6.1.5. Number of Foils

The TR-spectrum for a various number of foils N_f is shown in figure 6.6. By using

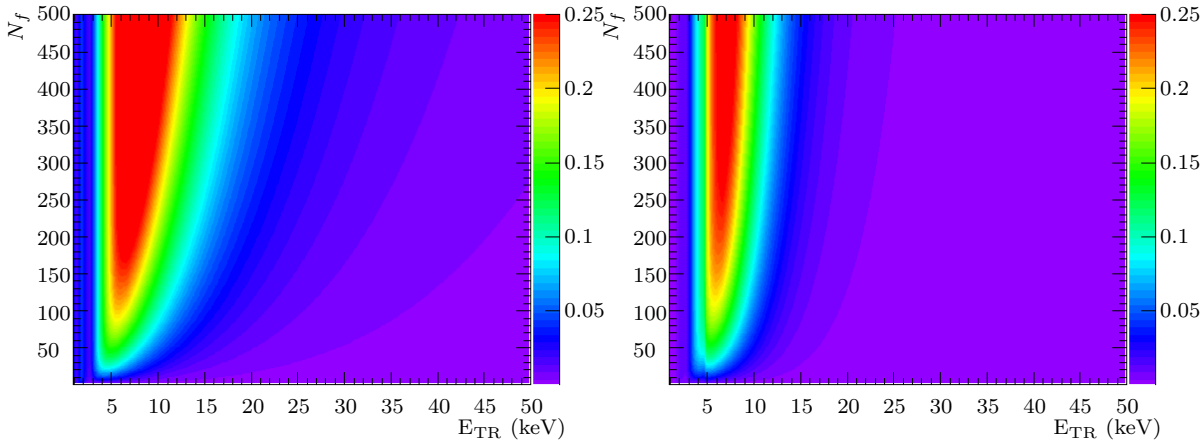

Fig. 6.6: TR-yield emission spectrum (left) and spectrum of photons deposited within the 2011 detector (right) calculated for polyethylene foil ($l_1 = 15\,\mu$m) and air ($l_2 = 300\,\mu$m) as function of number of foils N_f for 2.0 GeV/c electrons

a higher number of foils, the TR-yield can be increased. The TR-spectrum is slightly shifted to higher photon energies, beginning at 4 keV at some 50 foils up to 8 keV at 500 foils.

In summary, all input parameters contribute to the uncertainties of the radiator simulation. Particle momentum and the density of the gas in the gap can be neglected due to their small impact. Usually, there is a perfect knowledge of the foil number in regular radiators and therefore no uncertainty arises from this parameter in contrast to irregular radiators. Since the number of layers is a statistical variable as well as foil and gap thickness (compare to chapter 4.1.2) in case of irregular radiator materials like foams and fiber mats, it can be assumed, that there is a correlated, large impact of these uncertainties on the total TR-yield. Another influence on the total TR-yield which has not been discussed yet is due to material imperfection/inhomogeneity like foil thickness leading to an irregularity even in regular foil radiators. An other important source of uncertainty is the detector absorption spectrum. From several previous in beam tests we know that the amount of used glue is one of the main sources of photon absorption between detector and radiator. Since the TR-spectrum cannot be measured separately using a MWPC without a strong magnetic field and a large distance between radiator and detector, it will not be possible to deconvolute the effects of all parameters in the in beam measurement.

6.2. Optimization Procedure

It will be shown, that it is possible to calculate the optimal radiator parameters, like foil material, thickness, gap material and thickness, as function of characteristic detector properties, like absorption probability depending on the gas mixture and the passive photon absorbers, e.g. gas entrance window. This will be done using the example of the 2011 MWPC prototypes. The absorption maximum $\omega_{max}^{abs.}$ of the 2011 prototypes is at 7.88 keV (5.66 keV for the 2012 prototypes), as presented in figure 6.7. The two parameters l_1 and l_2, with the largest influence on the spectrum shape, number and position of

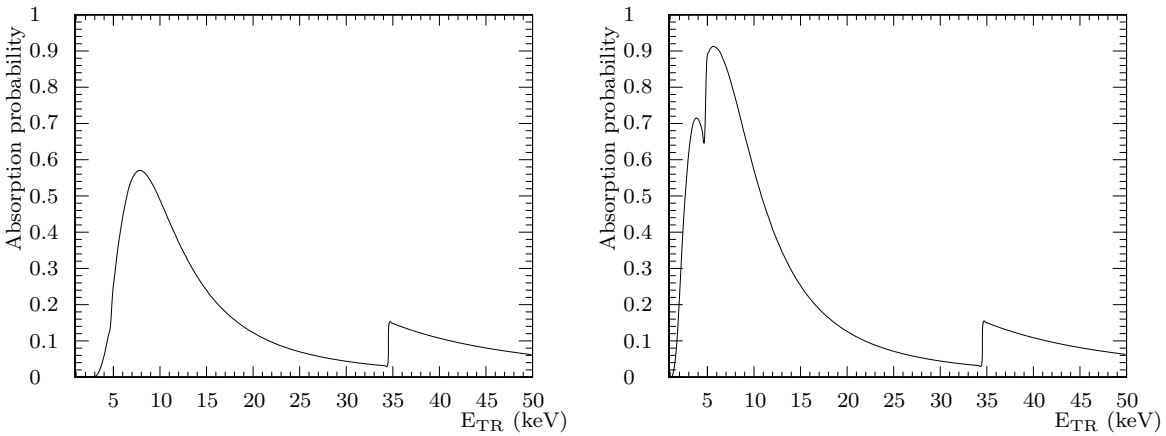

Fig. 6.7: Approximated photon absorption probability of the 2011 (left) and 2012 prototypes (right) using Xe/CO_2 (80/20).

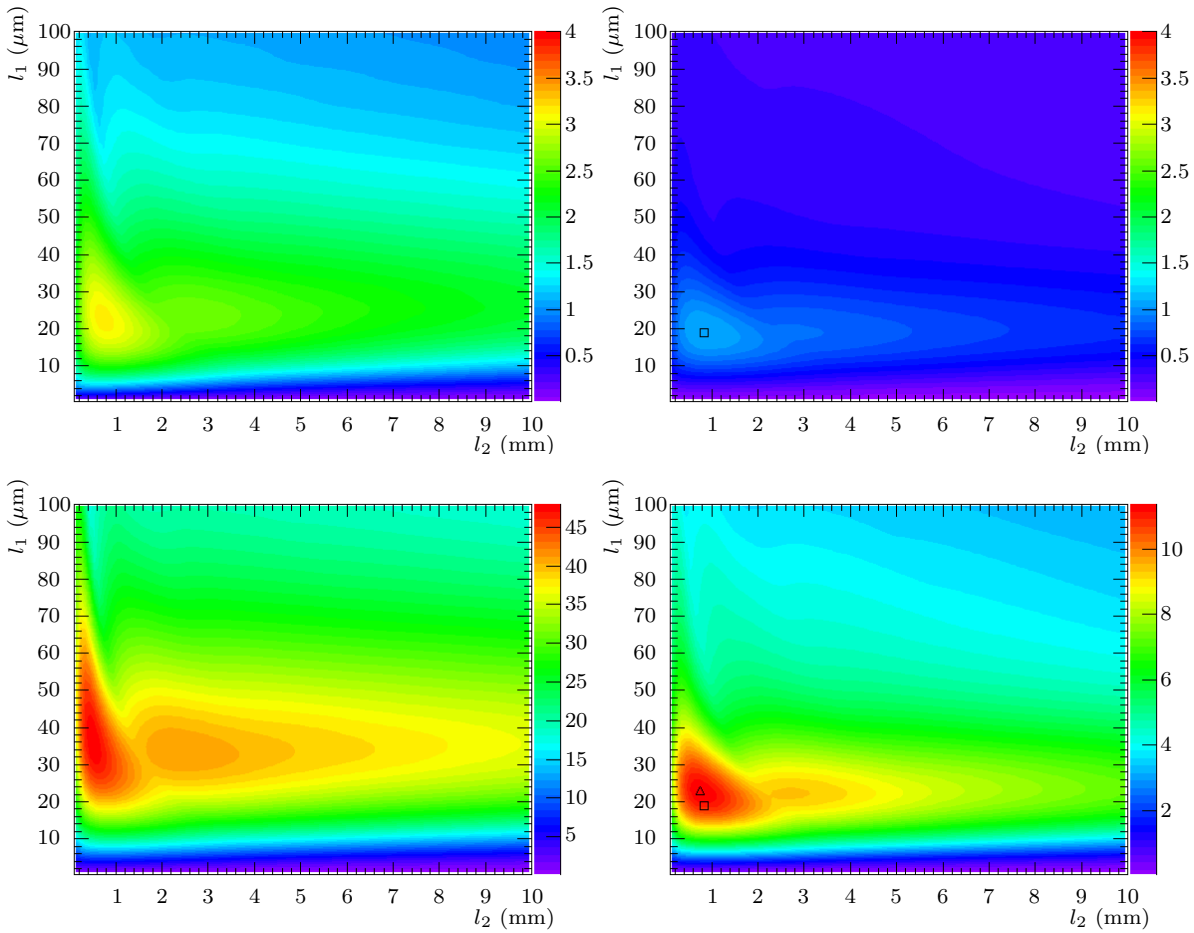

Fig. 6.8: Simulation for 200 Polyethylene foils of variable foil thickness and gap thickness for 2.0 GeV/c electrons using the 2011 detector. Upper row: Integrated TR-yield emission spectrum (left) and spectrum of absorbed photons within the active gas (right) including the TR absorption in the entrance window. Lower row: Average energy loss via TR (left) and average TR energy deposited within the detector per electron (right). All spectra include self-absorption in the radiator.

maxima, were chosen for the following optimization. The optimization was done numerically by varying the parameters l_1 in the range between 0 and 100 μm and l_2 between 0 and 10 mm. It was found that mean TR-energy lossis a better radiator characterization parameter compared to the average number of produced TR-photons for single material combinations as shown in figure 6.8. The maximum number of produced photons per particle is reached at smaller values of l_1 compared to the largest energy deposit due to TR-photons per particle. In addition, the average total deposited energy per particle has to be taken into account for the comparison of different radiator materials. The optimal parameters l_1 and l_2 for a 200 foil radiator and 2 GeV/c electrons for all materials listed in table 6.1 can be found in appendix D.

6.2.1. Effect of Number of Foils on the Optimized Foil and Gap Thickness

Since the method described up to now considers only the effect of one single parameter variation or up to two parallel parameter variations out of three free parameters, there might also be a correlation between all three parameters. Since the parallel variation of three parameters would lead to the need of a 4-dim representation, only 3-dim projections for one constant parameter can be used to investigate on those correlations. The average energy-loss via TR-photon production and absorption as function of increasing number of foils, foil thickness (figure 6.9) and gap thickness (figure 6.10) are chosen. Only small

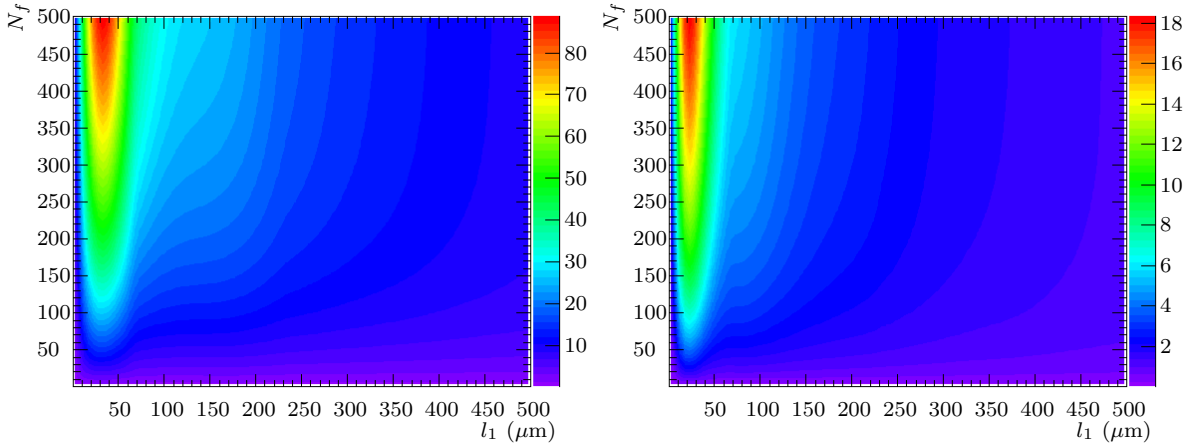

Fig. 6.9: Average energy loss via TR $\langle E_{TR} \rangle$ per electron (left) and average energy loss via TR $\langle E_{TR} \rangle$ of photons deposited within the 2011 detector per electron (right) calculated for variable number of Polyethylene foils of variable foil thickness l_1 at optimal gap thickness of $l_2^{opt.} = 700\,\mu$m for 2.0 GeV/c electrons.

effects on the optimal foil thickness $l_1^{opt.}$ at optimal gap thickness $l_2^{opt.} = 700\,\mu$m of a few percent due to a variation of the foil number can be seen. The effect on the optimal gap thickness $l_2^{opt.}$ at optimal foil thickness of $l_1^{opt.} = 23\,\mu$m is also of the order of several percent. The average TR-energy loss is more or less constant in the range of $650\,\mu\text{m} < l_2 < 1000\,\mu\text{m}$ and there is no clear correlation of the optimal gap thickness to the number of foils. A large drop of the average energy loss via TR-photon emission for a constant number of foils can be observed only at very small gap thicknesses below 650 μm. This indicates that the optimal parameter set for a regular radiator has to be evaluated iteratively. Since the total effect is in the range of a few percent and the accuracy of the effective radiator description is given with 15%, this was not followed up in detail.

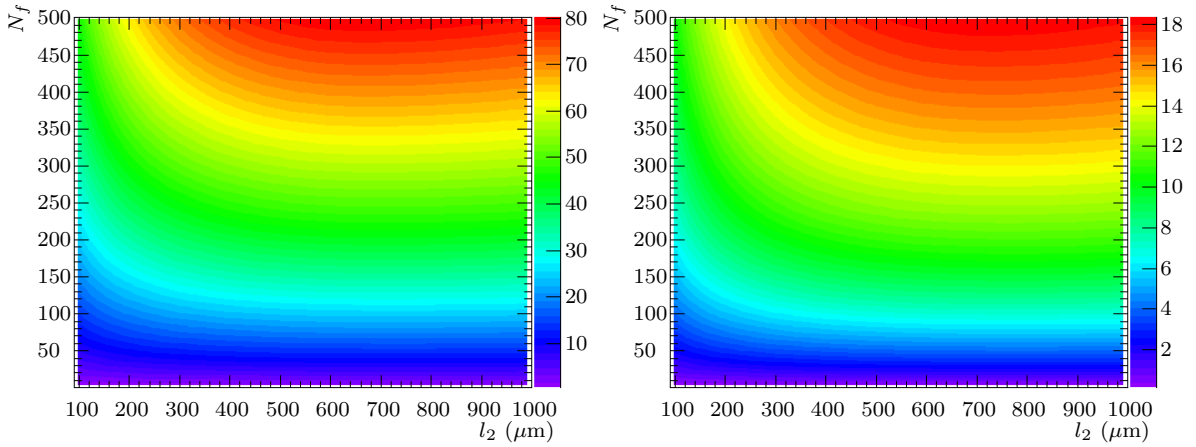

Fig. 6.10: Average energy loss via TR $\langle E_{TR} \rangle$ per electron (left) and average energy loss via TR $\langle E_{TR} \rangle$ of photons deposited within the 2011 detector per electron (right) calculated for variable number of Polyethylene foils of variable gap thickness l_2 at optimal foil thickness of $l_1^{opt.} = 23\,\mu$m for 2.0 GeV/c electrons.

6.3. First Generation Prototypes

From the previous approximation, it can be seen that the most promising foil candidates for first regular radiator prototypes are Polyethylene (15 μm), Polypropylene (25 μm) and POKALON N470 (24 μm). All should have a performance of > 1 TR-photon per electron for 250 foils. The gap thickness will be adjusted by using low density PE and PP foam foils (perforated and unperforated) and 700 μm thick aluminum frames. First irregular radiator prototypes have been built from different PE foam foils and PP fiber mats (LRP 375 BK Freudenberg). For the next generation prototypes, it might be possible to use foils with optimized l_1. For these prototypes it will be shown that the total material budget of the radiator can be drastically decreased, if no mechanical support frame is used. This can be realized by using a self-supporting and nearly frame-less structure inspired by paper-back books (option A). Two of four sides will be stabilized by an epoxy binding. The frame can be left out, since there is no mechanical tension needed, to adjust the foil positions. A sandwich structure undertakes the task of the frame. The foil position is fixed by the adhesive force between foil and spacer. Another option (option B) is to use micro structured foils, which are self-supporting. Such a micro-structure has to provide mechanical stability to adjust regular foil spacing. This property is directly connected to the mechanical stability of a single foil which is correlated to the oxygen content (hydrogen bond between a hydrogen atom and an electronegative atom) and molecular binding structure of the material. The best ratio of mechanical stability to low material density is obtained for POKALON N470 which has good thermoforming characteristics.

6.3.1. Regular Foil Radiators

The new regular radiator prototypes built in Münster (B, [Bshort, B++,] C and D shown in figure 6.11) and Frankfurt (FFM) have been designed according to the $\langle E_{TR} \rangle$ optimization procedure. The existing ones (E and F shown in figure 6.11) are used to verify the theoretical prediction. To keep the prototype costs low, I use bulk commodity, which is available only in certain foil thicknesses. The gap thickness and number of foils can be optimized for a given foil thickness in the same way as described. The spacer thick-

nesses are rounded to common commercial aluminum sheet thicknesses. The resulting parameter sets presented in table 6.2 are marked in figure 6.13.

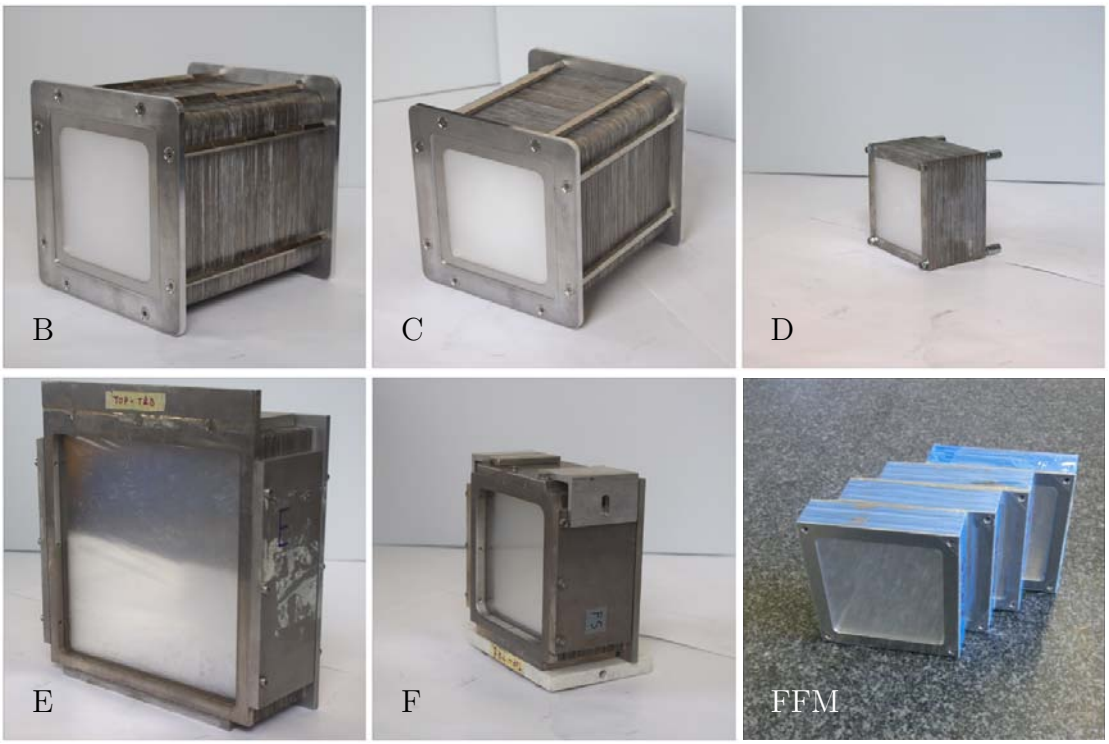

Fig. 6.11: The five regular radiator prototypes from Münster (B-F) and five prototype modules produced by our colleges in Frankfurt (FFM0.5, FFM0.7 andFFM1.2) are presented. B, C and D have been built between 2010 and 2012, were E and F have been built before 2010. The characteristic parameters can be found in table 6.2. A detailed description of the FFM prototypes and measurements is given by A. Arend [Are13].

Tab. 6.2: Regular foil radiator prototypes from Münster (MS) and Frankfurt (FFM).

	Name	Material	l_1 (μm)	l_2 (μm)	N_f
MS	Bshort	POKALON N470	24	700	100
	B	POKALON N470	24	700	250
	B++	POKALON N470	24	700	350
	C	Polypropylene	15	700	200
	D	Polypropylene	15	700	100
	E	Polyethylene	20	500	120
	F	Polyethylene	20	250	220
FFM	FFM0.5×100	Polyethylene	20	500	100
	FFM0.5×200	Polyethylene	20	500	200
	FFM0.5×350	Polyethylene	20	500	350
	FFM0.7×100	Polyethylene	20	700	100
	FFM0.7×200	Polyethylene	20	700	200
	FFM0.7×350	Polyethylene	20	700	350
	FFM1.2×100	Polyethylene	20	1200	100
	FFM1.2×200	Polyethylene	20	1200	200
	FFM1.2×350	Polyethylene	20	1200	350

The corresponding emission and absorption TR-spectra at a particle momentum of 2.0 GeV/c are presented in figure 6.12. It is obvious, that the radiator with the highest

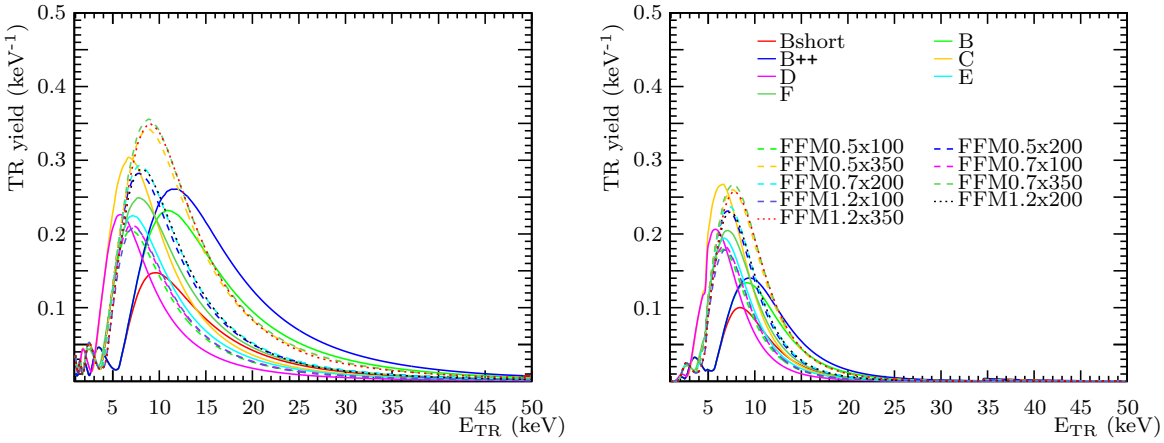

Fig. 6.12: TR-photon emission (left) and absorption spectra (right) for electrons at 2.0 GeV/c based on the chamber material budget of 2012. Input parameters are listed in table 6.2.

emission yield does not lead to the highest absorption yield, if the emission spectrum does not match the chamber absorption probability distribution. The performance of different radiator parameter sets of foil thickness and gap diameter are more obvious, if presented for the same number of interfaces. Therefore, all values are calculated for a constant number of foils $N_f = 200$ at 2.0 GeV/c to have better comparability. The TR-absorption was calculated based on the chamber material budget of 2012. The parameter sets realized in Münster prototypes (MS) are marked by a $'+'$, where the Frankfurt prototype (FFM) parameters are represented by a $'\times'$ in the following figures. The optimal l_1 and l_2 combinations are represented by open symbols. The parameter set for the highest average number of absorbed photons within the gas volume is marked by an open square. The parameter set for the highest average energy deposit by TR-photons within the gas volume are marked by an open triangle. The highest average energy deposit (dE/dx + TR) within the gas volume are marked by an open cross. Mean electron energy loss including TR and approximated pion efficiency for 10 detector hits are presented in figure 6.13. Comparing the presented average number of absorbed TR-photons and the corresponding mean deposited TR-energy per electron for a polyethylene radiator, one finds very similar distributions, as already presented in chapter 6.2. The maximum is slightly shifted towards larger foil thickness. The optimal foil spacing does not change in case of Polyethylene foil. The maximum itself is triangular shaped with a small extension towards increasing gap diameters at foil thicknesses around 20 μm. The mean total energy loss of electrons within the active gas volume as presented in figure 6.13 exhibits the same structure around the optimal parameters. These parameters are very close to the parameter set found for the maximum average energy deposit due to TR-photons per electron, as expected. The estimated pion efficiency approximated for 10 detector hits (based on one million simulated electrons and pions per parameter set) has a broad minimum, with a topology comparable to the distribution of total energy loss per electron. The best commercial available material thicknesses close to the simulated optimal parameter for polyethylene foil is 15 or 20 μm. The parameters which have been used to build radiator prototypes in our lab at Münster and by our colleagues at Frankfurt are highlighted. These parameters are all within the area of highest pion rejection. It can clearly be seen that the pion efficiency is dominated by statistical fluctuations at a more

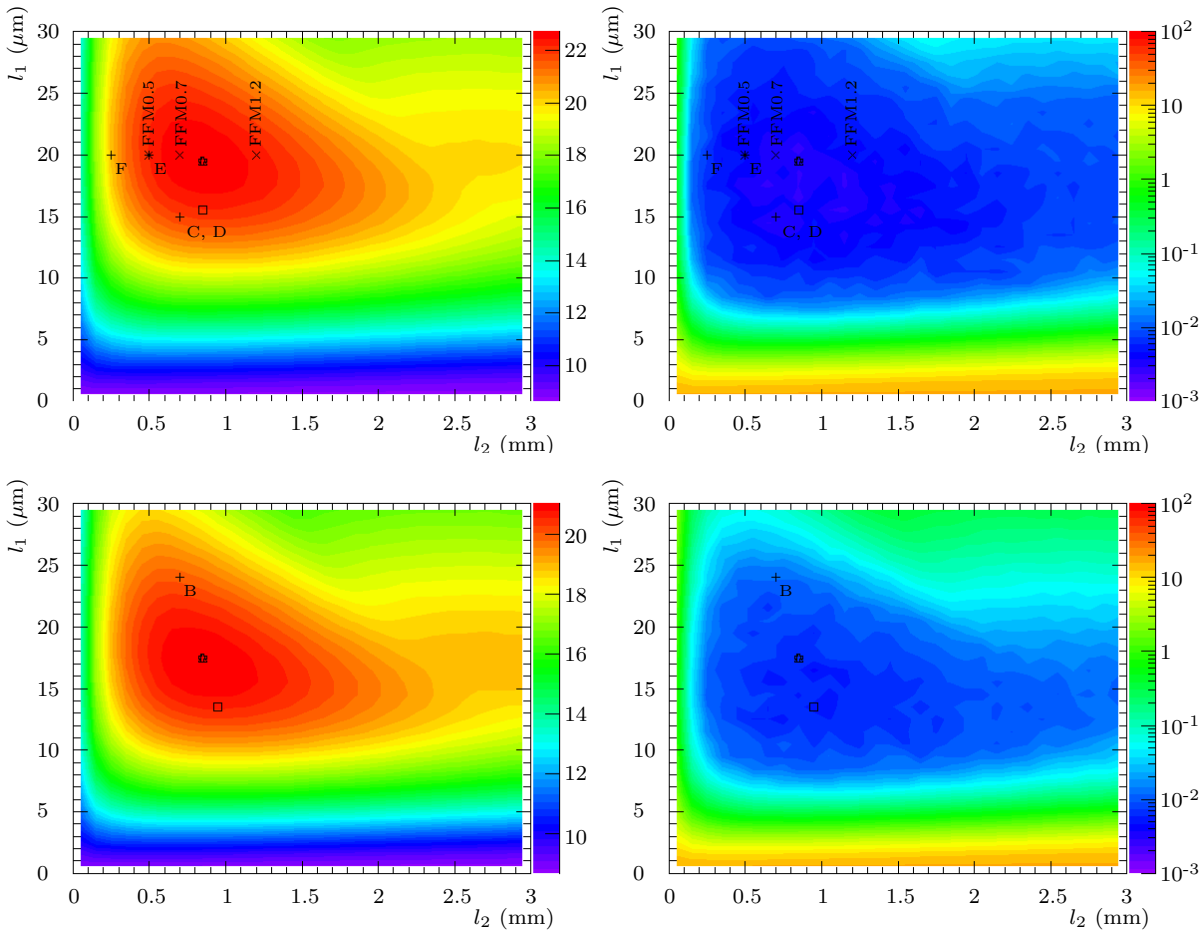

Fig. 6.13: Simulated TR-yield for Polyethylene (upper row) and POKALON N470 (lower row) radiators are presented. The values are calculated for $N_f = 200$ at 2.0 GeV/c based on the chamber material budget of 2012. Mean electron energy loss including TR on the left and approximated pion efficiency for 10 detector hits on the right side are presented. The highest average energy deposit (dE/dx + TR) within the gas volume is marked by an open cross. The highest average energy deposit by TR-photons within the gas volume are marked by an open triangle (overlapped by the open cross). The highest average number of absorbed photons within the gas volume is marked by an open square. The parameter sets realized in Münster prototypes (MS) are marked by a +, where the Frankfurt prototype (FFM) parameters are represented by a × (see table 6.2).

or less constant level of pion rejection performance for all prototypes, where one finds large differences in the mean signal per electron distribution. Therefore the mean energy loss per electron seems to be the clearer radiator criterion. The TR-yield of a POKALON N470 radiator with 200 interfaces is lower compared to a polyethylene radiator with the same parameters due to the presence of oxygen in the material. This leads to an increase in the photon absorption cross section of the radiator. The over all spectrum shape is similar to the polyethylene one. The highest number of produced and absorbed photons is shifted towards lower foil thickness and larger gap thickness. Going from the average number of produced photons to the mean energy of these photons the maximum of the distribution moves towards larger foil thickness and smaller foil distance. The optimal parameter sets for pure TR-energy loss and total energy loss are expectedly identical. Since the smallest bulk produced POKALON foil thickness is 24 μm the foil thickness of the radiator prototypes (B and K) are far away from the optimum. But the foil spacing matches rather well the optimum for the given foil thickness (compare to figure 6.13).

The TR-yield difference between the optimum and the simulated yield based on the realized radiator parameters is of the order of 10% for Polyethylene based radiators and 5% in case of POKALON.

6.3.2. Self-Supporting PE Foam Foil Spacer Mixed Radiator

To overcome the drawback of classical regular foil radiators, several options have been investigated. The first one is replacing the massive frame structure by a sandwich of POKALON N470 foils and a lightweight spacer material, which produces TR-photons itself in the best case. Such active spacer material can be e.g. plastic foam foils or plastic fiber sheets. The first prototype (presented in figure 6.14) is a sandwich radiator made from polyethylene foam foils and POKALON N470 foils of 24 μm thickness as summarized in table 6.3. One half of the spacer has been perforated (66 holes) in order

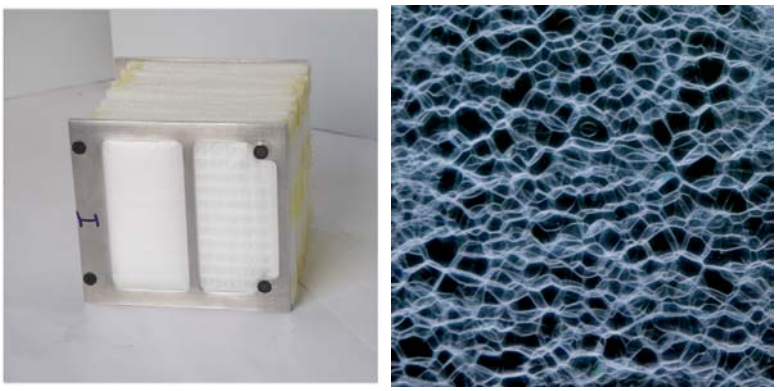

Fig. 6.14: Radiator I consists of two sections; unperforated (u) on the left half of the radiator and perforated (p) on the right half of the radiator are shown in the left figure. A $10 \times 10\,\mathrm{mm}^2$ foam foil, 700 μm thickness and $0.091\,\mathrm{g/cm}^3$ density is presented in the right figure.

Tab. 6.3: Components and parameters of self-supporting foam foil spacer mixed radiator prototype.

Name	Material	ρ ($\mathrm{g/cm}^3$)	$\langle l_1 \rangle$ (μm)	$\langle l_2 \rangle$ (μm)	$N_m \times \langle N_f \rangle / N_m = \langle N_f \rangle$
I(p,u)	POKALON N470	1.15	24	613	$5 \times 55 = 275$
	PE foam	0.026	12	550	$275 \times 1.1 = 311$

to study the influence of the foam to the total TR-yield (see figure 6.15). The perforation diameter of 10 mm was chosen to leave as less foam by giving the foil as much mechanical stability as possible. The used PE foam foil has a thickness of $\sim$700 μm and a density of $0.091\,\mathrm{g/cm}^3$ with an average bubble diameter of 550 μm. The radiator prototype consists of five separate sections. Each section was built from a stack of 55 PE foam foil layers (see figure 6.16c). The projectivity perforation has been drilled using the hole template shown in figure 6.15. The spacer layers within a single stack are mechanically connected by three glue bands of a fast hardening, two component epoxy glue applied to one side of the stack (see figure 6.16b). The spacer foil positions are adjusted by four screws, to keep the perforated side projective during the gluing procedure. Then, POKALON N470 foil layers of $13.5 \times 13.5\,\mathrm{cm}^2$ are inserted. Two pieces of $1 \times 1\,\mathrm{cm}^2$ are cut out, in order to use the first and last hole of the spacer as fitting hole. The same gluing frame is used for the three glue bands on second side of the spacer to fix the position of the foil between the foam spacers. The five sectors are threaded on two plastic sticks through

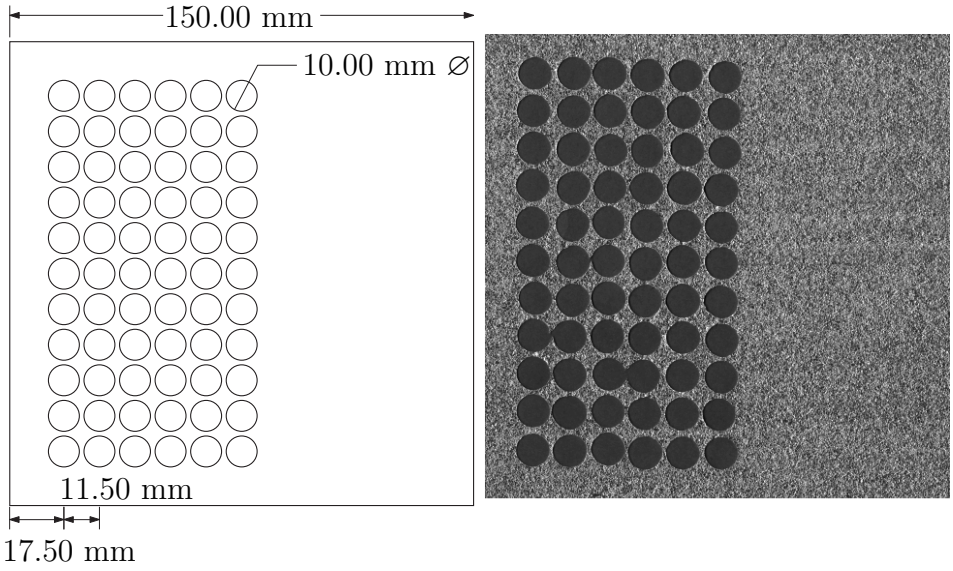

Fig. 6.15: A schematic on the left and one perforated foam foil on the right side. The left half of the foam foil is regular perforated with 38.6% left over PE foam material [Hei13].

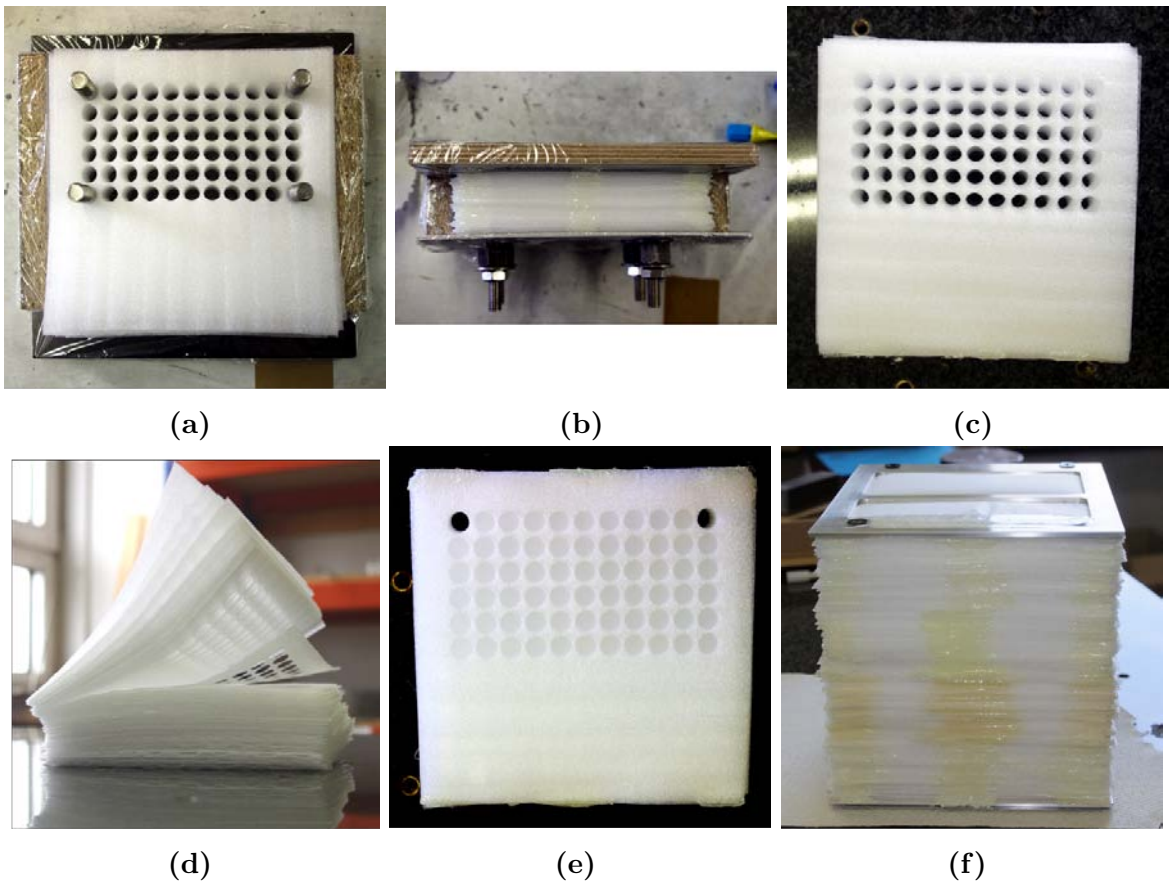

Fig. 6.16: Production steps: 55 perforated foam foils are mounted to the gluing frame (a). The total spacer thickness is adjusted by four screws to a 3.4 cm. The spacer layers are connected at one side by three glue bands of a fast hardening two component epoxy glue (b). The projectivity and movability of the spacers are tested (c and d). Afterwards, POKALON N470 foil layers of 13.5 cm×13.5 cm are inserted between each two spacer layers. One radiator stack is shown in figure (e). The final radiator, including stack support, structure is shown in figure (f).

the fitting hole connecting two aluminum frames. These frames are used to assure the total thickness of the radiator and keeping the perforation of the individual stacks as projective as possible. With an optimum spacer thickness of 613 μm and a POKALON N470 foil thickness of 24 μm, each stack has a total height of 35 mm within the stack support structure. The scaling from the prototype dimensions to the final detector size will be challenging. The projective of the perforation can be realized with fitting holes like it is done in the prototype. But the larger material weight will demand for larger and stiffer frames which will increase the material budget. It has also to be investigated if the performance can be enhanced by an hole projectivity with respect to the average particle track direction. This would result in an individual radiator for each module. This effort can only be justified by a large gain in performance which will be quantified by the comparison between the pion efficiency difference of the perforated and unperforated half prototype.

6.3.3. Self-Supporting Micro-Structured Foil Radiator

The second approach is to replace the external mechanical support frames by adding mechanical stability to the foil itself. This can be realized by adding a micro-structure to the foil like it is done in case of corrugated cardboard. The burling structure which was chosen for radiator prototype K (figure 6.17, radiator parameters are listed in table 6.4) is presented in figure 6.18. The structure was designed to be staggered by half a

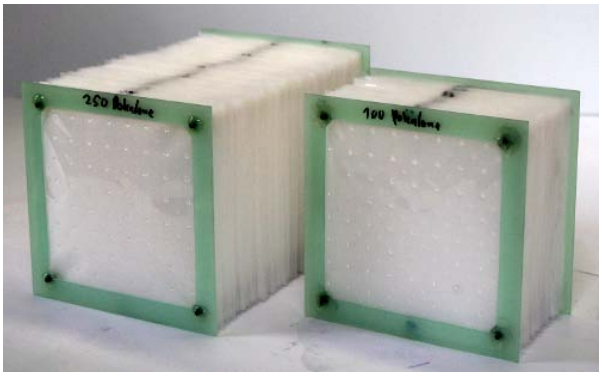

Fig. 6.17: Self-Supporting Micro-Structured Foil Radiator K is presented on the left and Kshort on the right side. The combination of both prototypes is called K++.

Tab. 6.4: Sel-supporting micro-structured foil radiator prototypes from Münster.

Name	Material	l_1 (μm)	l_2 (μm)	N_f
Kshort	POKALON N470	24	700	100
K	POKALON N470	24	700	250
K++	POKALON N470	24	700	350

burling distance after a foil rotation of 180° as indicated in the blue print. The four holes in the corners are used to keep the foils in position. POKALON N470 foil was chosen for two reasons, first it gives possibility to compare an identical, classical prototype (B) for different number of foil layers with the micro-structured prototype (K) and with the first self-supporting radiator prototype I. On the other hand, POKALON has higher mechanical stability compared to polyethylene or polypropylene foil with the same thickness and better thermal deep-drawing properties. The foil production as illustrated

in figure 6.19 is laborious and up to now not scalable to bulk production, since the burling deep-drawing has to be done burling by burling. The pre-cut foil is first put on top of the

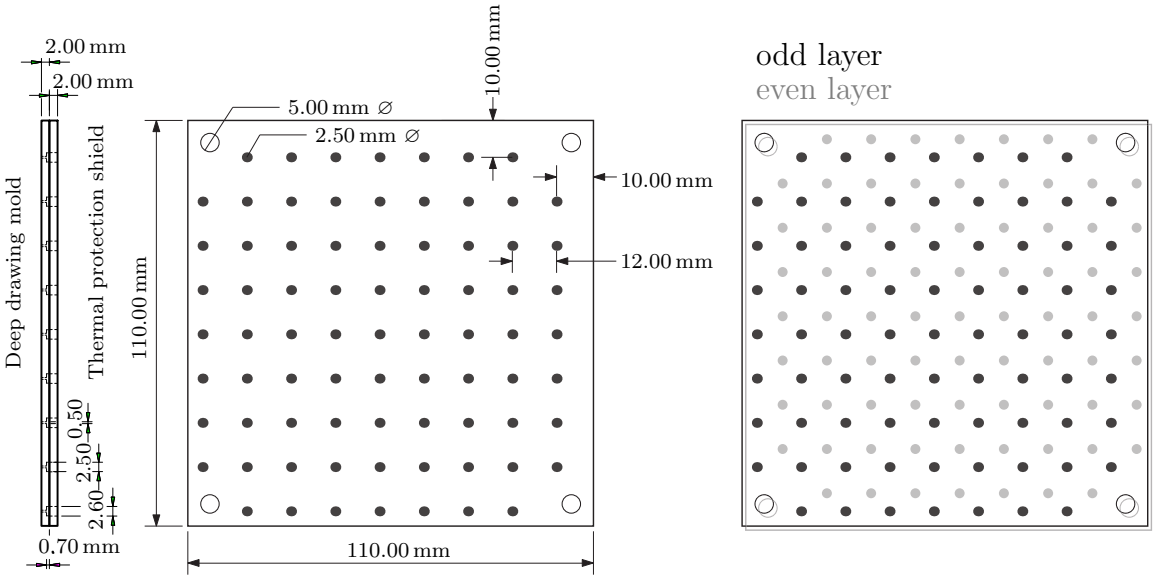

Fig. 6.18: Blue print of the deep-drawing mold on the left and schematic overlay of two micro structured foils on the right side [Hei13]. The odd foils are rotated by 180° to ensure a burling position shift of half period between even and odd foil layers.

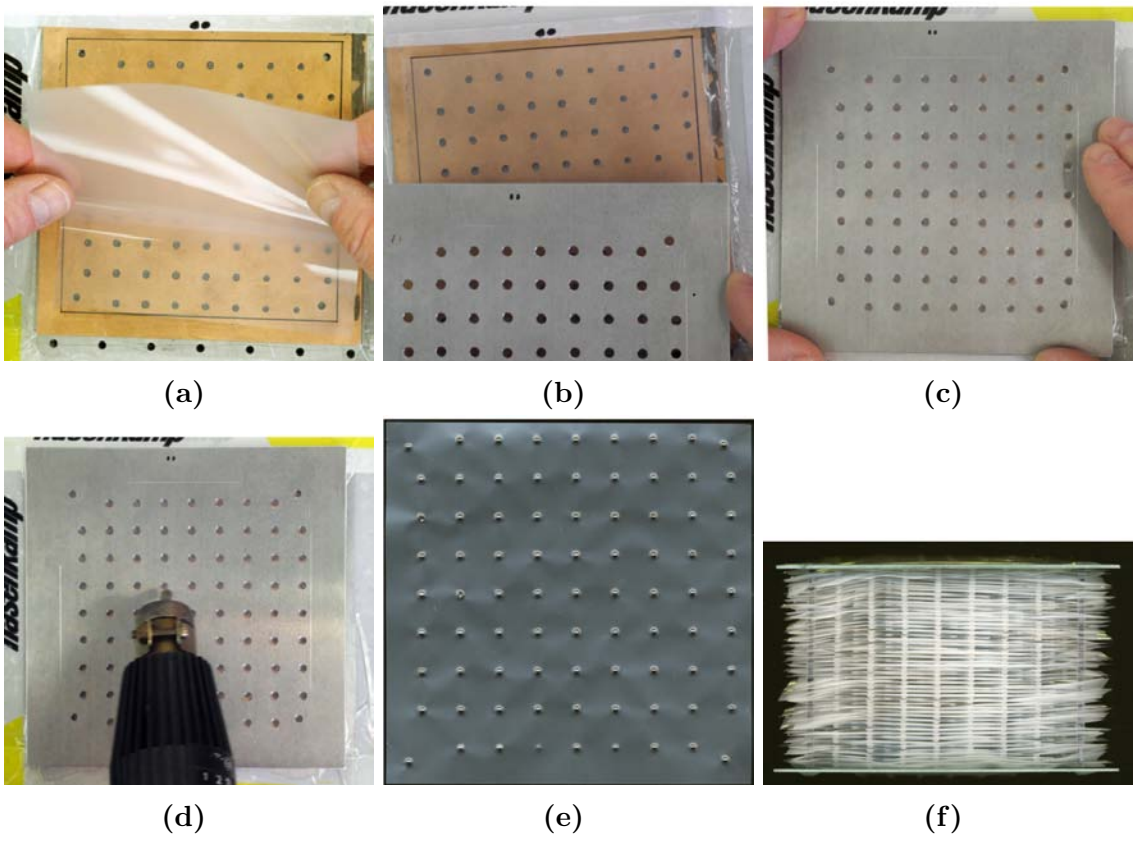

Fig. 6.19: The foil is first put on top of the deep-drawing mold connected to a vacuum pump (a). The foil is covered in the thermal protection shield (b) and (c). The uncovered foil is heated up using a hot air gun collimated to a diameter of 5 mm burling by burling (d). The last two sub-figures are showing one foil after the described procedure (e) and the side view on the 100 foil stack radiator (f).

deep-drawing mold connected to a vacuum pump. The molds are 700 μm deep in order to achieve a burling height of the same size. The foil is covered by the thermal protection shield made from 2 mm aluminum. The uncovered foil is heated up burling by burling using a hot air gun collimated to a diameter of 5 mm. The individual foils are threaded on four carbon fiber beams, which are glued to a green FR4 support frame (compare to figure 6.17). The complete stack is closed by a second green FR4 support frame. The side view on the 100 foil stack radiator is presented in figure 6.19f. It illustrates the adequate regularity of the foils, which is reached by adding burlings of 2.5 mm diameter to 3.12% of a single foil surface. A burling area occupancy of 6.24% is reached after assembly due to the rotation of the odd layers. In principle, the presented procedure can be scaled to any size. In order to reduce costs and workload one has to automate the production process. There are two options, to build up a special deep-drawing device or use a commercial embossing production line.

6.3.3.1. Commercial Embossing Tests

Instead of thermal deep-drawing embossing can be used to structure the plastic foils. A first test with commercial embossing in cooperation with Bischof + Klein GmbH & Co. KG to micro-structure polypropylene foil of 24 μm thickness was performed. The embossing machine is shown in figure 6.20. Two foil probes of $12 \times 12\,\mathrm{cm}^2$ are shown in figure 6.21. First results using POKALON are promising in terms of mechanical

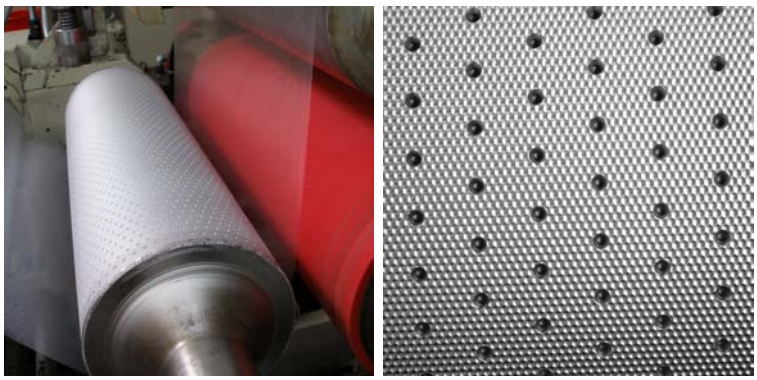

Fig. 6.20: Commercial embossing test with a negative embossing roller and a felt roller. The embossing machine is presented in the left figure. The negative embossing roller presented on the right side has a double micro-structure. The pre-heated (50% of 200 W radiant heater) polypropylene foil is squeezed between the embossing roller and the felt roller (70 shore) with an adjustable force of (110 bar) which gives the possibility to create different structure height. The foil is transported with 1 m/min from the right to the left.

stability and structure depth but there are still mechanical problems to adjust a stable structure height of 700 μm. A dynamic structure height between several μm can be adjusted for negative embossing by a variation of the pressure between both rollers and the stiffness of the felt on the second roller. The speed of the assembly line is optimal at 1 m/min. The structure height decreases at higher production speed as well as increasing preheating. A heat power of 100 W at foil transport speed of 1 m/min results in the best structures. Systematic tests are still ongoing. The double structure leading to an increased mechanical stability was chosen as shown in figure 6.21. The effect of the double micro-structure has to be investigated during a mixed electron-pion beam test. A positive embossing has not been tested up to now but would also be an alternative. The polypropylene foil at 20 μm could not overcome a structure depth of 300 μm in first result where the POKALON reached the design goal already in the first

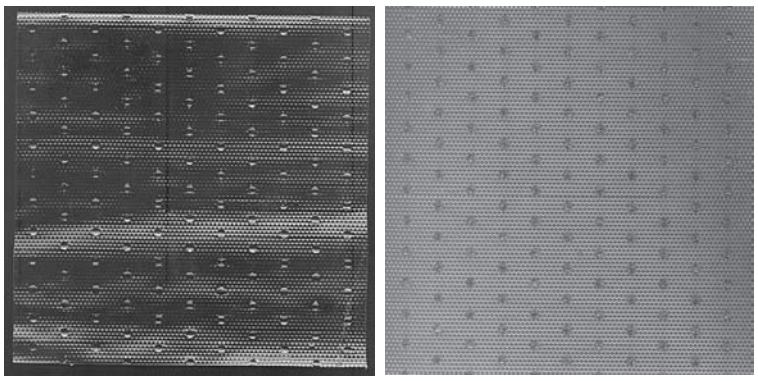

Fig. 6.21: A polypropylene foil probe of $12 \times 12\,\mathrm{cm}^2$ with a double structure is shown on the left. A POKALON foil probe $20\,\mu$m with an equivalent size is presented on the right . The last sample has a more detailed micro-structure and higher macro-structure with a better mechanical stability.

tests. The structure height varies between 520 and 820 μm [HR13]. The procedure has to be improved to decrease the variance of the structure height. The effect on the radiator performance arising from heating up the complete foil has also to be tested in beam to evaluate this production procedure.

6.3.4. Irregular Radiators

Irregular radiators are the option of choice for large surface TRDs like ALICE TRD or ATLAS TRT. The benefit of irregular radiator materials is they are available as foams or fibers with different material properties like density and stiffness and they are easy to build. They can be used as mono-material or in mixtures. The drawback is the TR-production model, there are different models and theoretical descriptions which match measurements more or less accurate as described in chapter 4.1.2. The different irregular radiator prototypes built from pure foam, fibers (microscope pictures are presented in figure 6.22) and mixtures of both, which have been tested since 2010, are shown in figure 6.23. Prototype an is ALICE'like built from two 8.0 mm Rohacell HF71 sheets sandwiching eight 4.0 mm thick LRP 375 BK polypropylene fiber layers. The front side is covered by a carbon fiber layer which is glued to a Mylar foil on the outer surface. The G10, G20 and G30 radiator are made from the pure LRP 375 BK polypropylene fiber layers which are bundled into groups of 10, 20 and 30 layers using commercially sellotape, as can be seen in the illustration. Packaging polyethylene foam foil with an average thickness of 2.0 mm has been piled up in a cardboard box in case of prototype H (125 layers) and H++ (177 layers). J is made from dust filter polyethylene or polypropylene fibers (exact type not known). Polyethylene foam foil (Cell-air) has been stacked in cardboard boxes for L (5.0 mm thickness) and M (1.0 mm thickness). N25 consists of 25×10.0 mm PE foam blocks which are used to build electronic packaging. In case of O5x5 five PE foam blocks are thermally glued to a block. Five of these blocks are put together to reach the same radiator thickness of 5×50.0 mm PE foam as N25. 30 mm Rohacell HF110 and 30 mm WF110 have been tested as well as 50 mm EF700 PE foam, which is used for thermal insulation of buildings. The material properties are listed in more details in table 6.5. Comparing the different materials in table 6.5 it can be seen that Rohacell HF110 and HF71 (as well as the LRP 375 BK) have an average bubble diameter which is a factor of 10 smaller compared to other materials, where the largest difference between the solid structure sizes is only a factor of around 4. Since the

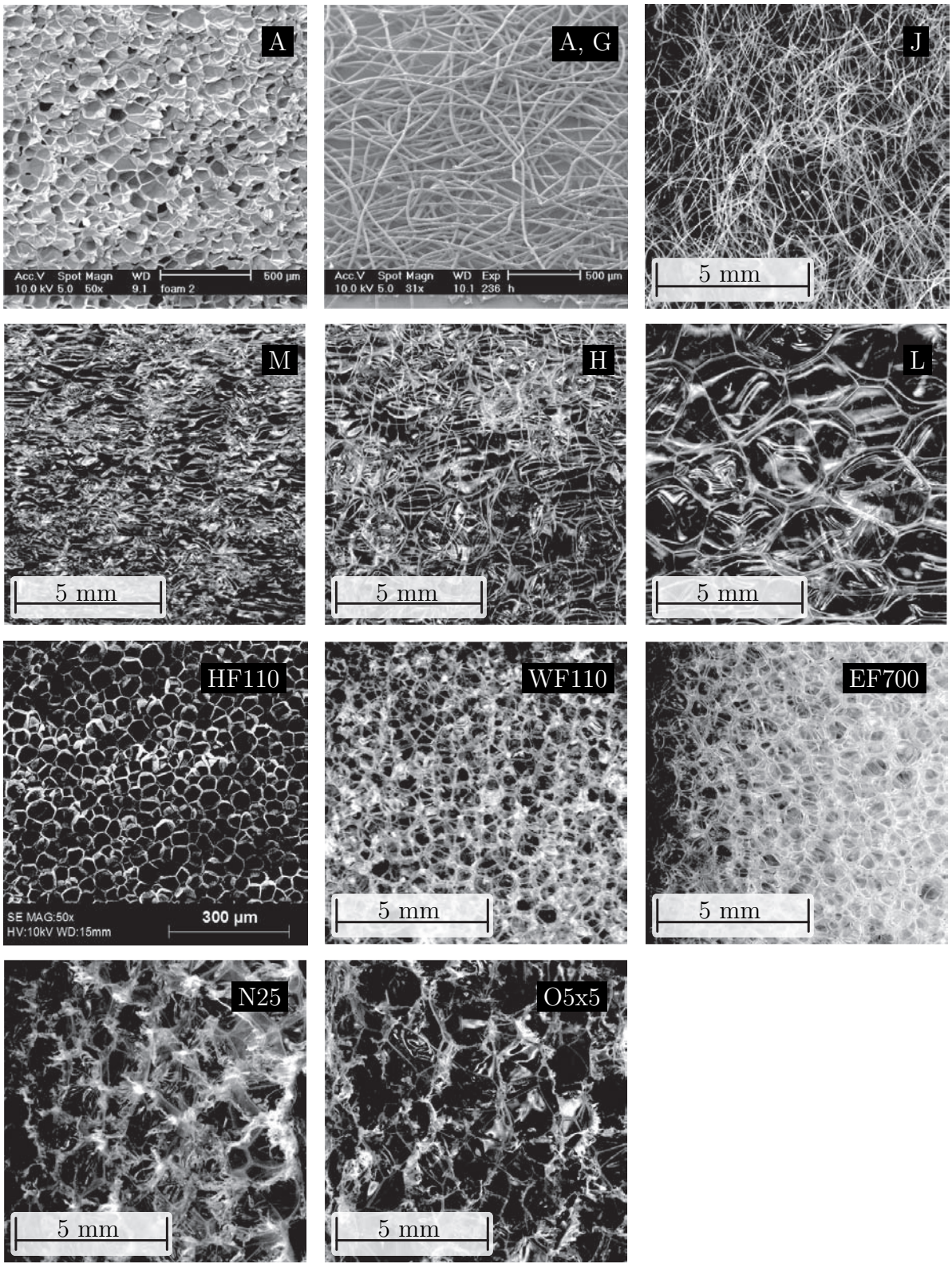

Fig. 6.22: Irregular material close-ups are presented. One Rohacell HF71 (A) and PP fiber LRP 375 BK (A, G) electron microscope scanning [ALI03], J, $10 \times 10\,\mathrm{mm}^2$ CellAir foam foil layer with 1.0 mm (M), 2.0 mm (H) and 5.0 mm (L). Prototype H is build of 177 layer Cell-Air whereas prototype L consists of 52 sheets of Cell-Air and prototype M is made up of 260 layer of Cell-Air, Rohacell WF110, Rohacell HF110 electron microscope scanning [Ent13], EF700, N25, and O5x5 (compare to table 6.5)

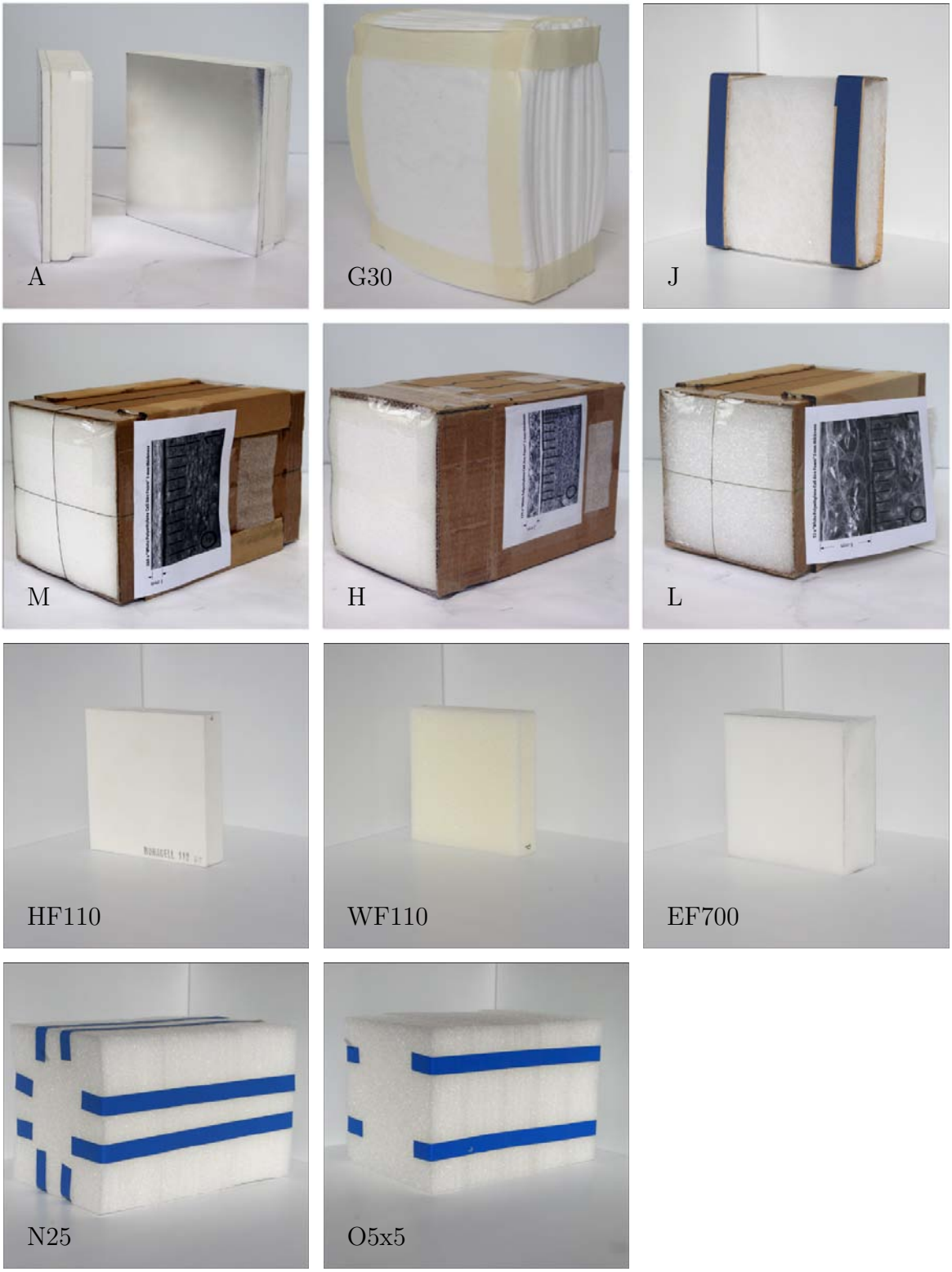

Fig. 6.23: Irregular radiator prototypes compilation is shown. A: 2×8 mm Rohacell HF71 and 8×4 mm PP LRP 375 BK fibers, G30: 30×4 mm PP LRP 375 BK fibers, J: 6×9.4 mm, M: 260×1.0 mm PE foam, H: 125 × 2.0 mm PE foam , PE fibers, L: 52 × 5.0 mm PE foam, HF110: 30 mm Rohacell HF110, WF110: 30 mm Rohacell WF110, EF700: 55 mm Rohacell, EF700, N25: 25 × 10.0 mm PE foam, and O5x5: 5 × 50.0 mm PE foam

Tab. 6.5: Irregular radiator prototypes: Material, measured density of the total radiator ρ, average solid structure size $\langle l_1 \rangle$, average gaseous gap size $\langle l_2 \rangle$ and average number of interfaces $\langle N_f \rangle$ are presented. $\langle N_f \rangle$ is given as number of material layers N_m times the average number of interfaces per material layer $\langle N_f \rangle / N_m$ and the resulting average total number of interfaces in case of composite radiators.

Name	Material	ρ (g/cm^3)	$\langle l_1 \rangle$ (μm)	$\langle l_2 \rangle$ (μm)	$N_m \times \langle N_f \rangle / N_m = \langle N_f \rangle$
A	PP fiber (LRP 375 BK)	0.064-0.074	17	50	$8 \times 59.7 = 478$
	Rohacell HF71	0.075	8	75	$2 \times 96.4 = 193$
G10	PP fiber	0.064-0.074	17	50	$10 \times 59.7 = 597$
G20	PP fiber	0.064-0.074	17	50	$20 \times 59.7 = 1194$
G30	PP fiber	0.064-0.074	17	50	$30 \times 59.7 = 1791$
I(p,u)	POKALON N470 (LRP 375 BK)	1.15	24	613	$5 \times 55 = 275$
	PE foam	0.026	12	550	$275 \times 1.1 = 311$
J	PE fibers	0.013	10	900	$6 \times 9.9 = 59$
H	PE foam (Cell-Air)	0.026	12	900	$125 \times 2.2 = 274$
H++	PE foam (Cell-Air)	0.026	12	900	$177 \times 2.2 = 388$
L	PE foam (Cell-Air)	0.015	24	2000	$52 \times 2.5 = 128$
M	PE foam (Cell-Air)	0.017	12	600	$260 \times 1.6 = 425$
N25	PE foam	0.027	15	1400	$25 \times 7.1 = 177$
O5x5	PE foam	0.022	15	1400	$5 \times 35.4 = 177$
WF110	Rohacell WF110	0.106	25	700	41
HF110	Rohacell HF110	0.122	8	45	333
3xEF700	PE foam	0.110	35	800	3×66

estimation of parameters like solid and gaseous structure sizes and their distribution is complex and often not homogeneous within the same material, the listed values are only rough approximations. On the other hand, the pure photon spectrum defies any attempts of direct measurement with a MWPC. Therefore it is even harder to test theoretical predictions on the photon spectrum. The emission and absorption spectra based on the material budget of the 2012 MWPC prototypes calculated for a regular toy model radiator are presented in figure 6.24, figure 6.25. The parameters listed in table 6.5 have been used to estimate these spectra based on equation 4.9. In most cases, the solid and gaseous structure sizes can only be influenced within a narrow region. It can be seen that for polyethylene and polypropylene (plasma frequency and density are equivalent and therefore only one histogram is shown for both) foam and fiber parameter sets are not optimal but within the orange or yellow region in the mean energy loss distribution. It is obvious that the plasma frequency and the density of polymethylmethacrylate (PMMA) are higher leading to a lower maximum mean energy loss of electrons compared to polyethylene and polypropylene. In parallel, the approximated maximum pion efficiency is one order of magnitude lower. Most commercial PMMA foams have quite sufficient solid structure dimensions but far too small bubble diameters, except Rohacell WF110.

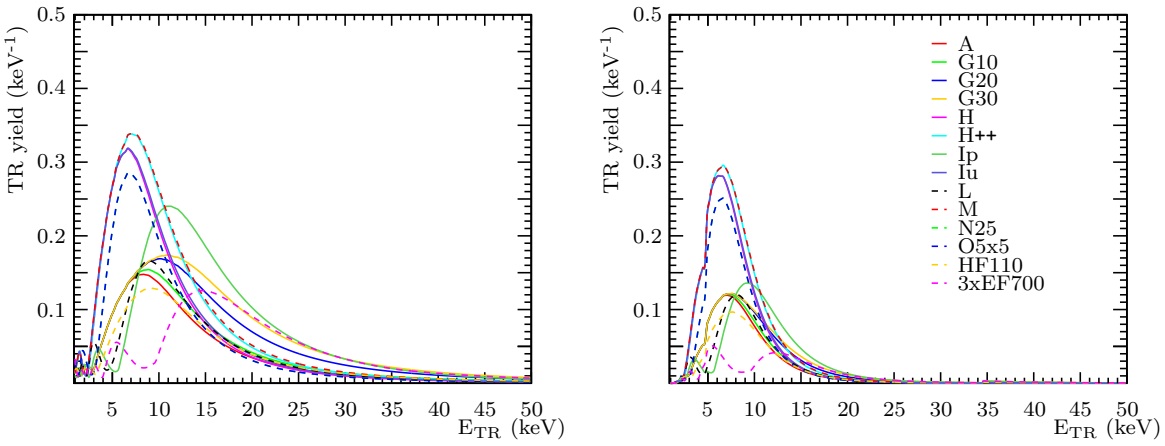

Fig. 6.24: TR-photon emission (left) and absorption spectra (right) for electrons at 2.0 GeV/c based on the chamber material budget of 2012. Input parameters are listed in table 6.5.

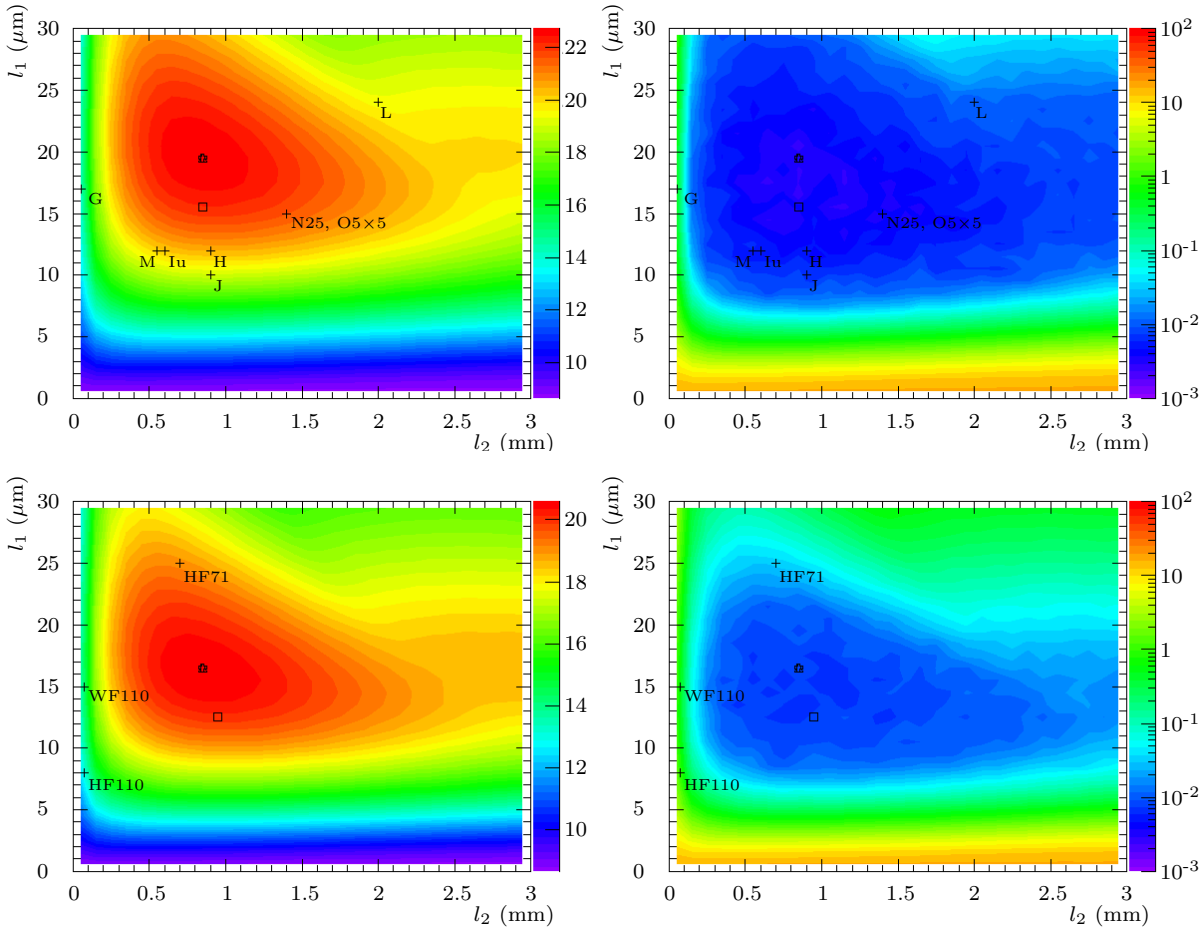

Fig. 6.25: The values are calculated for a polyethylene (upper row) and a PMMA (lower row) radiator with $\langle N_f \rangle = 200$ at 2.0 GeV/c based on the chamber material budget of 2012. Mean electron energy loss including TR on the left and approximated pion efficiency for 10 detector hits on the right side are presented. The parameter set of radiator prototypes are marked by the cross (see table 6.5), where parameter set for the highest total average energy deposit (dE/dx + TR) are marked by an open cross and for highest average energy deposit by TR-photons are marked by an open triangle (overlapped by the open cross). The parameter set for the highest average number of absorbed photons within the gas volume is marked by an open square. The parameter sets realized in Münster prototypes are marked by a +.

It is already on the high side of the solid structure diameter but has an average bubble diameter close to the optimum. Since most of the commercial available foam samples are more or less far away from optimal parameter sets, it would be of great advantage to evaluate the possible influence on the foam parameters due to variations of foam production process parameters. The benefit of irregular foam radiators is the high intrinsic mechanical stability. In combination with controllable bubble diameter and solid bubble film thickness a foam radiator would be a promising radiator option for the CBM TRD.

7. Read-Out Electronics Prototypes

The read-out electronic used by the TRD group from Münster is a combination of SPADIC (Self-triggered Pulse Amplification and Digitization asIC) v0.3 Rev3 & SUSIBO (SuS Interface BOard) in 2011 and 2012. In addition one SPADIC v1.0 & SP605 Xilinx FPGA-board have been tested in 2012 as well as in combination with a SUSIBO in dedicated lab tests (presented in figure 7.1). SPADIC is a development of the Chair of

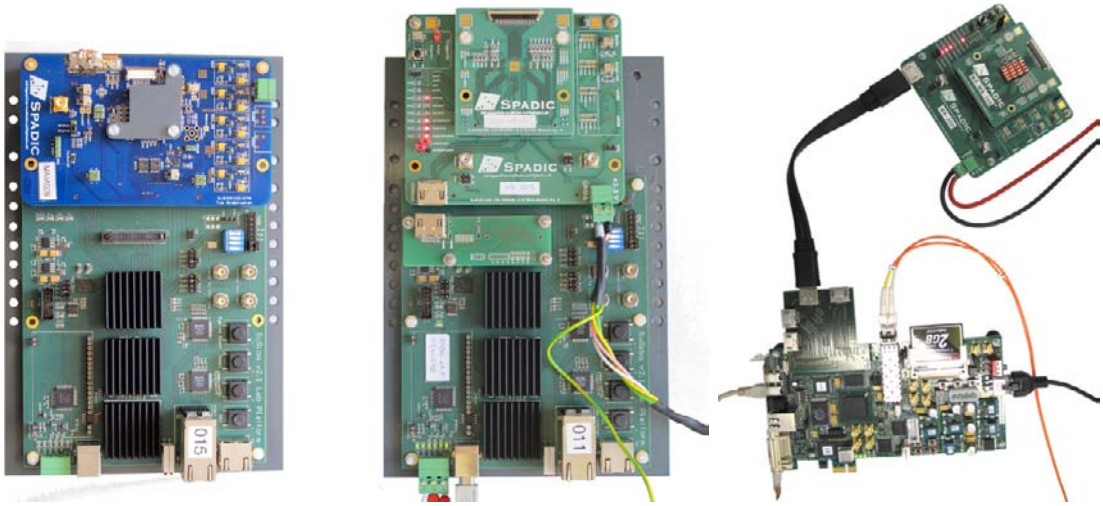

Fig. 7.1: SPADIC v0.3 Rev3 (blue) & SUSIBO (green) is presented on the left, SPADIC v1.0 (light green) & SUSIBO is shown in the center and SPADIC v1.0 & SP605 (dark green) can be found on the right side [Arm13].

Circuit Design (Heidelberg University) and is essentially the result of the PhD thesis of T. Armbruster [Arm13]. The project is continued by Michael Krieger. This ASIC is designed to read-out and process detector signals on a single chip and to implement the CBMnet protocol of the CBM DAQ system. The latest SPADIC version 1.0, which is the first functional prototype, is a 32-channel mixed-signal read-out chip dedicated for the read-out of the CBM TRD. The former version 0.3 supports only 8-channels. SPADIC v1.0 provides low-noise and low-power analog pre-amplification, 8 bit digitization, infinite impulse response signal processing, self-triggered hit detection, neighbor read-out, full pulse recording, meta data generation, synchronization mechanisms, digital filtering to suppress the ion tail, to separate double hits, and various other features. The peaking time is 86.7 ns at 100 ke^-. The chip has a dynamic range of 75 fC corresponding to 468.1 ke^- (40 fC in case of v0.3). The second order shaper has a shaping time of 80 ns, where the full Charge Sensitive Amplifier (CSA) has a shaper of first order (CR-RC). The nominal sampling frequency is 25 MHz with a maximum number of 32 (45 in case of v0.3) samples per event. The read-out speed of version 0.3 is limited by the USB connection of the SUSIBO. Since the version 1.0 was not in an operational mode it could not be used as standard read-out option in 2012 even though first SPADIC boards were available. A short specification summary of SPADIC v0.3 and v1.0 can be found in table 7.1.

The equivalent noise charge is correlated to the input capacity, as was simulated by T. Armbruster [Arm13] for the SPADIC v1.0 at room temperature. The resulting distribution is shown in figure 7.2. The figure includes the corresponding simulation results of the positive front-end with (blue) and without (green) external decoupling (roughly 100 nF for decoupling were in each case connected to all crucial bias nodes). This simulation

Tab. 7.1: SPADIC v0.3 and v1.0 specification summary from different sources [AFP09], [AK12], [Arm13], [AFP10], and different other publications, which can be found at `http://spadic.uni-hd.de/publications/`

Parameter	Design-Value	
	v0.3	v1.0
channels/chip	8	32
maximum input capacity		40 pF
maximum hit rate/channel	8 kHz	250-300 kHz
shaping time	82-90 ns	80 ns
peaking time	80 ns	86.7 ns
noise (@ 100 ke$^-$)	387+11 e$^-$/pF	not jet measured
assumed average charge/hit	120 ke$^-$ $\approx$ 19.2 fC	120 ke$^-$ $\approx$ 19.2 fC
dynamic range	40 fC	75 fC $\approx$ 468.1 ke$^-$
ADC resolution	8 bit	8 bit
input clock	25 MHz	250 MHz
internal clock domains	25 MHz	250, 125, and 25 MHz
order of shaper	2nd	2nd
order of complete CSA	1st (CR-RC)	1st (CR-RC)

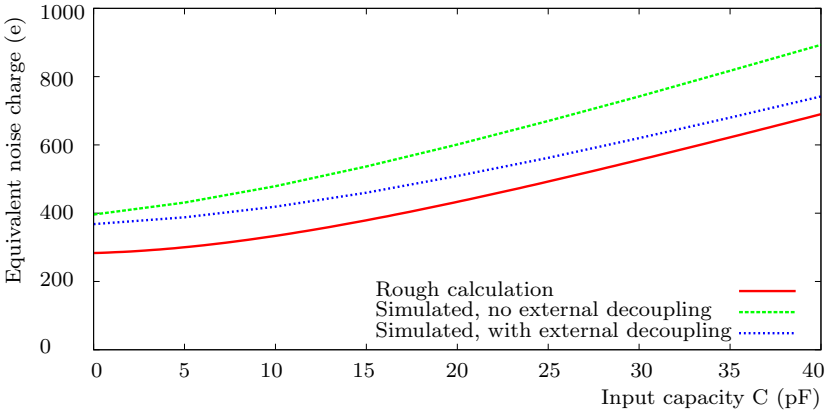

Fig. 7.2: Calculated and simulated equivalent noise charge of the positive frontend implemented in SPADIC v1.0 as a function of input capacity is presented [Arm13].

gives a first impression on the real noise level which includes many minor noise sources of the real implementation summing up to a significant contribution. Based on the simulation results it is obvious that the pad-plane layout has to guarantee a minimum input capacity and a low noise level. It was found that the pick-up noise of ASIC and MWPC prototypes (2010/11 as well as 2012) is highly sensitive to the grounding scheme. The best results have been achieved by gluing a copper tape across the carbon-fiber layer on the back-panel. The glue covering the back-panel was removed with sandpaper to enhance the electrical connectivity between copper tape and carbon-fiber in the back-panel. The copper tape is glued to the aluminum frame of the back-panel and the carbon-fiber layer of the back-panel. The grounding copper line is soldered to an additional copper tape which is soldered on the other side to the SPADIC v0.3 ground-pads as presented in figure 7.3. The floating ground of the HV-power channels are also connected to the common ground of the chamber body, using a cable between the HV-filter board ground bar and the aluminum frame of the back-panel. The ground potential of the pad-plane is connected to a global reference ground potential using a copper braid. The ground

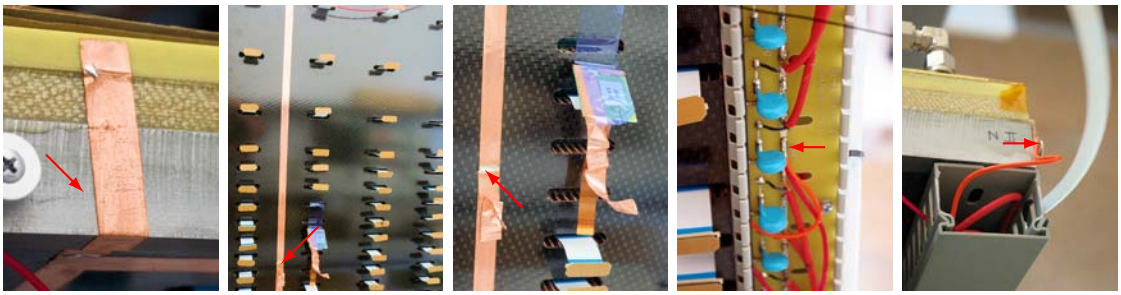

(a) (b) (c) (d) (e)

Fig. 7.3: ASIC grounding scheme on the prototypes in 2012 is shown. A copper tape is glued to the back-panel aluminum frame and to the carbon-fiber sheet covering the back-panel (figure a and b). A second copper tape is soldered to the ground line (figure c). The 8-channel Kapton signal cable is shielded single sided by a copper tape, which is glued on one side to the adapter board (connected to the 32-channel cable connected to the pad-plane) and on the other side soldered to the SPADIC ground-pads. The HV floating ground potential (ground bar on the HV-filter board) is connected to the aluminum back-panel frame by the orange cable (figure d and e).

potential of the LV-power lines to the SUSIBO and SPADIC have been interconnected to reduce potential fluctuations. It was also found, that an electrical connection between chamber and beam table and/or mounting structure has to be avoided to reduce the pick-up noise level. An additional ground potential is due to the USB connection between the DAQ-PC and the SUSIBO. The influence on the noise level has not been investigated in detail, but an optical read-out seems to be favorable anyway.

8. Beam Tests

All in beam tests after 2010 are done at CERN PS T9. The TRD group used a gas mixture of Xe/CO_2 (80/20). The objective of the CBM TRD beam times are a parallel development of all possible MWPC based TRD detector solutions in order to find not a single one, but the detector-radiator-ASIC combination best coping with the CBM environment. The TRD groups have not been able to test the different detector flavors under all relevant conditions up to now. Two systematic detector geometries (MWPCs with and without drift and with different entrance windows) as well as radiator tests (regular, irregular and mixed prototypes) have been carried out. The benefit of a common test beam campaign is the bundling of the individual subgroup efforts in terms of logistic, preparation of common components like DAQ, reference detectors, high/low-voltage and gas supply. On the other hand are limitations in available space, a relatively large amount of material budget in the beam and cave access times of the different groups which are unavoidable. In total the advantages far outweigh the disadvantages.

8.1. CERN PS T9 2011

The in beam test setup consists of RICH, TRD and TOF prototypes as well as three PID reference detectors and an external position reference detector. The PID reference is done based on two Cherenkov counters and one Pb-glass calorimeter. The external position reference was realized by a fiber hodoscope between the first Scintillator $Sc1$ and the RICH prototype. The beam is coming through the two Cherenkov counters (Ch1 and Ch2). The particles are passing through the first Scintillator (Sc) and the Fiber Hodoscope (FH). The first detector prototype in beam direction is the real dimension CO_2 filled RICH detector. Afterward are eight TRD prototypes from three research sites: two from Bucharest (Romania), four from Münster and two from Frankfurt. Behind the Münster prototypes and just in front of the Frankfurt detectors there is a finger scintillator (FSc). The last prototype detectors are two TOF RPC detectors from Bucharest followed by the second scintillator $Sc2$ and the Pb-glass calorimeter. The complete setup can be seen in figure 8.1. The full DAQ system schematic is presented in figure 8.2. Two Multi Branch System (MBS) [NK10] nodes (MBS1 and MBS2) as well as two Data Acquisition Backbone Core (DABC) [AMEKL09] PCs (master PC1 and slave PC2) and one Experimental Physics and Industrial Control System (EPICS) [DLH+93] monitoring PC (PC3) were used for event building and to store all relevant data from all subcomponents. PC1 collected read-out data from the SUSIBO/SPADICs on the Frankfurt prototypes 44, 55, 55, and 66 via USB, where PC2 read-out the data from the Münster MWPCs 336/10, 336/11, 444/10 and 444/11. The mapping between Münster prototypes and SUSIBO IDs are listed in table 8.1.

Tab. 8.1: Münster detector Ids 2011

Detector Id	Geometry/year	upper SUSIBO ID	lower SUSIBO ID
TRD1	336/10	001	002
TRD2	336/11	011	012
TRD3	444/10	003	006
TRD4	444/11	015	018

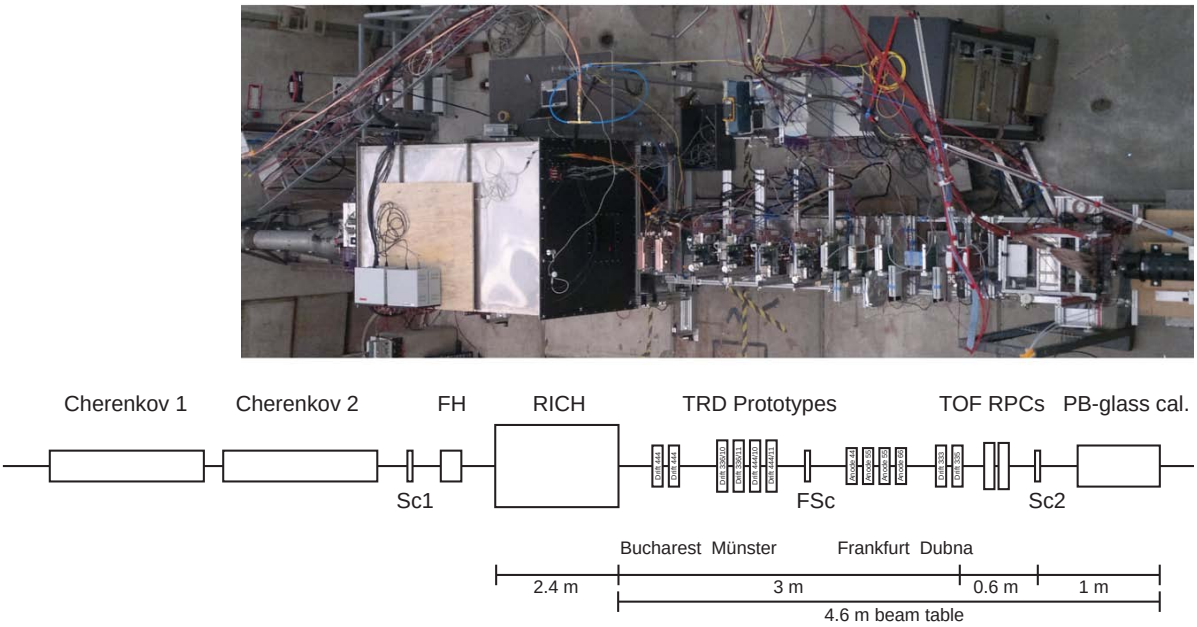

Fig. 8.1: Photo and schematic of the in beam test setup 2011 at CERN PS T9. The beam is coming from the left through the second Cherenkov counter, passing the first scintillator and the fiber hodoscope. The first detector prototype in beam direction is the real dimension RICH detector. Afterwards are two TRD prototypes from Bucharest and four detectors from Münster followed by the finger scintillator. The Frankfurt TRDs are just following the finger scintillator. The last prototypes are two TOF RPC detectors from Bucharest, followed by the second scintillator and the Pb-glass calorimeter.

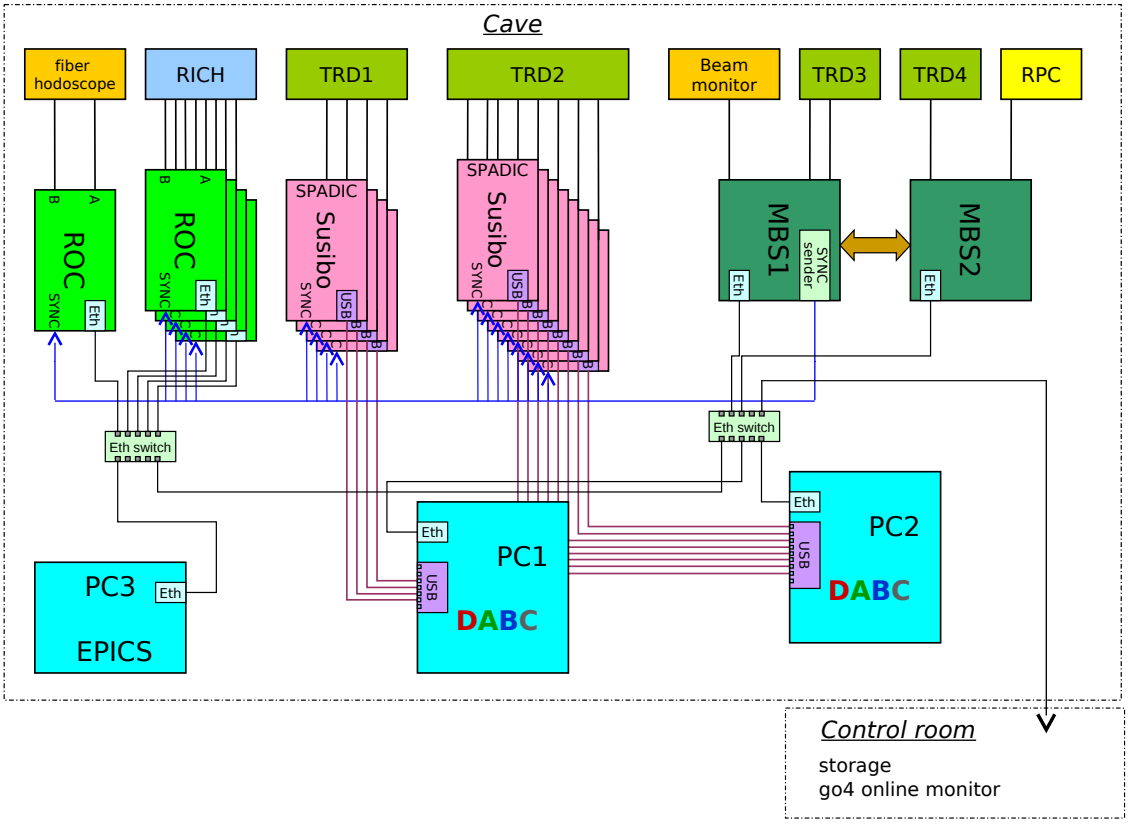

Fig. 8.2: Schematic of the DAQ system used during the in beam test 2011 at CERN PS T9 [Lin12].

The four prototypes from Münster MS336/10, MS336/11, MS444/10 and MS444/11 are presented in figure 8.3 with radiator prototypes G, F, E and J (compare to chapter 6.3) mounted as well as the upper read-out electronic combination SPADICv0.3, SUSIBO on the gray plastic support boards. The mechanical support structure allows

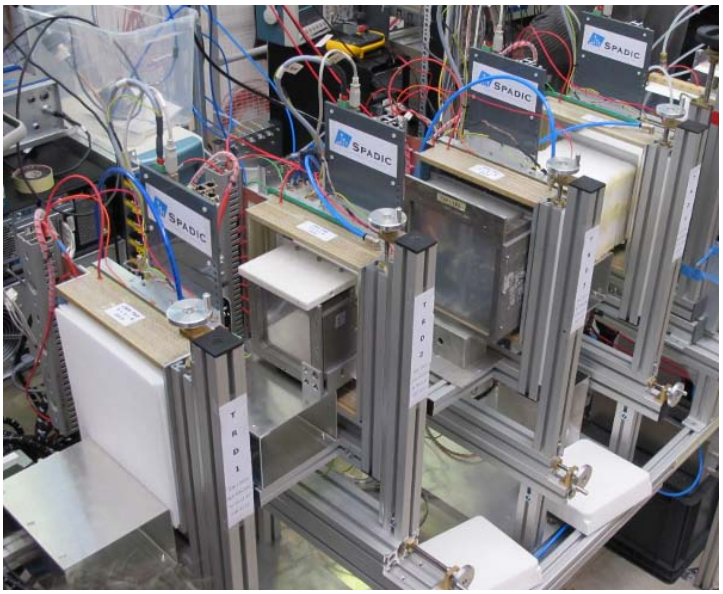

Fig. 8.3: MS TRD in beam test setup 2011 at CERN PS T9 consisting of the two 336 prototypes followed by the 444 MWPCs in combination with radiator G, F, E and J (from left to right).

precise positioning and alignment of each prototype and radiator in vertical an horizontal direction.
Since SPADICv0.3 was used for the first time in beam on a MWPC, the grounding scheme of the ASIC on the detector was not optimal. This results in a relatively high level of correlated noise. One example for a measured pulse shape is shown in figure 8.4 on the left side as well as the online noise and baseline compensated pulse on the right side. The first step of noise reduction is the baseline compensation. This is done based

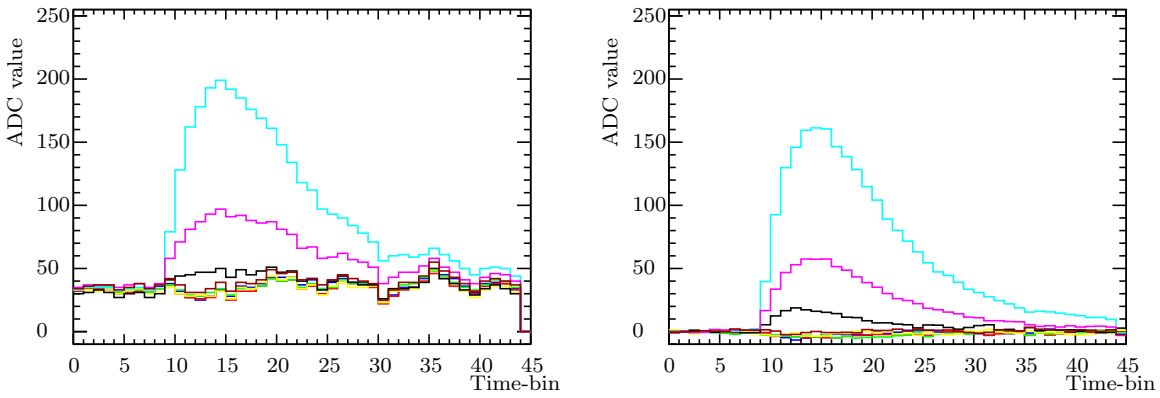

Fig. 8.4: Example of a measured event. On the left side the raw pulse shape, on the right pedestal compensated and after noise reduction.

on the average of each channel using the first three time-bins per channel (presented in figure 8.5). This value is subtracted from all time-bins of each channel. The baselines of the different prototype ASIC combinations are relatively wide, which is a first indicator

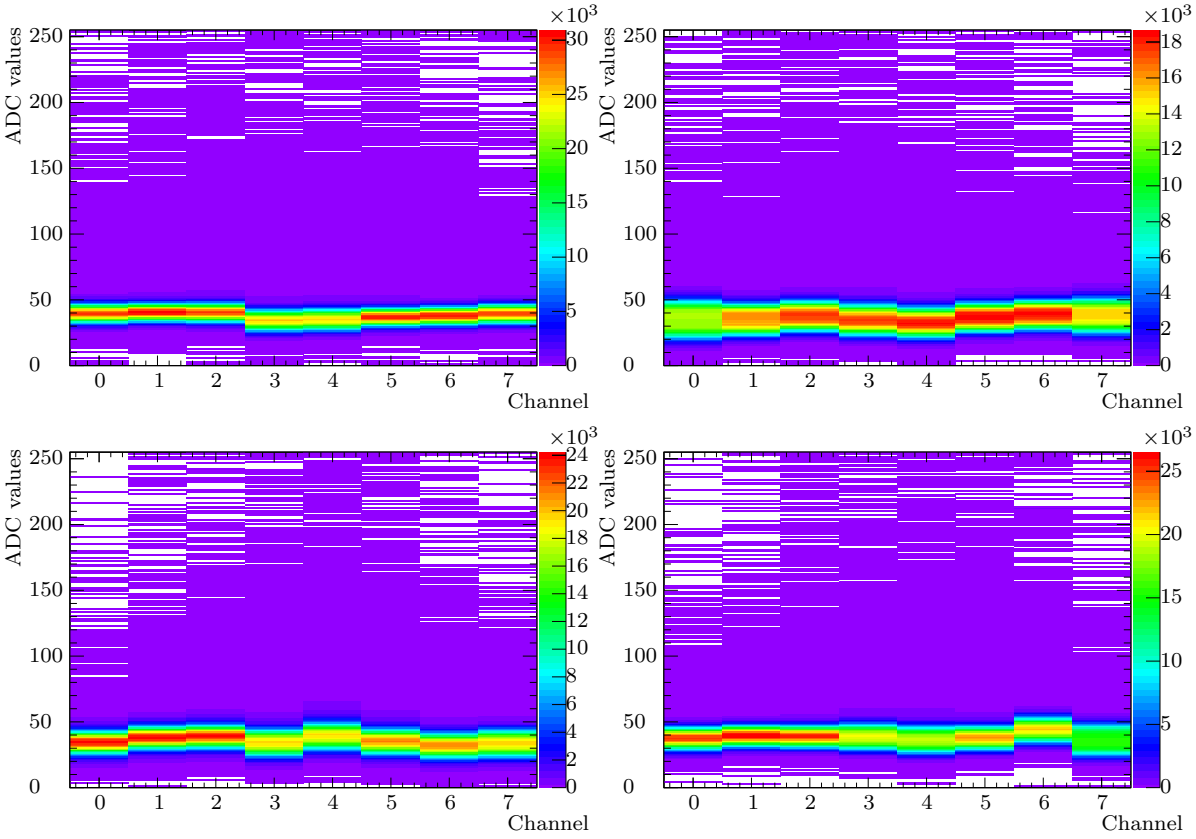

Fig. 8.5: Pedestal distribution based on the first three time-bins of each channel for MS336 (first row) MS444 (second row) prototypes from 2010 on the left side and 2011 on the right. The measurement was done at 3 GeV/c at 1750 V and 1950 V on the anode wires and a drift voltage of 600 V and 400 V.

of the high common noise level. The following step is the identification of the common noise. The channel with the lowest integrated signal is identified for each event. The correlation of the common noise is the highest, if no additional signal or real signal is present. A minimal example for a noise identification/reduction algorithm based on an approach of P. Dillenseger [Dil13] using functionality provided by the ROOT class *TPrincipal*[1] is presented in source code 8.1. The separation is done based on a noise level dependent correlation threshold. The maximum signal amplitude as function of the covariance matrix value is shown in figure 8.6. The noise channels are accumulated at high correlation values and low amplitudes, while the overflow signals are in a cloud like structure between 200 and 256 Analogue to Digital Converter (ADC) values and covariance entries between 0 and 0.1. Channels with a correlation below the noise threshold (listed in table 8.2) are signal channels, the others are noise channels.
Another problem which was observed during the data analysis is a systematic trigger jitter found in the SPADIC mounted on SUSIBO 02 (compare to figure 8.7). Since the SPADIC has been used in a triggered mode, the maximum amplitude should always be found within a thin time-bin window. This window ([10, 20]) has therefore been used to reduce the events with a 'slow' trigger and overflow events at the same time. Nevertheless there are remaining effects of the trigger jitter resulting in a smearing of the integrated ADC signal. The impact on the analysis will be discussed in the following. The average of all identified noise channels in time-bin i is subtracted from the ith time-bins of all

[1]Source code and documentation is available at `http://root.cern.ch/root/html/TPrincipal.html`.

```
#define NUM_SPADIC_CHA          8          //number of channels per ASIC
#define SPADIC_TRACE_SIZE      45          //number of time-bins per channel
#define SPADIC_ADC_MAX        255          //maximum ADC value

void Noise_Reduction_Cova(TH1D* inPulse[NUM_SPADIC_CHA], float threshold){
    TH1D *noise = new TH1D("noise", "noise", SPADIC_TRACE_SIZE, 0, SPADIC_TRACE_SIZE);
    TPrincipal* principal = new TPrincipal(NUM_SPADIC_CHA, "ND");
    int minCh = 0;
    double tempIntegral(0.0), minIntegral(SPADIC_TRACE_SIZE * SPADIC_ADC_MAX);
    double inputarray[SPADIC_TRACE_SIZE][NUM_SPADIC_CHA] = {{0.0}};
    for (int ch = 0; ch < NUM_SPADIC_CHA; ch++){
       tempIntegral = 0.0;
       for (int bin = 0; bin < SPADIC_TRACE_SIZE; bin++){
         inputarray[bin][ch] = inPulse[ch]->GetBinContent(bin);
         tempIntegral += inputarray[bin][ch];
       }
       if (tempIntegral < minIntegral){          //identify channel with lowest integrated signal
         minIntegral = tempIntegral;
         minCh = ch;
       }
    }
    for (int bin = 0; bin < SPADIC_TRACE_SIZE; bin++){
       principal->AddRow(inputarray[bin]);
    }
    principal->MakePrincipals();
    TMatrixD* cova = (TMatrixD*)principal->GetCovarianceMatrix();
    double covaRow[NUM_SPADIC_CHA];
    int noise_ch_counter = 0;
    for (int ch = 0; ch < NUM_SPADIC_CHA; ch++){
      covaRow[ch] = TMatrixDRow (*cova, minCh)(ch);
      if (covaRow[ch] > threshold){
        noise->Add(inPulse[ch]);                 //this is a noise channel
        noise_ch_counter++;
      }
    }
    noise->Scale(1./(double)noise_ch_counter);
    for (int ch = 0; ch < NUM_SPADIC_CHA; ch++){
      for (int bin = 0; bin < SPADIC_TRACE_SIZE; bin++){
        inPulse[ch]->SetBinContent(bin, inputarray[bin][ch] - noise->GetBinContent(bin));
      }
    }
    delete noise;
    delete principal;
    delete cova;
}
```

Source Code 8.1: Minimal example for a covariance matrix based noise identification and reduction algorithm using functionality provided by the ROOT class *TPrincipal*[1].

channels. The noise distribution is shown in figure 8.8. It can be seen that the electronic is very sensitive to internal and external noise coupling to the system. But at the same time this correlated noise, detected by all channels in parallel and individual baseline pedestals can be compensated rather well. The algorithm and applied cuts are described in more detail in section 8.2. The quality of these algorithms can be cross-checked based on the Pad Response Function (PRF). A comparison between the measurement and the theoretical prediction can be seen in figure 8.9. The symmetric shape of the distribution without artefacts indicates high quality of the pedestal correction and sufficient noise

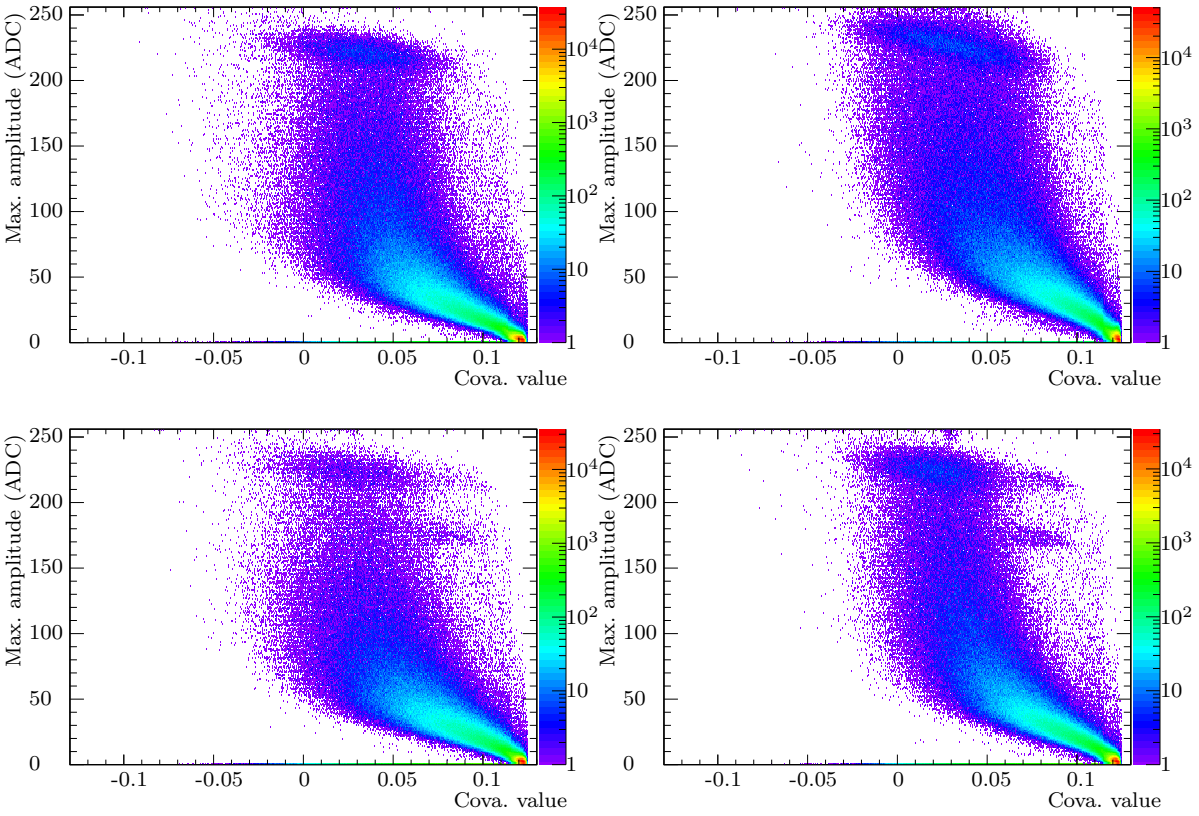

Fig. 8.6: Maximum amplitude after pedestal and noise correction as function of covariance matrix value for each channel for MS336 (first row) MS444 (second row) prototypes from 2010 on the left side and 2011 on the right. The measurement was done at 3 GeV/c with 1750 V and 1950 V on the anode wires and a drift voltage of 600 V and 400 V. The noise correction was already included in the maximum amplitude estimation to reduce the spreading due to noise in order to visualize the applied signal/background cuts. Overflow and underflow events are included.

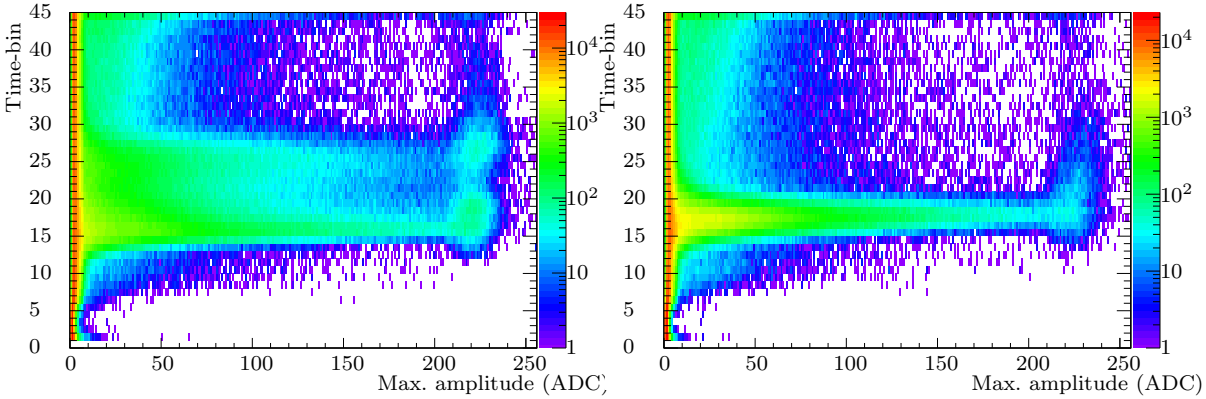

Fig. 8.7: Time of maximum amplitude as function of amplitude value after pedestal and noise correction of MS336/10 (left) and MS444/10 (right).

reduction by the algorithm. The rather large discrepancy between theoretically predicted K_3 values and measured one is found for all prototypes. This might be due to the relatively high noise level. An other possible reason could be the applied anode voltage which was chosen at the lower limit in order to avoid signal overflows. No effects of the trigger jitter of the ASIC of MS336/10 are visible since these affect all channels of the

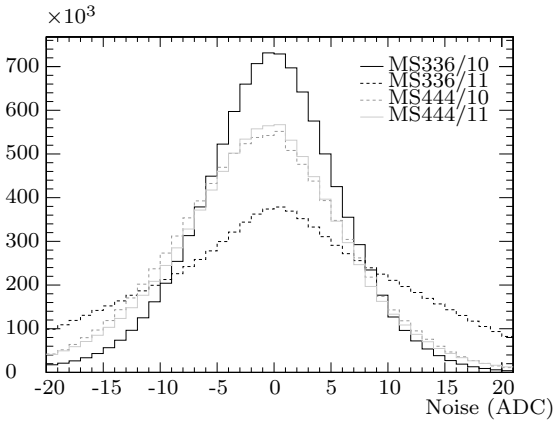

Fig. 8.8: Subtracted average noise distribution after pedestal correction for MS336 and MS444 prototypes at 3 GeV/c with an anode voltage of 1750 V (MS336) and 1950 V (MS444) and a drift voltage of 600 V (MS336) and 400 V (MS444).

Tab. 8.2: Noise reduction cuts 2011

Cut name	MS336/10	MS336/11	MS444/10	MS444/11
covariance matrix	0.114	0.115	0.116	0.115
min. ampl. (ADC values)	20	20	20	20
min. integ. signal (ADC values)	50	50	50	50
hit time window (time-bin)	[10, 20]	[10, 20]	[10, 20]	[10, 20]

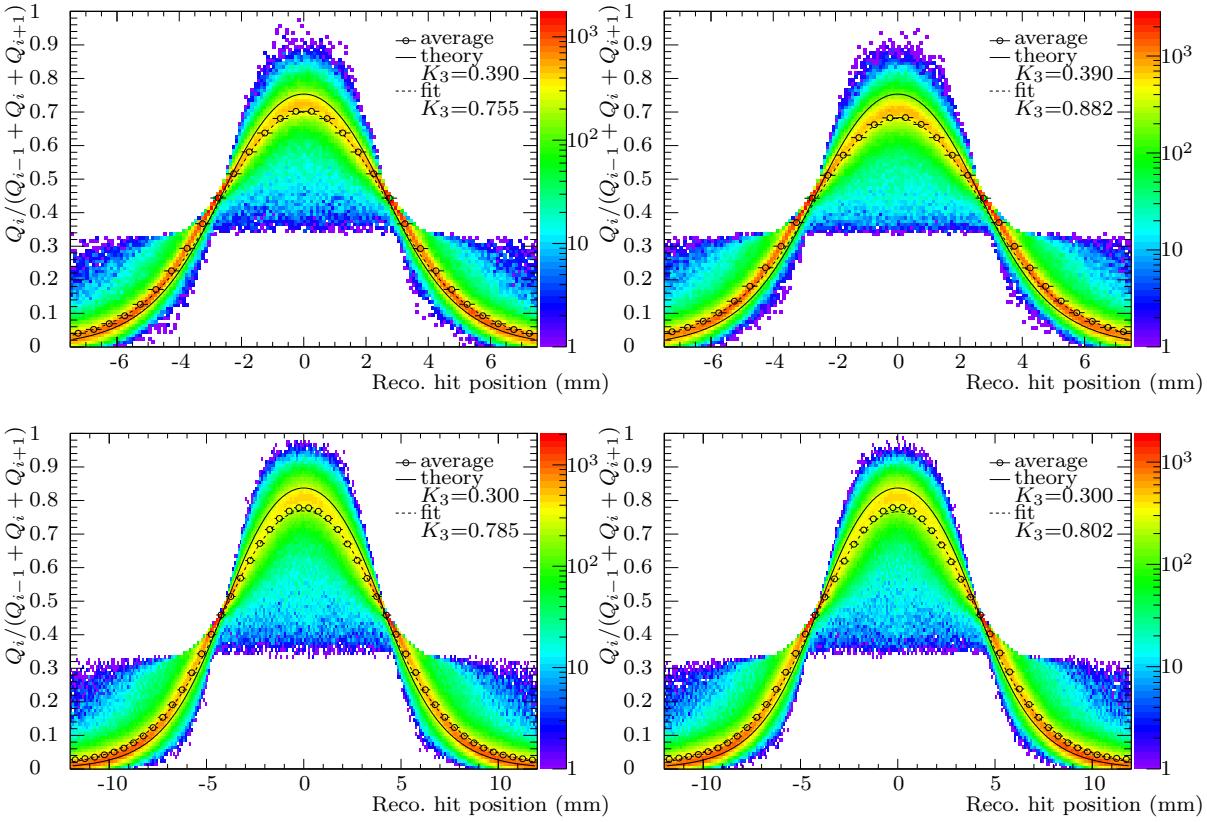

Fig. 8.9: PRF for MS336 (first row) and MS444 (second row) prototypes from 2010 on the left and 2011 on the right side at 3 GeV/c at 1750 V and 1950 V on the anode wires and a drift voltage of 600 V respectively 400 V. The average distributions have been fitted to the Mathieson formula (equation 4.36) given by the dashed line with equation 4.36. The theoretical prediction using K_3 according to the chamber parameters (table 4.1) is also shown for comparison (solid line).

SPADIC in the same way for each event. Therefore the charge ratio of the three highest channels is conserved and the PRF is not influenced.

8.1.1. Particle Identification Performance

A combination of two Cherenkov counters and one Pb-glass calorimeter are used as PID reference. The measured spectra at 3 GeV/c are shown in figure 8.10. For electrons and

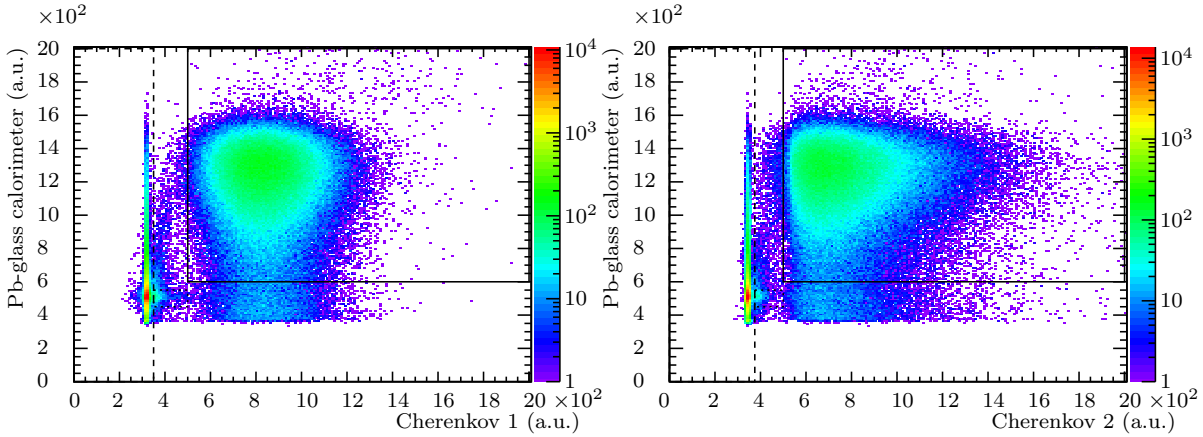

Fig. 8.10: Measured spectra for electrons, muons and pions at 3 GeV/c at a common CBM in beam test at CERN PS 2011. The cut conditions for electrons (Ch1 [500, 4000], Ch2 [500, 4000] and Pb-glass [600, 4000]) are represented by the solid lines. Dashed lines are used for pion cut conditions (Ch1 [0, 350], Ch2 [0, 375] and Pb-glass [0, 4000]). Muons (Ch1 [350, 500], Ch2 [375, 500] and Pb-glass [450, 550]) are surrounded by the pointed lines. Pulser events are not excluded from the total number of events.

pions are requested to fulfill all three cut conditions for Cherenkov 1, 2 and the Pb-glass calorimeter at the same time, where the muons have only to be conform with at least one of the two Cherenkov conditions but always with the Pb-glass calorimeter thresholds. The 1-dim. spectra (same as in figure 8.10) of the different PID reference detectors are presented in figure 8.11 in comparison with a simple superposition of three independent Gaussian distributions, describing the Cherenkov counter spectra up to 1600 ADC values. The distance of the fitted mean values of the superposition in multiples of the Gaussian distribution width σ, gives a criterion of the separation and data efficiency of each detector for each particle listed in table 8.3. Since the applied cuts, especially in case of electron cuts are highly asymmetric with respect to the fitted mean value of the distributions the values on the diagonal of table 8.3 b) are average of the upper and lower PID cut value.

In the following it will be discussed how an upper limit on the efficiency of the PID reference system can be estimated based on a pure statistical bases without any knowledge of the distribution. Assuming that the fraction of muons in the data sample is insignificant relative to the number of electrons or pions, only the efficiencies for electron to pion separation are presented. The efficiency to detect an electron within the pion cut conditions ϵ_π and to find a pion within the electron selection area ϵ_e are the two important numbers to determine which will be derived from a 2-dim. case using a single Cherenkov counter and one calorimeter as indicated in figure 8.12. An upper limit on both efficiencies can be calculated assuming the signals in the Cherenkov counters and the calorimeter are independent measurements. The efficiency for finding electrons when making cuts for pions is

$$\epsilon_e < \epsilon_{Ch,e} \cdot \epsilon_{Cal,e} \tag{8.1}$$

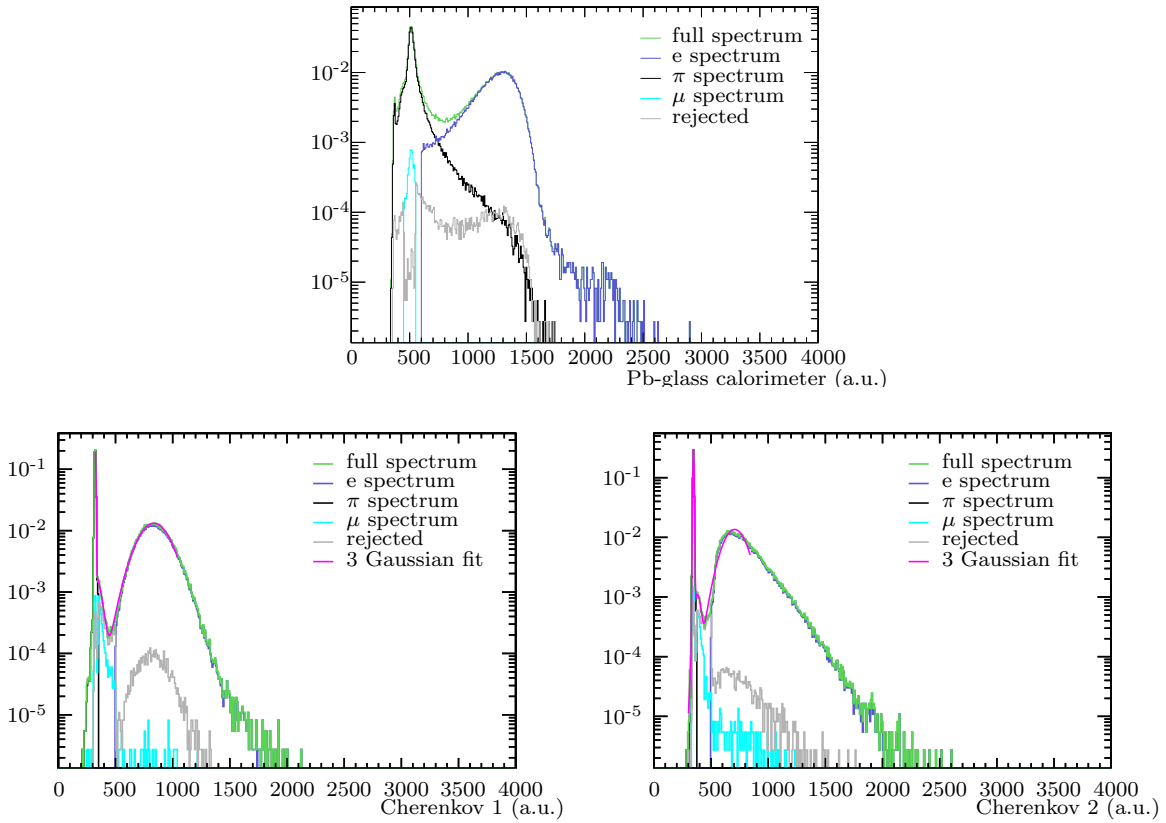

Fig. 8.11: Pb-glass calorimeter (upper) Cherenkov 1 (left) and 2 (right) spectra at 3 GeV/c are presented without PID cuts (green), for electrons (blue), pions (black) and excluded events (gray). The full distributions of both Cherenkov counters are fitted to the sum of three Gaussian distributions (pink).

Tab. 8.3: Particle separation efficiency for the three reference detectors using 3 GeV/c data. Efficiency is represented by the distance between the fitted $mean_x$ values in multiples of the Gaussian distribution width σ_x ($|mean_x - mean_y| / \sigma_x$) in a). The distance between the fitted $mean_x$ and the closest PID cut value as multiples of the fitted Gaussian distribution width σ_x are presented in b).

	Cherenkov 1			Cherenkov 2		
a)	π	μ	e	π	μ	e
π	0.00	0.34	3.97	0.00	1.35	3.74
μ	5.15	0.00	4.11	7.31	0.00	3.38
e	146.22	10.12	0.00	76.51	12.74	0.00

	Cherenkov 1			Cherenkov 2		
b)	π	μ	e	π	μ	e
π	50.10	0.47	1.36	39.83	1.09	1.59
μ	12.22	2.25	1.50	1.37	2.44	1.23
e	139.15	6.43	13.59	70.57	8.10	18.17

with $\epsilon_{Ch,e}$ and $\epsilon_{Cal,e}$ being the efficiencies for the Cherenkov counter and the calorimeter. Four different selection criteria can be defined. With X_e and X_π defined as the number of electrons and pions after the selection criteria X the total number of particles X_{total} is given as

$$X_{total} = X_e + X_\pi = xX_e, \text{ where } x > 1. \tag{8.2}$$

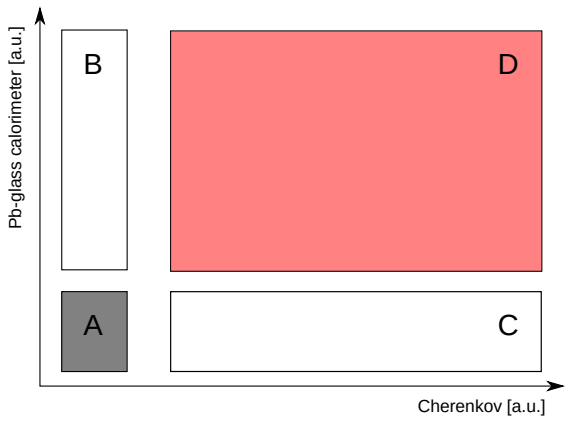

Fig. 8.12: Four different selection criteria in order to estimate the PID purity are presented. **A:** Pion identification cuts in both the Cherenkov counter and the calorimeter (gray colored selected pion sample). **B:** Pion identification cut in the Cherenkov counter and electron identification cut in the calorimeter. **C:** Electron identification cut in the Cherenkov counter and pion identification cut in the calorimeter. **D:** Electron identification cuts in both the Cherenkov counter and the calorimeter (red colored selected electron sample).

Since the cuts on the Cherenkov counter and the calorimeter are independent the efficiency of the calorimeter can be written as

$$\epsilon_{Cal,e} = \frac{C_e}{C_e + D_e}. \tag{8.3}$$

However, the large number of particles in region an on figure 8.10 indicate a large contamination of pions in the electron beam and equation 8.3 will be a pessimistic estimate. The final definitions are

$$\epsilon_{Cal,e} = \frac{1}{1 + D_e/C_e}, \qquad \epsilon_{Ch,e} = \frac{1}{1 + D_e/B_e} \tag{8.4}$$

$$\epsilon_{Cal,\pi} = \frac{1}{1 + A_\pi/B_\pi}, \qquad \epsilon_{Ch,\pi} = \frac{1}{1 + A_\pi/C_\pi} \tag{8.5}$$

based on [Ege98a]. By adding a third PID reference detector the problem becomes three dimensional as depicted in figure 8.13. The PID reference detector efficiencies for electrons and pions are defined analogously to equations 8.4 and 8.5:

$$\epsilon_{Cal,e} = \frac{1}{1 + D_e/E_e}, \qquad \epsilon_{Ch1,e} = \frac{1}{1 + D_e/F_e}, \qquad \epsilon_{Ch2,e} = \frac{1}{1 + D_e/G_e} \tag{8.6}$$

$$\epsilon_{Cal,\pi} = \frac{1}{1 + A_\pi/B_\pi}, \qquad \epsilon_{Ch1,\pi} = \frac{1}{1 + A_\pi/C_\pi}, \qquad \epsilon_{Ch2,\pi} = \frac{1}{1 + A_\pi/H_\pi}. \tag{8.7}$$

The total efficiencies for electrons

$$\epsilon_e < \epsilon_{Ch1,e} \cdot \epsilon_{Ch2,e} \cdot \epsilon_{Cal,e} \tag{8.8}$$

and pions

$$\epsilon_\pi < \epsilon_{Ch1,\pi} \cdot \epsilon_{Ch2,\pi} \cdot \epsilon_{Cal,\pi} \tag{8.9}$$

is defined as product of all three efficiencies. In case of the PID reference spectra and PID cuts presented in figure 8.10 these results in the following efficiencies limits;

$$\epsilon_e < 3.6900\text{E-}04 \cdot 5.2731\text{E-}06 \cdot 4.7619\text{E-}02 \ll 1/\text{n events} \tag{8.10}$$

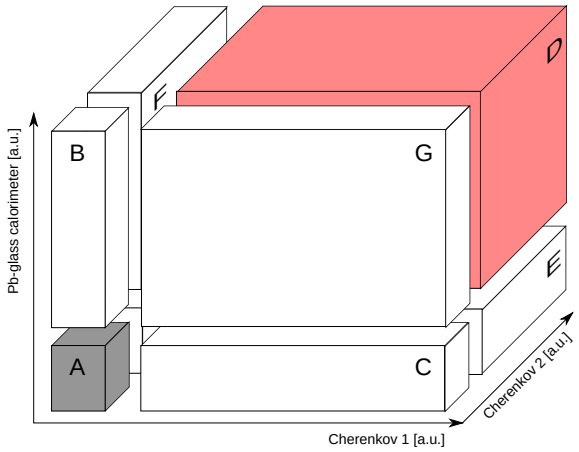

Fig. 8.13: Eight different selection criteria in order to estimate the PID purity are presented. **A:** Pion identification cuts in both Cherenkov counters and the calorimeter (gray colored selected pion sample). **B:** Pion identification cut in the Cherenkov counter 1 and 2 and electron identification cut in the calorimeter. **C:** Electron identification cut in the Cherenkov counter 1 and pion identification cut in second Cherenkov counter and the calorimeter. **D:** Electron identification cuts in both the Cherenkov counters and the calorimeter (red colored selected electron sample). **E:** Electron identification cuts in both Cherenkov counters and pion conditions in the calorimeter. **F:** Electron conditions in Cherenkov counter 2 and pion conditions in Cherenkov 1 and the calorimeter. **G:** Electron conditions in Cherenkov counter 1 and the calorimeter and pion conditions in Cherenkov counter 2. **H:** Electron cuts in Cherenkov counter 2 and pion conditions in Cherenkov 1 and the calorimeter (Behind A, below F and left of E).

to find an electron within the pion sample with a data efficiency (selected electrons / all events) of 51.68% for electrons and

$$\epsilon_\pi < 2.7100\text{E-}03 \cdot 2.5510\text{E-}03 \cdot 6.2168\text{E-}06 \ll 1/\text{n events} \tag{8.11}$$

to misidentify an electron as pion with a data efficiency of 43.83% (pulser events are excluded). The purities of the two samples are below the expected efficiencies of the TRD prototypes and therefore sufficient for the following analysis.
The average event number per measurement in 2011 is of the order of 200,000 to 350,000 which is 5-10 times lower compared to the statistic accumulated in 2012.
The resulting spectra as function of integrated ADC values have been calibrated to energy loss in keV to compare simulated and measured spectra. This is done by fitting the range of the pion spectra between the first bin above 0.001% of the maximum amplitude and the first bin below 70% of the peak value with a Landau distribution multiplied with a Gaussian distribution sharing a common mean parameter. The ratio of the two mean values are used to calibrate the measured spectra. The calibrated energy loss spectra for electrons and pions are compared to simulated spectra in figure 8.14. The simulated electron spectrum is based on the simulated energy loss of the electrons due to ionization and the simulated pure TR-spectrum including self-absorption of the radiator material as well as due to the material budget of the entrance window and the absorption within the active gas volume. The average number of produced photons per electron is given by the integral of the photon yield spectrum. The absolute number of produced photons is assumed to be Poisson distributed. The total energy loss due to TR-photon production is given by the energy of all photons per electron reaching and being absorbed in the active volume. This method results in rather big deviations between measurement and simulation without any corrections. Therefore, the TR-spectrum is multiplied by a

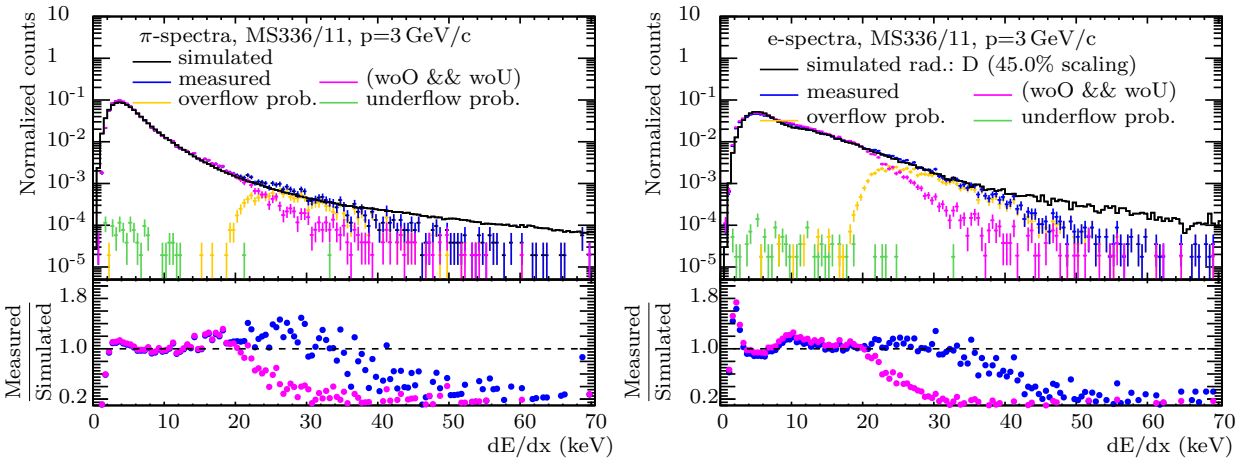

Fig. 8.14: Measured energy loss spectra including overflow and underflow signals (blue) and excluded fragmented signals (pink) for pions (left) and electrons (right) at 3 GeV/c using MS336/11 with radiator D in comparison with simulated spectra (black). The calibration quality is monitored using the ratio between measurement and simulation.

scaling factor smaller 1 to take into account uncertainties due to the radiator material properties like foil density, regularity and photon cross-section (all scaling factors are listed in table 8.8). These uncertainties can not be disentangled and are therefore represented by one correction factor. The scaling factor is estimated in several iterations to minimize the deviation between the measurement and the simulation. Afterwards, a good agreement between 2 keV and 35 keV is found between measurement and simulation. The deviation at higher dE/dx values are due to the increasing probability to run out of the SPADIC ADC range. The deviation at lowest energy loss values of pions is due to the minimum amplitude threshold, which was applied to separate signal from noise events. The impact on the pion spectrum is bigger, since the spectrum starts at lower values compared to the electron spectrum. A first criterion on the electron pion separation power is the ratio $\langle dE/dx \rangle_e \,/\, \langle dE/dx \rangle_\pi$. Based on these spectra one can extrapolate the pion efficiency for any number of identical prototypes. The results of the radiator comparison to simulated data are shown in figure 8.15. First of all, a good matching bet-

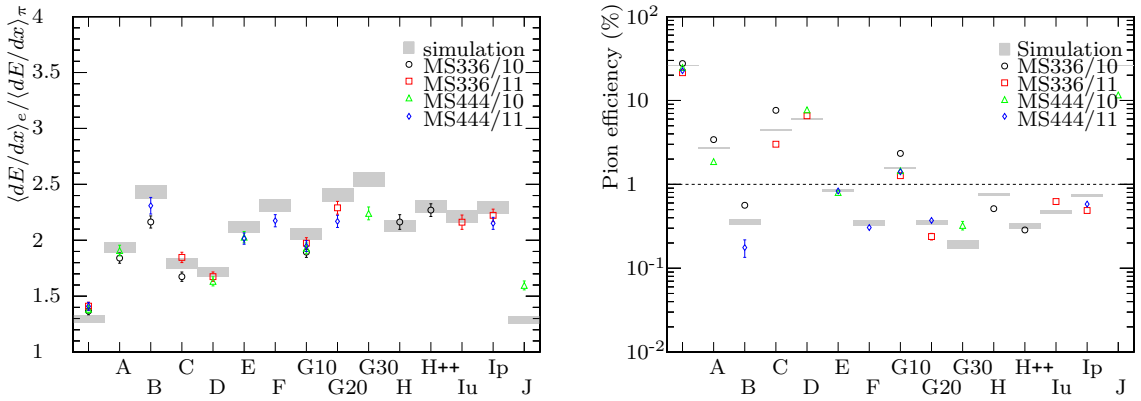

Fig. 8.15: Comparison of $\langle dE/dx \rangle_e \,/\, \langle dE/dx \rangle_\pi$ ratios for different radiator prototypes at 3 GeV/c (left) and the pion efficiency at 90% electron efficiency with 10 detector hits (right).

ween simulation and measurement was found, where the simulation is always above the measured ratio, which might by resulting from the non physical limitation of the spectra due to overflow signals. Comparing this to the final pion efficiency at 90% electron

efficiency with 10 detector hits, a good agreement for most regular prototypes between simulation and measurement within the errors is found, where the deviation in case of irregular prototypes extends. This suggests that the description of irregular radiators by a regular alternate radiator with the average parameters of the irregular material is a first rough approximation but not sufficient to deliver a full model. This first test of the theoretical description has also to be tested at different particle momenta in order to get a description for the simulation implementation. A systematic underestimation is found for TRD MS336/10 (black markers) due to the trigger jitter presented in figure 8.7. This jitter results in a broadening of the spectrum. Since the TR-production included in the simulation is tuned to reproduce the measured spectra, the estimated simulated pion efficiency is also influenced. A comparison between B, H, I(u) and I(p) shows better agreement between I(p) and I(u) and H than B. This indicates the foil spacing by foam foils even if perforated does not lead to a TR-production comparable to the performance of a regular radiator. The dominant photon fraction seams to be produced in the foam not by the foils. A theory on this is, that the regularity of the foil spacing is rather poor. The integrated pion overflow probability presented in figure 8.16 can be used as reference for the noise level (figure 8.8), ASIC gain and pedestal stability (figure 8.5). The ASIC

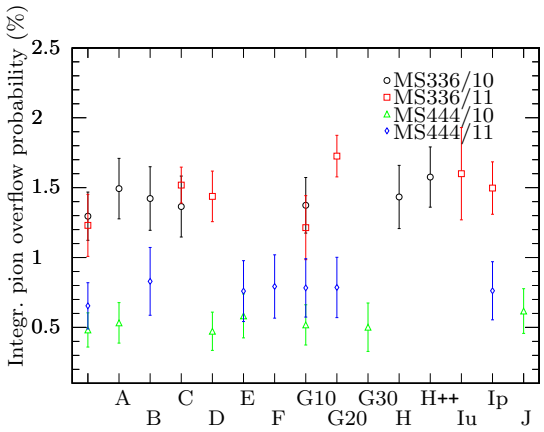

Fig. 8.16: Radiator comparison: Integrated pion overflow probability at 3 GeV/c

gain stability is given within the errors and varies within several percent between the individual ASICs. This variation can be due to the different noise level as well as due to a real gain difference. The different radiators do not contribute to this effect, since only pions are used for this estimation. It is also possible to derive design parameter for the full CBM TRD from the pion efficiency analysis presented above. A minimum number of detector hits per track can be approximated for each detector/radiator combination as presented in figure 8.17. The best radiator option in combination with the 2011 MWPC prototypes are B, G30 or H++. Mixed radiators like J(u,p) or other regular radiators do not reach this performance level.

The 2011 beam test of small ALICE-like MWPC prototypes in combination with the different regular and irregular radiators and ASIC prototypes has triggered several developments: The efficiency of noise reduction algorithms was improved. The measured PRF was used to develop a realistic detector response algorithm for the TRD simulation. The radiator simulation was updated based on the measured energy loss spectra for electrons and pions. The presented results are pointing towards the need of entrance window material optimizations. A reduction of the entrance window material enhances TR-photon transmission which leads to improved PID performance, implemented in TRD prototypes in 2012. In addition the need of an ASIC with a better gain matching

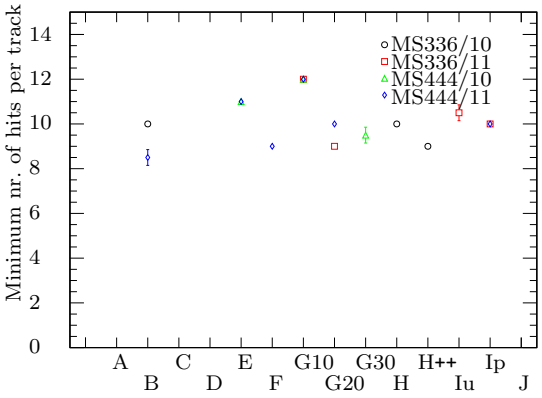

Fig. 8.17: Radiator comparison: Minimum number of detector hits to reach 1% pion efficiency at 90% electron efficiency at 3 GeV/c.

and lower noise level became obvious.

8.2. CERN PS T9 2012

The TRD subject of the third common CBM in beam test at CERN PS T9 in 2012 was the optimization of the PID performance by minimization of the material budget of the entrance window, of a real-size detector prototypes. The complete setup can be seen in figure 8.18. The PID reference is done based on two air/CO_2 Cherenkov counters

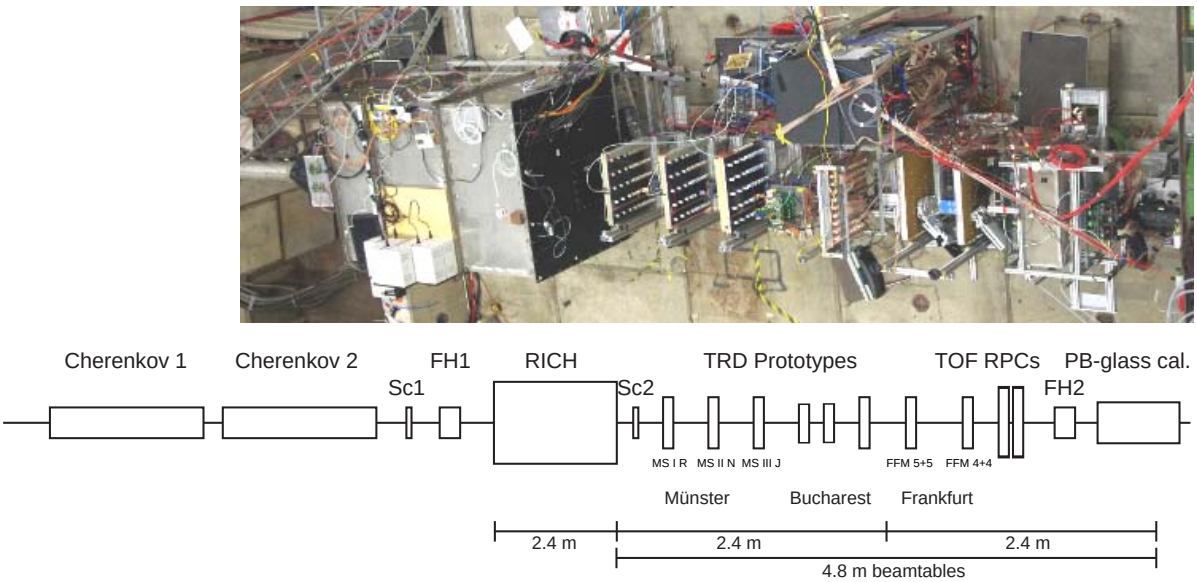

Fig. 8.18: CERN PS T9 beam test setup. The photo has been rotated and shifted to match the schematic below. The beam is coming from the left through the second Cherenkov counter passing the first scintillator and the first fiber hodoscope. The first detector prototype in beam direction is the real dimension RICH detector followed by the second scintillator. Afterwards are eight TRD prototypes from Münster, Bucharest and Frankfurt. The last prototype detectors are two TOF RPC detectors from Bucharest followed by the second fiber hodoscope and the Pb-glass calorimeter.

and one Pb-glass calorimeter. The external position reference and triggering system was realized by two fiber hodoscopes, one between the first scintillator $Sc1$ and the RICH prototype and the other in front of the Pb-glass counter. The RICH is followed by the TRDs from Münster, Bucharest and Frankfurt. Behind the TRDs are two RPC TOF prototypes from Bucharest installed in the beam line.
The DAQ system is condensed in the following schematic 8.19, which was used to record 34,294,869 events. The third generation CBM MWPC TRD prototypes from Münster with a foil gas entrance window made from 25 μm single sided aluminized Kapton foil has been tested on a mixed electron, pion and muon beam with variable particle momenta between 1 and 10 GeV/c at CERN PS T9 in order to determine the particle identification and position reconstruction performance. The energy resolution of 11% has been tested in a separate lab test using a different gas mixture (Ar/CO_2 (80/20)) and a collimated ^{55}Fe source (see chapter 5.10.2). All TRD prototypes have been operated with a common pre-mixed gas mixture of Xe/CO_2 (80/20) with an EPICS monitored total gas flux of 8.6 l/h in average for the chambers of the different institutes, as presented in figure 8.20. This main gas line was splitted into three individual gas lines. The total gas flux from the gas bottle to the cave, as well as the flux to the three separate gas lines (2.9 l/h) has been controlled using Kobold KFR-acrylic manual flow-meter. The total flux has been monitored using an Aalborg Mass Flow Meter (GFM) in combination with an Aalborg Totalizer Input/Output (TIO). High fluctuations of the gas flux are visible between the

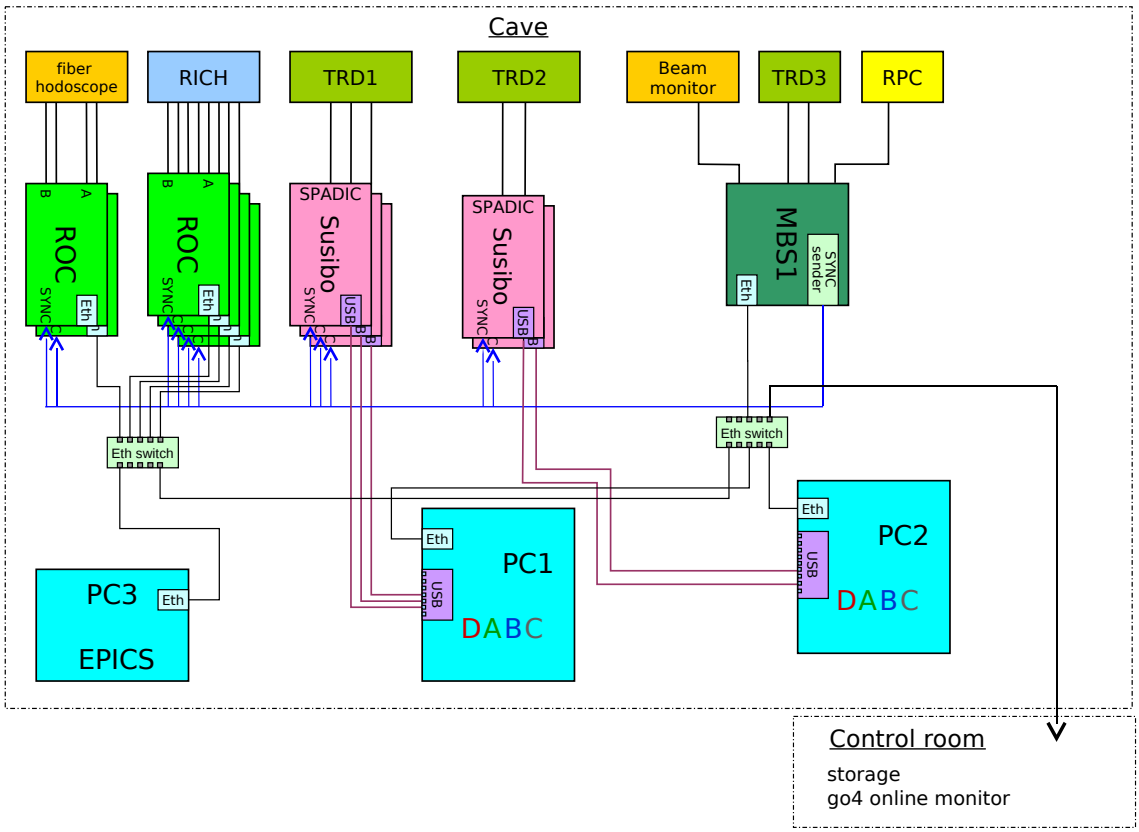

Fig. 8.19: Schematic of the DAQ system used during the in beam test 2012 at CERN PS T9 based on [Lin12].

30th of October and 3rd November resulting from calibration procedure. The overall fluctuation amplitude decreases in time due to the stabilization of the system. The high, but short spikes after the 7th of November are correlated to short fluctuations in the environment temperature in the PS experimental area. There is nothing comparable visible in the air pressure spectrum. These points to an extremely sensitive response of the gas system of several ten meter of copper gas pipe between the gas mixing station (gas bottle with 3000 l) outside the cave and the gas line splitting station close to the detectors to short temperature fluctuations of several degrees. The orbisphere at the end of the gas line, separated by several meters of gas pipe between the last detector and the gas analyzer, was not included in the EPICS monitoring system, but monitored manually after each run. Lab tests and tests after mounting of the detectors in T9 have shown good tightness of the first two identical TRD modules.
The geometrical details, read-out (SUSIBO) Ids and naming of the prototypes from Münster (see figure 8.21) are listed in table 8.4. All following steps in order to reduce

Tab. 8.4: Münster detector Ids 2012 in beam direction

Detector Id	Type	Geometry/year	SUSIBO Id
TRD1 R I	open	3.5 3.5 5.0/12	011
TRD2 N II	open	3.5 3.5 5.0/12	010
TRD3 J III	classic	3.5 3.5 5.0/12	018

background events, signal pedestal and noise are used for the position resolution as well as for the pion suppression performance analysis. The total noise trigger rate (dark rate)

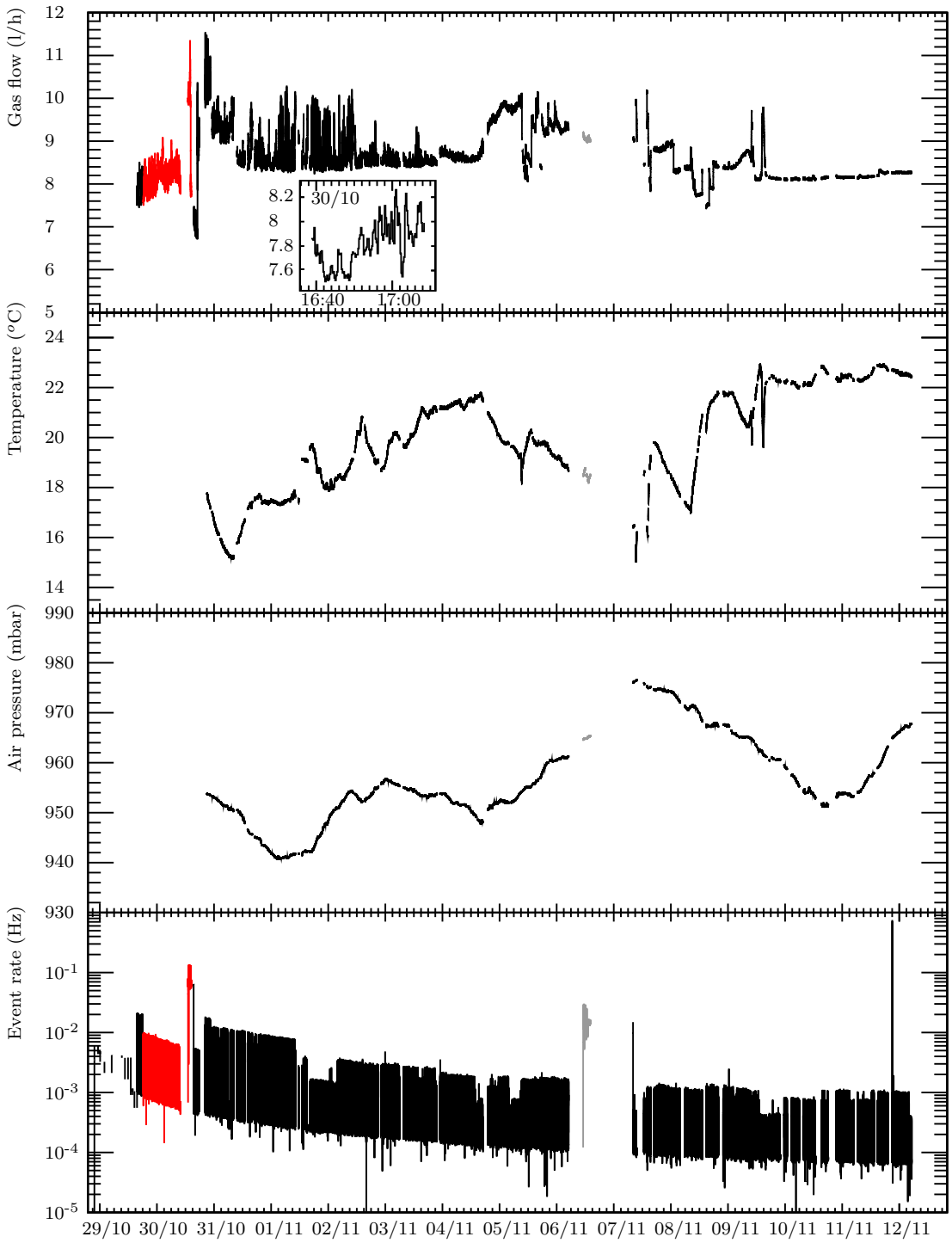

Fig. 8.20: EPICS monitoring of total gas flux, temperature, air pressure(last two measured by the RICH gas rack outside of the cave) and event rate as function of time. Red lines indicate runs with an oxygen contamination above 0 ppmV_b and gray corresponds to source runs. The small histogram within the first row shows a gas flow during a single run (Be_run29 30.10.12 16:38-17:16) with a duration of 38 minutes.

from the two fiber hodoscopes have been reduced based on the PID reference detectors in a first step. All events without a signal above the pedestal of one or both Cherenkov counters (350 ADCs) and a signal above the pedestal of the Pb-glass calorimeter at 350 ADCs at the same time are excluded, as well as the pulser events. This reduces

Fig. 8.21: Münster prototypes R I, N II and J III in the beam line T9 at CERN, with radiator prototypes B++, K++ and G30 from left to right side.

the number of all triggered events about 23.71%, but leads to a significant speed up of the analysis and reduces the background events. The noise and channel depending pedestal level of the SPADIC v0.3 ASIC is illustrated based on one single pulse example as presented in figure 8.22. On the left is the raw pulse shown, the compensated pulse

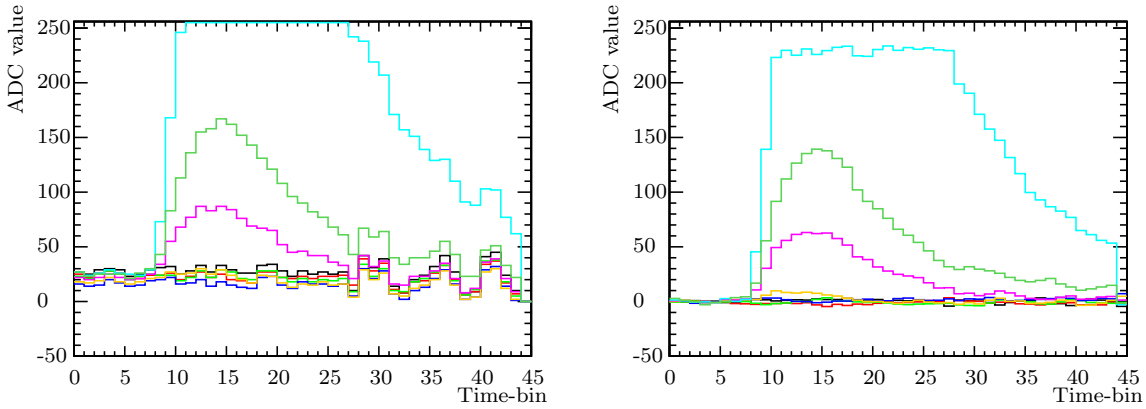

Fig. 8.22: Fragmented pulse shape measured by TRD1 before and after pedestal and noise reduction are shown.

is presented on the right hand side. It is visible that there is a high common noise level and a channel depending pedestal. The baseline has been adjusted to 30 ADC values in order to avoid signal losses due to signal underflow. The pedestal compensation is done off-line by subtracting the average baseline of the first three time-bins per channel and event from each time-bin of the signal. The width of the channel individual ADC pedestal distribution gives a first estimation of the common noise distribution, which is not channel depending within the same read-out ASIC. After pedestal correction the noise level is reduced. In order to do this, one has to separate the signal channels from the pure noise channels. This is done by calculating the covariance matrix for the channel with the lowest integrated signal per event. Since the common noise has a higher correlation level for channels without additional signal compared to those with a Landau

shaped signal this correlation is a good separation criterion. The noise channels signal is sharply peaked at high correlation and low maximum amplitudes. The cut values have to be estimated for each chamber depending on the common noise level of each chamber and run. The signals going into the overflow are within the cloud structure between 200 and 256 ADC values. In case of raw signals, there is a sharp horizontal line at 256 ADC values, which is spread due to the channel individual pedestal. The cut maximum line of the overflow signal is still flat at a constant ADC level after the pedestal correction. The lower noise level in TRD2 leads to a broadening of the covariance matrix value distribution, since the correlation of the noise channels is reduced. Since the read-out electronic was operated in a triggered mode, the highest signal amplitude is always found between time-bin 10 and 20, which is also used to separate signal from background. Such a criterion thin out the overflow events at the same time. An analog phenomenon can not be observed in the correlation of the time-bin of highest amplitude per channel as function of the corresponding covariance matrix value histogram. The low correlated channels (signal channels) have a signal peak just between the 10th and 20th time-bin as shown in figure 8.23. The 'roughed' overflow top has the same shape as the

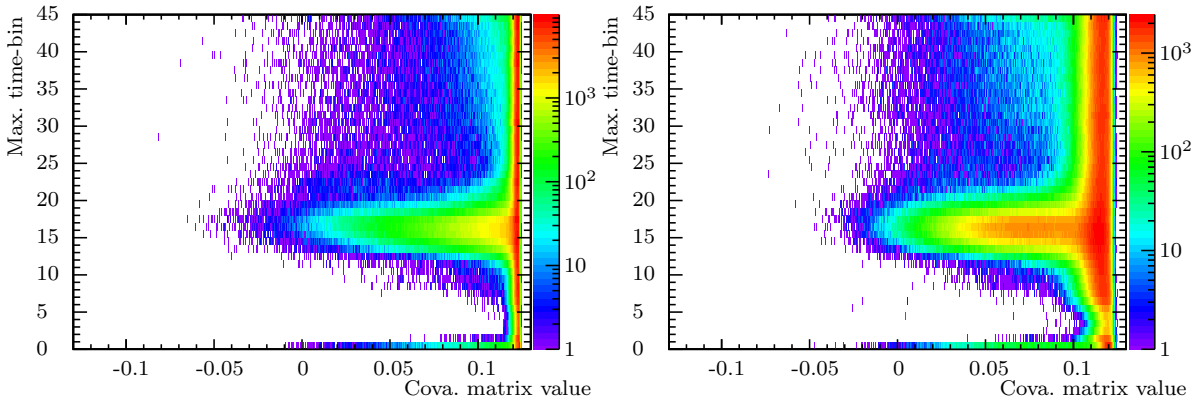

Fig. 8.23: Hit time (time-bin of maximum amplitude) after pedestal correction as function of covariance matrix value and after pedestal correction for each channel for TRD1 (left) and TRD2 (right) at 8 GeV/c for 1775 V on the anode wires and a drift voltage of 500 V

average noise signal and therefore a higher covariance matrix entry compared to a non fragmented pulse. This leads to a shift of the overflow signals towards the noise channels in this representation. It can also be seen that the noise channels in TRD1 are sharper correlated compared to TRD2. The covariance matrix noise reduction approach resulting in a first signal clustering. This can be seen in figure 8.24. The covariance matrix values are filled to a *std* :: *list* which is sorted according to rising matrix values. The number of left over list entries (channels) with a higher matrix element are filled to the histogram as function of the covariance value of the active list entry beginning at the lowest value. The resulting distribution can be used to evaluate the distribution of noise channels as function of the covariance matrix cut value, which is used to separate noise from signal channels. The cut value for TRD1 is set to 0.120 and in case of TRD2 to 0.112. A first basic cluster size distribution can be evaluated by integrating all entries below the covariance matrix cut value. In order to avoid misidentified noise channels, additional criteria have been applied. A maximum amplitude below 30 (TRD1) respectively 16 ADC values (TRD2) of the pedestal compensated pulse is demanded if this highest amplitude is found between the 5th and 20th time-bin to identify a noise channel. These criteria have been used to evaluate the presented cluster size distributions in figure 8.25.

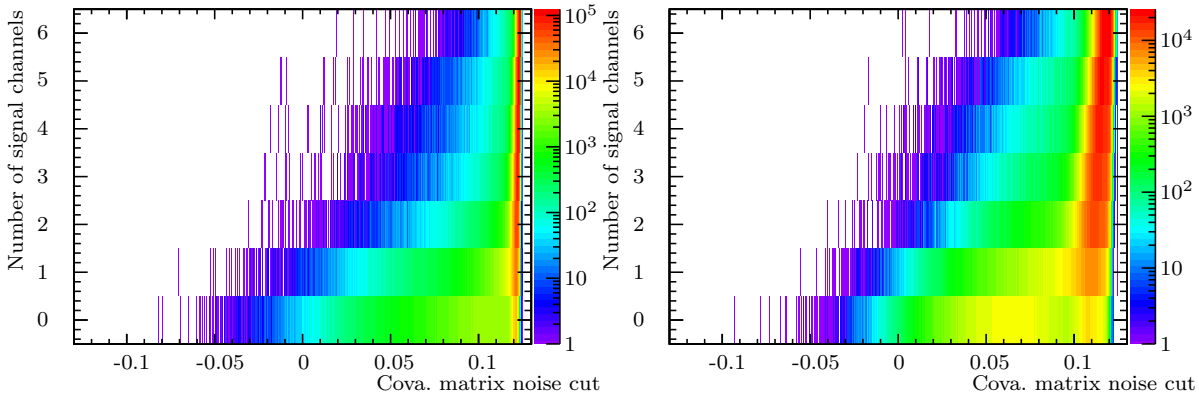

Fig. 8.24: Number of channels with a lower covariance matrix value (identified as signal channels) than the corresponding cut value depicted on the axis of abscissas for TRD1 (left) and TRD2 (right) at 8 GeV/c for 1775 V on the anode wires and a drift voltage of 500 V.

In addition, a continuous channel number around the channel with the highest signal

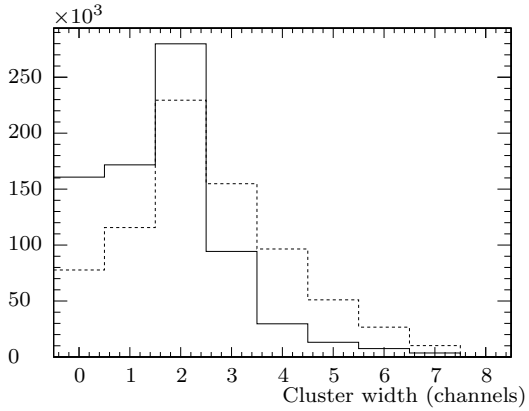

Fig. 8.25: Cluster size distribution for TRD1 (solid) and TRD2 (dashed) at 8 GeV/c for 1775 V on the anode wires and a drift voltage of 500 V. Continuous signal channel numbers around the maximum signal channel are demanded in addition to the previous noise identification cuts.

amplitude within the identified signal channel collection without gaps for each event has to be demanded. Only 39.15% of all externally triggered events have been seen by TRD1 where 39.92% of these have been measured by TRD2 and 33.04% events have been registered simultaneously by both after all cuts. The distribution of the first prototype is faster falling towards bigger clusters. The average of all identified noise channel pulses is subtracted from all channels per event. The subtracted noise distribution is presented in figure 8.26. The noise distribution is peaked at zero, indicating that the pedestal reduction worked fine. There are several additional cuts applied after the pure noise and pedestal reduction to further reduce the noise level and fragmented signals. These cuts are listed in table 8.5. The whole pedestal and noise reduction algorithm is tested based on the calculation of the PRF as presented in figure 8.27. The Mathieson fit was done with three parameters h [1.25, 4.00], r_a [0.0018, 0.0022] and s [2.4, 2.6] according to equation 4.37. The limits of r_a and s have been chosen to reflect the production accuracy in the worst case, where the range of h is limited by the parametrization itself. The fit does not give reasonable results within this restricted parameter range as can be seen by the high level of χ^2/NDF. All parameters are as the limits and the result can still not match the average response of the chamber in a proper way. Since the MWPCs had to

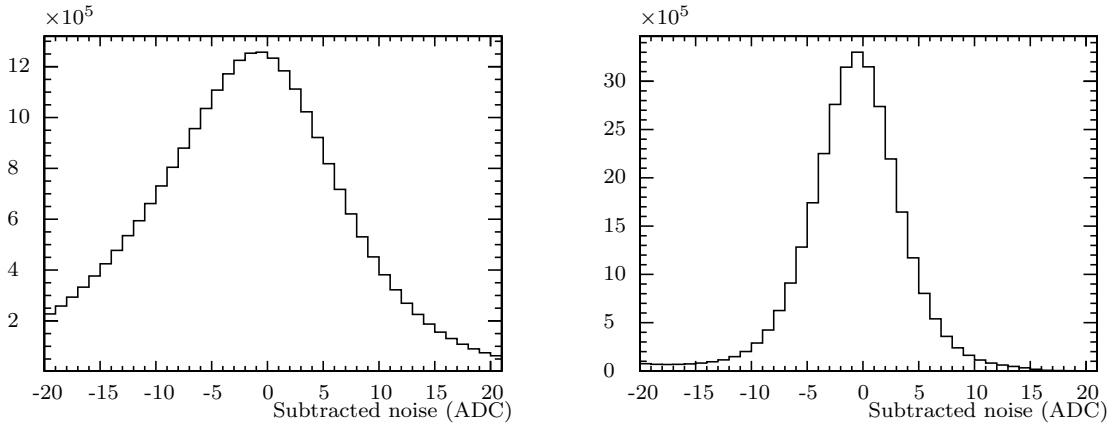

Fig. 8.26: Subtracted average noise distribution after pedestal correction for TRD1 (left) with a width of 7.65 ADC values and TRD2 (right) with a width of 3.46 ADC values at 8 GeV/c for 1775 V on the anode wires and a drift voltage of 500 V.

Tab. 8.5: Noise reduction cuts 2012

Cut name	TRD1	TRD2
covariance matrix	0.120	0.112
minimum amplitude (ADC values)	12	15
minimum integrated signal (ADC values)	25	25
hit time window (time-bin)	[10, 20]	[10, 20]

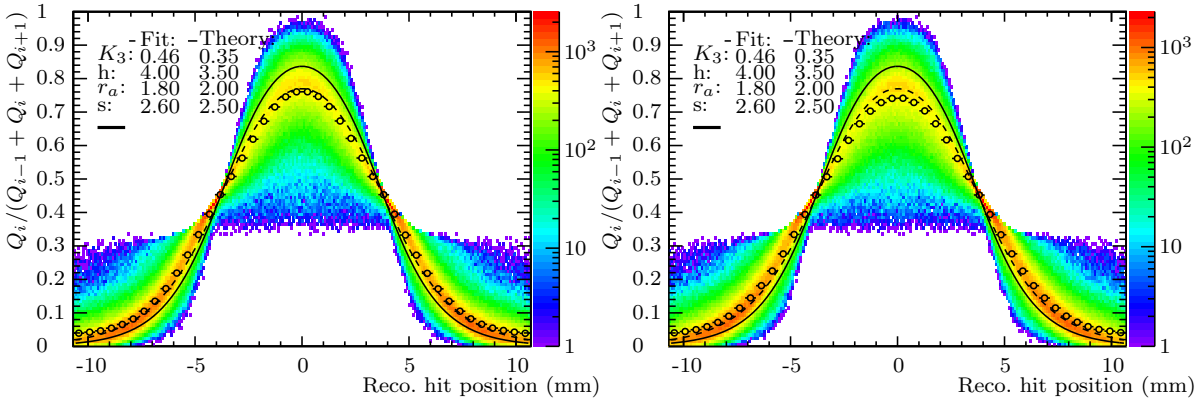

Fig. 8.27: PRF for TRD1 (left) and TRD2 (right) at 8 GeV/c for 1775 V on the anode wires and a drift voltage of 500 V. The average distributions have been fitted to the Mathieson formula (equation 4.36) given by the dashed line with the K_3 parametrization presented in equation 4.37. The theoretical prediction using $K_3 = 3.5$ according to the chamber parameters ($h = 3.5\,\text{mm}$, $r_a = 20\,\mu\text{m}$ and $s = 2.5\,\text{mm}$) is also shown for comparison (solid line).

be operated at the absolute lower limit of anode voltage to avoid signal overflows this might result the observed deviation of the PRF from the theoretical prediction. One other possible reason could be the flexible foil entrance window. It can be concluded that the essential MWPC parameters can not be estimated by fitting the average PRF to equation 4.36.

8.2.1. Particle Identification Performance

The average total event statistics per measurement (1,000,000-2,000,000) is 5-10 times higher compared to the previous beam test 2011. The PID reference detectors Cherenkov 1 and 2 as well as the Pb-glass calorimeter have been used to measure electron and pion spectra for different MWPC/radiator combinations. There are only additional PID cuts applied to identify electrons, muons and pions. These cuts are presented for one data set at 3 GeV/c in figure 8.28. Electrons and pions are requested to fulfill all three

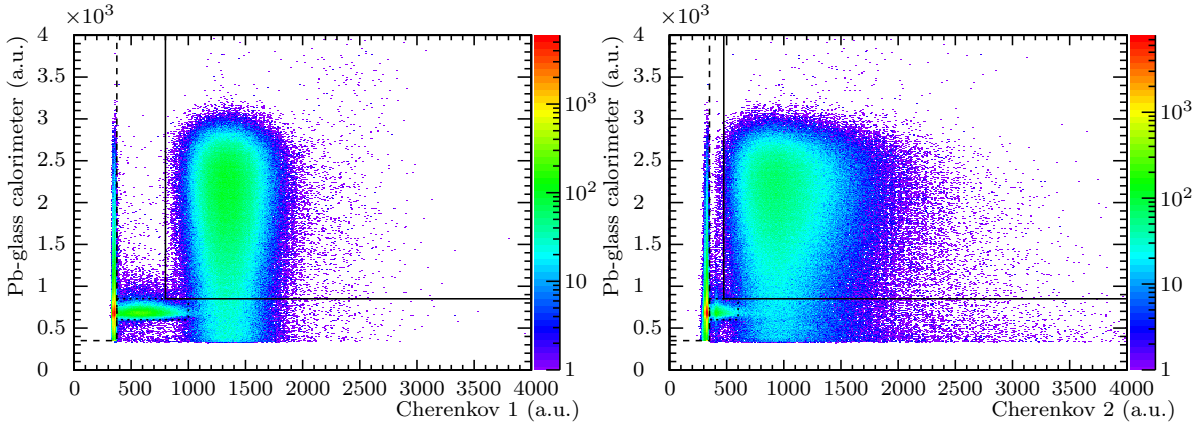

Fig. 8.28: Measured spectra for electrons, muons and pions at 3 GeV/c at a common CBM in beam test at CERN PS 2012. The cut conditions for electrons (Ch1 [800, 4000], Ch2 [475, 4000] and Pb-glass [850, 4000]) are represented by the solid lines, for pions (Ch1 [0, 375], Ch2 [0, 350] and Pb-glass [350, 4000]) by the dashed lines and the muons (Ch1 [375, 1000], Ch2 [350, 600] and Pb-glass [600, 850]) are surrounded by the pointed lines.

cut conditions for Cherenkov 1, 2 and the Pb-glass calorimeter. At the same time, the muons have only to be conform with at least one of the two Cherenkov conditions but always with the Pb-glass calorimeter thresholds. The 1-dim. spectra (same as in figure 8.28) of the different PID reference detectors are presented in figure 8.29 in comparison with a simple superposition of three independent Gaussian distributions describing the Cherenkov counter spectra up to 1600 ADC values. The distance of the fitted mean values of the superposition in multiples of the Gaussian distribution width σ gives a criterion of the separation and data efficiency of each detector for each particle listed in table 8.6. Since the applied cuts especially in case of electron cuts are highly asymmetric with respect to the fitted mean value of the distributions the values on the diagonal of table 8.6 b) are average of the upper and lower PID cut value.
The cut efficiencies ϵ_e (equation 8.8) and ϵ_π (equation 8.9) calculated for the PID reference spectra and PID cuts presented in figure 8.28 are

$$\epsilon_e < 2.9163\text{E-}04 \cdot 1.9191\text{E-}06 \cdot 1.1111\text{E-}01 \ll 1/\text{n events} \tag{8.12}$$

to find an electron within the pion sample with a data efficiency (selected electrons / all events) of 57.99% for electrons and

$$\epsilon_\pi < 9.7087\text{E-}03 \cdot 4.1493\text{E-}03 \cdot 4.2667\text{E-}06 \ll 1/\text{n events} \tag{8.13}$$

to misidentify an electron as pion with a data efficiency of 26.08% (pulser events are excluded). The purities of the two samples are below the expected efficiencies of the TRD prototypes and therefore sufficient for the following analysis.
The applied cuts on the TRD data are the following. Overflow events as well as underflow

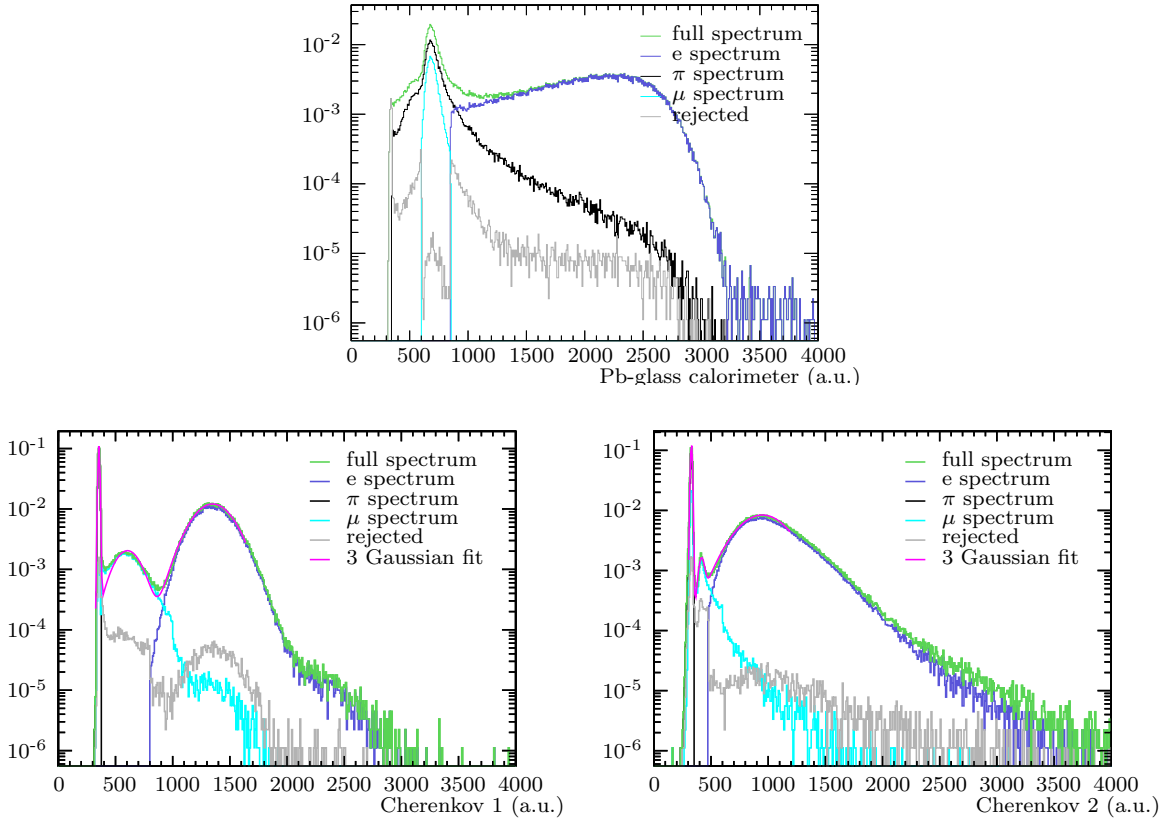

Fig. 8.29: Pb-glass calorimeter (upper) Cherenkov 1 (left) and 2 (right) spectra at 3 GeV/c are presented without PID cuts (green), for electrons (blue), pions (black) and excluded events (gray). The full distributions of both Cherenkov counters are fitted to the sum of three Gaussian distributions (pink).

Tab. 8.6: Particle separation efficiency for the three reference detector using 3 GeV/c data. Efficiency is represented by the distance between the fitted $mean_x$ values in multiples of the Gaussian distribution width σ_x ($|mean_x - mean_y| / \sigma_x$) in a). The distance between the fitted $mean_x$ and the closest PID cut value as multiples of the fitted Gaussian distribution width σ_x are presented in b)

	Cherenkov 1			Cherenkov 2		
a)	π	μ	e	π	μ	e
π	0.00	2.16	5.91	0.00	3.60	2.93
μ	33.23	0.00	4.43	10.88	0.00	2.52
e	132.29	6.43	0.00	76.96	21.87	0.00

	Cherenkov 1			Cherenkov 2		
b)	π	μ	e	π	μ	e
π	24.93	0.18	2.65	21.68	0.88	0.69
μ	30.53	2.70	1.16	8.24	5.13	0.28
e	129.58	3.02	9.51	74.32	14.35	8.32

events are included in the spectra. The electron and pion spectra measured at an anode voltage of 1775 V and a drift voltage of 500 V and a particle momentum of 3 GeV/c using the same radiator type made from POKALON with different number of foils are presented in figure 8.30. It can be seen comparing the pion spectra, that the pedestal and noise compensation works well, as does the calibration. The electron spectra mean value

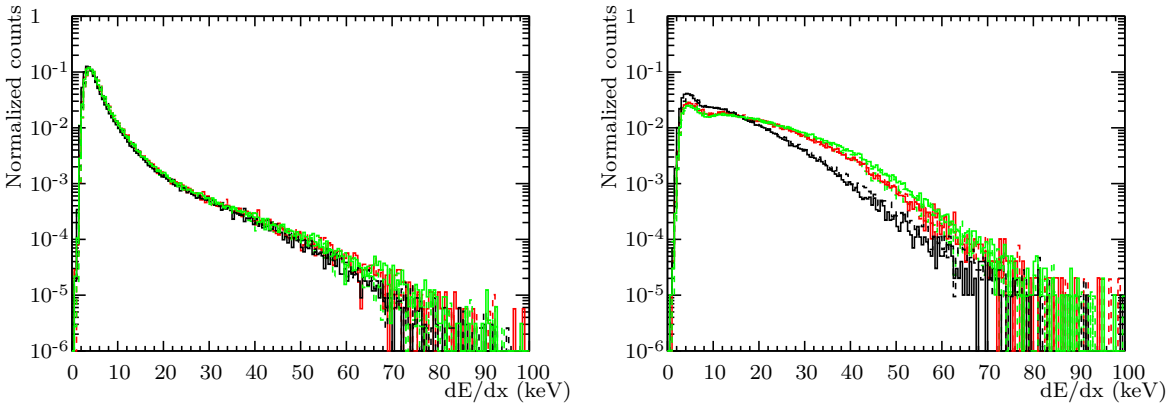

Fig. 8.30: Measured spectra for pions (left) and electrons (right) at 3 GeV/c using SPADICv0.3Rev2 at a common CBM in beam test at CERN PS 2012. An anode voltage of 1775 V and a drift voltage of 500 V was applied to the chambers. Solid lines represent measurements with classical radiator, dashed lines those with micro-structured radiator. Black curves correspond to $N_f = 100$, red to $N_f = 250$ and green to $N_f = 350$. The pion spectra are not affected by the radiator type or number of used foils, as expected. Both electron and pion spectra are in good agreement within small variations due to the energy calibration. The enhancement of the deposited TR-energy as function of increasing number of foils is clearly visible, but there is no difference between classical and micro-structured radiator.

is shifted with increasing number of foils as expected starting with the black ($N_f = 100$) over to the red ($N_f = 250$) and finally the green ($N_f = 350$) spectra. The dashed spectra correspond to the micro-structured self-supporting radiator K where the solid spectra have been measured using the classical radiator type B. This first comparison indicates a good agreement between both construction concepts which will be investigated in more detail later on.

The dynamic range of the SPADICv0.3Rev2 was investigated in more detail in order to get a better matching to the MWPC gain. This was done based on the calibrated pion spectra. The maximum reached amplitude of the highest channel is presented as function of the estimated total corresponding energy loss in figure 8.31. The onset of fragmented

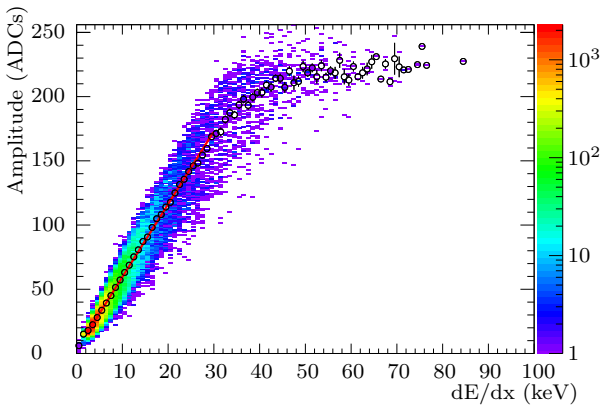

Fig. 8.31: Amplitude vs. dE/dx for 3 GeV/c pions 1775 V anode voltage and 500 V drift voltage measured with TRD R I SUSIBO 11 . The maximum amplitude for a given energy loss of a 3 GeV/c pion can be calculated according to a first order polynomial fit (red line) of the average values (open circles) by $f(x) = (5.673 \pm 0.045)x + (2.839 \pm 0.300)$.

signals in the ADC overflow is at 30 keV. In order to avoid signals in overflow for a measurement of an energy loss of 100 keV at highest chamber gain (1800 V anode voltage)

a SPADICv0.3 gain reduction of a factor 2.6 would be necessary assuming a linear signal amplification between 1 and an input signal corresponding to an energy loss of 100 keV. The results for different MWPC anode voltages are listed in table 8.7. The presented

Tab. 8.7: read-out electronic gain calibration using 3 GeV/c pions at variable detector gain settings. First order polynomial fit $f(x) = mx + b$ of dE/dx vs. max. amplitude distribution.

	Anode voltage (V)	m	b	ASIC gain red.
TRD R I				
	1750	4.924 ± 0.045	3.115 ± 0.310	1.94
	1775	5.673 ± 0.045	2.839 ± 0.300	2.23
	1800	6.553 ± 0.044	2.961 ± 0.291	2.57
TRD N II				
	1750	4.838 ± 0.047	2.488 ± 0.328	1.90
	1775	5.621 ± 0.046	1.998 ± 0.314	2.20
	1800	5.873 ± 0.043	2.332 ± 0.303	2.30

results can be cross-checked by comparing the overflow fraction (figure 8.32) and the ratio of the mean energy losses between electrons and pions ($\langle dE/dx_e \rangle$ / $\langle dE/dx_\pi \rangle$). The

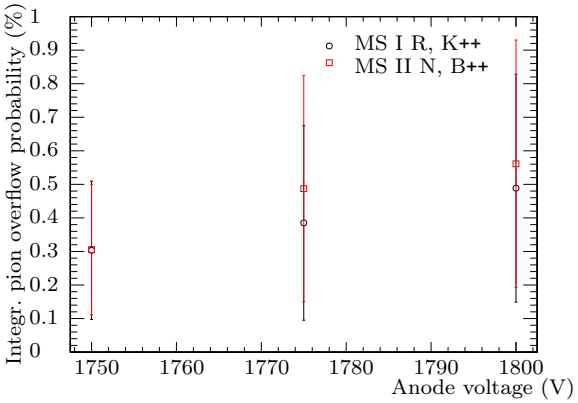

Fig. 8.32: Integrated pion overflow probability as function of anode voltage at 3 GeV/c for radiators K++ and B++.

overflow fraction increases from 0.3% at 1750 V to 0.5% and 0.55% respectively. The onset is not zero since the gain of SPADIC0.3 is not well matched to the chamber gain and a lower chamber gain is not preferable due to the relatively high noise level as presented before. Based on this observations an anode voltage setting of 1750 V was chosen for the following measurements as compromise between good signal to noise separation and increasing fraction of fragmented signals due to overflows. The ratio of the mean energy losses $\langle dE/dx_e \rangle$ / $\langle dE/dx_\pi \rangle$ is not sensitive to the chamber gain in the investigated range as well as the pion efficiency (presented in figure 8.33). Both are constant over the full range of anode voltages tested 2012. This observation is not trivial to explain since one would accept a correlation between a shape modification of the spectra to result in a modification of the pion efficiency. But the fraction of overflow signals is rather small (below 1% for pions) and therefore the influence on the pion efficiency negligible. The radiator performance at different particle momenta will be investigated in the following. The integrated pion signal overflow probability (figure 8.34) is used to monitor the stability of the chamber gain during the measurements. All measurements

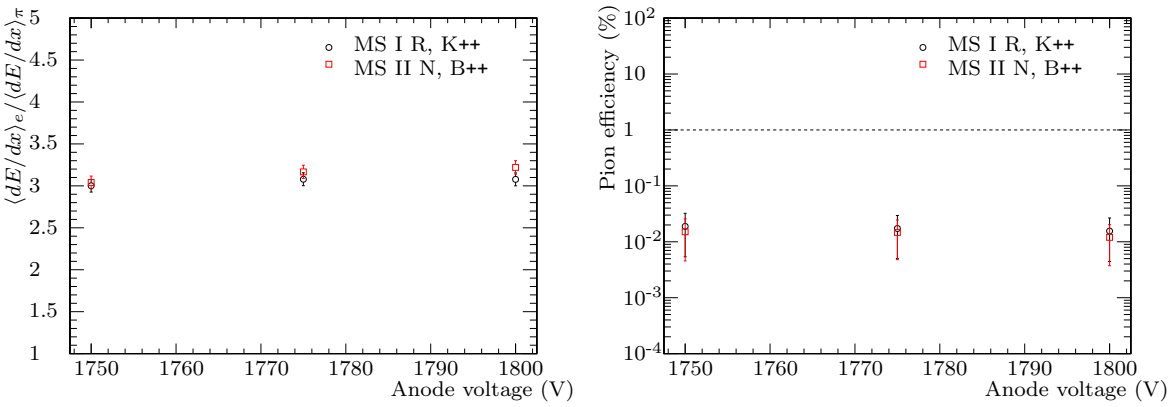

Fig. 8.33: Ratio of the mean energy losses $\langle dE/dx_e \rangle / \langle dE/dx_\pi \rangle$ (left) and the final pion efficiency at 90% electron efficiency with 10 detector hits (right) as function of anode voltage at 3 GeV/c for radiators K++ and B++.

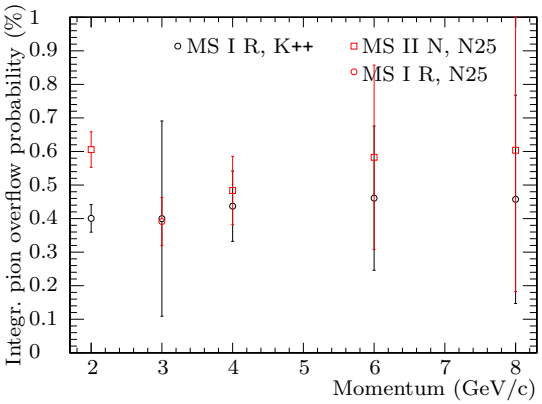

Fig. 8.34: Integrated pion overflow probability as function of particle momentum for radiators K++ and N25.

except 3 GeV/c were done consecutively. The gain during these measurements can be assumed to be stable within the error bars. The performance of the radiators as function of the particle momentum is presented in figure 8.35. The measured pion efficiency is

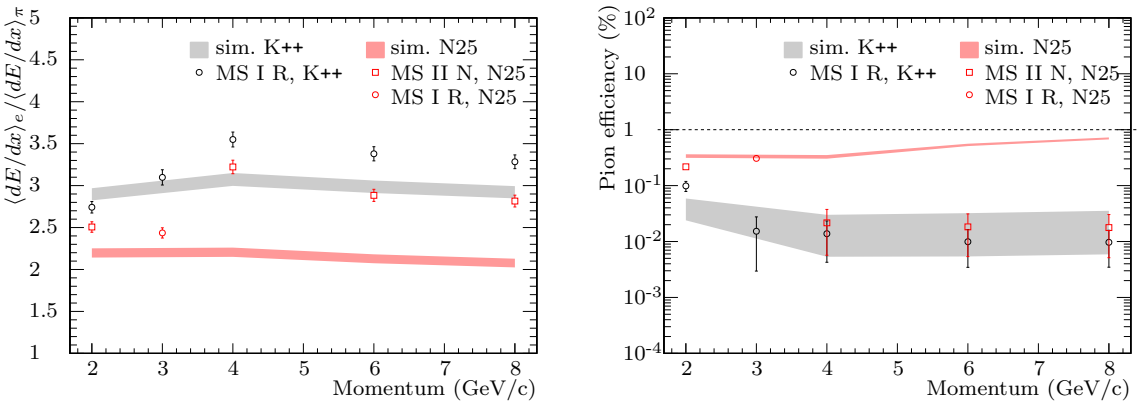

Fig. 8.35: Ratio of the mean energy losses $\langle dE/dx_e \rangle / \langle dE/dx_\pi \rangle$ (left) and the final pion efficiency at 90% electron efficiency with 10 detector hits (right) as function of particle momentum using radiators K++ and N25. The simulation has been tuned to fit the spectra shape at 3 GeV/c.

enhanced between 2 and 4 GeV/c for both radiators. The irregular radiator N25 was

only used on TRD R I at 3 GeV/c, which allows for a comparison of the two MWPC performances. It can be seen that the point for N25 at 3 GeV/c breaks the tendency of the measurements performed with TRD N II. The simulation has been tuned to fit the spectra shape at 3 GeV/c for both radiators. The tendency of the pion efficiency is well described for the regular prototype K++ where a larger discrepancy was found in case of the irregular foam radiator N25. This leads to the conclusion that the parametrization of irregular radiators by a regular model radiator at a single momentum is not sufficient for a full radiator simulation. The integrated pion overflow probability presented in figure 8.36 can be used as reference for the noise level (figure 8.26), ASIC pedestal stability and quality of the spectrum calibration (figure 8.30). A constant fraction of overflow

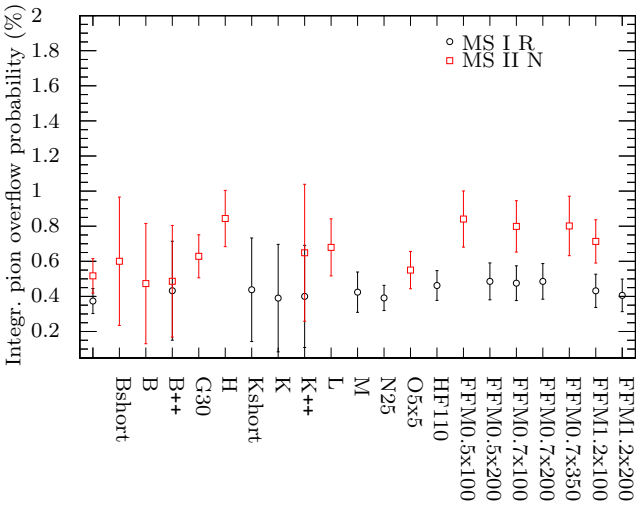

Fig. 8.36: Radiator comparison: Integrated pion overflow probability

signals within the error bars is found for each MWPC prototype, which indicates a good comparability due to gain and pedestal stability during the measurements. The ratio of the mean energy losses $\langle dE/dx_e \rangle / \langle dE/dx_\pi \rangle$ for the different radiator prototypes which have been tested at CERN PS T9 2012 are presented in figure 8.37. First of all, a

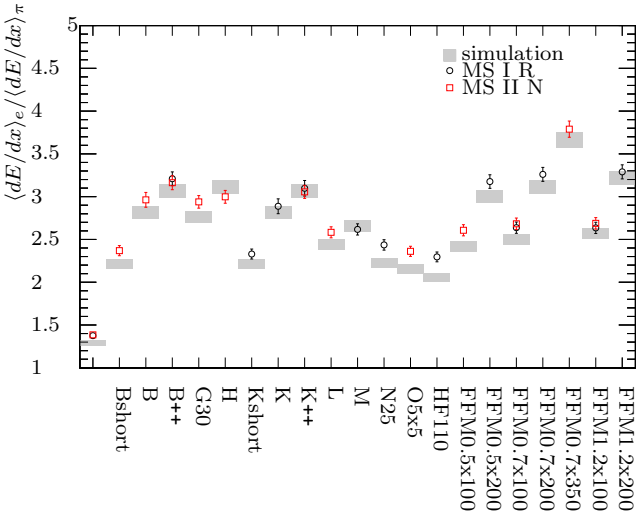

Fig. 8.37: Comparison of $\langle dE/dx \rangle_e / \langle dE/dx \rangle_\pi$ ratios for different radiator prototypes at 3 GeV/c.

good matching between simulation and measurement was found, where the simulation

is always below the measured ratio. Comparing this to the final pion efficiency at 90% electron efficiency with 10 detector hits (see figure 8.38) a good agreement for most regular prototypes between simulation and measurement within the errors is found. The spreading in case of irregular prototypes extends. The minimum number of detector hits

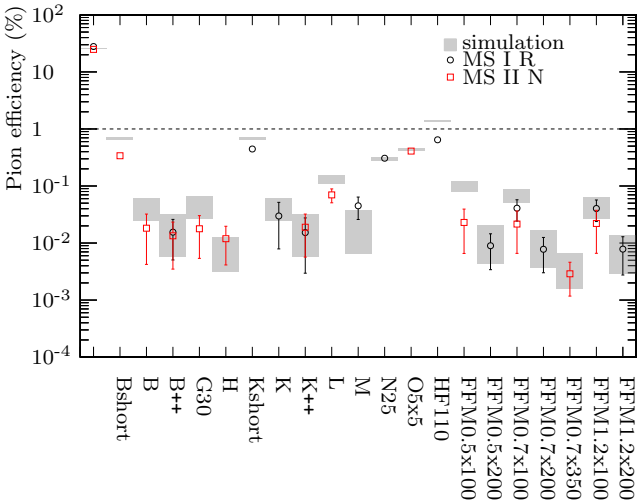

Fig. 8.38: Radiator comparison of the pion efficiency at 90% electron efficiency with 10 detector hits

per track to achieve the CBM TRD design goal of 1% pion efficiency at 90% electron efficiency for the different radiator prototypes is summarized in figure 8.39. It can be seen

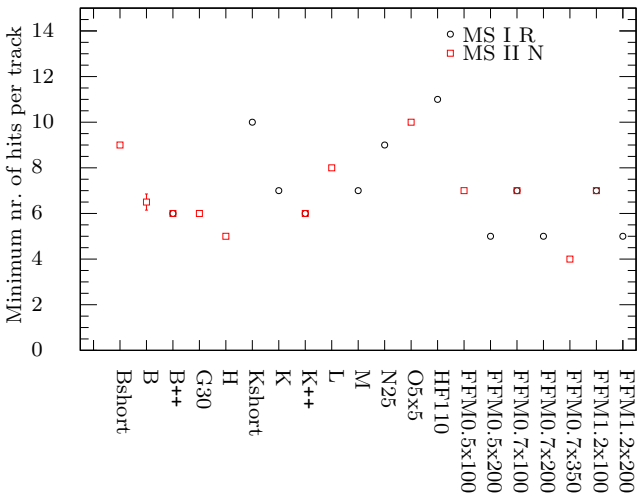

Fig. 8.39: Radiator comparison: Minimum number of detector hits to reach 1% pion efficiency at 90% electron efficiency

that the most efficient radiator is a regular radiator made from PE-foil. Such a radiator is not an option for the CBM experiment since the foil support frames increase the material budget of the TRD to a value which can not be tolerated. The best self-supporting candidates are G30 (PP-fibers), H (PE foam foils) and K++ (regular micro-structured POKALON foil). Considering the pure material price, this excludes the PP-fibers as well as the POKALON foil. The ongoing efforts to transfer the progress on the field of regular micro-structured self-supporting radiators from POKALON based prototypes to

PP or PE foil based radiators have not reached a status allowing an in-beam test, yet. The theoretical regular radiator description was tested using radiators with different number of foils and gap dimensions at fixed foil material for particles at 3 GeV/c. The ratio of average electron dE/dx and pion dE/dx as function of N_f and l_2 are presented in figure 8.40. Both data sets show good agreement between the measurement and the

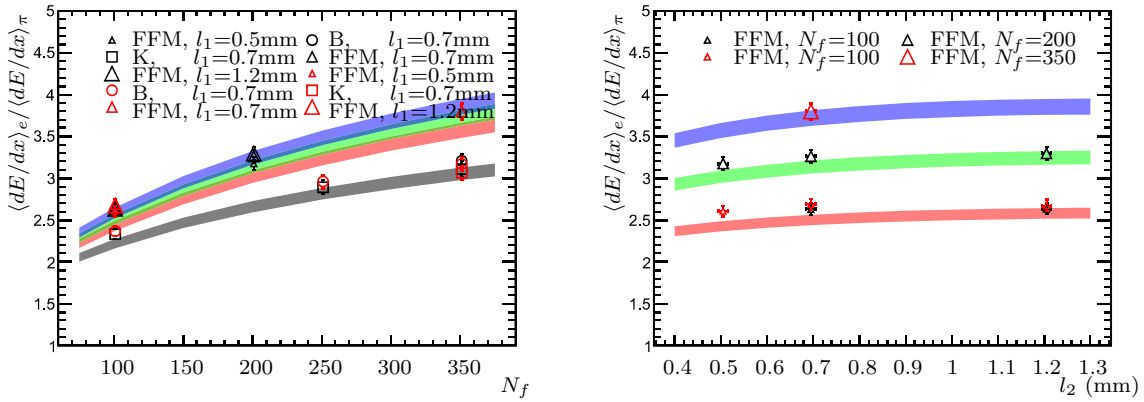

Fig. 8.40: Ratio of average electron dE/dx and pion dE/dx as function of N_f (left) and l_2 (right). **Left:** Simulation of POKALON 24 μm foil and 700 μm gap (■). FFM radiator simulations for l_2 =500 μm (■), l_2 =700 μm (■) and l_2 =1200 μm (■) at 20 μm foil thickness. **Right:** FFM radiator simulations are shown for N_f =100 (■), N_f =200 (■) and N_f =350 (■) at 20 μm foil thickness. Black symbols correspond to measurements done with TRD I R, where red symbols are related to TRD II N measurements.

simulation. The pion efficiency for 10 detector hits per track as function of N_f and l_2 at 90% electron efficiency is shown in figure 8.41. The approximated pion efficiency based

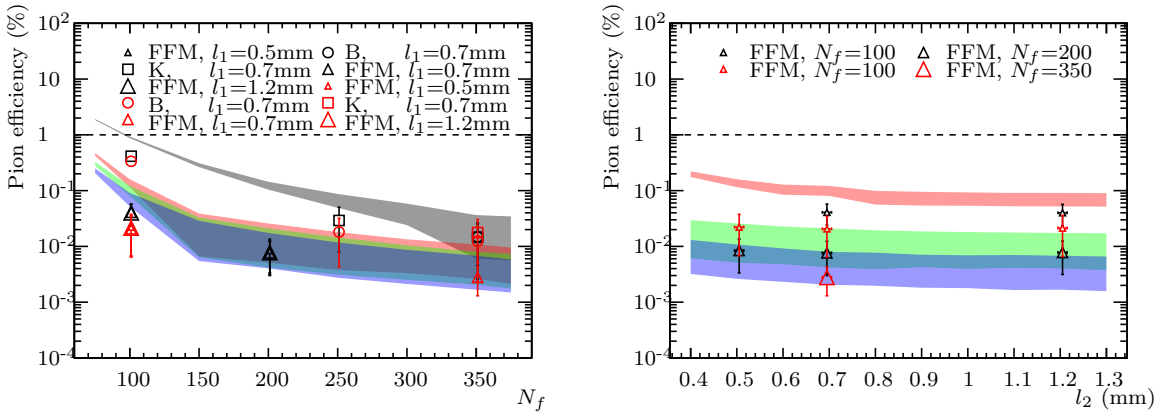

Fig. 8.41: Pion efficiency for 10 detector hits per track as function of N_f (left) and l_2 (right) at 90% electron efficiency. **Left:** Simulation of POKALON 24 μm foil and 700 μm gap (■). FFM radiator simulations for l_2 =500 μm (■), l_2 =700 μm (■) and l_2 =1200 μm (■) at 20 μm foil thickness. **Right:** FFM radiator simulations are shown for N_f =100 (■), N_f =200 (■) and N_f =350 (■) at 20 μm foil thickness. Black symbols correspond to measurements done with TRD I R, where red symbols are related to TRD II N measurements.

on the measured spectra as function of N_f is matching well with the simulated values, where the l_2 parameter scan especially for small radiators ($N_f < 200$) has a large offset. Since the MC simulation from above assumes a perfect geometrical acceptance which is never given in a real detector environment, a realistic detector acceptance has to be taken into account in addition. A first approximation can be derived from the geometry $v12f$ in

CbmRoot. The distribution of the number of TRD-points per MC-track can be used as input for the MC simulation as described in chapter 4.4. Instead of using a fixed number of layers for the Likelihood method one can use a random number of layers following the MC-TRD-point distribution per MC-track taken from CbmRoot. This results in a first estimation on the PID performance of the TRD within a fixed momentum bin. The next step would be to implement simulated or measured TR-spectra for all relevant momentum bins into CbmRoot and use the framework itself to simulate the total PID performance. The discrepancy between the simulated and measured electron spectra was compensated by a scaling factor which was estimated in 2011 and 2012 individually. The results are presented in table 8.8 in comparison with different radiator parameters like solid structure and gap dimensions.

Tab. 8.8: All radiator prototypes: Material, solid structure l_1 or $\langle l_1 \rangle$, gap dimensions l_2 or $\langle l_2 \rangle$ and scaling factor for best simulation to measurement agreement based on the parameters listed in table 6.2 and 6.5. Some radiator prototypes have been built between 2011 and 2012 and have therefore not been tested in 2011. And some existing radiators have not been tested due to limitations in time during the in beam test 2012.

Name	Material	l_1 or $\langle l_1 \rangle$ (μm)	l_2 or $\langle l_2 \rangle$ (μm)	Scaling factor 2011	2012
A	PP fiber (LRP 375 BK)	17	50	0.65	-
	Rohacell HF71	8	75		
Bshort	POKALON N470	24	700	-	0.65
B	POKALON N470	24	700	0.55	0.65
B++	POKALON N470	24	700	-	0.65
C	Polypropylene	15	700	0.31	-
D	Polypropylene	15	700	0.45	-
E	Polyethylene	20	500	0.65	-
F	Polyethylene	20	250	0.66	-
G10	PP fiber	17	50	0.70	-
G20	PP fiber	17	50	0.79	-
G30	PP fiber (LRP 375 BK)	17	50	0.80	0.78
H	PE foam (Cell-Air)	12	900	0.50	0.78
H++	PE foam (Cell-Air)	12	900	0.50	-
I(p,u)	POKALON N470	24	613	0.46, 0.55	-
	PE foam	12	550		-
J	PE fibers	10	900	0.20	-
Kshort	POKALON N470	24	700	-	0.65
K	POKALON N470	24	700	-	0.65
K++	POKALON N470	24	700	-	0.65
L	PE foam (Cell-Air)	24	2000	-	0.60
M	PE foam (Cell-Air)	12	600	-	0.50
N25	PE foam	15	1400	-	0.42
O5x5	PE foam	15	1400	-	0.39
WF110	Rohacell WF110	25	700	-	-
HF110	Rohacell HF110	8	45	-	0.65
3xEF700	Rohacell EF700	35	800	-	0.40

There is no clear correlation between the weighting factors and other radiator parameters.

8.2.2. Position Resolution

The position resolution of a detector can be estimated in different ways. If no external position reference is available, the deviation of the reconstructed track positions in at least two identical detectors can be used. In case of a test beam setup including an external position reference system or more than two position sensitive detectors, a straight line tracking approach can be chosen. The usable position sensitive detectors included in the beam test 2012 at CERN are presented in figure 8.42. For the following analysis

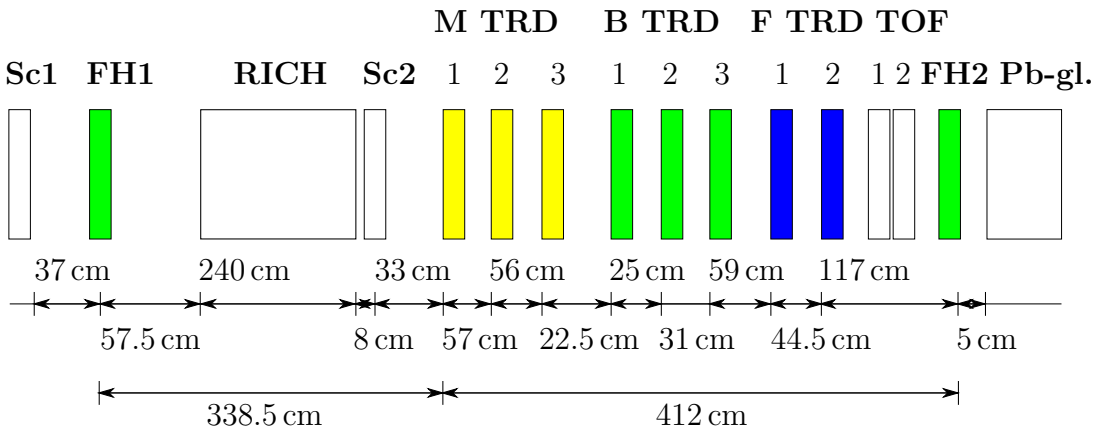

Fig. 8.42: Sketch of the setup (figure 8.18) with special focus on tracking devices. The global reference system composed of fiber hodoscope 1 and 2 (FH1 and FH2) and the eight TRD prototypes under test; three TRDs from Münster (M TRD 1-3), three prototypes from Bucharest (B TRD 1-3) and two MWPCs from Frankfurt (F TRD 1,2). Detectors providing x and y-coordinates are green where prototypes measuring only the x component are yellow and those reconstructing the y-coordinate are colored in blue.

are the two first identical TRD from Münster and the two fiber-hodoscopes used. The two fiber-hodoscopes with an active area of $64 \times 64\,\mathrm{mm}^2$ consist of two arms (x and y-direction). Each arm is composed of 64×4 scintillating fibers with a fiber diameter of 1 mm. The data provided by the two fiber-hodoscopes are used as external position reference system as well as trigger system. The reconstructed beam profiles of the reference system at a momentum of 8 GeV/c are presented in figure 8.43. The first reconstructed

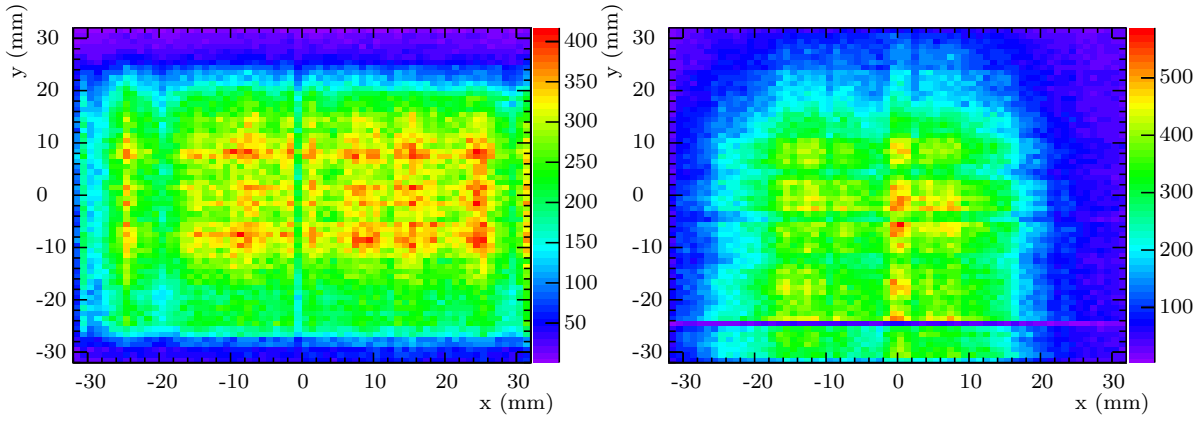

Fig. 8.43: Reconstructed beam profiles by first (left) and second (right) fiber-hodoscope at 8 GeV/c.

beam profile fills an area larger than the active area of the first fiber-hodoscope. The

profile is homogeneous in the central part. After passing 7.5 m between the two fiber-hodoscopes and the included material budget of the RICH, scintillator 2, the eight TRD detectors and two TOF RPC prototypes the second beam profile is approximated. It can be seen that the beam profile has diminished in x-direction. This indicates a not perfectly parallel beam optic. Under the assumption that the full beam profile is visible in the first hodoscope the horizontal beam width can approximate to be 60 mm. In the second hodoscope the width is estimated to 45 mm. There are two scenarios possible. First the beam focus is between the two fiber-hodoscopes or behind the setup. Since the beam optic was adjusted to *parallel* beam optic, the first option can be excluded. Based on the distance between the two hodoscopes and the width of the reconstructed beam profiles, a lower limit on the narrowing of the beam of 2.00 mm/m or a relative angle between the particles in the boundary area of the beam profile relative to the central ones of 0.057° can be calculated. Following this, the beam focus is at least 30 m downstream relative to the position of the first hodoscope at 8 GeV/c. The position resolution of the external fiber hodoscope system is approximated after misalignment compensation to be 5.41 ± 0.68 mm in horizontal and 5.71 ± 0.76 mm in vertical direction (compare to figure 8.44) based on the residual distribution of the relative reconstructed track position deviation. The width of the distribution is divided by $\sqrt{2}$, since the width

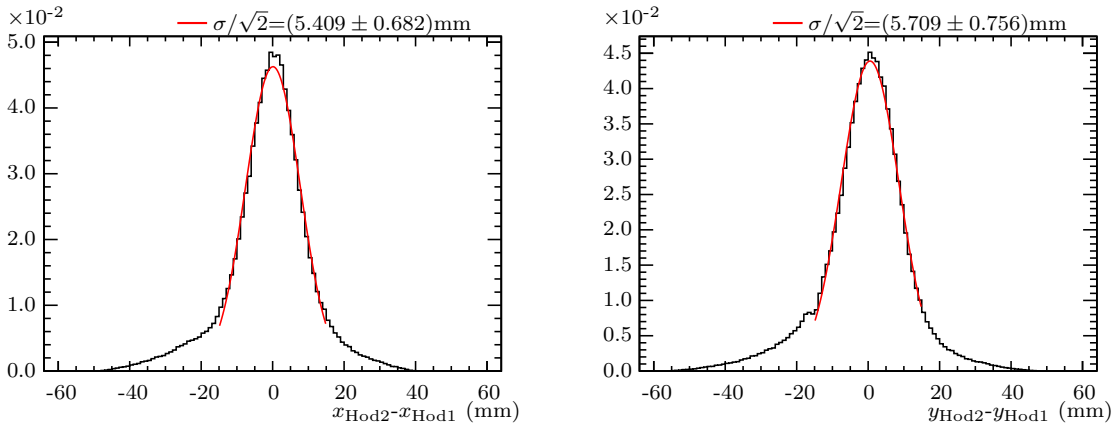

Fig. 8.44: Reconstructed position resolution after misalignment and beam focus compensation of the full hodoscope system in x- (left) and y-direction (right) at 8 GeV/c.

results from the position resolution of two identical detectors. Comparing the results with the theoretical resolution limit of $1\,\text{mm}/\sqrt{12} = 0.29\,\text{mm}$ which was confirmed by a reference measurement at COSY 2012 [Rei12] a rather large discrepancy is found. From this discrepancy it is possible to get a rough approximation of the homogeneous radiation length equivalent of the setup between the two hodoscopes using the modified Highland-Lynch-Dahl approximation [Hig75] used in GEANT4 [Gea].

$$\theta_{proj}^{rms} = \frac{13.6\,\text{MeV}}{\beta pc} z \sqrt{\frac{X}{X_0}} \left[1 + 0.038 \ln\left(\frac{X}{X_0}\right)\right] \tag{8.14}$$

Here θ_{proj}^{rms} is the width of the projected angle distribution (which is approximately Gaussian distributed for small scattering angles), p, βc and z are the momentum, velocity and charge number of the incident particle, and X/X_0 is the true path length in radiation length unit. The mean width of the scattering angle distribution is assumed to be 0.039° resulting in a single object with a homogeneous radiation length X/X_0 of 18.3%, filling the space between the two fiber-hodoscopes. This value is rather small compared to the

real material budget. The homogeneous material approximation implies continuous scattering with a lower total material budget. The scattering of the particles in the real setup arises manly at restricted position in the setup with large free path length in between.

To get a first approximation on systematical misalignment of the two identical MWPC prototypes from Münster the correlation between the measured position of the same track in both chambers is used. Such a correlation distribution of the channels providing the highest integrated signal per event for both chambers within the same event is presented in figure 8.45. This representation gives a first estimation on systematic misalignments

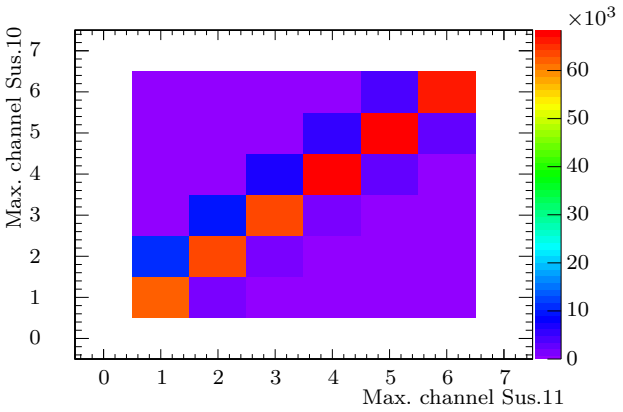

Fig. 8.45: Correlation of channels with the highest integrated signal in both chambers at 8 GeV/c. An anode voltage of 1775 V and a drift voltage of 500 V was applied. Radiator N25 and K++ have been used.

of both detectors. A more detailed analysis of geometric misalignments can be done by correlation of the reconstructed hit position within both chambers. Events which are only seen by a signal chamber are ignored as well as events with maximum amplitude on the first or the last pad (reduction of the active area by 1/4). The efficiency to see a single in both chambers for one particle track was around 28%, where the single detection efficiency was around 40% per chamber. The efficiencies were rather small, since a triggered read-out chain consisting of a SPADIC 0.3Rev3 SUSIBO combination was used with a rather high minimum amplitude threshold presented in table 8.5. The trigger was provided by the two fiber hodoscopes with a relatively high dark count rate. The correlation between both chambers is clear, which points to a good relative alignment of both pad-planes.

The horizontal beam profiles of the hodoscopes are now compared to the beam profile estimated based on the TRD data to find the best suited algorithm. The TRD prototypes from Münster reading 8 pads in one row provide an active area of $57 \times 75\,\mathrm{mm}^2$. The reconstructed beam profile applying four different reconstruction algorithms are presented in figure 8.46. There are obviously large discrepancies between the reconstructed beam profiles using the four different algorithms presented in chapter 4.3. There is a clear overestimation in the central region of each pad by the weighted displacement and Gaussian approximation approach where the PRF fit and SECHS algorithm showing less systematic effects and a more homogeneous beam distribution which are in good agreement with the horizontal beam profiles provided by the two hodoscopes.

The following step is the precise alignment determination and misalignment compensation, which is done using the presented different position reconstruction algorithms. The compensation is done based on a linear fit ($f(x) = a \cdot x + b$) of the average relative deviation of the central pads which gives information about parallel displacement

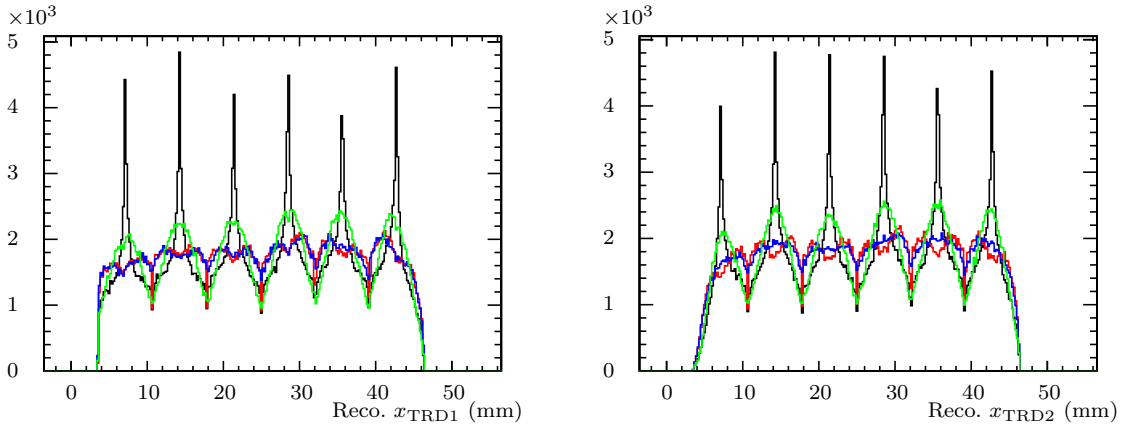

Fig. 8.46: Reconstructed beam profiles using four different reconstruction algorithms at 8 GeV/c. The TRDs are operated at 1775 V on the anode wires and a drift voltage of 500 V. TRD1 is used in combination with radiator N25 and TRD2 with radiator K++. The first reconstruction algorithm is based on simple Gaussian approximation described by equation 4.46 (green line), second approach is based on a weighted Gaussian approximation given by equation 4.49 (black line). Also a PRF based fitting function with two bound parameters as represented by equation 4.36 (red line) is tested. The hyperbolic secant squared (SECHS) approximation as presented in equation 4.52 (blue line).

of the pad-planes along the wire direction (constant term of the fit) as well as a rotation around the axis perpendicular to the wire direction and the beam axis of one or both chambers (slope of the fit function). Any other displacement of both chambers due to rotation or shifts along the other axis can not be estimated based on a linear fit. Systematic effects from the reconstruction algorithm itself should appear periodically for each pad. These effects are estimated and compensated therefore based on a fit like $f(x) = c \cdot \sin(d \cdot x + e)$. The relative compensated deviation of the two reconstructed positions is drawn as function of one of the reconstructed positions after misalignment compensation in figure 8.47 in combination with the resulting residual distribution. The systematic effects of the different algorithms can not be fully compensated, which results in non physical structures within the presented alignment histograms. Especially the cross like structure of the weighted displacement is leading to a systematic decrease in position resolution. Since the PRF fit is leading to the smallest systematic effects and at the same time a reasonably good position reconstruction accuracy it was used as default position reconstruction algorithm. The other three algorithms have been used to approximate the average error of position resolution. The accuracy of the reconstructed x-coordinates are approximated by a Gaussian fit to the residual distributions of the hodoscope and TRD detectors. The width of the distribution is divided by $\sqrt{2}$, since the width results from the position resolution of two identical detectors. A systematic cross check is performed by an iterative linear fit tracking approach with five iteration steps to compensate for detector misalignments. Hodoscope 1 and 2 are used in combination with the two TRD prototypes from Münster. The z-positions (presented in figure 8.42) are fixed and assumed to be well known. The deviation of the individual reconstructed coordinates from the fitted track is used to determine the position resolution of each detector. The presented values correspond to the mean value of both detectors. The position resolution as function of the particle momentum is presented in figure 8.48. The tracking approach is assumed to be insensitive to beam optic effects. The comparison of the position resolution estimated with the straight line fit algorithm of 0.608 ± 0.085 mm and the residuals of both TRD prototypes (0.660 ± 0.021 mm) gives an indication on

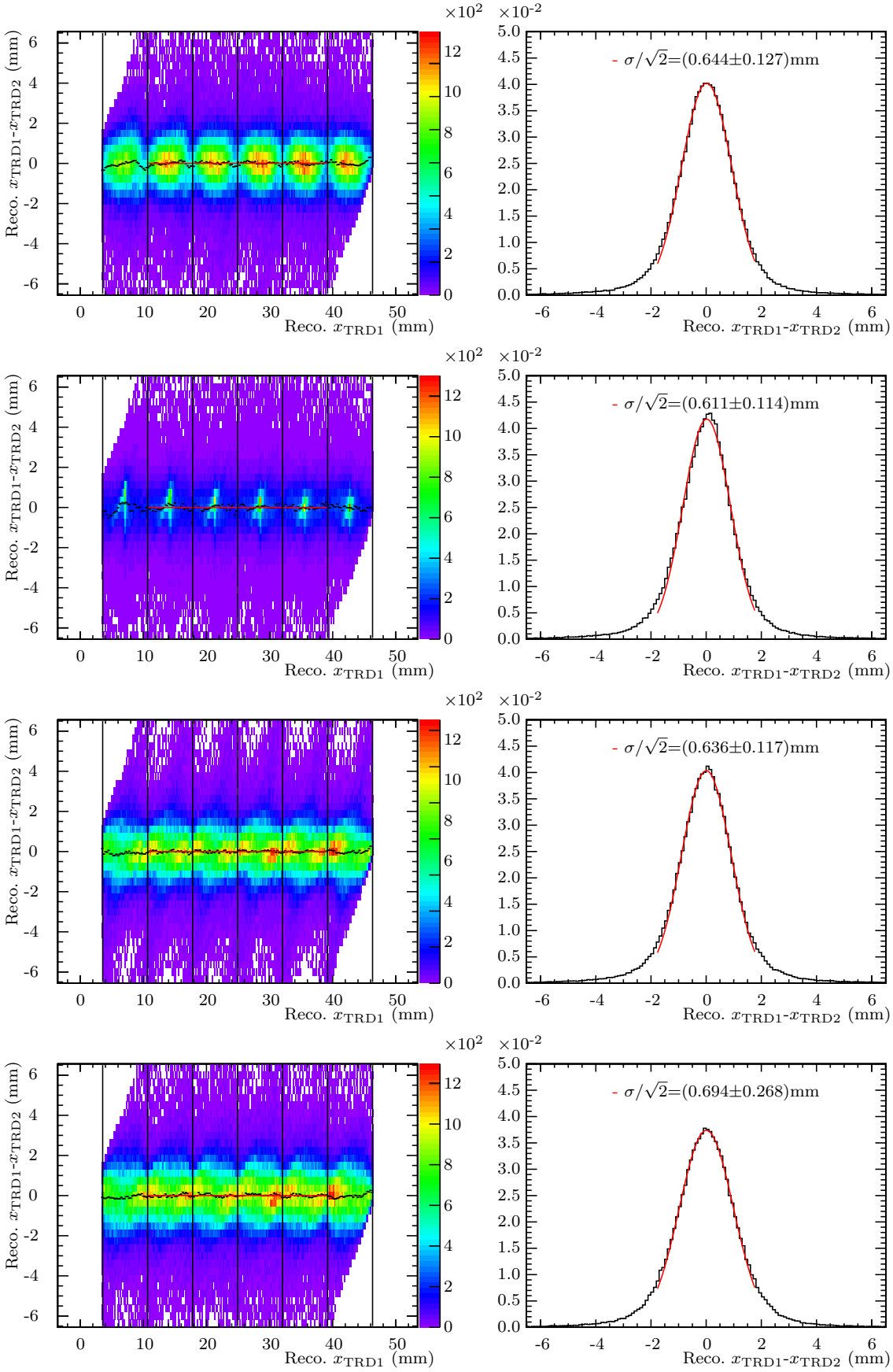

Fig. 8.47: Position resolution is estimated after misalignment compensation based on residuals of the first two identical prototypes. An anode voltage of 1775 V and a drift voltage of 500 V was applied. Radiator N25 and K++ have been used. The following algorithms have been used: **First row:** Gaussian approximation, **Second row:** weighted displacement, **Third row:** PRF fit and **Fourth row:** SECHS.

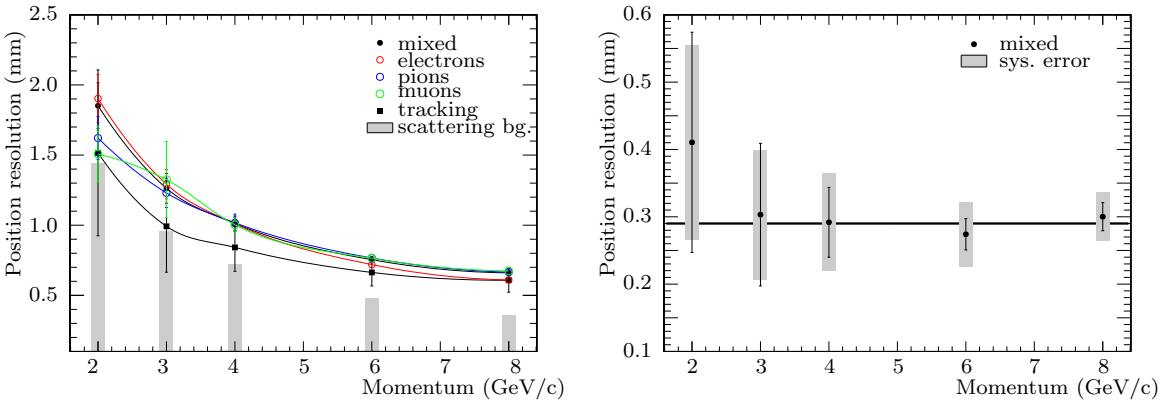

Fig. 8.48: Position resolution as function of particle momentum at an anode voltage of 1775 V and 500 V drift voltage using PRF fit. The position resolution represented by circles is estimated after misalignment compensation based on residuals of the first two identical prototypes where position resolution represented by squares is estimated based on a linear track fit with iterative misalignment compensation and including data from the two FH as external position reference (left). The gray boxes correspond to the simulated mean displacement between the track crossing TRD1 and TRD2 Δx_{scat} due to beam scattering within the material budget. Position resolution using PRF fit for mixed particle beam at an anode voltage of 1775 V including misalignment compensation based on residuals of TRD1 and TRD2 after scattering compensation (right). The resulting position resolution is $290 \pm 15\,\mu$m estimated by a constant fitting function. The systematic uncertainties (10% of Δx_{scat}) of the simulation are visualized by gray boxes. The errors of the data points include fitting errors and statistical uncertainties.

the influence of the beam optic on the residual algorithm, which is of the order of 10% for a relative detector distance of 57 cm. In addition, the broadening of the residual distribution due to scattering can be approximated for a mixed electron, myon and pion beam (1:1:1) using equation 8.14. The used approximation is assumed to be accurate within 10% [Gea]. The scattering angle distribution is assumed to be Gaussian distributed. There are three main material budgets within the RICH in front of the first two TRD prototypes: two gas windows made from 2 mm PMMA ($X/X_0 = 2 \times 0.58\%$) and the 6 mm SIMAX glass mirror ($X/X_0 = 5.1\%$), 168.45 cm behind the entrance window. Also the two scintillators with $X/X_0 = 2 \times 3.0\%$ as well as the first fiber-hodoscope ($X/X_0 = 2.0\%$) and the first TRD prototype with $X/X_0 = 1.54\%$ and radiator N25 ($X/X_0 = 1.5\%$) and K++ ($X/X_0 = 3.09\%$) are taken into account. The relative positions of all components are depicted in figure 8.42. Dimensions and radiation lengths of the detectors and radiators are listed in appendix C and section 5.8 respectively. The total radiation length in front of TRD2 is approximated to be 20.39% which is already 2.09% above the approximation of an object with a homogeneously distributed radiation length between the two hodoscopes, which was done based on the residual broadening observed in the hodoscope at 8 GeV/c relative to a reference measurement. Multiple scattering within the air between the detectors is neglected. The scattering angle distribution is assumed to be Gaussian distributed. The mean displacement between the track crossing TRD1 and TRD2 Δx_{scat} is calculated based on the presented radiation length and particle momentum at 2 GeV/c, 3 GeV/c, 4 GeV/c, 6 GeV/c, and 8 GeV/c to be 1.441 mm, 0.960 mm, 0.720 mm, 0.480 mm, and 0.360 mm. A constant position resolution based on the residual distribution of the two TRD prototypes of 0.290 ± 0.015 mm (constant fit after systematic uncertainty due to scattering subtraction: 0.290 ± 0.015 mm) can be estimated by taking the systematic uncertainties due to scattering within all detector

material in front of TRD2 into account. The systematic uncertainties do not cover the full material budget between the reference detectors and are therefore not comparable to the results obtained with the tracking approach. The exponential decrease of position resolution can be interpreted as result from the non vanishing material budget of the RICH and other detectors in front of the TRD prototypes leading to a momentum dependent scattering cross section. The influence of the focused beam optic seems to be rather small at a level of 10%. The position resolution as function of the chamber anode voltage is presented in figure 8.49. The influence of a variation of the anode voltage

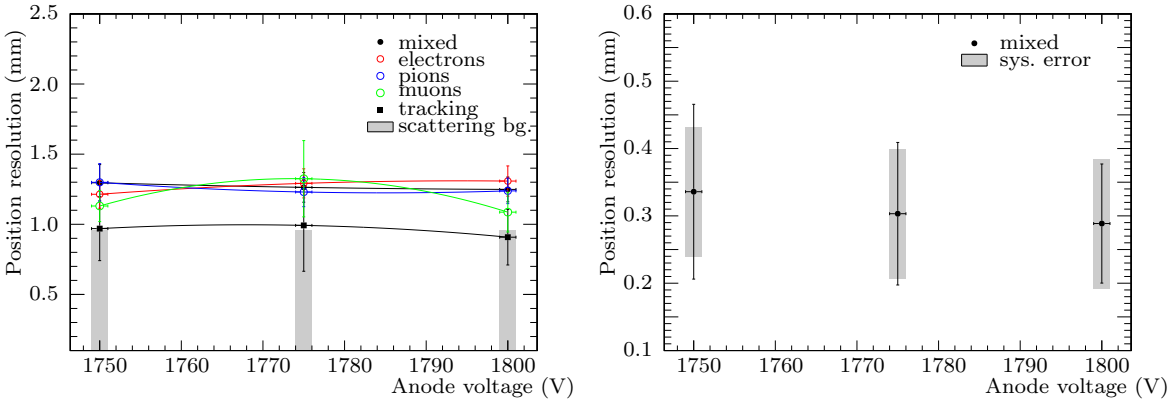

Fig. 8.49: Position resolution as function of anode voltage at 3 GeV/c and 500 V drift voltage using PRF fit. The position resolution represented by circles is estimated after misalignment compensation based on residuals of the first two identical prototypes where position resolution represented by squares is estimated based on a linear track fit with iterative misalignment compensation and including data from the two FH as external position reference (left). The gray boxes correspond to the simulated mean displacement between the track crossing TRD1 and TRD2 Δx_{scat} due to beam scattering within the material budget. Position resolution using PRF fit for mixed particle beam including misalignment compensation based on residuals of TRD1 and TRD2 after scattering compensation (right). The systematic uncertainties (10% of Δx_{scat}) of the simulation are visualized by gray boxes. The errors of the data points include fitting errors and statistical uncertainties.

between 1750 and 1800 V is not leading to a significant change of the position resolution at 3 GeV/c within the errors. The increasing gain should lead to an increase of signal to noise ratio resulting in a higher position reconstruction accuracy in theory. The very low effect can be interpreted to be due to the fact that the ASIC dynamic range is already saturated at lowest chamber gain settings. This would result in a constant signal but increasing overflow fraction as already presented in figure 8.32. The signal range is saturated and for gain independent constant noise this would lead to a constant signal to noise ratio. Tracking and alignment approach agree within the statistical uncertainties.

9. Summary & Outlook

The focus of this thesis is the development of a Transition Radiation Detector (TRD) for the Compressed Baryonic Matter (CBM) experiment at FAIR. The TRD sub-detector will contribute to the global particle identification and track reconstruction of charged particles. The technical design goal for the TRD is to identify 90% electrons with a maximum pion contamination of 1%. The TRD and Ring Image CHerenkov (RICH) detector should reach a common pion rejection of 10^4, in order to measure charmonium and low-mass vector mesons. The position resolution should be between 200 and 300 μm in the anode wire direction. The most demanding aspect of the CBM TRD design is the high interaction rate of up to 10^7 Hz resulting in a charged particle rate of up to 100 kHz/cm^2 in the central part of the detector planes at SIS300 conditions. It is crucial to find the optimal radiator detector combination with a minimum material budget to limit scattering and background due to conversions and at the same time reach a sufficient pion rejection and position resolution.

In this thesis it is confirmed that a Multi-Wire Proportional Counter (MWPC) with a Xe/CO_2 gas thickness of 12 mm provides sufficient absorption probability for TR-photons in combination with self-supporting low density PE foam or micro-structured foil radiators. A continuous investigation aiming at an optimal wire and pad-plane geometry, as well as a minimization of the material budget between active gas and radiator has been presented in hard- and software. A minimum photon absorption cross-section of the entrance window was realized with a thermally stretched aluminized Kapton foil, glued to a G11 support grid support frame. This structure limits the mechanical deformation of the entire window to 1 mm/mbar. All MWPC prototypes include two wire planes. A symmetric amplification region of 2×(3, 3.5 or 4) mm is followed by a short drift region of 6, 5 or 4 mm. The drift region reduces the gain variation due to deformation of the entrance window. Both radiator and detector prototypes have been designed and built in our institute in Münster with support of the detector laboratory at GSI.

The performance of two identical MWPC prototypes has been investigated using a ^{55}Fe-source emitting 5.9 keV X-ray photons in laboratory and with mixed electron, pion beams with momenta between 2 and 8 GeV/c at CERN PS. The position resolution was determined using an external position reference system of two identical fiber-hodoscopes with a measured internal position resolution of 5.4 mm in x- and 5.7 mm in y-direction at 8 GeV/c. Based on a straight line tracking algorithm the position resolution of the TRD prototypes was estimated to be momentum dependent between 0.7 and 1.9 mm in anode wire direction. Even at 8 GeV/c this position resolution is at least a factor of 2 above the design value. The rather large impact of the particle momentum on the position resolution can be explained by multiple scattering within the detector material in front of the TRD prototypes. Based on this material budget it was shown that the position resolution of the presented prototypes is compatible with an upper limit of 290 μm over the full momentum range within the evaluated systematic uncertainties due to beam scattering. The prototypes reach an energy resolution of 10-11% in radioactive source tests, using Ar/CO_2 (82/18) in laboratory. All measurements have been performed with (SPADIC) read-out electronic, which was designed at the same time for this application. The latest TRD design (3.5 3.5 5 mm) has shown a total signal collection time of the order of 200 ns in simulations at 100 V/mm drift voltage using a Xe/CO_2 (80/20) gas mixture. Particle identification based on the pulse shape, like performed in ALICE, was tested based on a simulation and seems not feasible using a second order shaper with a shaping time of 90 ns (SPADIC) on our current detector design.

The radiator prototype materials were chosen with special focus on performance and mechanical stability. All eligible materials have been simulated in full radiator parameter space (γ, l_1, l_2 and N_f) to find optimal materials and parameters with respect to the TR-photon absorption characteristic of the chamber. The best candidates were built in small scales and the simulations were compared to measurements. It was found that the regular radiator model is sufficient to describe all measurements between 2 and 8 GeV/c, if extended by a material dependent constant scaling factor. At the same time, this model is inadequate in case of irregular radiators. The two best radiator candidates for CBM TRD are a micro-structured self-supporting POKALON foil radiator and a foam foil radiator, reaching the PID design goal with at least five to six detector hits per track.

The chamber geometry was implemented in the simulation framework (CbmRoot) of the CBM experiment. The measured charge spectra for electrons including TR-photons were reproduced based on a regular radiator model for all tested prototypes, in order to provide a realistic input for the TRD in the simulation. For the first time the TRD simulation includes a realistic detector response simulation and clusterization.

In summary, the new real-size TRD prototype providing electron/pion discrimination and tracking of charged particles in high counting rate environments was developed. It was demonstrated that they fulfill the requirements of the CBM experiment at the FAIR facility in terms of particle identification. A final test with respect to the performance in a high counting rate environment has still to be performed. The results encourage the further development of this new design principle for a TRD for the CBM experiment. Based on the prototype performance demonstrated in this thesis, a new generation of TRD prototypes has been developed and is currently under construction.

Zusammenfassung und Ausblick

Der Schwerpunkt dieser Arbeit ist die Entwicklung eines Übergangsstrahlungsdetektors (TRD) für das Compressed Baryonic Matter (CBM) Experiment bei FAIR. Der TRD Sub-Detektor wird zur globalen Teilchenidentifikation und Spurrekonstruktion geladener Teilchen beitragen. Das technische Designziel für den TRD liegt bei 90% richtig identifizierter Elektronen mit einer maximalen Pion-Kontamination von 1%. TRD und Ring Image Cherenkov (RICH) Detektor sollen eine gemeinsame Pion Unterdrückung von 10^4 erreichen, um eine Messung von Charmonium und Vektor-Mesonen geringer Masse zu ermöglichen. Die Positionsauflösung sollte zwischen 200 und 300 μm sein. Der anspruchsvollste Aspekt des CBM TRD-Designs ist die hohe Interaktionsrate von bis zu 10^7 Hz, was eine Rate von geladenen Teilchen bis zu 100 kHz/cm^2 im zentralen Teil jeder Detektorebene bei SIS300 ergibt. Um gleichzeitig eine ausreichende Pion Unterdrückung und Positionsauflösung zu erreichen, ist es entscheidend eine optimale Radiator-Detektor Kombination mit einem Minimum an Streuung am Detektormaterial und Hintergrund durch Konversionen zu finden.

In dieser Arbeit wird bestätigt, dass ein Vieldraht-Proportionalzähler (MWPC) mit einer Xe/CO_2 Dicke von 12 mm ausreichende Absorptionswahrscheinlichkeit für TR-Photonen bietet in Kombination mit mechanisch-selbsttragendem Schaum mit geringer Dichte oder mikrostrukturierten Folienradiatoren. Eine kontinuierliche Entwicklung mit dem Ziel einer optimalen Draht- und Pad-Ebenen Geometrie, sowie eine Minimierung des verwendenten Materials zwischen aktivem Gas- und Radiator in Hard- und Software wurde vorgestellt. Ein minimaler Photonenabsorptionsquerschnitt des Eintrittsfensters wurde mit einer thermisch gedehnten, aluminisierten Kaptonfolie erreicht, die auf einem Gitterraster aus G11 als Trägerrahmen geklebt wurde. Diese Struktur begrenzt die mechanische Verformung des gesamten Fensters auf 1 mm/mbar überdruck. Alle MWPC Prototypen besitzen zwei Drahtebenen. Ein symmetrischer Verstärkungsbereich von 2×(3, 3,5 oder 4) mm wird von einem kurzen Driftbereich von 6, 5 oder 4 mm ergänzt. Der Driftbereich reduziert die Verstärkungsvariation aufgrund der Verformung des Folienfensters durch Druckschankungen. Sowohl Radiator als auch Detektor Prototypen wurden in unserem Institut in Münster entwickelt und mit Unterstützung des Detektorlabors an der GSI gebaut.

Die charakteristischen Merkmale von zwei identischen MWPC Prototypen wurden mit einer ^{55}Fe-Quelle im Labor untersucht, die 5,9 keV Röntgenphotonen emittiert, sowie mit gemischten Elektron-, Pion-Strahlen im Impulsbereich zwischen 2 und 8 GeV/c am CERN PS Beschleuniger. Die Positionsauflösung wurde mit einem externen Positionsreferenzsystem aus zwei identischen Faserhodoskopen mit einer gemessenen internen Positionsauflösung von 5.4 mm in x- und y-Richtung zu 5.7 mm bei 8 GeV/c bestimmt. Basierend auf einem linearen Tracking-Algorithmus konnte so die Positionsauflösung der TRD Prototypen zwischen 0,7 und 1,9 mm in Anodendrahtrichtung, abhängig vom Teilchenimpuls bestimmt werden. Selbst bei 8 GeV/c liegt diese Positionsauflösung mindestens um den Faktor 2 über dem Designziel. Den recht großen Einfluss des Teilchenimpulses auf die Positionsauflösung konnte auf die Mehrfachstreuung durch das Detektormaterial aller Prototypen entlang der Strahllinie vor den MWPC Prototypen zurückgeführt werden. Basierend auf diesem Materialbudget wurde gezeigt, dass ein oberes Limit für die Ortsauflösung von 290 μm über den gesamten Impulsbereich innerhalb der systematischen Unsicherheiten auf Grund der Strahlstreuung verträglich ist. Die Prototypen erreichen eine Energieauflösung von 10-11% in Tests mit einer radioaktiven Quelle und Ar/CO_2 (82/18) im Labor. Alle Messungen wurden mit der (SPADIC) Ausleseelektro-

nik, die gleichzeitig für diese Anwendung entwickelt wurde, durchgeführt. Das neueste TRD-Design (3,5 3,5 5) mm hat eine Gesamtsignalerfassungszeit in der Größenordnung von 200 ns in Simulationen bei 100 V/mm Driftspannung mit einem Xe/CO_2 (80/20) Gasgemisch gezeigt. Partikelidentifikation auf Grundlage der Pulsform, wie in ALICE, wurde auf der Basis einer Simulation getestet und scheint mit einem Shaper zweiter Ordnung mit einer Shapingzeit von 90 ns (SPADIC) auf unserem Detektordesign nicht umsetzbar.

Die Materialien der Radiator Prototypen wurden mit speziellem Fokus auf Leistung und mechanische Stabilität ausgewählt. Alle in Frage kommenden Materialien sind im vollen Radiator Parameterraum (γ, l_1, l_2 und N_f) simuliert worden, um optimale Materialien und zugehörige Parameter in Bezug auf die TR-Photonen-Absorptionscharakteristik der Kammer zu finden. Die besten Kandidaten wurden in kleinen Größen gebaut und die Simulationen mit den Messungen verglichen. Es wurde festgestellt, dass das Modell zur Beschreibung regelmäßiger Radiatoren ausreichend, um alle Messungen zwischen 2 und 8 GeV/c zu erklären, wenn dieses um einen materialabhängigen, konstanten Skalierungsfaktor erweitert wird. Gleichzeitig ist dieses Modell bei unregelmäßigen Radiatoren unzureichend. Die beiden besten Radiatoren Kandidaten für den CBM TRD sind ein mikrostrukturierter, selbsttragender POKALON Folienradiator und ein Schaumfolienradiator. Beide erreichen das Auslegungsziel hinsichtlich der PID mit mindestens fünf bzw. sechs Hits pro Teilchenspur.

Die volle Detektorgeometrie wurde in dem Simulations-Framework (CbmRoot) des CBM-Experiments implementiert. Die gemessenen Ladungsspektren für Elektronen, einschließlich TR-Photonen wurden auf der Grundlage des regelmäßigen Radiatormodells für alle getesteten Prototypen abgebildet, um einen realistischen Input für die TRD Simulation zu schaffen. Zum ersten Mal beinhaltet der TRD in der Simulation ein realistisches Detektorantwortverhalten und Clusterisierungs-Modell.

Zusammenfassend wurden neue TRD Prototypen zur Elektron/Pion Diskriminierung und Positionsrekonstruktion von geladenen Teilchen bei hohen Teilchenraten entwickelt. Es konnte gezeigt werden, dass die Anforderungen des CBM-Experiments an der FAIR-Beschleunigeranlage in Bezug auf die Teilchenidentifikation erfüllt werden. Ein abschließender Test in Bezug auf die Leistung bei hohen Zählraten muss noch durchgeführt werden. Diese Ergebnisse motivieren die weitere Entwicklung dieses neuen Konstruktionsprinzips für den TRD des CBM-Experiments. Basierend auf den präsentierten Ergebnissen wird momentan eine neue Generation von Prototypen entwickelt und in Kürze gefertigt.

A. Blue Prints

A.1. 2012 Open TRD Prototype

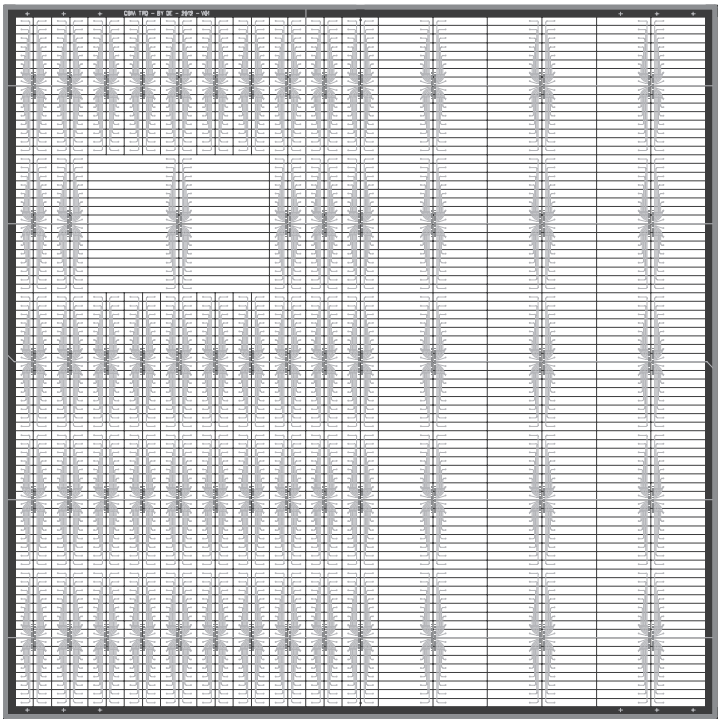

Figure A.1: 2012 pad-plane [Ems13b]

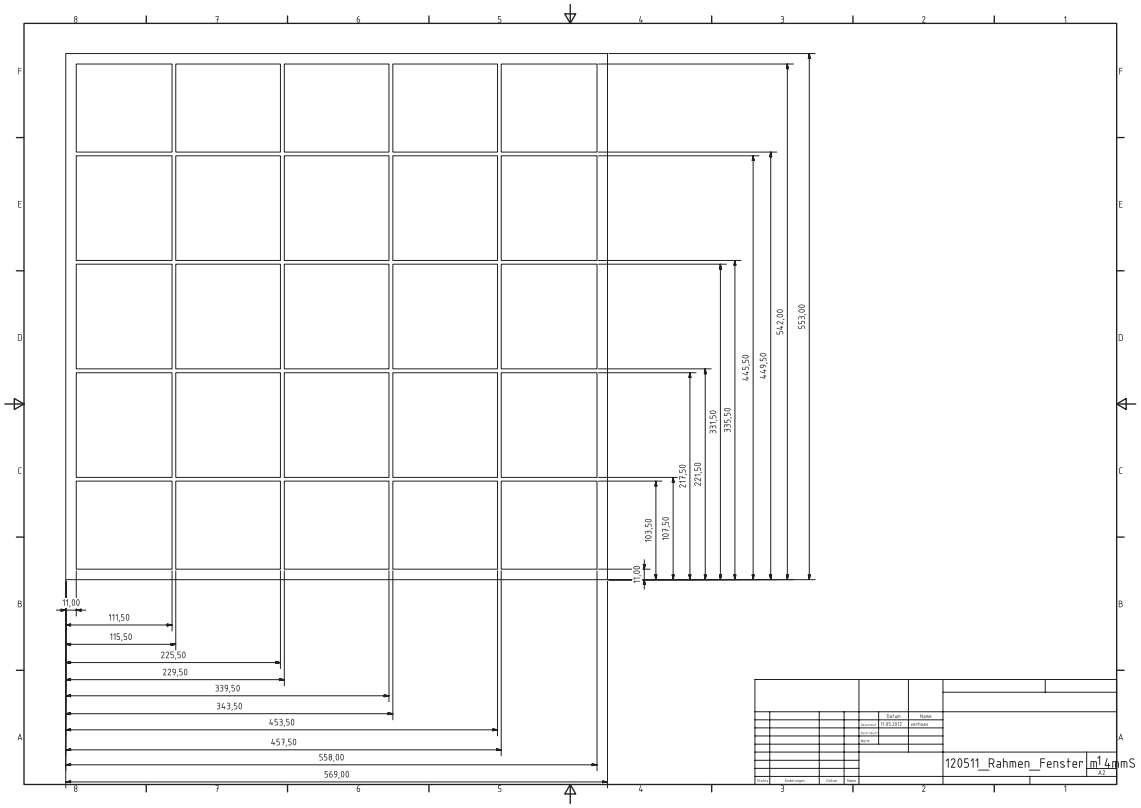

Figure A.2: 2012 support grid 4 mm lattice width [Ver13]

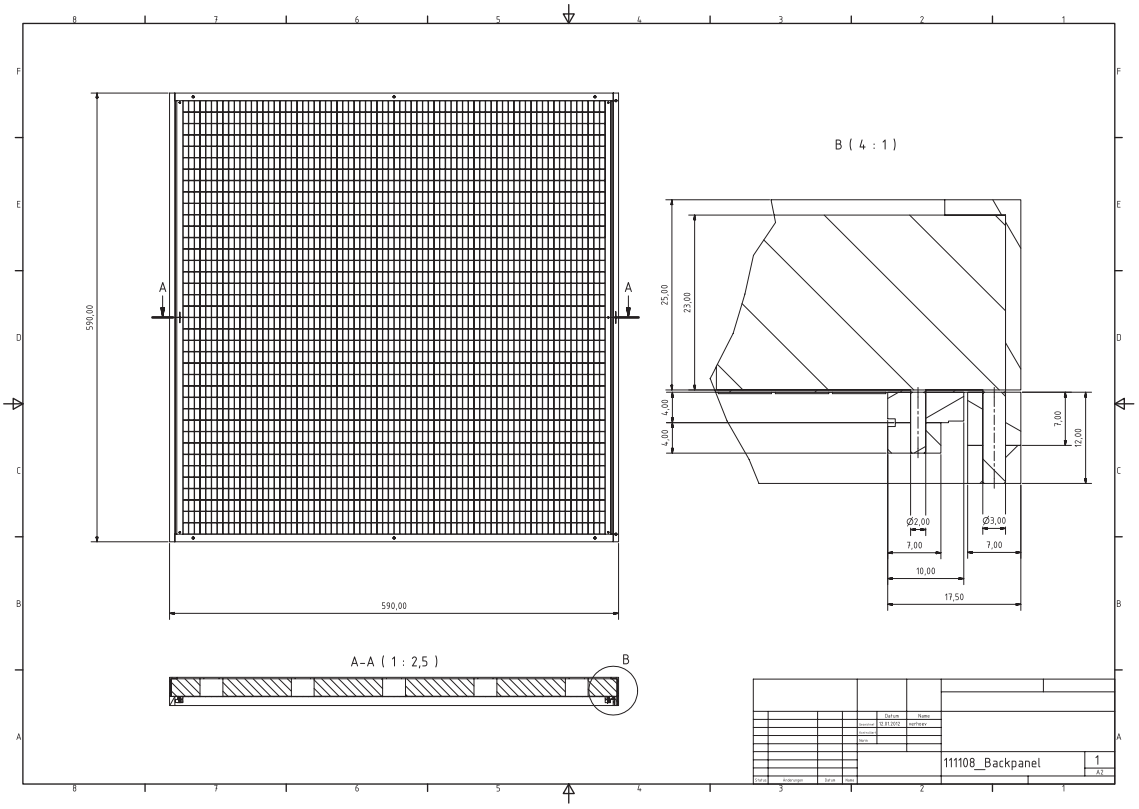

Figure A.3: 2012 back-panel [Ver13]

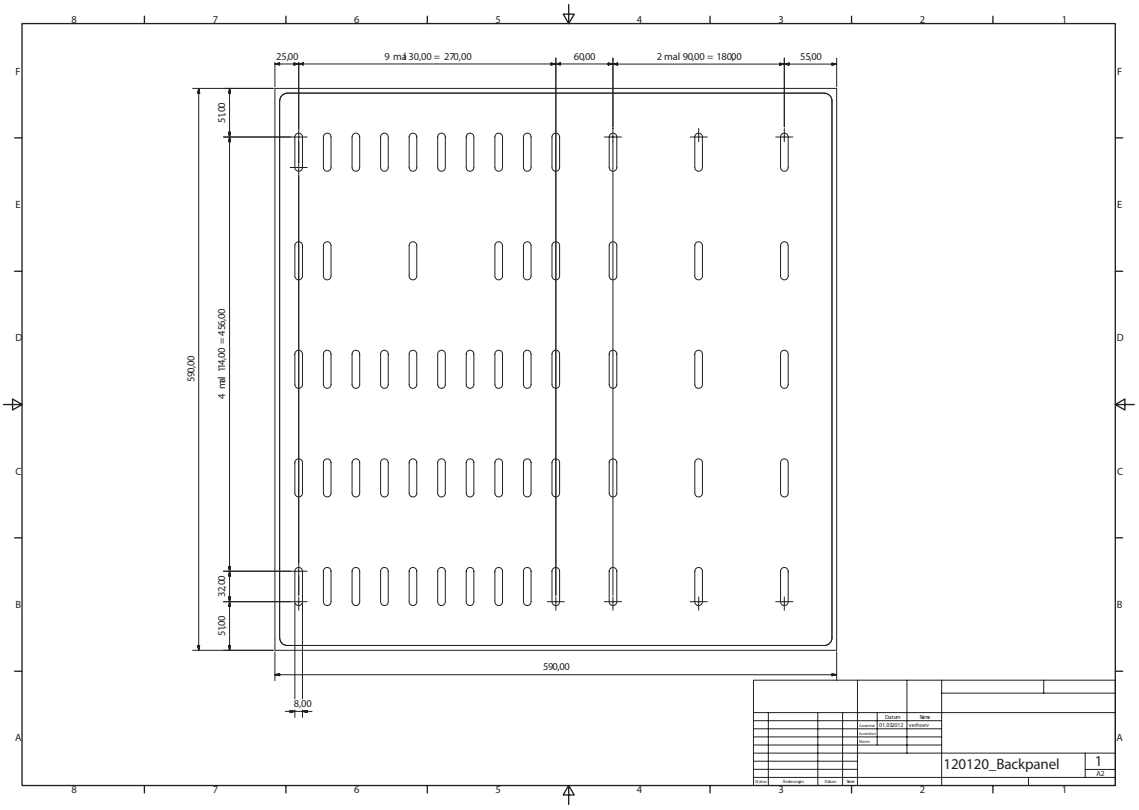

Figure A.4: 2012 back-panel signal cable holes [Ver13]

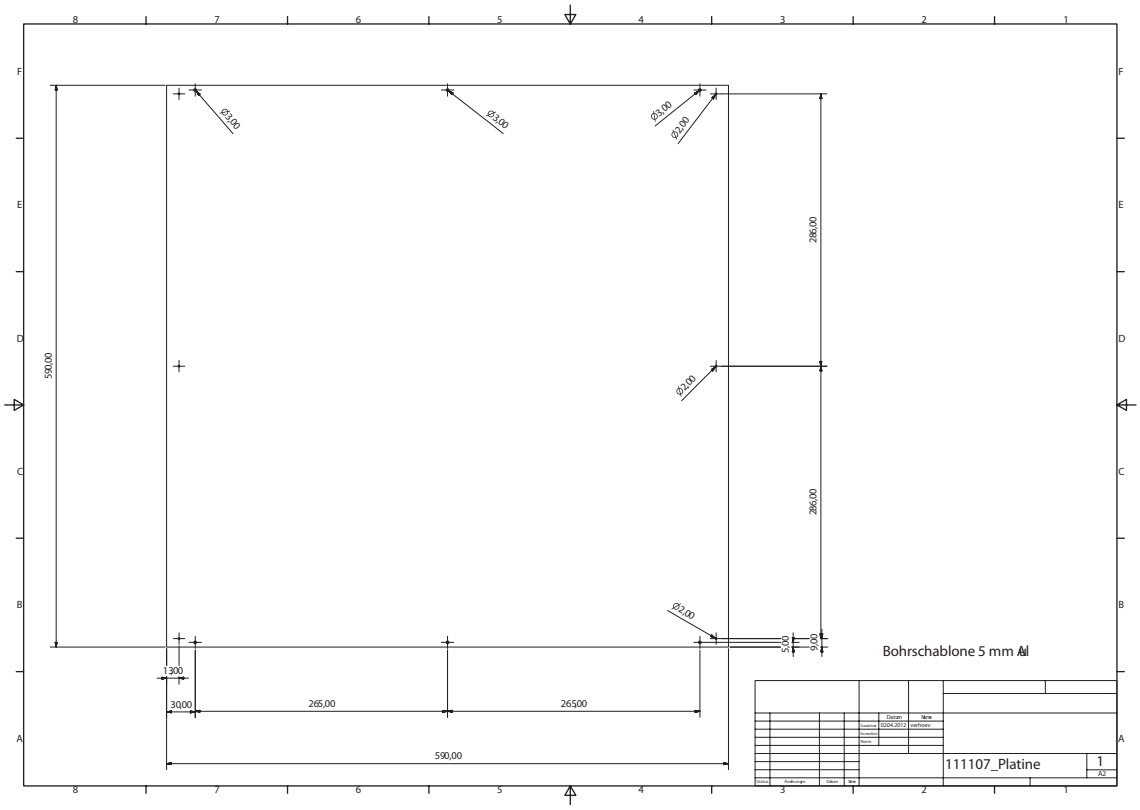

Figure A.5: 2012 filler plate hole template [Ver13]

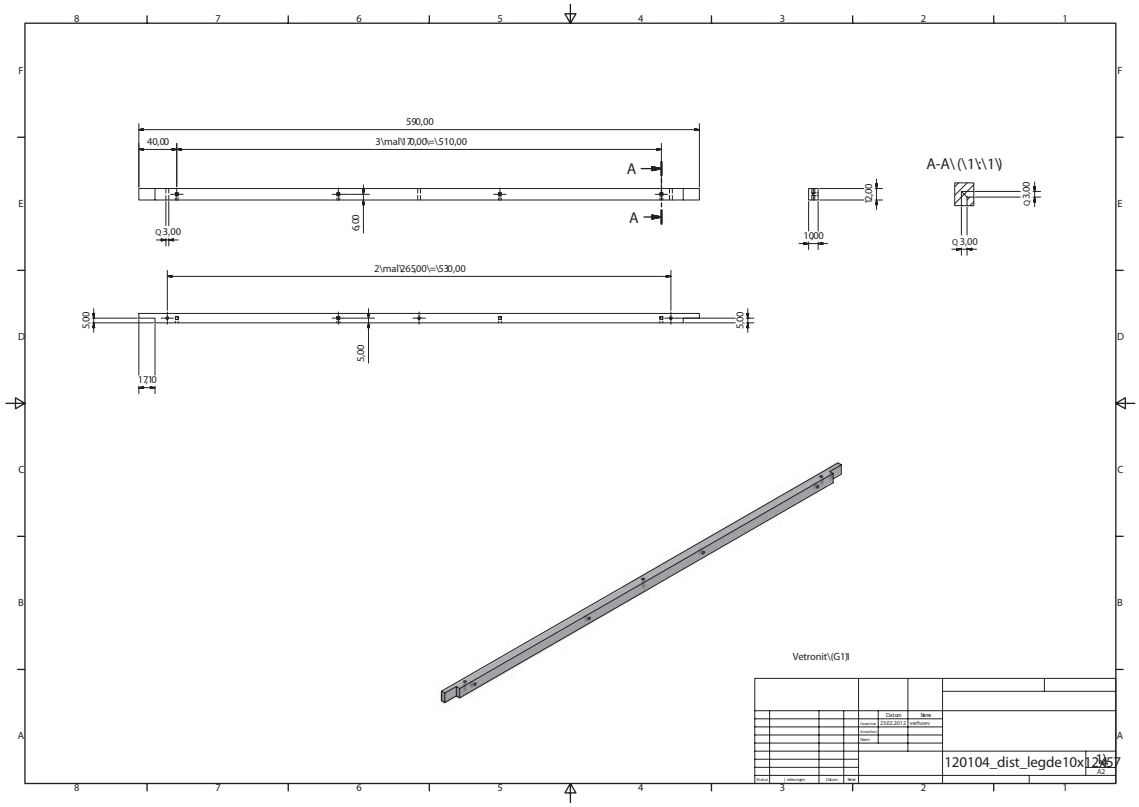

Figure A.6: 2012 wire distance ledge $10 \times 12 \times 590\,\text{mm}$ [Ver13]

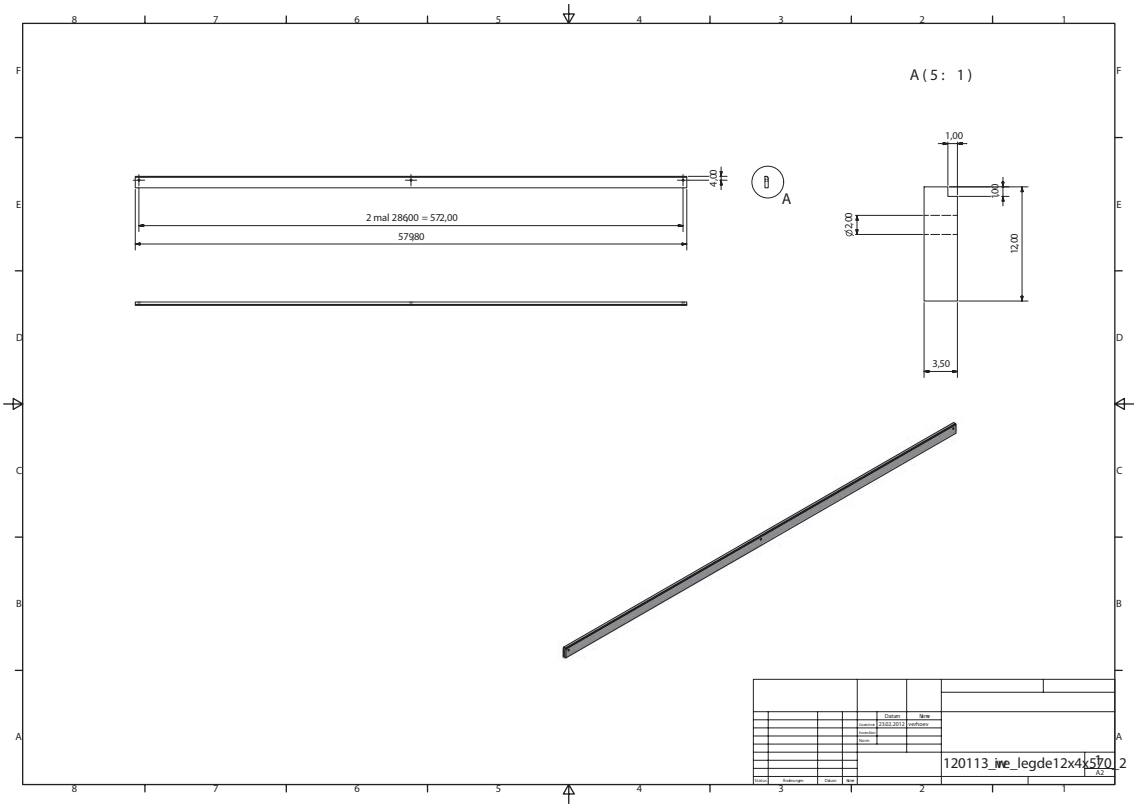

Figure A.7: 2012 wire distance ledge $12 \times 3.5 \times 579.8\,\text{mm}$ [Ver13]

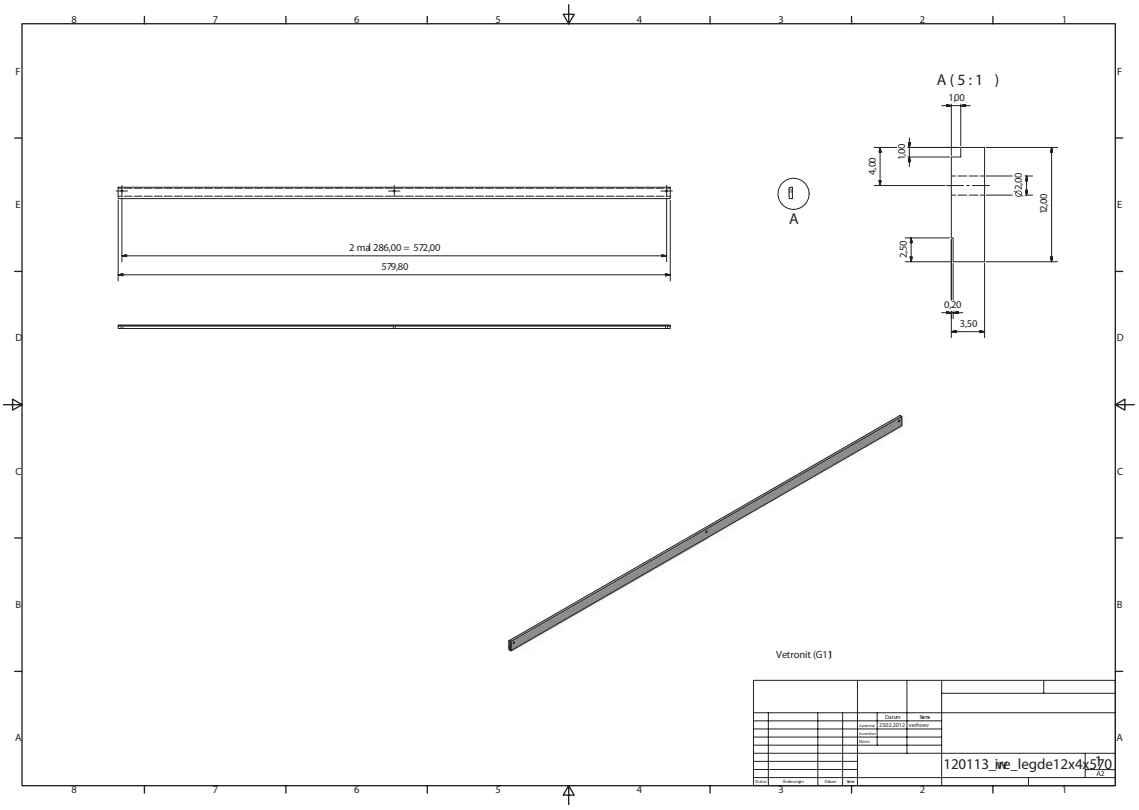

Figure A.8: 2012 wire distance ledge $12 \times 3.5 \times 579.8\,\text{mm}$ [Ver13]

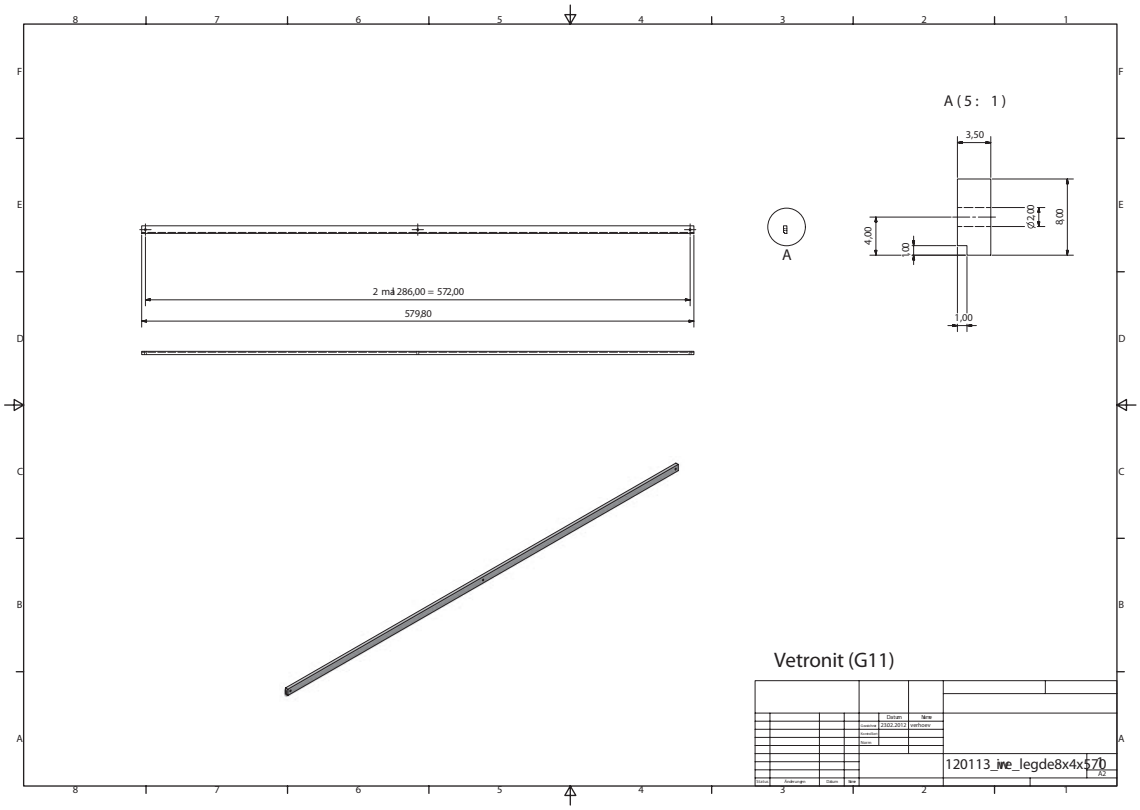

Figure A.9: 2012 wire distance ledge $8 \times 3.5 \times 579.8\,\text{mm}$ [Ver13]

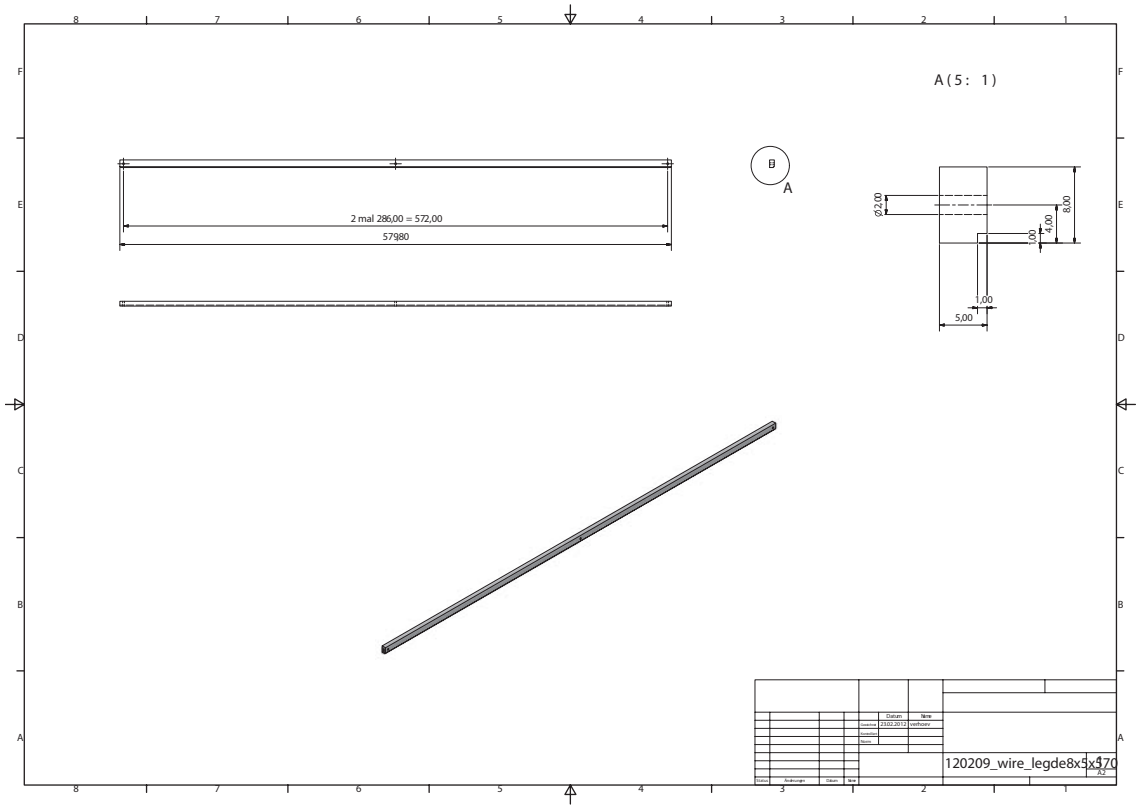

Figure A.10: 2012 wire distance ledge $8 \times 5 \times 579.8\,\text{mm}$ [Ver13]

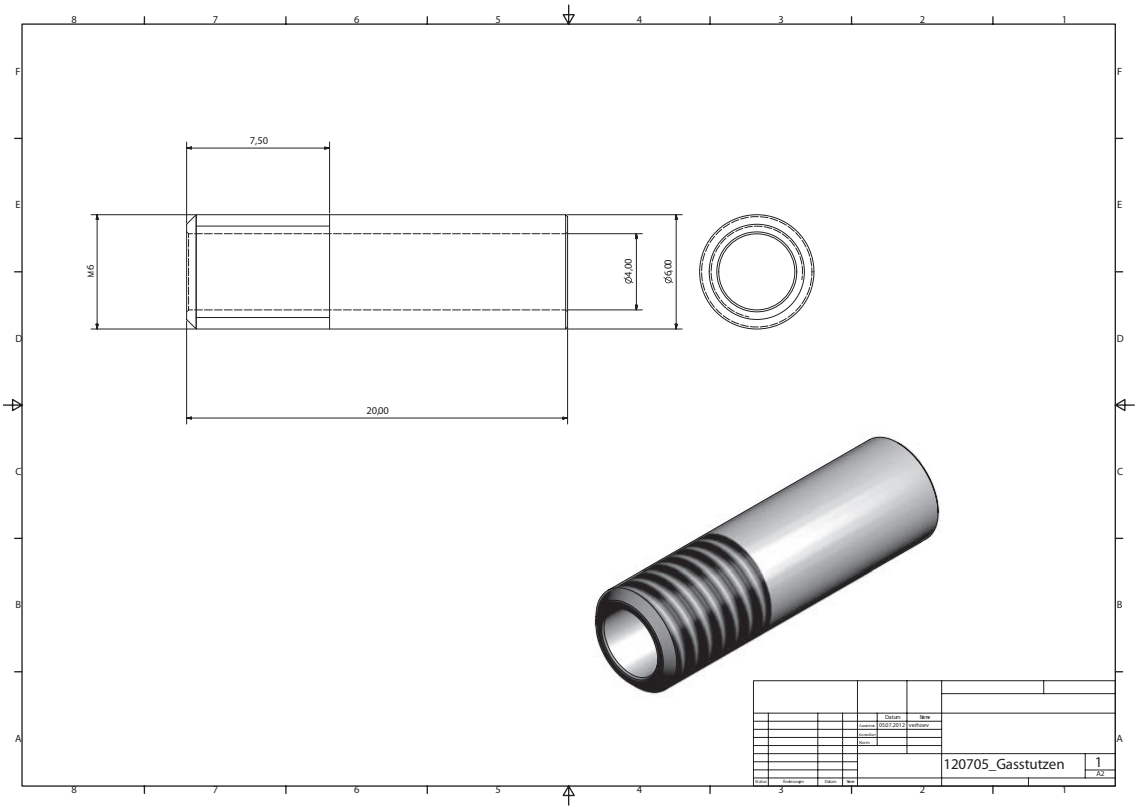

Figure A.11: 2012 gas feed through [Ver13]

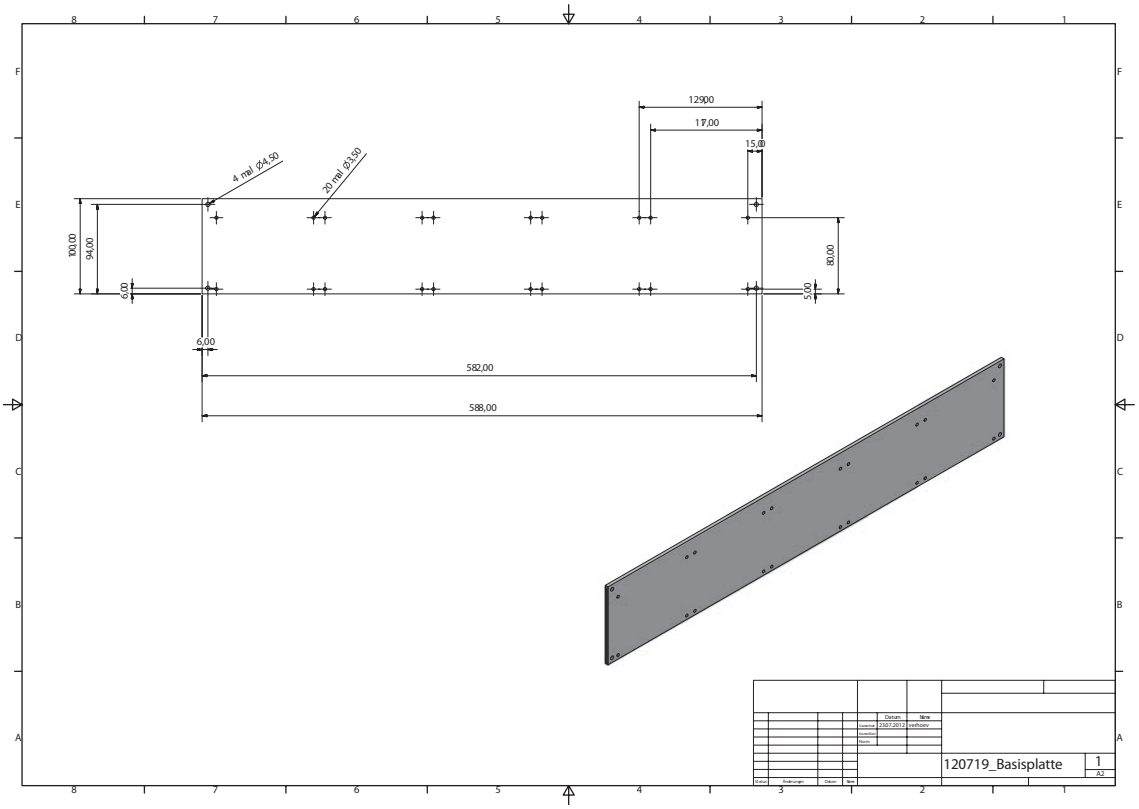

Figure A.12: 2012 ground plate [Ver13]

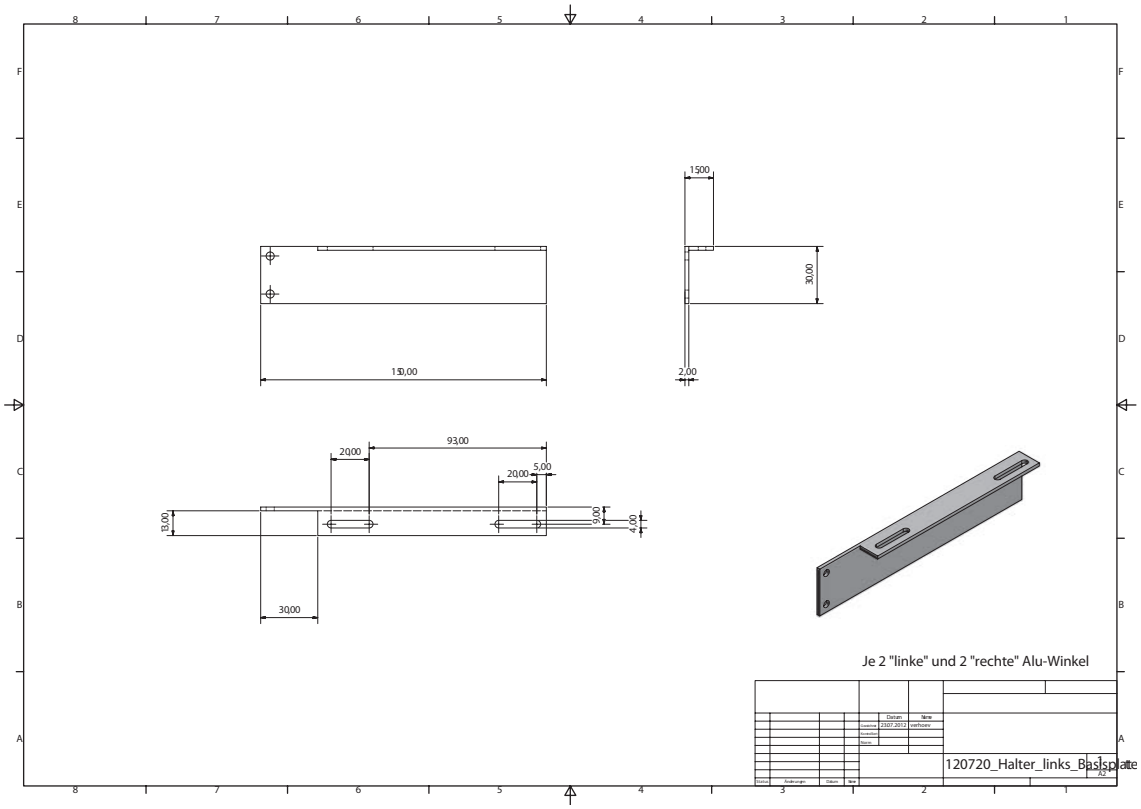

Figure A.13: 2012 left ground plate mounting [Ver13]

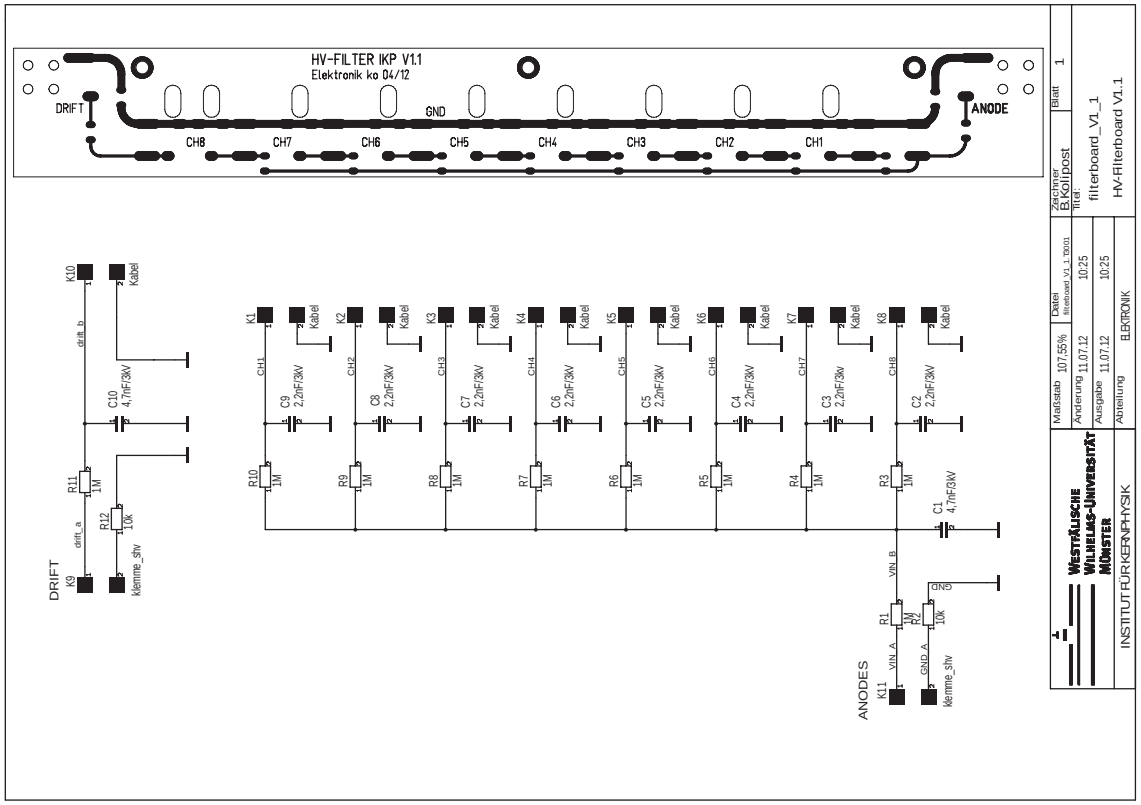

Figure A.14: 2012 HV filter board [Kol12]

A.2. Peripheral Equipment

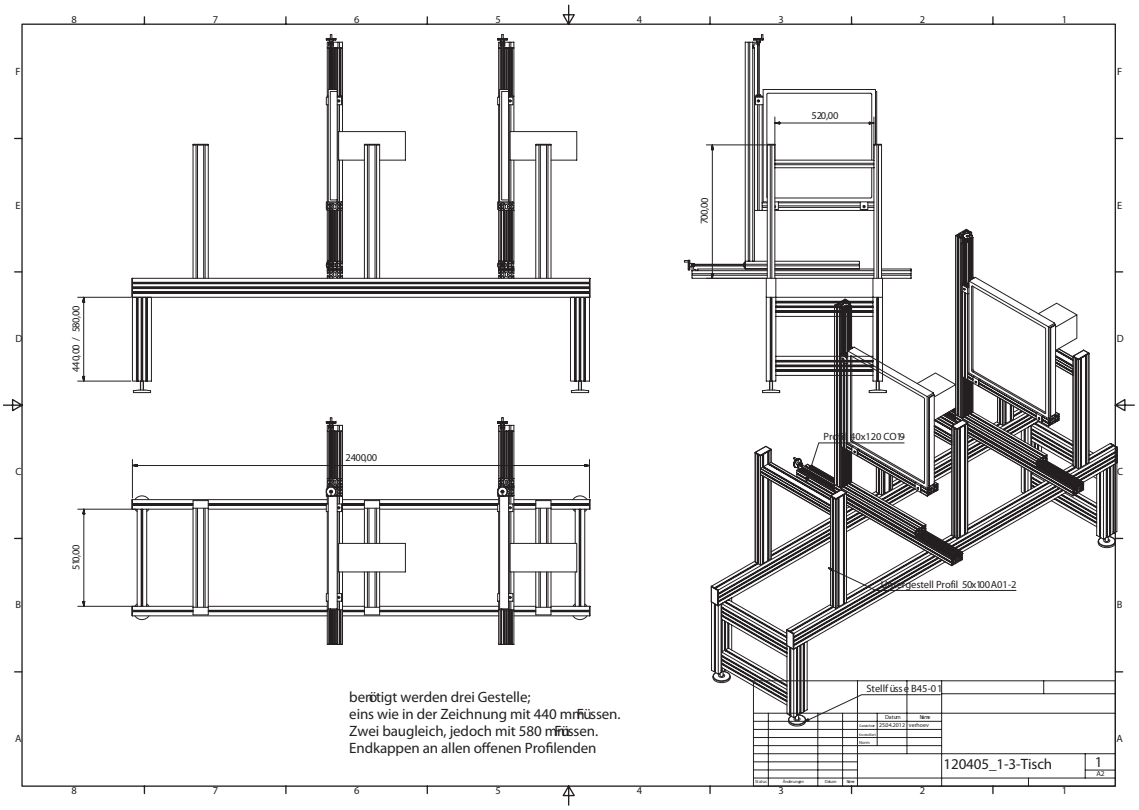

Figure A.15: 2012 test beam table [Ver13]

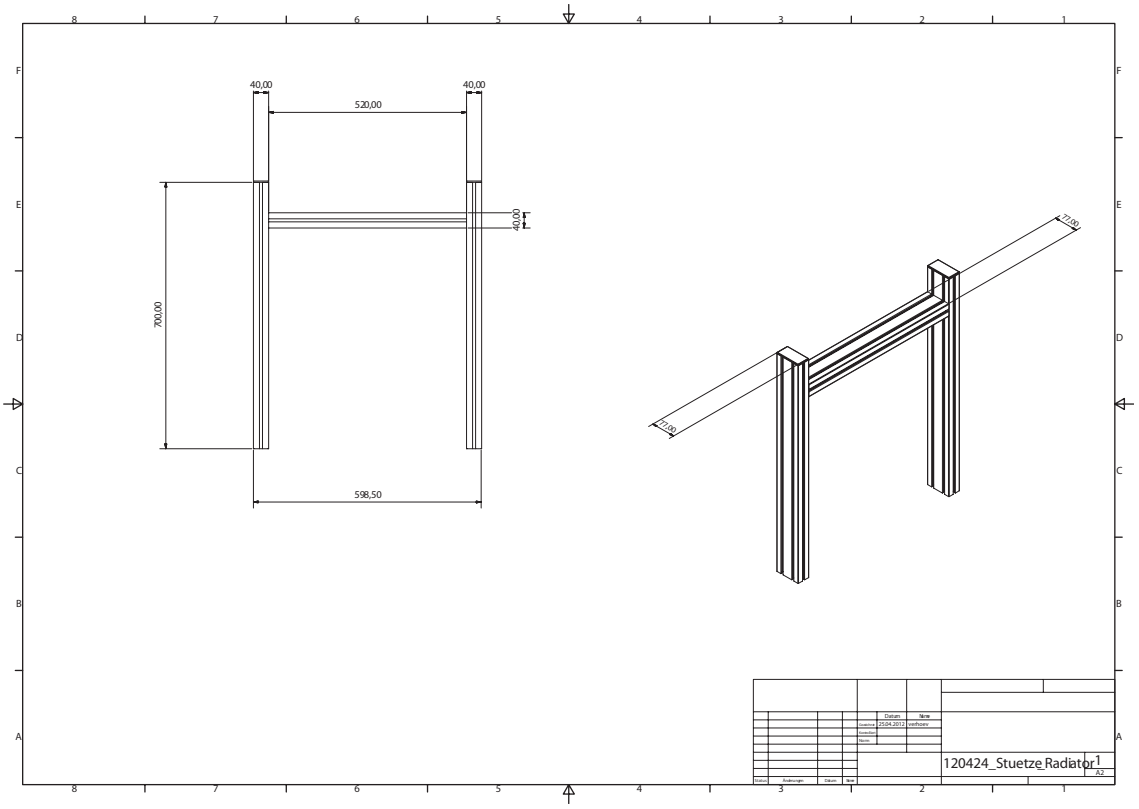

Figure A.16: 2012 radiator mounting [Ver13]

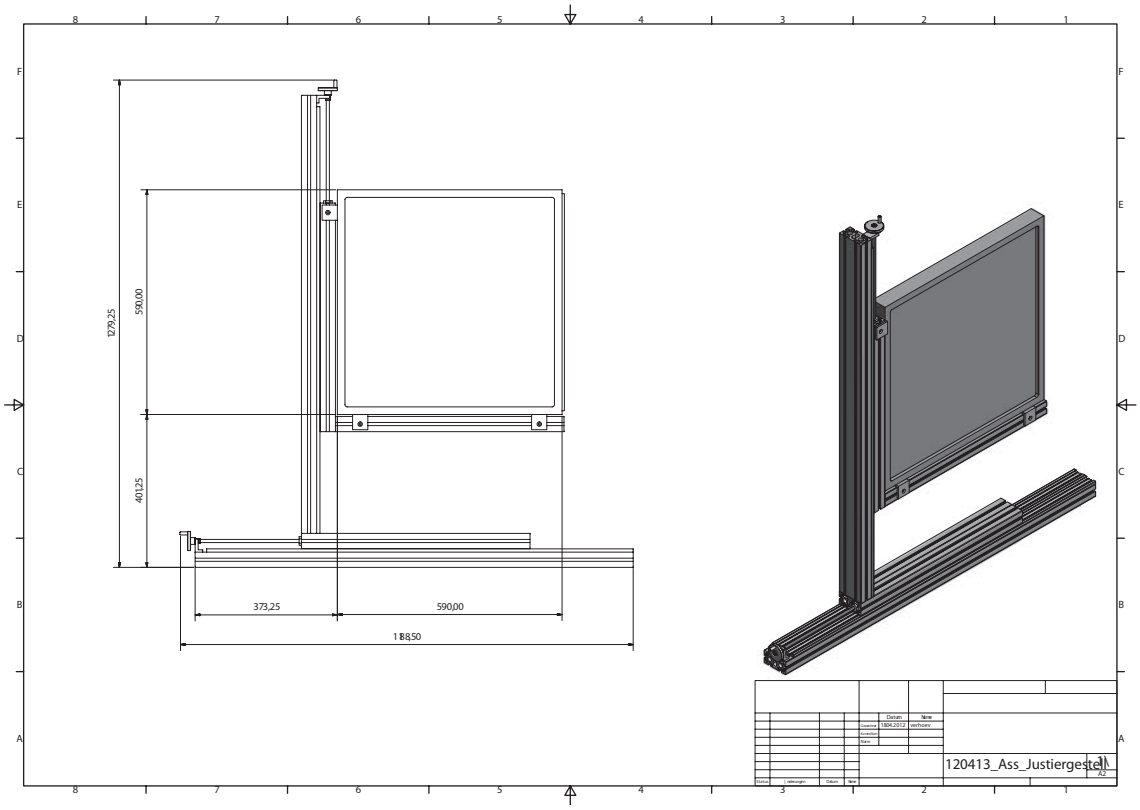

Figure A.17: 2012 TRD chamber positioning device [Ver13]

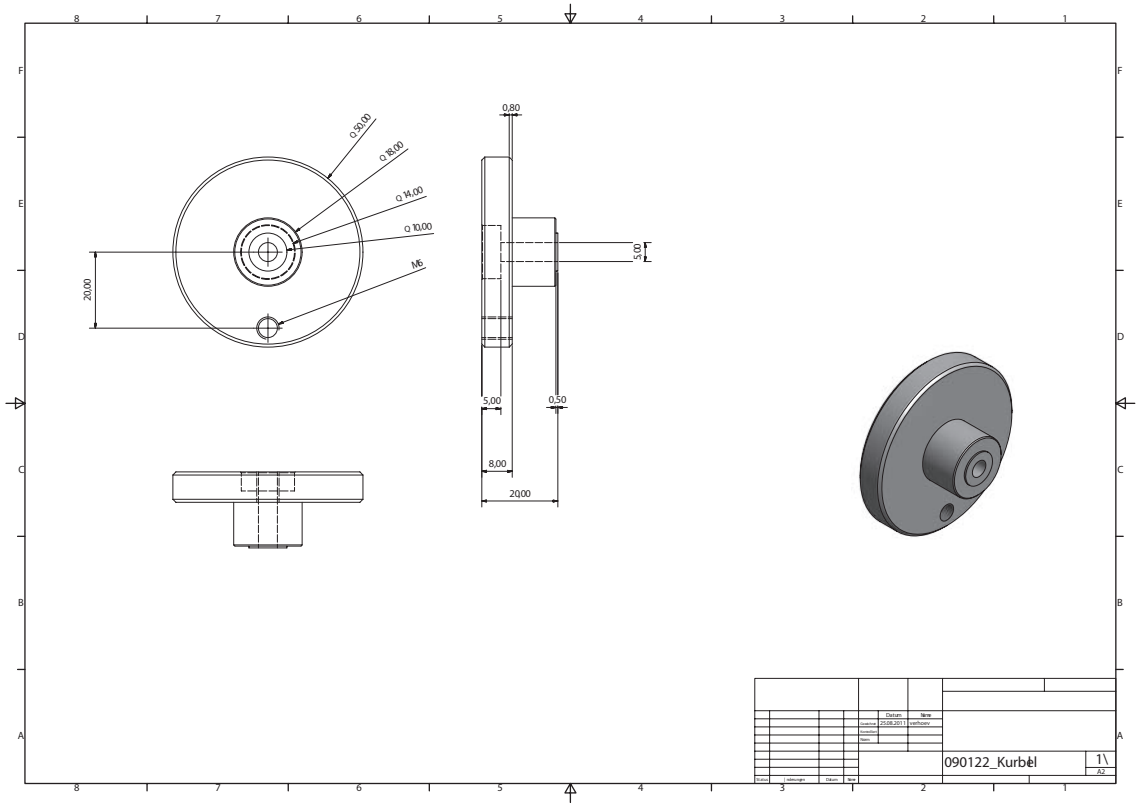

Figure A.18: 2012 crank handle [Ver13]

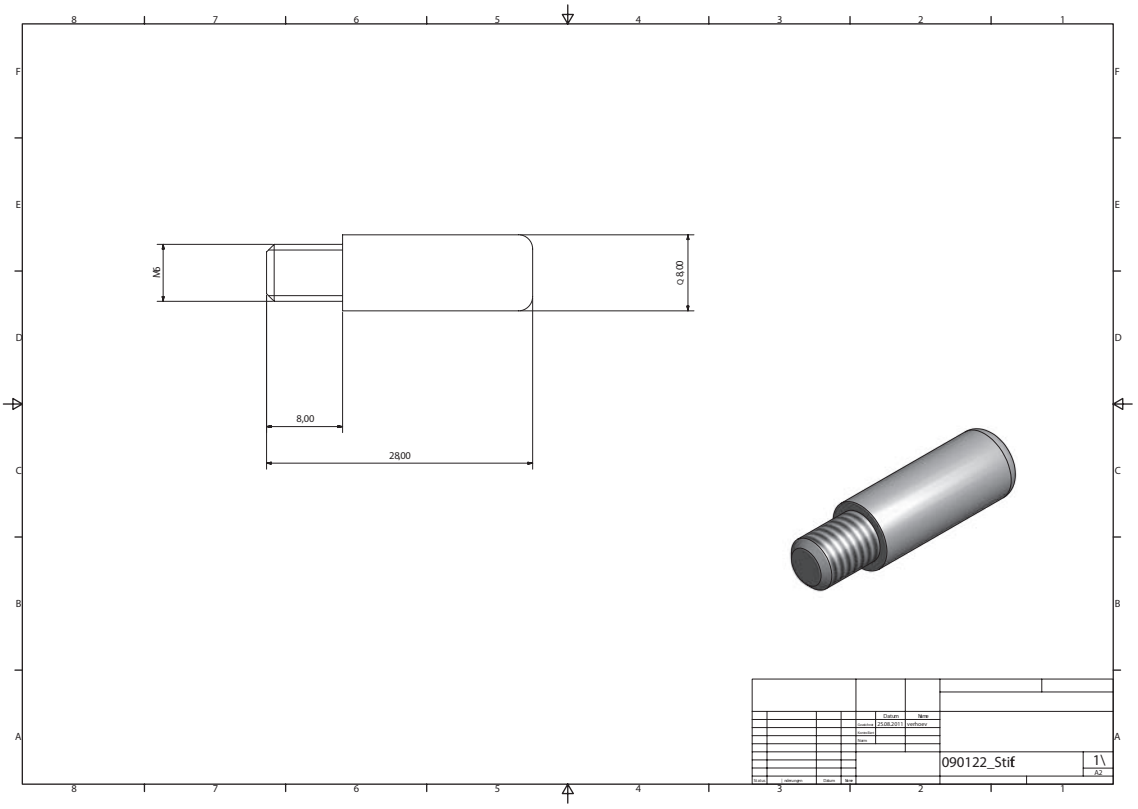

Figure A.19: 2012 pin [Ver13]

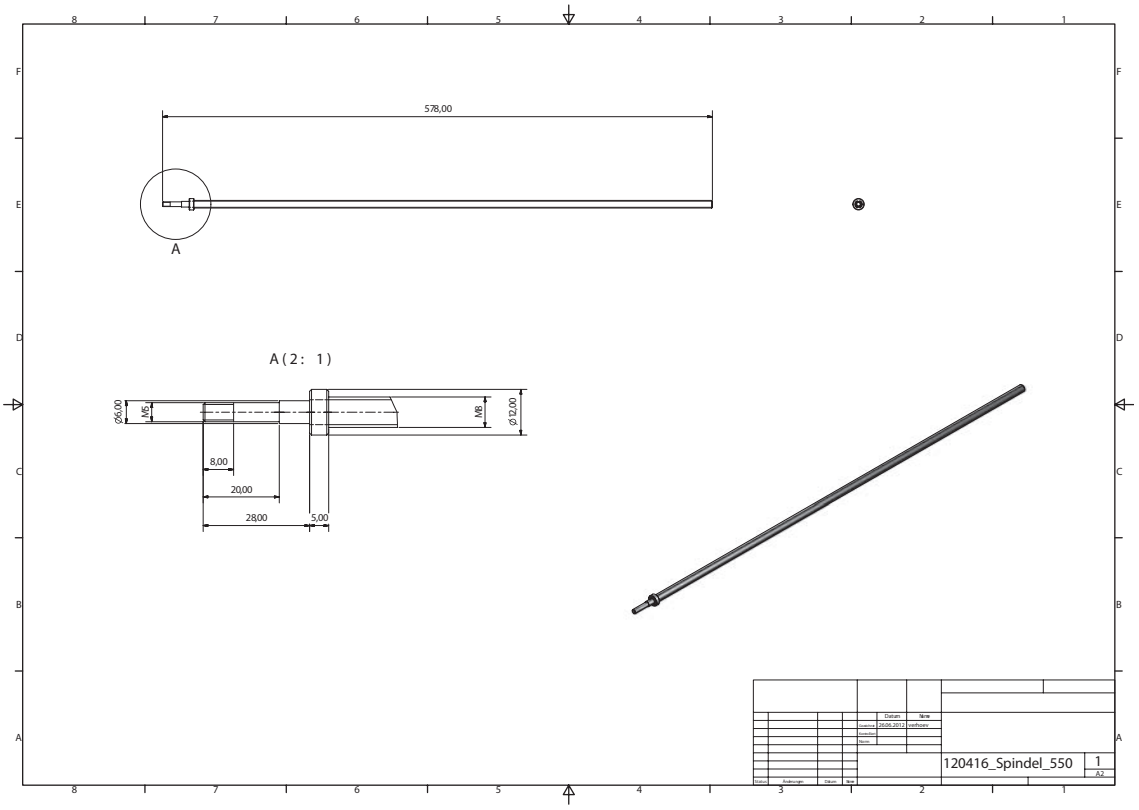

Figure A.20: 2012 arbor [Ver13]

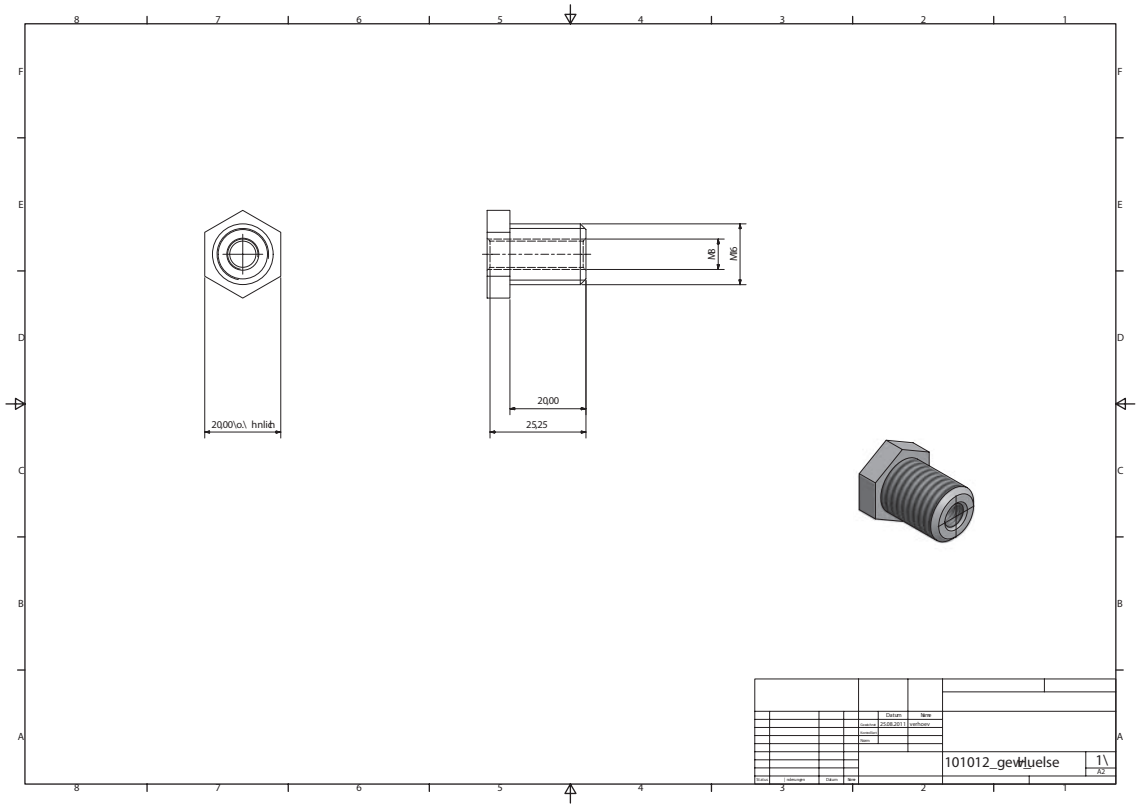

Figure A.21: 2012 bolt [Ver13]

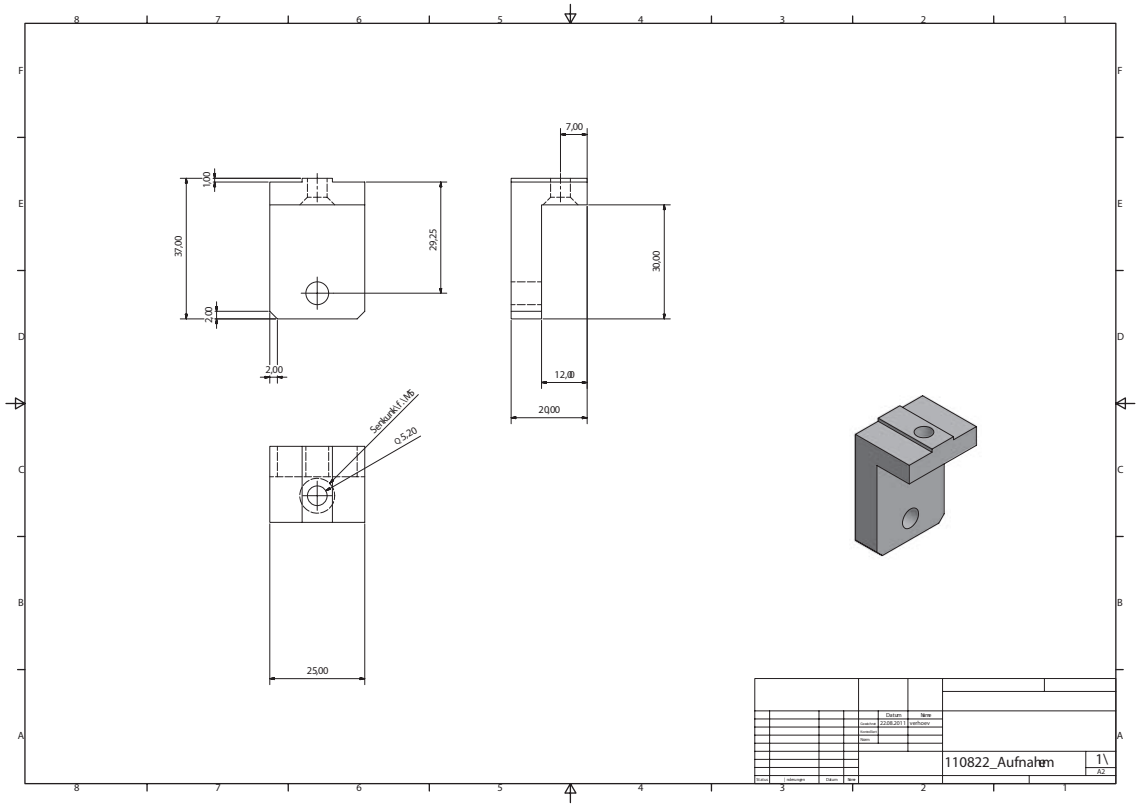

Figure A.22: 2012 casing [Ver13]

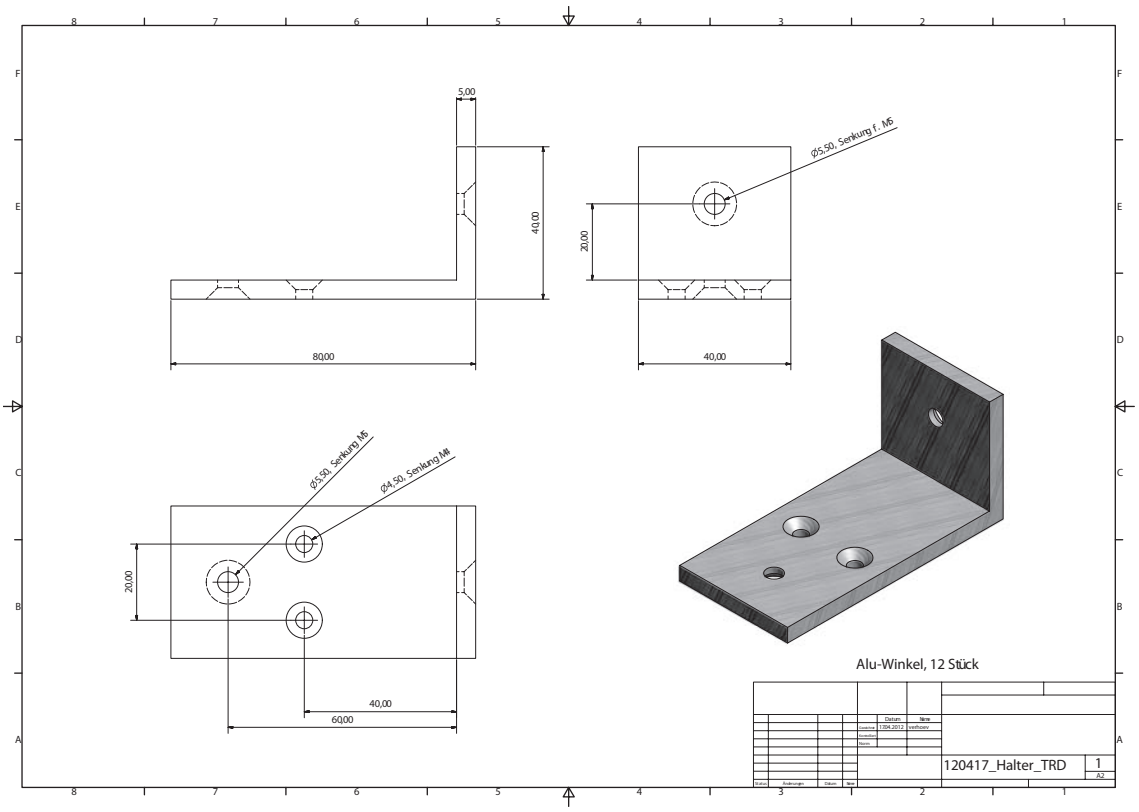

Figure A.23: 2012 TRD fixture [Ver13]

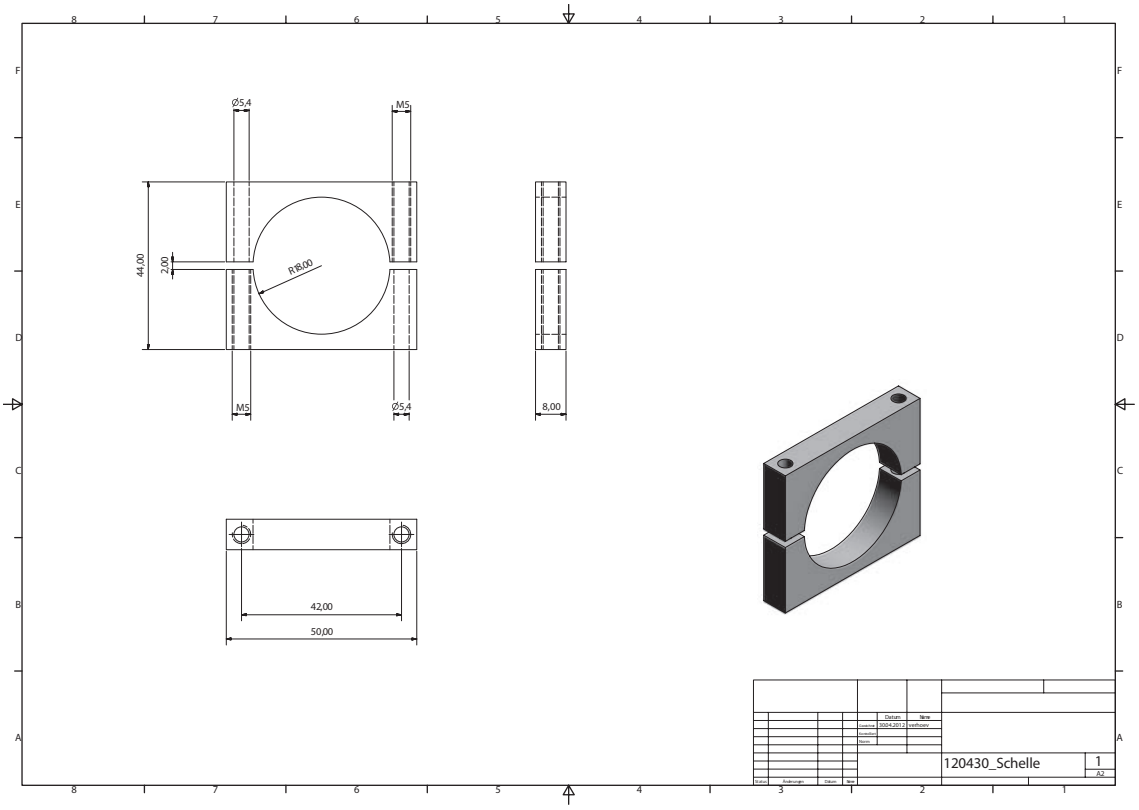

Figure A.24: 2012 clamp [Ver13]

B. Run Logs

Table B.1: Run logbook CERN PS T09 beam test 2011: only runs with good datasets are listed.

Date	Run ID	p (GeV/c)	Ms336/10	Ms336/11	Ms444/10	Ms444/11	Comments
			1800V/600V		2000V/400V		
21.10.12	Be_run12,13,15	3	H	E	F	I(p)	
			1700V/600V		1900V/400V		
	Be_run17-19						
			1750V/600V		1950V/400V		
	Be_run20-24,26						
22.10.12			1750V/300V		1950V/200V		
	Be_run00						
			1750V/30V		1950V/20V		
	Be_run01						
			1750V/600V		1950V/400V		
	Be_run10-12		G(10)	G(10)	G(10)	G(10)	
23.10.12	Be_run00-02		-	-	-	-	
	Be_run03		B	C	D	E	
	Be_run04		C	D	E	F	
	Be_run05-09		A	G(20)	J	I(p)	
	Be_run10,11		H	I(p)	A	G(20)	
	Be_run12-15,26-29		H	I(u)	G(30)	B	
24.10.12	Be_run00		H	I(u)	G(30)	B	
	Be_run03		H++	I(u)	G(30)	B	
	Be_run17,18	2					
	Be_run22-25	4					
25.10.12	Be_run01-03						
	Be_run04-12	6					
	Be_run13	10					
	Be_run14	8					

Date	Run ID	p (GeV/c)	Ms336/10	Ms336/11	Ms444/10	Ms444/11	Comments
26.10.12	Be_run01						
	Be_run02-05		H	H(1/3)	G(30)	B	
	Be_run06-8,10	4					90^o rotated around z-axis
27.10.12	Be_run01-10,13,14						
	Be_run15-17		black foam				
	Be_run18-20		white foam				
	Be_run21-23,25-26,28	2					
28.10.12	Be_run01-03						
	Be_run05-13		H	H(1/3)	A	B	30^o tilted around y-axis
29.10.12	Be_run01						

Table B.2: Run logbook CERN PS T09 beam test 2012: all missing run IDs have the the same conditions like the last one listed before.

			TRD R I			TRD N II		
Date	Run ID	p (GeV/c)	Rad.	Anode (V)	Drift (V)	Rad.	Anode (V)	Drift (V)	Comments
28.10.12	Be_run1	4	-	1800	500	-	1800	500	Trigger: Hod1&&Hod2
29.10.12	Be_run5		B++			K++			-
	Be_run8								realignment of TRDs
	Be_run10		B			K			-
	Be_run14	3							-
	Be_run18								started full EPICS read-out
	Be_run21								disconnected bubbler
	Be_run22								$O_2 > 1.675\ V\%$
30.10.12	Be_run30								-
	Be_run35		B++			K++			$O_2 > 1.200\ V\%$
	Be_run36								$O_2 > 644\ ppmV_b$
	Be_run41								$O_2 = 0\ ppmV_b$
	Be_run42			1775			1775		-
	Be_run45								$O_2 > 1000\ ppmV_b$
	Be_run49			1750			1750		$O_2 = 0\ ppmV_b$
31.10.12	Be_run50			1775			1775		-
	Be_run51			1750			1750		-
	Be_run57		B			K			-
	Be_run60								O_2 fluctuation [0,2000] between 13:30 and 14:30
	Be_run61								$O_2 > 1.000\ V\%$
	Be_run62		Bshort			Kshort			-
01.11.12	Be_run69		K++			B++			-
	Be_run71		L			M			-

			TRD R I			TRD N II			
Date	Run ID	p (GeV/c)	Rad.	Anode (V)	Drift (V)	Rad.	Anode (V)	Drift (V)	Comments
	Be_run73								Trigger: (Hod1&&Hod2) && (Ch1||Ch2)
02.11.12	Be_run82								-
	Be_run88		-			-			-
	Be_run93								EPICS break down
	Be_run96		O5×5			N25			-
03.11.12	Be_run102								-
	Be_run114		G(30)			HF100			-
	Be_run125		N25			K++			MBS break down
	Be_run126	8							-
04.11.12	Be_run128								-
	Be_run147	6							-
05.11.12	Be_run155								-
	Be_run168	4							-
06.11.12	Be_run188								-
07.11.12	Be_run208	2							-
	Be_run212								new baseline Sus11
08.11.12	Be_run224								-
	Be_run240	3	H(25)			H(25)			common radiator run
	Be_run247		FFM1.2×100			FFM1.2×100			-
09.11.12	Be_run251								-
	Be_run264		FFM0.7×100			FFM0.7×100			MBS break down
10.11.12	Be_run283								-
	Be_run293		H			FFM0.7×200			-
11.11.12	Be_run310								-
	Be_run321		FFM0.5×100			FFM0.5×200			-
	Be_run337		FFM0.7×350			FFM1.2×200			-
	Src_run338								^{55}Fe run

Date	Run ID	p (GeV/c)	Rad.	TRD R I Anode (V)	TRD R I Drift (V)	Rad.	TRD N II Anode (V)	TRD N II Drift (V)	Comments
	Src_run339								^{55}Fe run
	Src_run340								^{55}Fe run
	Be_run341								-
12.11.12	Be_run348								-
	Be_run362								last run

C. Radiator Prototype Properties

Table C.1: List of all produced radiator prototypes available until 2013 in Münster. The radiation length is given for the active area neglecting the mechanical support material like frames.

Name	Active area (cm^2)	Length (cm)	Weight (g)	X/X_0 (%)
A	18×18	4.8	117	0.83-0.90
Bshort	11×11	7.2	6100	0.88
B	11×11	17.8	15200	2.21
B++	11×11	25	21300	3.09
C	11×11	18	15200	0.64
D	8×8	6.5	1588	0.32
E	18×18	8	>2000	0.50
F				0.90
G(10)	22×22	4	155	0.57-0.65
G(20)	22×22	8	310	1.13-1.31
G(30)	22×22	12	465	1.70-1.96
H25	15.5×15.5	5	37	0.39-0.51
H	16.5×16.5	27	297	1.19-1.57
H++	16.5×16.5	36	334	1.46-1.92
I(u,p)	2×6.5×13	16	393	5.21-5.27
J	12×12	5.5	46	0.88
Kshort	9.5×9.5	7.2	50	0.88
K	9.5×9.5	17.8	126	2.21
K++	9.5×9.5	25	176	3.09
L	16.5×16.5	26	307	0.91
M	16.5×16.5	26	318	0.99
N25	18×18	25×1	25×9	1.50
O5×5	18×18	5×5	5×34	1.22
WF110	15×15	3	75	0.78
HF110	15×15	3	82	0.90
3×EF700	15×15	3×5.5	3×142	4.45

D. Radiator Material Simulation

Table D.1: List of simulated radiator materials and parameters optimized according to section 6.2 based on the 2011, 2012 MWPC material budget.

Foil	Gap	$l_1^{opt.}$ (μm) $\pm 1\,\mu$m		$l_2^{opt.}$ (μm) $\pm 100\,\mu$m		$\langle E_{TR}(N_f = 200)\rangle$ (keV) $\pm 1\%^{\text{syst.}} \pm 10\%^{\text{theo.}}$	
		2011	2012	2011	2012	2011	2012
Polyethylene	Air	23	20	700	800	11.34	14.28
POKALON N470	Air	20	17	700	800	10.31	12.60
POKALON N331	Air	20	17	700	800	10.51	12.88
ARYPHAN N681	Air	19	16	700	800	10.51	12.88
TACPHAN OG863	Air	18	16	700	800	9.22	11.02
Mylar	Air	17	15	700	800	10.19	12.27
Polypropylene	Air	23	20	700	800	11.34	14.28
Polyvenylchlorid	Air	20	17	600	700	2.56	2.87
Polyoxymethylen	Air	16	14	700	800	9.62	11.49
Kapton	Air	17	14	700	800	10.57	12.76
Cellulose	Air	19	16	700	800	9.10	10.90
Polystyrene	Air	20	17	700	800	11.47	14.26
Aluminum	Air	12	10	500	600	3.80	4.15
Lithium	Air	47	40	700	700	11.58	16.69
Beryllium	Air	15	13	600	700	17.20	22.72
Sodium	Air	26	23	700	800	3.57	4.08
Magnesium	Air	16	14	600	700	3.83	4.26

E. Clusterizer Benchmark Based on Geometry $v12f$

E.1. Hit Efficiency

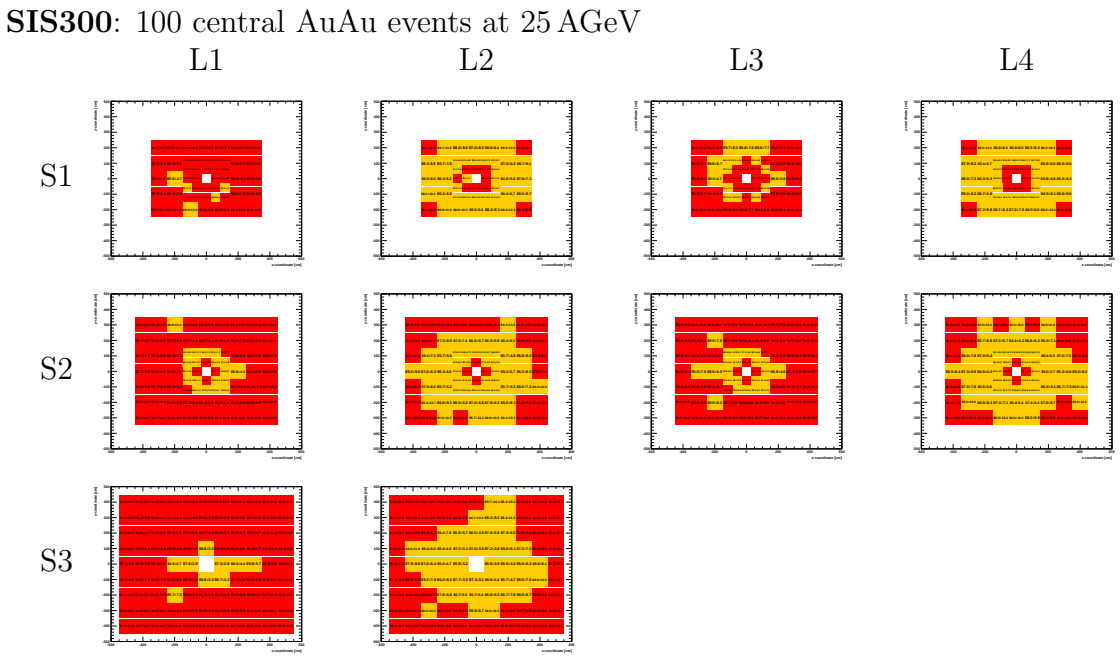

Figure E.1: Average hit efficiency for 100 AuAu events at 25 AGeV for geometry $v12f$.

E.2. Ghost Rate

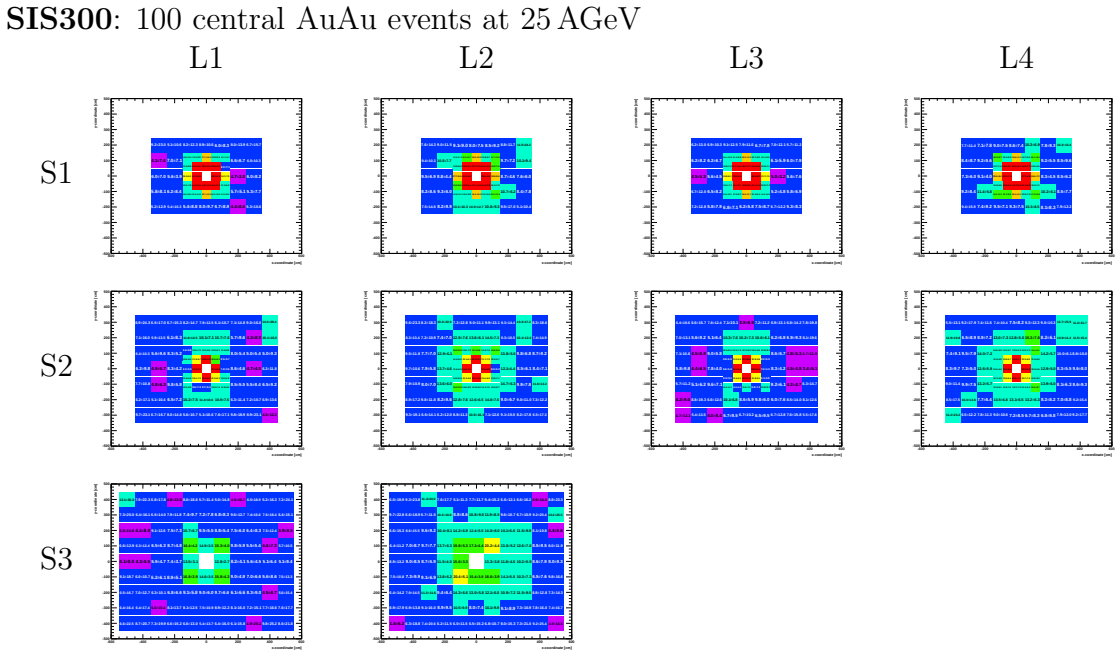

Figure E.2: Average ghost hits for 100 AuAu events at 25 AGeV for geometry $v12f$.

E.3. Lost Hit Fraction

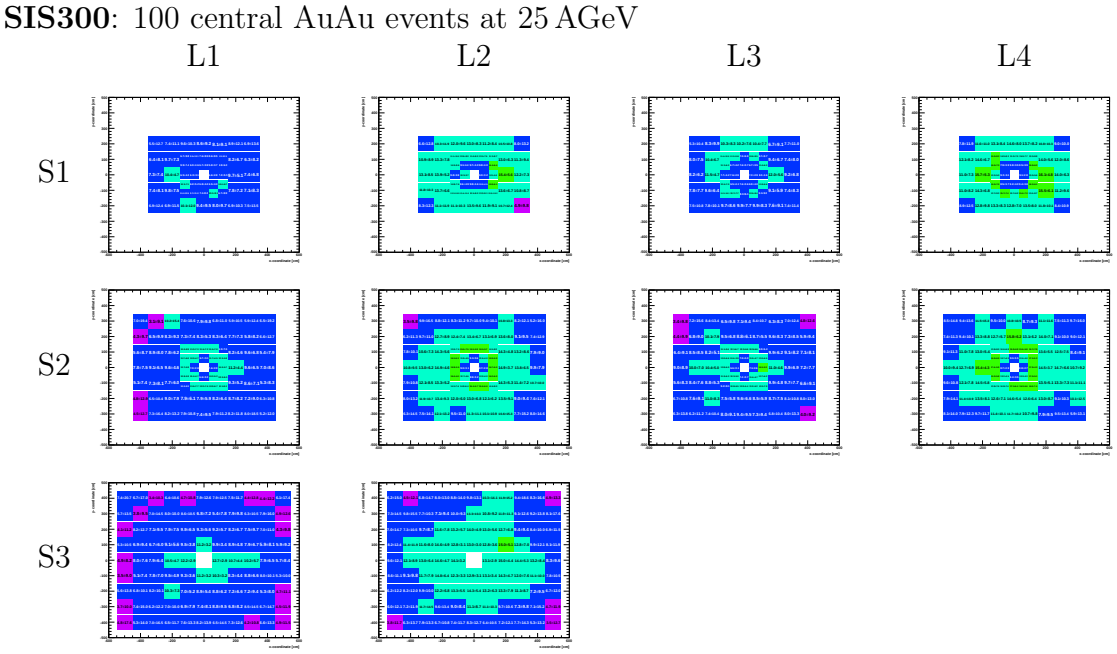

Figure E.3: Average lost points for 100 AuAu events at 25 AGeV for geometry $v12f$.

F. $\mathbf{K_{3,\perp}}$ Fitting Procedure

The used fit function to parametrizes $K_{3,\perp}$ as function of h/s for five different (r_a/s) ratios is a polynomial of fourth degree

$$K_{3,\perp}(h/s = x) = p_1(r_a/s) + p_2(r_a/s)x + p_3(r_a/s)x^2 + p_4(r_a/s)x^3 + p_5(r_a/s)x^4 \quad \text{(F.1)}$$

where the four parameters p_i are all functions of (r_a/s). This approach was chosen in order to get a reasonable description of the data in absence of a theoretical model. The obtained functions are presented in figure F.1. The resulting parameters p_i are fitted to

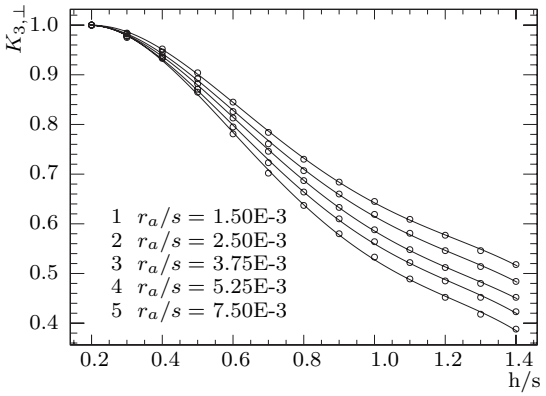

Figure F.1: 13 values taken from figure 4.15 fitted $K_{3,\perp}$ as function of h/s for five different (r_a/s) ratios (enumerated from top to bottom in the original figure 4.15).

a polynomial of third degree (equation F.2) and presented in figure F.2

$$p_i(r_a/s) = u_0 + u_1(r_a/s) + u_2(r_a/s)^2 + u_3(r_a/s)^3 \quad \text{(F.2)}$$

The full two-dimensional parametrization of $K_{3,\perp}$ as function of h/s and (r_a/s) within the parameter ranges given by the five original curves presented in figure 4.15

Table F.1: Obtained fitting parameters p_i and u_j using equation F.1 and F.2.

	u_0	u_1	u_2	u_3
p_1	0.89	22.15	-3769.00	118932.90
p_2	1.16	-216.68	48178.04	-2447131.05
p_3	-3.49	569.45	-154406.27	9295879.37
p_4	3.01	-659.90	178653.38	-11385860.38
p_5	-0.88	241.10	-64171.15	4194790.72

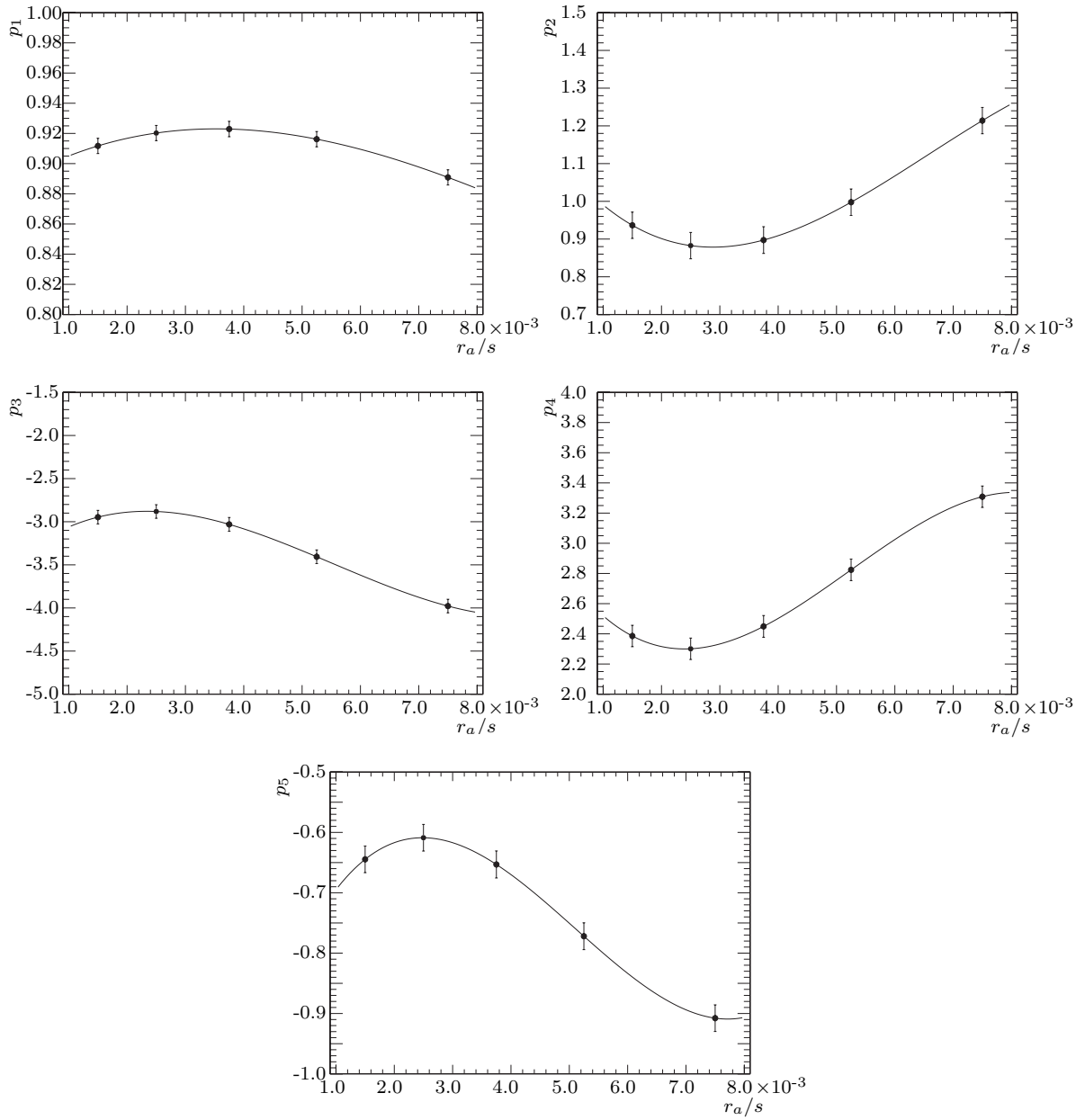

Figure F.2: Fit-parameters p_i as function of (r_a/s) fitted to a polynomial of third degree.

G. Double Hit Identification

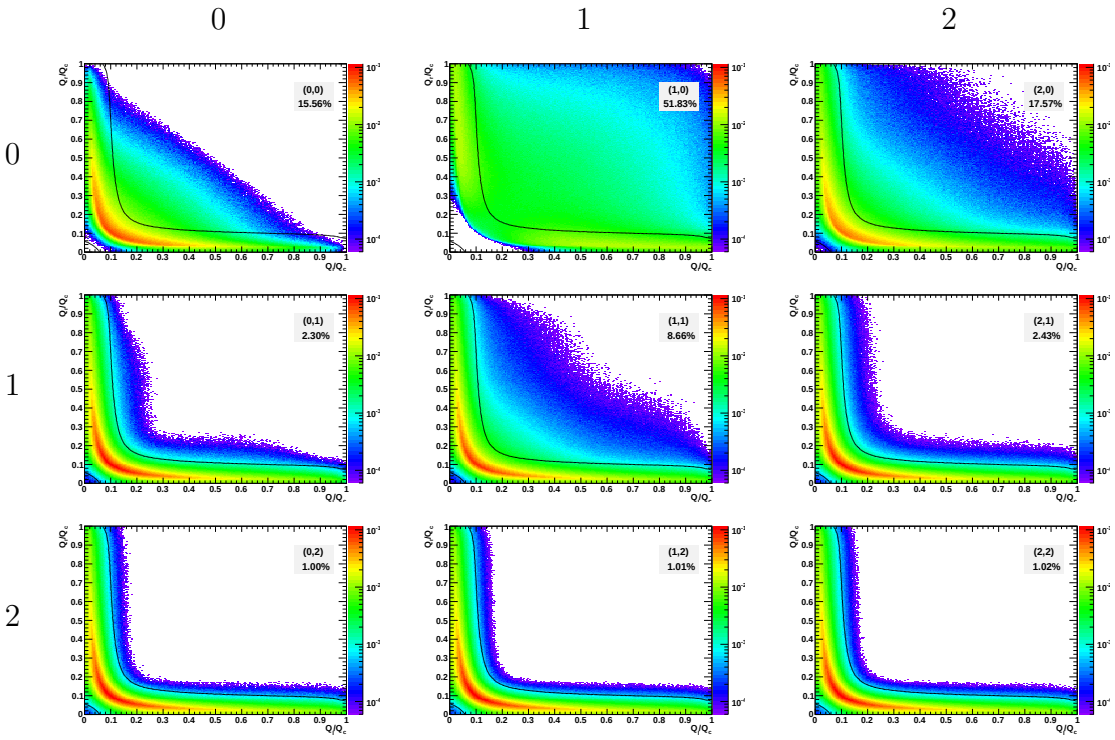

Figure G.1: Double hit distributions classes (x, y) of horizontal charge ratio (A) with cut values for 1% single hit misidentification (black line). The logarithmic color scale cover the range between $5 \cdot 10^{-5}$ and 1.

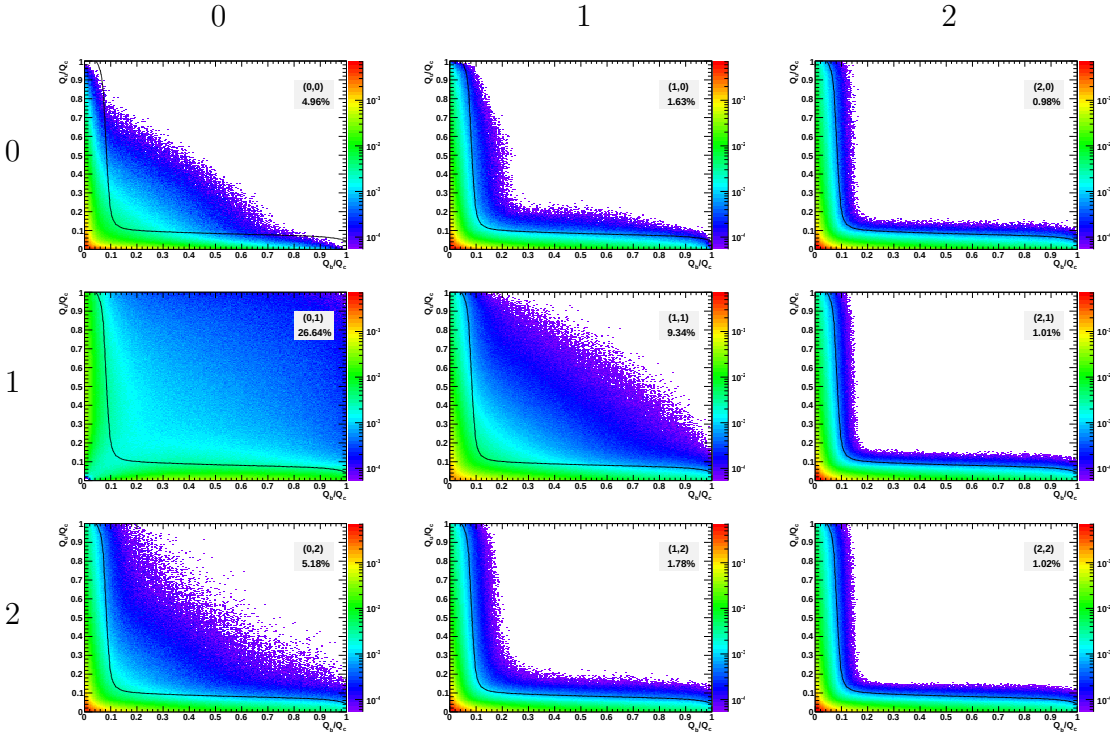

Figure G.2: Double hit distributions classes (x, y) of vertical charge ratio (B) with cut values for 1% single hit misidentification (black line). The logarithmic color scale cover the range between $5 \cdot 10^{-5}$ and 1.

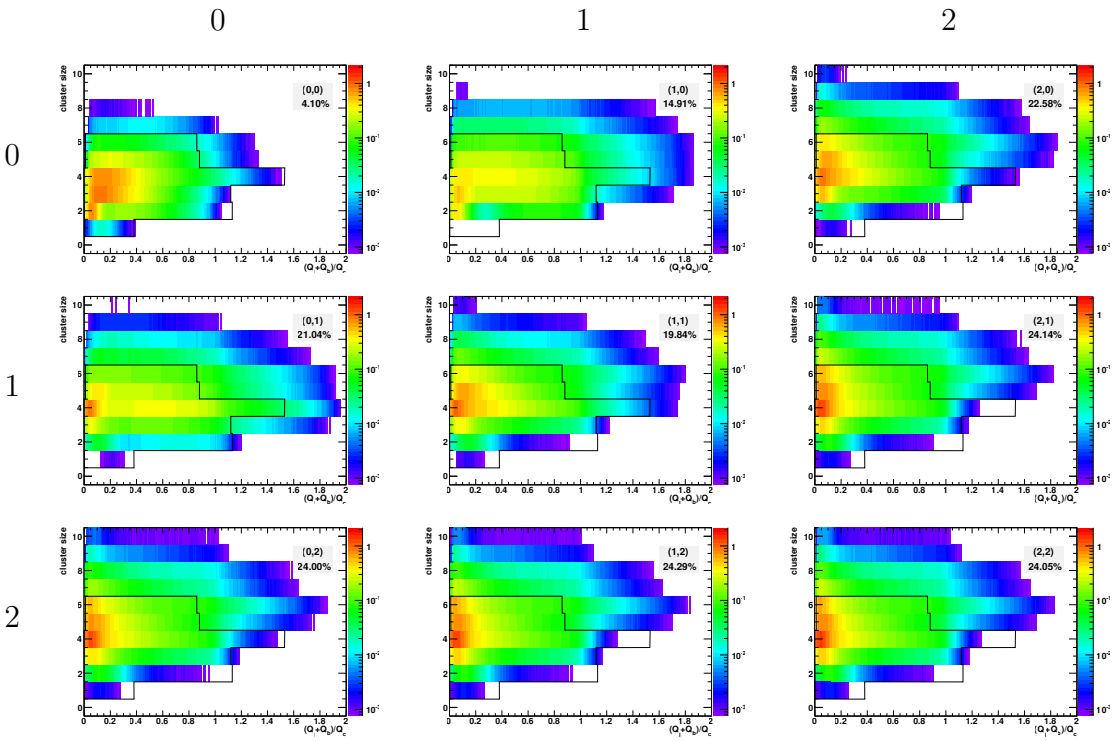

Figure G.3: Double hit distributions classes (x, y) of cluster size vs. $(Q_{[x-1,y]} + Q_{[x,y-1]})/Q_{[x,y]}$ (C) with cut values for 1% single hit misidentification (black line). The logarithmic color scale cover the range between $5 \cdot 10^{-5}$ and 1.

H. List of Acronyms

Table H.1: A collection of some important acronyms:

Acronym	Introduced	Explanation
ADC	p. 109	Analogue to Digital Converter
ALICE	p. 6	A Large Ion Collider Experiment
ASIC	p. 46	Application-Specific Integrated Circuit
CBM	p. 9	Compressed Baryonic Matter
CERES	p. 5	ChErenkov Ring Electron Spectrometer
CERN	p. 5	Conseil Européen pour la Recherche Nucléaire
Ch	p. 106	Cherenkov counter
CR	p. 9	Collector Ring
CSA	p. 103	Charge Sensitive Amplifier
DABC	p. 106	Data Acquisition Backbone Core
DAQ	p. 17	Data AcQuisition
DCC	p. 3	Disoriented Chiral Condensate
DLS	p. 4	DiLepton Spectrometer
ECAL	p. 14	Electromagnetic Calorimeter
eE	p. 39	electron Efficiency
EPICS	p. 106	Experimental Physics and Industrial Control System
FAIR	p. 9	Facility for Antiproton and Ion Research
FEB	p. 45	Front-End-Board
FEE	p. 48	Front-End-Electronic
FFM	p. 90	Frankfurt
FH	p. 106	Fiber Hodoscope
FLUKA	p. 44	Fluktuierende Kaskade (German: Fluctuating Cascade)
FPGA	p. 103	Field Programmable Gate Array
FR4/G10/G11	p. 45	glass-reinforced epoxy laminate; Vetronit
FSc	p. 106	Finger Scintillator
Garfield	p. 36	GAs R... FIELD
GEANT	p. 44	GEometry ANd Tracking
GEM	p. 16	Gas Electron Multiplier
GFM	p. 120	Aalborg mass flow meter
HADES	p. 5	High Acceptance DiElectron Spectrometer
HELIOS	p. 5	High Energy Lepton and IOn Spectrometer
HESR	p. 9	High-Energy Storage Ring
HHG	p. 6	Hot Hadron Gas
HSD	p. 5	Hadron-String Dynamics
KEK	p. 5	National laboratory for high energy physics in Tokyo
L	p. 55	Layer
LHC	p. 6	Large Hadron Collider
LQ	p. 38	Likelihood on total deposited charge (Q)
MAPD	p. 17	Multi-Avalanche Photo-Diodes
MAPS	p. 15	Monolithic Active Pixel Sensors
MB	p. 5	Minimum Bias
MBS	p. 106	Multi Branch System
MC	p. 47	Monte Carlo

Acronym	Introduced	Explanation
MS	p. 90	Münster
MUCH	p. 14	MUon CHamber system
MVD	p. 14	Micro-Vertex Detector
MWPC	p. 18	Multi-Wire Proportional Chamber (Counter)
NDF	p. 32	Number of Degrees of Freedom
neBEM	p. 58	nearly exact Boundary Element Method
NESR	p. 9	New Experimental Storage Ring
NIST	p. 19	National Institute of Standards and Technology
NLO	p. 8	Next-to-Leading Order
NN	p. 36	Neural Network
NUSTAR	p. 9	NUclear STructure, Astrophysics and Reactions
PANDA	p. 9	anti-Proton ANhilation at DArmstadt
PDF	p. 36	Probability Density Function
pE	p. 39	pion Efficiency
PE	p. 23	PolyEthylene
PHENIX	p. 5	Pioneering High Energy Nuclear Interaction eXperiment
PID	p. 14	Particle IDentification
PLUTO	p. 45	event generator for hadronic interactions
PMMA	p. 71	Poly(Methyl MethAcrylate)
PMT	p. 15	PhotoMultiplier Tube
POM	p. 81	PolyOxyMethylene
PP	p. 80	PolyPropylene
PR	p. 18	Position Resolution
PRF	p. 31	Pad Response Function
PS	p. 45	Proton Synchrotron
PS	p. 81	PolyStyrene
PSD	p. 14	Projectile Spectator Detector
PVC	p. 81	PolyVenylChlorid
PYTHIA	p. 45	event generator for hadronic interactions
QCD	p. 1	Quantum ChromoDynamics
QFT	p. 1	Quantum Field Theory
QGP	p. 1	Quark-Gluon Plasma
RHIC	p. 5	Relativistic Heavy Ion Collider
RICH	p. 14	Ring Imaging CHerenkov detector
ROOT	p. 44	Rapid Object-Oriented Technology
RPC	p. 14	Resistive Plate Chamber
S	p. 55	Station
S/N	p. 29	Signal to Noise ratio
Sc	p. 106	Scintillator
SECHS	p. 34	SECant Hyperbolic Squared
SL	p. 37	Significance Level
SPADIC	p. 103	Self-triggered Pulse Amplification and Digitization asIC
SPS	p. 5	Super Proton Synchrotron
STAR	p. 6	Solenoidal Tracker At RHIC
STS	p. 14	Silicon Tracking System
Super-FRS	p. 9	Superconducting Fragment Separator
SUSIBO	p. 106	SuS Interface BOard

Acronym	Introduced	Explanation
TEC	p. 25	Time Expansion Chamber
TIO	p. 120	Totalizer Input/Output
TOF	p. 14	Time Of Flight
TPC	p. 75	Time Projection Chamber
TR	p. 18	Transition Radiation
TRD	p. 14	Transition Radiation Detector
UrQMD	p. 44	Ultra-relativistic Quantum Molecular Dynamics
WLS	p. 17	WaveLength Shifting
XCOM	p. 19	NIST photon cross sections database

References

[Å+89] T. Åkesson et al. Inclusive photon production in pA and AA collisions at 200 GeV/u. *Z. Phys. C*, 46(CERN-EP-89-113):369–375. 19 p, Sep 1989.

[A+95] G. Agakichiev et al. Enhanced Production of Low-Mass Electron Pairs in 200 GeV/Nucleon S-Au Collisions at the CERN Super Proton Synchrotron. *Phys. Rev. Lett.*, 75(7):1272–1275, Aug 1995.

[A+98] G. Agakishiev et al. Systematic study of low mass electron pair production in p Be and p Au collisions at 450-GeV/c. *Eur.Phys.J.*, C4:231–247, 1998.

[A+00a] M.M. Aggarwal et al. Direct Photon Production in 158 A GeV ^{208}Pb + ^{208}Pb collisions. `arXiv:nucl-ex/0006007`, 2000.

[A+00b] M.M. Aggarwal et al. Observation of Direct Photons in Central 158 A GeV 208Pb+208Pb Collisions. `arXiv:nucl-ex/0006008`, 2000.

[A+00c] A.L.S. Angelis et al. Excess of continuum dimuon production at masses between threshold and the J/Ψ in S-W interactions at 200 GeV/c/nucleon. *The European Physical Journal C - Particles and Fields*, 13(3):433–452, 2000.

[A+03a] M.M. Aggarwal et al. Interferometry of Direct Photons in Central 280Pb+208Pb Collisions at 158A GeV. `arXiv:nucl-ex/0310022`, 2003.

[A+03b] S. Agostinelli et al. Geant4-a simulation toolkit. *Nucl. Instr. Meth. A*, 506(3):250–303, 2003.

[A+05] S.S. Adler et al. Centrality Dependence of Direct Photon Production in $\sqrt{s_{NN}}$ = 200 GeV Au+Au Collisions. `arXiv:nucl-ex/0503003`, 2005.

[A+06] R. Arnaldi et al. First Measurement of the ρ Spectral Function in High-Energy Nuclear Collisions. *Phys. Rev. Lett.*, 96:162–302, 2006.

[A+07] G. Agakichiev et al. Dielectron production in C-12+C-12 collisions at 2-AGeV with HADES. *Phys.Rev.Lett.*, 98:052302, 2007.

[A+08a] D. Adamová et al. Modification of the ρ meson detected by low-mass electron-positron pairs in central PbAu collisions at 158 AGeV/c. *Physics Letters B*, 666(5):425–429, 2008.

[A+08b] C. Amsler et al. Review of Particle Physics. *Physics Letters B*, 667(1-5):1–6, 2008. Review of Particle Physics.

[A+09a] A. Adare et al. Enhanced production of direct photons in Au+Au collisions at $\sqrt{s_{NN}}$ = 200 GeV and implications for the initial temperature. `arXiv:0804.4168 [nucl-ex]`, 2009.

[A+09b] A. Andronic et al. Hadron Production in Ultra-relativistic Nuclear Collisions: Quarkyonic Matter and a Triple Point in the Phase Diagram of QCD. `arXiv:0911.4806 [hep-ph]`, 2009.

[A+13] L. Adamczyk et al. Dielectron Mass Spectra from Au+Au Collisions at $\sqrt{s_{\mathrm{NN}}}$ = 200 GeV. `arXiv:1312.7397 [hep-ex]`, 2013.

[Adl05] C. Adler. TRD Chamber Construction Manual Version 1.2. http://cbm.uni-muenster.de/prototype/more/construction/manual/TRD-CCM.pdf, 2005.

[Adl06] C. Adler. Radiation length of the ALICE TRD. http://www.physi.uni-heidelberg.de/~adler/TRD/Radiation%20Length/Radiationlength.pdf, 2006.

[AFP09] T. Armbruster, P. Fischer, and I. Perić, editors. *A Self Triggered Amplifier/Digitizer Chip for CBM*, number 006 in TWEEP-09, 2009.

[AFP10] T. Armbruster, P. Fischer, and I. Peric. SPADIC - A self-triggered pulse amplification and digitization ASIC. *NSS Conference Record, 2010 IEEE, Knoxville, USA*, pages 1358–1362, Nov. 2010.

[AK12] T. Armbruster and M. Krieger. SPADIC1.0 Data Sheet, Version 0.27. http://spadic.uni-hd.de/spadic10/data/spadic10spec.pdf, Oct. 2012.

[ALI01] ALICE Collaboration. ALICE TRD Technical Design Report. Technical report, ALICE, October 2001.

[ALI03] ALICE TRD Collaboration. ALICE Transition Radiation Detector scanning electron microscope images of the radiator materials. Rohacell and fibres. ALICE Collection., Jan 2003.

[AMEKL09] J. Adamczewski-Musch, H. G. Essel, N. Kurz, and S. Linev. Dataflow Engine in DAQ Backbone DABC. Conference record accepted of IEEE NPSS realtime conference Beijing, May 2009.

[Are13] A. Arend. *CBM TRD*. PhD thesis, Institut für Kernphysik Goethe-Universität Frankfurt, 2013. To be submitted.

[Arm13] T. Armbruster. *SPADIC - a Self-Triggered Detector Readout ASIC with Multi-Channel Amplification and Digitization*. PhD thesis, ZITI, Heidelberg University, 2013.

[ATBUK08] M. Al-Turany, D. Bertini, F. Uhlig, and I. König. CBM (Fair) Simulation & Analysis Framework. ALICE Workshop, 08 2008.

[AW11] A. Andronic and J. P. Wessels. Transition Radiation Detectors. arXiv:1111.4188 [physics.ins-det], 2011.

[AYM75] X. Artru, G. B. Yodh, and G. Mennessier. Practical theory of the multilayered transition radiation detector. *Phys. Rev. D*, 12(5):1289–1306, Sep 1975.

[B+85] L.S. Barabash et al. A study of the detection accuracy of proportional chambers with cathode read-out. *Nucl. Instr. Meth. A*, 236(2):271–273, 1985.

[B+02] R. Barlow et al. Recommended Statistical Procedures for BABAR. http://www.slac.stanford.edu/BFROOT/www/Statistics/Report/report.pdf, May 2002.

[B+07] G. Battistoni et al. The FLUKA code: Description and benchmarking. *AIP Conference Proceeding*, 896:31–49, Sep. 2007.

[BBB+98] S. A. Bass, M. Belkacem, M. Bleicher, et al. Microscopic Models for Ultrarelativistic Heavy Ion Collisions. `arXiv:nucl-th/9803035`, 1998.

[BC08] E.L. Bratkovskaya and W. Cassing. Dilepton production and off-shell transport dynamics at SIS energies . *Nuclear Physics A*, 807(3-4):214–250, 2008.

[BCRW98] E.L. Bratkovskaya, W. Cassing, R. Rapp, and J. Wambach. Dilepton production and m_T-scaling at BEVALAC/SIS energies. *Nuclear Physics A*, 634(1-2):168 – 189, 1998.

[Ber09] C. Bergmann. Development and Test of a Transition Radiation Detector Prototype for CBM @ FAIR, 2009.

[BHS+98] J. Berger, J.H. Hubbell, S.M. Seltzer, J. Chang, J.S. Coursey, R. Sukumar, D.S. Zucker, , and K. Olsen. XCOM: Photon Cross Sections Database. NIST Standard Reference Database 8, 3 1998.

[BR94] W. Blum and L. Rolandi. *Particle Detection with Drift Chambers*. Springer, 1 edition, 1994.

[BR97] R. Brun and F. Rademakers, editors. *ROOT - An Object Oriented Data Analysis Framework*, AIHENP'96 Workshop, Lausanne, Sep. 1997. Nucl. Inst. Meth. in Phys. Res. A 389 (1997) 81-86.

[BR02] G.E. Brown and M. Rho. On the manifestation of chiral symmetry in nuclei and dense nuclear matter. *Physics Reports*, 363(2):85–171, 2002.

[Bre06] M. Breitwieser. Dichte und Ausdehnungskoeffizient von Plexiglas, PMMA (Polymethylmetacrylat). `http://www.unimeter.net/`, April 2006.

[BRR08] W. Blum, W. Riegler, and L. Rolandi. *Particle Detection with Drift Chambers*. Springer, 2 edition, 2008.

[C+83] J. Chiba et al. Study of position resolution for cathode readout MWPC with measurement of induced charge distribution . *Nucl. Instr. Meth.*, 206(3):451–463, 1983.

[CFG+88] M. Castellano, C. Favuzzi, N. Giglietto, E. Nappi, and P. Spinelli. A Monte Carlo program to design a transition radiation detector. *Computer Physics Communications*, 51(3):431–441, 1988.

[CMPT74] M. L. Cherry, H. G. Müller, D. Prince, and A. Thomas. Transition radiation from relativistic electrons in periodic radiators. *Phys. Rev. D*, 10(11):3594–3607, Dec 1974.

[Col05] Collaboration, CBM. Compressed Baryonic Matter Experiment-Technical Status Report , 01 2005. `https://www-alt.gsi.de/documents/DOC-2005-Feb-447.html`.

[CTF+13] M. W. Conroy, J. C. Taylor, J. P. Farley, J. W. Fleming, and R. Ananth. Liquid drainage from high-expansion (HiEx) aqueous foams during and after filling of a container. *Colloids and Surfaces A: Physicochemical and Engineering Aspects*, 426(0):70–97, 2013.

[Dam07] S. Damjanovic. NA60 results on the ρ spectral function in in-in collisions. *Nuclear Physics A*, 783(1-4):327–334, 2007. Proceedings of the 2nd International Conference on Hard and Electromagnetic Probes of High-Energy Nuclear Collisions Hard Probes 2006.

[Dil13] P. Dillenseger. Charakterisierung und Signalanalyse von TRD-Prototypen für das CBM Experiment. Master's thesis, Institut fÃ$\frac{1}{4}$r Kernphysik FB 13 Goethe-Universität Frankfurt am Main, September 2013.

[Dja12] C. Djalali. Medium modification of vector mesons. In *HIgh energy Physics in the LHC Era 4th international Workshop*, Valparaiso - Chile, Jan 2012.

[DLH+93] Dalesio, L., Hill, J., Kraimer, M., Murray, D., Hunt, S., Claussen, M., Watson, C., Dalesio, and J. The experimental physics and industrial control system architecture. submitted to ICALEPCS, Oct. 1993.

[DuP11] DuPont. Technical Data Sheet: DuPont Kapton HN polyimide film. `kapton.dupont.com`, 2011.

[E+04] S. Eidelman et al. Review of Particle Physics. *Physics Letters B*, 592(1-4):1–5, 2004. Review of Particle Physics.

[EC96] W. Ehehalt and W. Cassing. Relativistic Transport Approach for Nucleus-Nucleus Collisions from SIS to SPS Energies. `arXiv:hep-ph/9507274`, 1996.

[Ege98a] U. Egede. Simulation of the transition radiation spectrum. `http://www.hep.lu.se/atlas//thesis/egede/thesis-node62.html`, August 1998.

[Ege98b] U. Egede. *The search for a standard model Higgs at the LHC and electron identification in the ATLAS tracker*. PhD thesis, Departmet of physics, Lund University, Sweden, 1998.

[Ems13a] D. Emschermann. CbmRoot TRD geometries. private comunication & CbmRoot SVN, 2010-2013.

[Ems13b] D. Emschermann. Pad-plane design. private comunication, 2010-2013.

[Ems13c] D. Emschermann. CBM TRD - David Emschermann - Physics R&D and IT services. `http://cbm.uni-muenster.de/`, 2013.

[Ent13] M. Entrup. SEM HF110 probe anaylsis. private comunication, Dec. 2013.

[F+07] I. Froehlich et al. Pluto: A Monte Carlo Simulation Tool for Hadronic Physics. `arXiv:0708.2382 [nucl-ex]`, 2007.

[Fab77] C.W. Fabjan. Transition radiation spectra from randomly spaced interfaces. *Nucl. Instr. Meth.*, 146(2):343–346, 1977.

[FHK+11] B. Friman, C. Höhne, J. Knoll, S. Leupold, J. Randrup, R. Rapp, and P. Senger, editors. *The CBM Physics Book*, volume 814. Lecture Notes in Physics; Springer, 1 edition, 2011.

[FS75] C. W. Fabjan and W. Struczinkski. Coherent emission of transition radiation in periodic radiators. *Physics Letters B*, 57(5):483–486, 1975.

[Gea] *Physics Reference Manual Version: geant4 9.4 (17 December, 2010).*

[GF46] V. Ginzburg and I. Frank. Radiation of a uniformly moving electron due to its transition from one medium into another. *Zh. Eksp. Teor. Fiz.*, 16:15–28, 1946.

[GGY75] G.M. Garibian, L.A. Gevorgian, and C. Yang. The calculation of X-ray transition radiation generated in regular- and irregular-layered media. *Nucl. Instr. Meth.*, 125(1):133–137, 1975.

[GLO+79] E. Gatti, A. Longoni, H. Okuno, P. Semenza, et al. Optimum Geometry for Strip Cathodes on Grids in MWPC for Avalanche Localization Along the Anode Wires. *Nucl. Instr. Meth.*, 163:83–92, 1979.

[H+10] C. Höhne et al. Development of a RICH detector for CBM: simulations and experimental tests. *Nucl. Instr. Meth. A*, 639(1):294–297, 2010.

[Hal07] L. Hallermann. A GEM framing procedure developed at DESY, 2007.

[Hei13] N. Heine. Blue print by N. Heine. Private communications, Institut für Kernphysik, Westfälische Wilhelms-Universität Münster, 2010-2013.

[Heu12] J. M. Heuser. Quark Matter 2012. In *The Compressed Baryonic Matter experiment at FAIR-Physics at SIS-100 and SIS-300*, 2012.

[HGD93] B. L. Henke, E. M. Gullikson, and J. C. Davis. X-ray Interactions: Photoabsorption, Scattering, Transmission, and Reflection at E=50-30000 eV, Z=1-92. *Atomic Data and Nuclear Data Tables*, 54(2):181–342, July 1993.

[HH08] R. S. Hayano and T. Hatsuda. Hadron properties in the nuclear medium. `arXiv:0812.1702 [nucl-ex]`, Dec. 2008.

[Hig75] V. L. Highland. Some practical remarks on multiple scattering. *Nucl. Instr. Meth.*, 129(2):497–499, 1975.

[Höh12] C. Höhne. Physics of compressed baryonic matter . https://www-alt.gsi.de/documents/DOC-2012-Dec-62.html, 05 2012. `https://www-alt.gsi.de/documents/DOC-2012-Dec-62.html`.

[HR13] T. Hackfort and T. Reiß. First results from the foil micro-structuring test at Saueressig GmbH & Co KG. Privat Communication, July 2013.

[HS04] J. H. Hubbell and S. M. Seltzer. Tables of X-Ray Mass Attenuation Coefficients and Mass Energy-Absorption Coefficients from 1 keV to 20 MeV for Elements Z = 1 to 92 and 48 Additional Substances of Dosimetric Interest. NIST Standard Reference Database 126, 7 2004.

[Irm94] D. Irmscher. Search for Direct Thermal Photons in the NA45/CERES Experiment. *Nuclear Physics A*, 566(0):347–350, 1994.

[KB05] C. Klein-Bösing. *Production of Neutral Pions and Direct Photons in Ultra-Relativistic Au+Au Collisions.* PhD thesis, Institut für Kernphysik, Westfälische Wilhelms-Universität Münster, 2005.

[KB09] M. Klein-Bösing. *Development of a Transition Radiation Detector and Reconstruction of Photon Conversions in the CBM Experiment*. PhD thesis, Institut für Kernphysik, Westfälische Wilhelms-Universität Münster, 07 2009.

[KB13] C. Klein-Bösing. Study of the Quark-Gluon Plasma with Hard and Electromagnetic Probes. Habilitationsschrift, 2013. Institut für Kernphysik, Westfälische Wilhelms-Universität Münster.

[Kol12] B. Kolipost. Hv-filter-board design. private communication, Institut für Kernphysik, Westfälische Wilhelms-Universität Münster, 2012.

[Kri11] M. Krieger. Entwurf und Simulation eines digitalen Tail-Cancellation-Filters, 2011.

[Leo87] W. Leo. *Techniques for Nuclear and Particle Physics Experiments*. Springer-Verlag, 1987.

[LHLO12] S. Lebedev, C. Höhne, A. Lebedev, and G. Ososkov. Electron reconstruction and identification capabilities of the CBM Experiment at FAIR. *Journal of Physics: Conference Series*, 396(2):022029, 2012.

[Lin12] S. Linev. CBM Online Software - Present State. CBM Workshop on Online Data Processing, Sept. 2012.

[LP95] K. Lau and J. Pyrlik. Optimization of centroid-finding algorithms for cathode strip chambers. *Nucl. Instr. Meth. A*, 366(2-3):298–309, 1995.

[LST72] D.M. Lee, S.E. Sobottka, and H.A. Thiessen. A bifilar helical multiware proportional chamber for position sensitive detection of minimum ionizing particles. *Nucl. Instr. Meth.*, 104(1):179–188, 1972.

[Mag12] Magnet Workgroup and the CBM Collaboration. Technical Design Report for the CBM Superconducting Dipole Magnet. Technical report, 2012.

[Mat88] E. Mathieson. Cathode Charge Distributions in Multiwire Chambers. *Nucl. Instr. Meth. A*, 270:602–603, 1988.

[Maz00] M. N. Mazziotta. A Monte Carlo code for full simulation of a transition radiation detector. `arXiv:physics/9912042 [physics.comp-ph]`, 2000.

[N+06] M. Naruki et al. Experimental Signature of Medium Modifications for ρ and ω Mesons in the 12 GeV p+A Reactions. *Phys. Rev. Lett.*, 96:092301, Mar 2006.

[N+11] K. Nakamura et al. Jp g 37, 075021 (2010) and 2011 partial update for the 2012 edition 27. passage of particles through matter. `http://pdg.lbl.gov/`, February 2011.

[NK10] H.G.Essel N. Kurz. MBS manual and documentation. http://www-win.gsi.de/daq/, March 2010.

[OFRW79] H. Okuno, J. Fischer, V. Radeka, and A.H. Walenta. Azimuthal Spread of the Avalanche in Proportional Chambers. *IEEE Trans.Nucl.Sci.*, 26:160–168, 1979.

[OH+99] S. Ottini-Hustache et al. CATS, a low pressure multiwire proportionnal chamber for secondary beam tracking at GANIL. *Nucl. Instr. Meth. A*, 431(3):476–484, 1999.

[P+97] R.J. Porter et al. Dielectron cross-section measurements in nucleus-nucleus reactions at 1-A/GeV. *Phys.Rev.Lett.*, 79:1229–1232, 1997.

[Pis82] R. D. Pisarski. Phenomenology of the chiral phase transition. *Phys.Lett.B*, 110:155–158, Mar 1982.

[PSD12] PSD Workgroup and the CBM Collaboration. Technical Design Report for the CBM Projectile Spectator Detector (PSD). Technical report, 2012.

[RC06] J. Randrup and J. Cleymans. Maximum freeze-out baryon density in nuclear collisions. *Phys. Rev. C*, 74:047901, 2006.

[RC09] J. Randrup and J. Cleymans. Exploring high-density baryonic matter: Maximum freeze-out density. `arXiv:0905.2824 [nucl-th]`, 2009.

[Rei12] S. Reinecke. Status report fiberhodoscope analysis & report on measurements of the reflectivity of the photodetector cathodes. 19th CBM Collaboration Meeting, session P2 - RICH, Id: 93, March 2012.

[RIC12] RICH Workgroup and the CBM Collaboration. Technical Design Report for the CBM Ring Imaging Cherenkov (RICH) Detector. Technical report, 2012.

[RW00] R. Rapp and J. Wambach. Chiral symmetry restoration and dileptons in relativistic heavy ion collisions. *Adv.Nucl.Phys.*, 25:1, 2000.

[Sau77] F. Sauli. Principles of Operation of Multiwire Proportional and Drift Chambers, 1977. Lectures given in the Academic Training Programme of CERN, 1975-1976.

[SCS11] H.-C. Schultz-Coulon and J. Stachel. Lecture 2. `http://www.kip.uni-heidelberg.de/~coulon/Lectures/Detectors/Free_PDFs/Lecture2.pdf`, 2011.

[Sen09] P. Senger. Status of the CBM Experiment at FAIR. Technical report, CBM Progress Report, 2008,2009.

[SMS06] T. Sjostrand, S. Mrenna, and P. Skands. PYTHIA 6.4 Physics and Manual. `arXiv:hep-ph/0603175`, 2006.

[SOF12] SOFIA Collaboration. MWPC reconstruction algorithms. In *Collaboration meeting SOFIA*, pages 5–6. cea, IPN Orsay, June 2012.

[Ste06] M. A. Stephanov. QCD phase diagram: an overview. `arXiv:hep-lat/0701002`, 2006.

[STS12] STS Workgroup and the CBM Collaboration. Technical Design Report for the CBM Silicon Tracking System (STS). Technical report, Dec. 2012.

[Toi08] A. Toia. e^+e^- pairs: a clock and a thermometer of heavy ion collisions. *Journal of Physics G: Nuclear and Particle Physics*, 35(10):104037, 2008.

[TW01] A. W. Thomas and W. Weise. *The Structure of the Nucleon*. WILEY-VCH, Berlin, 2001.

[TYS74] Tsai and Yung-Su. Pair production and bremsstrahlung of charged leptons. *Rev. Mod. Phys.*, 46(4):815–851, Oct 1974.

[VAC10] VACOM Vakuum Komponenten & Messtechnik GmbH. Pumpenöle. `www.vacom.de`, October 2010.

[Vee10] R. Veenhof. Garfield Version 9. http://garfield.web.cern.ch/garfield/, 2010.

[Ver13] W. Verhoeven. Blue print by W. Verhoeven. Private communication, Institut für Kernphysik, Westfälische Wilhelms-Universität Münster, 2010-2013.

[VvE+94] Y.P. Viyogi, N. van Eijndhoven, et al. Photon multiplicity measurements in nucleus-nucleus collisions at 200 A GeV. *Nuclear Physics A*, 566:623–628, 1994. Copyright: Copyright (c) 2003 Elsevier B.V.

[W+08] M. H. Wood et al. Light vector mesons in the nuclear medium. *Phys. Rev. C*, 78:015201, Jul 2008.

[WBW96] R. Wurzinger, Y. Le Bornec, and N. Willis. Monte Carlo studies on Cathode Strip/ Pad Chambers for the ALICE Di-Muon Arm. DRAFT : 23/4/1996. http://cds.cern.ch/record/308074/files/SCAN-9608042.pdf, April 1996.

[Wie96] J. Wiedemann. *Leichtbau: Elemente*. Springer-Verlag GmbH, 2 edition, 1996.

[Wil04] A. Wilk. Elektronen- Pionen- Separation im ALICE TRD, 2004.

[Wil12] M. Wilde. Measurement of Direct Photons in pp and Pb-Pb Collisions with ALICE. `arXiv:1210.5958 [hep-ex]`, Oct. 2012.

[ZBH+07] X. Zhu, M. Bleicher, S.L. Huang, K. Schweda, H. Stoecker, N. Xu, and P. Zhuang. $D - \bar{D}$ Correlations as a sensitive probe for thermalization in high-energy nuclear collisions. `arXiv:hep-ph/0604178`, 2007.